Nanoparticle Charge and Shape Measurements using Tuneable Resistive Pulse Sensing

by

James 'Elf' Eldridge

A thesis
submitted to the Victoria University of Wellington
in fulfilment of the
requirements for the degree of
Doctor of Philosophy
in Physics.

Victoria University of Wellington

2016

Abstract

Accurate characterisation of micro- and nanoparticles is of key importance in a variety of scientific fields from colloidal chemistry to medicine. Tuneable resistive pulse sensing (TRPS) has been shown to be effective in determining the size and concentration of nanoparticles in solution. Detection is achieved using the Coulter principle, in which each particle passing through a pore in an insulating membrane generates a resistive pulse in the ionic current passing through the pore. The distinctive feature of TRPS relative to other RPS systems is that the membrane material is thermoplastic polyurethane, which can be actuated on macroscopic scales in order to tune the pore geometry.

In this thesis we attempt to extend existing TRPS techniques to enable the characterisation of nanoparticle charge and shape. For the prediction of resistive pulses produced in a conical pore we characterise the electrolyte solutions, pore geometry and pore ζ-potential and use known volume calibration particles. The first major investigation used TRPS to quantitatively measure the ζ-potential of carboxylate polystyrene particles in solution. We find that ζ-potential measurements made using pulse full-width half maximum data are more reproducible than those from pulse rate data. We show that particle ζ-potentials produced using TRPS are

consistent with literature and those measured using dynamic light scattering techniques.

The next major task was investigating the relationship between pulse shape and particle shape. TRPS was used to compare PEGylated gold nanorods with spherical carboxylate polystyrene particles. We determine common levels of variation across the metrics of pulse magnitude, duration and pulse asymmetry. The rise and fall gradients of resistive pulses may enable differentiation of spherical and non-spherical particles.

Finally, using the metrics and techniques developed during charge and shape investigations, TRPS was applied to *Rattus rattus* red blood cells, *Shewanella marintestina* bacteria and bacterially-produced polyhydroxyalkanoate particles. We find that TRPS is capable of producing accurate size distributions of all these particle sets, even though they represent non-spherical or highly disperse particle sets. TRPS produces particle volume measurements that are consistent with either literature values or electron microscopy measurements of the dominant species of these particle sets. We also find some evidence that TRPS is able to differentiate between spherical and non-spherical particles using pulse rise and fall gradients in *Shewanella* and *Rattus rattus* red blood cells. We expect TRPS to continue to find application in quantitative measurements across a variety of particles and applications in the future.

Acknowledgments

This thesis owes its completion to a large number of individuals, the majority of whom I have endeavoured to mention below. There will inevitably be omissions, for which I pre-emptively apologise.

Firstly to my mother and father, Barry and Cheryl Eldridge, and my siblings, Nicki, Kiri and Gavin, without whom I would not have had the support and confidence to start a thesis - let alone complete one.

To Mike Arnold and Jason Ryan for work culturing, isolating and providing optical microscope photographs of *Shewanella marintestina* cultures.

To Andrea Bubendorfer, John Beal and the Callaghan Innovation microfluidics team.

To Te Ropu Awhina, for support, whanau, friends, and the courage to persist in times of adversity.

To Catherine Davis and Shalen Kumar; the former for her contributions to attempts to photograph rat blood and bacteria, and for proofreading and to both for their friendship and unending support and understanding.

To the Victoria University School of Engineering and Computer Science, in particular to Craig Watterson, for their support during my thesis

writeup and edit.

To the MacDiarmid Institute for Advanced Materials and Nanotechnology for funding, mentorship and encouragement.

And finally, and most importantly, to my supervisor, Dr. Geoff Willmott, for his tireless patience, encouragement and tolerance of me and my many distractions during my experiments and write-up.

Contents

Publications and Presentations

Publications with Material Used in this Thesis

- J. Eldridge, A. Colby, G. R. Willmott, S. Yu and M. Grinstaff, in Selected Topics in Nanomedicine, ed. T. M. S. Chang, World Science, Singapore, 2013, vol. 3, ch. 10, pp. 219-255.
- J. Eldridge, R. Vogel, G. Willmott, Nanoparticle ζ-potential measurements using tunable resistive pulse sensing with variable pressure. *Journal of Colloid and Interface Science,* 429:45-52, September 2014.

Co-authored Publications Arising from PhD Studies

- R.Vogel, W. Anderson, J. Eldridge, B. Glossop, G. Willmott, A variable pressure method for characterising nanoparticle surface charge using pore sensors. *Anal. Chem.* 84:3215, 2012.
- J. Somerville, G. Willmott, J. Eldridge, M. Griffiths, Size and Charge

Characterization of a Submicrometre Oil-in-Water Emulsion using Resistive Pulse Sensing with Tunable Nanopores. *Journal of Colloid and Interface Science,* 394:1-26, March 2013.

- G. Willmott, M. Fisk, J.Eldridge, Magnetic Microbead transport during resistive pulse sensing. *Biomicrofluidics* 7:64104, 2013.

Major Conference Presentations

- Eldridge, J. A., Parry, B. & Willmott, G.R. (2011, February), *Tunable Nanopores: Solution Dependence for Detecting Polystyrene Spheres.* Poster presented at Fifth International Conference on Advanced Materials and Nanotechnology (AMN-5), Wellington, New Zealand.

- Eldridge, J. A., & Willmott, G. R., (2011, July), *Nanoparticle Detection and Charge Quantification using Tunable Nanopores.* Poster presented at New Zealand Institute of Physics conference, Wellington, New Zealand.

- Eldridge, J. A., Vogel, R. & Willmott, G. R. (2012, February), *Particle charge measurement for nanomedicine using resistive pulse sensing.* Talk given at 28th Australian Colloid and Surface Science Student Conference, Newcastle, Australia.

- Eldridge, J. A., Vogel, R. & Willmott, G. R. (2012, April), *Multiple methods for particle charge detection using tunable nanopores.* Talk given

at 3rd Australia and New Zealand Micro/Nanofluidics Symposium and Student Workshop, Wellington, New Zealand. **Best student speaker.**

- Eldridge, J. A., Vogel, R. & Willmott, G. R. (2012, July), *Interrogating nanoparticle with Nanopores: Tunable Nanopore methods for Charge Measurement.*, Poster presented at International Conference on Nanoscience and Nanotechnology, Paris, France. **Student poster prize.**

- Eldridge, J. A., Vogel, R. & Willmott, G. R. (2013, February), *Nanoparticle charge detection with resistive pulse sensing in tunable pores.* Talk given at Sixth International Conference on Advanced Materials and Nanotechnology (AMN-6), Auckland, New Zealand.

- Eldridge, J. A., Willmott, G. R., Anderson, W. A. & Vogel, R. R. (2013, April), *Nanoparticle investigations using tunable nanopore sensing.* Talk given at 4th Australia and New Zealand Micro/Nanofluidics Symposium and Student Workshop, Adelaide, Australia.

Symbols List

Symbol	Units	Description
α	m s^{-2}	acceleration due to external force
γ	Pa s m	drag coefficient
ε	C^2 N^{-1} m^{-1}	$\varepsilon = \varepsilon_0 \varepsilon_r$
ε_m	C^2 N^{-1} m^{-1}	medium permittivity
ε_p	C^2 N^{-1} m^{-1}	particle permittivity
ζ	V	ζ-potential
$\zeta_{particle}$	V	ζ-potential of particle
ζ_{pore}	V	ζ-potential of the pore walls
η	Pa s	fluid dynamic viscosity
κ	m^{-1}	inverse of the Debye length
$\lambda(z)$	m	pore radius function
λ_D	m	Debye length
μ_{eo}	m^2 V^{-1} s^{-1}	electro-osmotic mobility
μ_{eph}	m^2 V^{-1} s^{-1}	electrophoretic mobility
ρ_e	Ω m	electrolyte resistivity

ρ_d	kg m^{-3}	density
ρ_{df}	kg m^{-3}	fluid density
ρ_{dp}	kg m^{-3}	particle density
σ	C m^{-2}	surface charge density of a solid
$\sigma_e(y)$	C m^{-2}	charge density in a liquid adjacent to a surface located at $y = 0$
ψ	J C^{-1}	electrostatic potential field

---

a	m	radius of small pore opening
A	m	cross-sectional area
b	m	radius of small pore opening
C	mol L^{-1}	concentration
d	m	length of pore
D	m^2 s^{-1}	diffusion coefficient
e	C	charge of an electron
$\mathbf{E}$	V m^{-1}	electric field
f		structure factor
f_{CM}		Clausius-Mesotti factor
f_{factor}		pulse asymmetry factor
$\mathbf{f}$	N	body force
F	N	scalar body force such that $\mathbf{f} = \Delta F$
F_c	N	coulombic force
F_{DEP}	N	dieletrophoretic force

F_d	N	Stokes drag
g	m s^{-2}	gravitational acceleration
H		volume fraction occupied by an insulating particle
I	A	baseline current through the aperture
ΔI	A	resistive pulse magnitude
I_s	A	streaming current
J	s^{-1} m^{-2}	particle flux
J_{diff}	s^{-1} m^{-2}	particle flux due to diffusion
J_{eo}	s^{-1} m^{-2}	particle flux due to electro-osmosis
J_{eph}	s^{-1} m^{-2}	particle flux due to electrophoresis
J_{dep}	s^{-1} m^{-2}	particle flux due to dielectrophoresis
J_{pd}	s^{-1} m^{-2}	particle flux due to pressure driven flow
J_{diff}	s^{-1} m^{-2}	particle flux due to diffusion
k_B	m^2 kg s^{-2} K^{-1}	Boltzmann constant
n_0	mol L^{-1}	concentration of free ions in solution
n_i	mol L^{-1}	concentration of ion i in solution
P	Pa	net pressure applied across the membrane
P_0	Pa	pressure at balance point
$P_{inherent}$	Pa	inherent pressure head
$P_{applied}$	Pa	external pressure applied across the membrane

q	C	net charge on a particle
Q_p	$m^3\ s^{-1}$	pressure driven volumetric flow rate
r	m	radius of particle
r_H	m	hydrodynamic radius of particle
R	Ω	total resistance of system
R_{ends}	Ω	electrical resistance due to pore openings
R_{pore}	Ω	electrical resistance aperture filled with electrolyte
ΔR	Ω	increase in resistance of system due to presence of particle
$S()$		correction factor based on volume fraction
t	s	time
T	K	temperature in Kelvin
T_r	Pa s m^{-3}	net flow resistance to pressure driven flow $T_r = T_i + T_a$
T_i	Pa s m^{-3}	flow resistance to pressure driven flow from interior of aperture
T_a	Pa s m^{-3}	flow resistance to pressure driven flow from access to aperture
v	m s^{-1}	fluid velocity
V	V	applied voltage
V_{str}	V	streaming voltage
v_{eo}	m s^{-1}	electro-osmotic velocity

v_{eph}	m s^{-1}	electrophoretic velocity
v_{set}	m s^{-1}	settling velocity
x	m	radial distance from central pore axis (z)
X	m	distance between membrane mounting teeth (membrane stretch)
y	m	distance from surface (y = 0) into fluid through EDL
z	m	distance into pore from small pore opening (z = 0)
z_i		ion charge magnitude

List of Figures

List of Tables

Chapter 1

Introduction

> *"At the atomic level, we have new kinds of forces and new kinds of possibilities, new kinds of effects. The problems of manufacture and reproduction of materials will be quite different. I am, as I said, inspired by the biological phenomena in which chemical forces are used in a repetitious fashion to produce all kinds of weird effects (one of which is the author).*
>
> *The principles of physics, as far as I can see, do not speak against the possibility of manoeuvring things atom by atom. It is not an attempt to violate any laws; it is something, in principle, that can be done; but in practice, it has not been done because we are too big."*

The preceding quote, taken from Nobel laureate Richard P. Feynman's 1959 address entitled *"There's Plenty of room at the Bottom"* [1], is often cited as the birth of nanotechnology as a field. Feynman noted that, whilst there were significant technological barriers to overcome, there was vast poten-

tial for nanoscale technologies and he urged further study, in particular, of biological systems.

Science has made incredible advances since Feynman's speech and one field that particularly epitomises his vision of the unity between chemistry, biology and physics is the growing field of nanopore sensing. Stemming from Coulter's use of micropores to automatically count cells [2], nanopore sensing has blossomed with the creation of nanopores with widths from $\sim$1 nm to $>$1000 nm. This size range is relevant to nanoparticles, emulsions, bacteria, viruses, exosomes, platelets and even small molecules such as nucleotides relevant for 3rd generation DNA sequencing. The evolution of nanopore synthesis, from both biological and synthetic sources has charted a path through the interdisciplinary space between biology and physics. New Zealand's commercial foray into this sphere began with the patent and publication of a simple, cost-effective nanopore synthesis method by Sowerby *et al.* in 2007 [3]; the beginning of an endeavour that would ultimately end up in the founding of Izon Science (Christchurch). This thesis is concerned with understanding and developing tuneable resistive pulse sensing (TRPS), the distinctive nanopore technology commercialised by Izon.

This thesis begins by charting the path of nanopore development since Feynman's time to the modern application of nanopore sensing to tuneable resistive pulse sensing (TRPS). Chapter 1 provides some context for the TRPS research presented in the remainder of the thesis. Chapter 2

provides a detailed review of the literature relevant to TRPS; describing the production and use of robust, tuneable nanopores. We also explain where TRPS has found use in areas from nanoparticle characterisation to nanomedicine.

Chapter 3 discusses the theoretical background of RPS systems, centering on the use of the Nernst Planck equation to summarise nanoscale phenomena in TRPS. In addition, Chapter 3 introduces the semi-analytic model used to predict resistive pulses generated by particles traversing pores of known geometry. Chapter 4 introduces the materials and methodologies used during the experimental chapters (Chapters 5, 6 and 7) of this thesis. Chapter 4 also documents the results of the characterisation of pores used during TRPS experiments in the thesis.

Chapter 5 provides an experimental comparison of different methods of nanoparticle charge measurement using both TRPS and dynamic light scattering (DLS) techniques. In Chapter 6 we make TRPS measurements of rod-shaped gold nanorods to evaluate the ability of TRPS to determine the shape of nanoparticles beyond merely volume measurement. We also introduce asymmetry and pulse gradient as novel metrics for evaluating resistive pulses based on their shape characteristics. Chapter 6 also extends the semi-analytic model to allow for non-spherical particles and predicts the pulses generated by rotated spheroids. Chapter 7 then applies the metrics and practices developed in Chapter 5 and 6 to complex nanoparticle systems: whole *Rattus rattus* blood, rod-shaped *Shewanella marintestina*

bacteria and bacterial polyhydroxyalkanoate (BPHA) particles. Chapter 8 provides concluding remarks and comments on areas for future TRPS research.

We begin by providing some general context for this research by giving a brief overview of the fields where TRPS research fits: nanotechnology and medical device technologies.

1.1 Context: Nanotechnology and Medical Devices

Feynman closed his address by offering two prizes, which he hoped would foster growth and rapid developments in this field; one for developing an operating electric motor '*only 1/64 inch cube*' and one for fitting all the information on the page of a book and '*putting it on an area 1/25,000 smaller in linear scale in such a manner that it can be read by an electron microscope*' [1]. To even Feynman's surprise, both of these prizes were claimed within two decades, in 1960 and 1985 respectively [4], and stand as testament to the rapid development of the field of nanotechnology since then.

Half a century on from Feynman, nanotechnology has blossomed into an enormously diverse field of research, including aspects of physics, engineering, consumer electronics, medical care and fundamental biology. The modern definition of nanotechnology has drifted slightly from Feynman's description of the field as manipulation of individual atoms, to anything

involving length scales of 0.1-100 nm. Practically, the term *nanotechnology* is also often used to discuss any structures smaller than the wavelength of visible light, a fact that accounts for much of the colour-modifying effects of nano-structures such as the iridescence of butterfly wings [5].

The development of techniques for interacting with nano-scale particles, surfaces and structures, such as atomic force microscopy (AFM) and scanning tunnelling microscopy (STM), have enabled the control and commercialisation of nanoscale phenomena. However, even with modern technologies, interacting, measuring and characterising the nanoscale is still a non-trivial endeavour. The highest resolution nanoscale techniques often require sample treatment and preparation prior to measurement, adding both complexity and cost to any analysis. Techniques also necessitate the use of highly sophisticated and expensive equipment to make measurements or structures to nano-scale precision. Rapid, cheap and accurate nanoscale tools must also be developed to allow this field to continue to flourish. This includes both high specificity techniques such as ELISA (enzyme-linked immunosorbent assay) and non-specific techniques such as TRPS.

The broad commercial banner of medical device technologies (MDT), attempts to encompass a field that contains a range of sciences from the physics behind magnetic resonance imaging (MRI) machines to the chemistry and biology of novel microfluidic assays. MDT can trace its roots to the development of X-ray imaging and the electrocardiogram (ECG) in

the early 1900s, is still only in its infancy, and currently represents one of the most rapidly changing markets in the world [6]. A 'medical device' can be defined as any technology that can be used in the diagnosis, prevention, monitoring, treatment or alleviation of a disease, injury or during any other medical procedure or test relevant to the treatment of human beings [6]. Currently, the global market for medical technology is estimated at US$350 billion from 2008 data, the majority of which stems from government spending in the US (US$160 billion) and Europe (US$110 billion) followed by Japan (US$30 billion), China and India (US$5 billion) [6].

The MDT industry is characterised by several attributes that separate it from similar industries; the high product turnover time (50% of products are replaced after being on the market only 5 years) and a short investment recovery period (approximately 18 months [6]). Interestingly, spending on healthcare and MDT also increases in proportion to national expenditure in countries with higher income economies [6]. For example in 2008 the USA spent 17.3% of its GDP on healthcare whereas lower and middle income, but rapidly growing economies, such as India and China, only spend around 4.3% [6]. However as these economies continue to grow, their proportional healthcare expenditure is expected to shift to proportions that more similarly reflect that of typical western nations.

Within this industry environment TRPS has been driven to rapid development, deployment and application in order to keep pace with the market. The rate of publication for applications of TRPS in the qNano sys-

tem (reviewed in detail in Chapter 2) and the application of TRPS to more markets, suggests that this trend is likely to continue [7].

1.2 Rise of Resistive Pulse Sensing

RPS found application in bioscience as early as 1953 when Coulter patented the first 'Coulter Counter' as a device for sizing and counting cells in solution [2]. In a typical Coulter counter, pressure-driven flow is used to force cells through a microscale aperture bored in an insulating membrane. When filled with electrolyte and with an electric potential applied across the pore, ionic current flows through the aperture (Figure 1.1 a)). The passage of insulating particles through the aperture causes a current drop with magnitude approximately determined by the relative volume of aperture and particle - creating a resistive pulse (Figure 1.1 b)) [8]. The resolution of these devices is dictated primarily by the aperture size, and Coulter Counters are still used for reliable detection and counting of particles larger than 500 nm, including micro-organisms, blood cells, spermatozoa, platelets, algae and yeasts [9]. RPS is extensively reviewed in Chapter 2.

Initially RPS was used to detect individual cells of several micrometers in size, but by 1970 DeBlois and others had created pores in polycarbonate of down to 10 nm diameter by nuclear particle track etching [10]. These pores were able to detect polystyrene spheres down to a lower size limit of 60 nm. In 1978 DeBlois and co-workers used the same pores to count

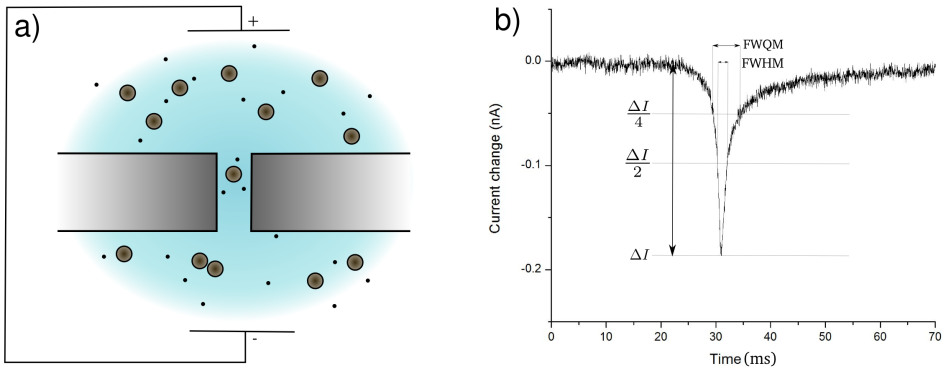

Figure 1.1: Figure a) illustrates a simple RPS sensing system with membrane, electrolyte and the presence of insulating particles. b) A typical pulse produced by the passage of a spherical 200 nm polystyrene particle in 0.1 M KCl electrolyte passing through a conical pore showing pulse characteristics of: magnitude (ΔI), full-width at half-maximum (FWHM) and full-width at quarter maximum (FWQM) durations.

individual virions of T2 bacteriophages and other viruses [11, 12] with diameters approaching 96 nm. Interestingly, by carefully controlling the pressure across the pore, DeBlois and Bean were also able to make electrokinetic measurements of sub-micron particles based on the change in their transition times through a long, cylindrical pore [11]. This provided an early indication of the potential for RPS to be developed into a detection system for more than simply the size of small particles. The drawback with these pores was their lack of reproducibility due to the complexity of their manufacture, leading researchers to extend their search using alternative synthetic (discussed in Chapter 2.1.3) and biological (discussed in Chapter 2.1.2) pore materials [13]. The next major step in RPS research occurred in the mid-1990s, when Kasianowicz [14] reported the detection

of nucleic acid by RPS in nanopores, hinting at the possibility of the use of RPS in nanopores to identify individual nucleotides. By this time, interest in biological and synthetic sub-micron particles had grown, and techniques suitable for nanoscale particle and pore fabrication had matured. In the 40 years following DeBlois's electrokinetic measurements, nanopores have been synthesized using a variety of materials and techniques in range of sizes (summarised in [15]). However RPS experiments can be limited by the reproducibility and cost associated with nanopore manufacture [16].

In 2007 Sowerby *et al.* [3] published a method for rapidly producing nanopores in a cheap material, thermoplastic polyurethane (TPU). The nanopores were made by mechanically puncturing a thin TPU layer with a tungsten needle chemically etched to nanoscale dimensions. When used for RPS, these nanopores could be stretched and relaxed to alter the nanoscale dimensions of a pore. This allowed the system to be 'tuned' to optimise the signal generated by the blockade events of particles, or to screen the passage of larger species in a disperse sample [17, 18].

Izon Science (previously Australo) commercialised the intellectual property associated with the manufacture and use of tuneable nanopores in membranes of TPU created by the method outlined in Chapter 4 [7]. These nanopores have been used to detect the passage of nanoparticles using tuneable resistive pulse sensing (TRPS). The use of TPU was a main point of differentiation between competing technologies for particle characterisation, such as DLS, due to its low cost, relatively high pore manufac-

ture rate and due to TPU's elastomeric properties. This prompted the use of terms such as 'adjustable', 'elastomeric' and 'tuneable' in the description of nanopores, all of which simply describe the ability of the pore to be adjusted. The combination of these technologies and use of Izon Science's proprietary software (Izon Control Suite) for analysing current trace and particle translocations, is occasionally referred to as Scanning Ion Occusion Microscopy (SIOS). TRPS has been applied to measurements of a fast-growing range of particles in various experimental contexts reviewed in Chapter 2.

To this existing body of work, this thesis adds a comparison of differing charge measurement methodologies, development of TRPS analysis of varied geometry particles, a detailed examination of the characteristic shape of individual events, various analysis tools, and the application of all of these to a range of complex particle distributions not previously studied using TRPS.

Chapter 2

Literature Review

In this Chapter we review literature and techniques relevant to the background of resistive pulse sensing (RPS) and similar techniques for nanoparticle detection and measurement. We begin by reviewing the history of RPS and the development of both biological and synthetic pore fabrication methods. We continue by presenting the publications underlying the development of tuneable resistive pulse sensing (TRPS). We discuss the application of TRPS to measurements of both nanoparticle size and charge and conclude by presenting a selection of comparable nanoparticle characterisation techniques.

2.1 Resistive Pulse Sensing (RPS)

A resistive pulse sensing (RPS) experiment (Figure 1.1) uses an individual micro- or nanopore which tunnels between the surfaces of a thin mem-

brane. The membrane is immersed in an aqueous electrolyte, wetting the pore, and when a voltage is applied to electrodes on either side of the membrane, a current is carried through the pore by mobile ions in the electrolyte. When insulating particles are introduced to the system and migrate through the pore, their presence restricts the flow of ions and thus is detectable as a transient decrease in the recorded current (Figure 1.1). This is known as a 'resistive pulse' or alternatively as a 'blockade', 'event' or 'translocation'. Events are usually characterised by three metrics: pulse current magnitude (ΔI), duration, and the frequency at which they occur. These blockades can be used to not only detect the presence of a particle in the pore, but also to measure the particle's size and other characteristics, to resolutions dictated by the size of the pore and other factors.

2.1.1 Early RPS

RPS was established as a microparticle sensing technique by Coulter in 1953, who patented his device as a 'Coulter Counter', used for rapid automatic counting and sizing of blood cells in solution [2, 19]. Originally Coulter created a cylindrical micropore (which he referred to as an aperture or orifice) in glass with a typical diameter and length of 100 μm and 70 μm respectively, with microparticles being driven through the pore due to an applied hydrostatic pressure differential across the membrane such that resistive pulse durations were between 10 and 20 μs. As Coulter himself noted, increasing the sample size from typical reported values of

around 500 total cells at a time would significantly reduce the random sampling error inherent in cell counting experiments, even accounting for potential coincidence events where multiple cells are simultaneously present in the aperture. Early Coulter counters were able to achieve cell count rates of >3000 per second with automated apparatus. Even at this early stage, Coulter noted that the exact coincidence of two cells would generate a pulse equal in height to the sum of two individual pulses, but that this was seldom observed because pulses were *'of a peaked form'* rather than rectangular which was expected for a cylindrical pore, hinting at the complex relationship between pore geometry, particle shape and pulse shape [19].

Subsequently Gregg and Steidley [20] developed theory around the properties of dielectric particles in a conducting solution traveling through a cylindrical aperture, considering the implications of particle capacitance (particularly for cellular samples) and resistivity. For spherical particles in an electrolytic solution they suggested a resistive pulse size of

$$\Delta R \approx \frac{\rho L \beta (1+\gamma)}{A\gamma} \tag{2.1}$$

where β is the ratio of volumes between cylinder and particle (given as $\beta = 4\pi a^3/3LA$), ρ is the electrolyte resistivity, a is the radius of the particle, and L and A are the length and cross-sectional area of the cylinder respectively. γ is a shape factor with $\gamma = 2$ for spheres and $\gamma = 1$ for cylindrical rods with their major axis aligned with the cylindrical pore axis.

The shape factor here was described as a consequence of the deviation of the electric field lines around a sphere with resistivity much greater than that of the electrolyte. The authors also predicted large changes in ΔR for spheroidal geometry particles such as ellipsoidal rods and disks due to 'end' effects dominating the resistance characteristics of these particles. They compared their theoretical predictions of ΔR to pulses produced experimentally in a Coulter Counter from mouse lymphoblasts (discs), latex particles (spheres) and pollen spores (rods). Whilst they reported reasonable agreement, they also observed spurious events that were attributed to off-axis motion of particles.

After the publication of a method for generating nanopores in polycarbonate by ion-track etching by Price *et al.* [21], DeBlois and Bean were able to push the resolution of RPS from 0.5 μm diameter particles down to 90 nm particles with tapered cylindrical pores. Pore diameters were determined to be 0.45 μm and 0.49 μm by optical microscopy, and a length of $\sim$3 μm was calculated from their measured resistance [10]. Using these pores they were also able to make measurements of 90 nm diameter spherical T2 bacteriophage virions. By comparison with the calculated fluid electro-osmotic flow time, DeBlois was able to discern the electrophoretic velocities of different charged subpopulations of these particles [11]. Whilst they were also able to detect and size Mason-Pfizer monkey virus and T4 bacteriophage with the same apparatus, complexities associated with viral particle geometries were implicated in the observation of unexpected

pulse magnitude and duration.

Two significant issues with many of these early approaches were the complexity of pore manufacture and the propensity, particularly for small pores, to become blocked or partially blocked due to the presence of debris in solution [11]. To this end researchers developed alternative techniques for creating pores from both biological and synthetic sources.

2.1.2 Biological Nanopores

Biological nanopores are notable not only for their sensing functionality but also because of the possibility of highly specific interactions with individual species, even in complex fluid environments such as the cytoplasm. A well-characterised biological nanopore, α-haemolysin (α-HL), has been used in conjunction with RPS to detect a variety of molecular species [16]. α-HL is a water-soluble, heptameric protein pore with minimum internal diameter of $\sim$2 nm, secreted by *Staphylococcus aureus*, that spontaneously assembles into lipid bilayer membranes. Once assembled, α-HL is robust (relative to other biological pores) across a range of temperatures and pHs [22].

In 1996, Kasianowicz *et al.* used RPS with an α-HL nanopore embedded in a lipid bilayer to detect and differentiate polynucleotide sequences [14]. This study triggered a new generation of RPS work, using both biological and synthetic nanopores to study molecular-scale processes such as protein folding, ion channel mechanics and DNA dehybridization [23, 24].

Most importantly, RPS became a contender for the third generation sequencing target of sequencing an entire genome in 24 hours for $<$ US$1000. Largely the appeal in nanopore sequencing technology lies in the minimal amount of chemical processing needed to prepare a genome for sequencing and the fact that steric effects allow long nucleotide strands to be passed through the pore in a sequential 'base-by-base' manner [16, 25]. Current second generation methods rely on the addition of fluorescent nucleotides and lengthy segment size separation, neither of which would be required in a functional nanopore sequencer.

Numerous biological nanopores can be used in place of α-HL, with diverse structures and functionalities that enable novel investigations of binding kinetics and ligand gating [23]. In some ion channels, the conformation change induced by a molecular binding event can cause restriction or expansion of the nanopore and consequently a shift in the current trace [23], leading to detection of an analyte with high specificity. Biological nanopores operate at single molecule scales, and are therefore much more selective than many of the synthetic nanopores described below, and unsuitable for studying particles larger than a few nanometres.

Clarification of Kasianowicz *et al.*'s results in 2001 by Meller and Branton [26] showed that the α-HL nanopore was detecting the secondary structure of the nucleotide sequence, due to the length (10-15 nm) of the pore's 'sensing' region. Since 2001, significant improvements have been made with the incorporation of cyclodextrin into the pore of α-HL and the

fusion of an exonuclease domain with the pore's mouth that allows continuous individual nucleotide identification [27]. Whilst the α-HL nanopore is extremely stable, the lipid membrane in which it is mounted is inherently unstable over long periods of time [28].

There are significant practical barriers to third generation sequencing with biological pores. The translocation speed of individual nucleotides in many nanopore technologies is of the order of a single base per microsecond, whilst nucleotides must occupy the pore for a full millisecond to allow correct identification using the resistive pulse technique [29]. As nanopores become smaller, the resistive pulse measurement technique begins to reach a fundamental limit of detection, where the access resistance of a nanopore becomes significant, even in an 'ideal' membrane with no thickness. This leads to a sensing zone of a pore that is physically able to transmit ssDNA (r $\sim$1.5 nm), extending approximately one diameter out into the solution on each side of the pore, and thus exhibiting a theoretical minimum size approaching 10 nm; far too large to allow single nucleotide detection on a continuous DNA strand [28, 30]. Many of these and similar issues for third generation DNA sequencing have been resolved, by either mutating the α-HL pore or by the use of hybrid systems where biological nanopores in lipid membranes are mounted in a solid-state 'shell' to increase stability [16, 23].

The goal of third generation sequencing currently dominates the field of molecular RPS. As of 2015, a pre-commercial biological nanopore se-

quencer (the MinION developed by Oxford Nanopore) has been shown to be able to sequence >50 kb strands of DNA in bacteria, albeit with a higher error rate than other platforms [31]. The content of this thesis however is concerned with larger particles and therefore more efficient fabrication and measurement methods. Synthetically produced pores, particularly those with conical geometry, are most comparable to TRPS.

2.1.3 Synthetic Nanopores

The use of biological nanopores brings some general limitations, such as their functional complexity and instability over time or in extremes of temperature or pH, particularly when compared with nanopores manufactured in solid-state membranes. Solid-state nanopores have been synthesised using a range of techniques, and good control over pore size and geometry has been developed. There are a wide variety of synthetic pore types and applications; for example graphene nanopores have been used to detect the passage of ssDNA across an atomic width membrane [25]. Here we focus mostly on synthesis techniques for the fabrication of cylindrical or conical polymeric nanopores used for rapid micro- and nanoparticle characterisation, with various techniques described below and summarised in Table 2.1.

The smallest synthetic nanopores have been fabricated in silicon-based membranes using beams of ions and electrons [16]. For example, Li *et al.* [32] reported production of nanopores with diameters between 1-60 nm

Table 2.1: Summary of solid-state nanopore synthesis techniques and sizes - adapted from [15].

Method	Substrate	Minimum Pore Width
Particle-beam Size Reduction		
TEM	SiO_2, Si_3N_4, SiC, Si	<2 nm
Field Emission SEM	$Boron-doped\ Si$, Si_xN_y	2-6 nm
FIB/ Ion Beam Sculpting	Al, Cr, SiC, Si_xN_y, SiO_2, $PMMA$, $Polyimide$	<2 nm
Laser Induced Shrinking	$Apiezon\ W\ wax$	6-20 nm
Size Reduction by Deposition		
ALD	Al_2O_3 on Si_3N_4	<2 nm
Electroless Plating	Au on $Polycarbonate$	<2 nm
Ion-beam Assisted	SiO_2 on Si	20-50 nm
Electron Beam Assisted	SiO_2 on Si_xN_y	<2 nm
Direct Drilling		
Mechanical Penetration	TPU	∼100 nm
TEM	Al, AlN, Al_2O_3, Au, C, Ni, Si, Si_3N_4, SiO_2, ZnO	<2 nm
Focussed-Ion Beam	SiC	2-6 nm
Dielectric Breakdown	*SiN*	1-25 nm
Etching		
Ion Track	$Polyimide$, PET, $Polycarbonate$	2-6 nm
Si Feedback-Controlled	Si	6-20 nm
Nanopipettes		
Laser-pulled capillaries	*Quartz Glass*	20-50 nm
Glass-encased wire etching	*Soda-Lime Glass*	20-50 nm

in silicon nitride membranes using ion-beam sculpting. Pores were made within larger (∼100 nm) bowl-shaped cavities by removing the surface above the cavity apex with a beam of 3 keV Ar+ ions. The pore diameter could be controlled by varying the duration of the ion-beam sculpting, and 5 nm diameter nanopores produced using this method were used to detect 500 base pair dsDNA using RPS. Ion beam sculpting has since been used to synthesise nanopores in silica, Al, Cr, poly(methyl methacrylate) (PMMA) and polyimide membranes [24]. Storm *et al.* [33], who also made

nanopores with openings as small as 2 nm diameter in silicon wafers, used a 300 keV electron beam from a TEM to complete pore fabrication. An initial pyramidal pore, less than 200 nm in size, was made by controlled wet etching of a 500 nm exposed square of silicon in a SiO_2 mask layer, defined using electron-beam lithography.

Relatively small pores can be formed in glass and silica without the use of large, costly, time-consuming equipment. It has long been known that small channels can be produced by careful mechanical separation of the two halves of a heated glass nanopipette. This technique can create two nanopipettes with diameters as low as 40 nm, as used in patch-clamp studies of cellular ion channels [15, 34, 35]. Nanopores have also been constructed in glass membranes by implanting electrochemically sharpened Au or Pt electrodes into the glass, then thinning the membrane by polishing. This technique can produce nanopores with diameters down to 10 nm [35]. Silica nanotubes that can detect DNA molecules have also been created by controlled oxidation of chemical vapours deposited on silicon nanowires [24].

The recent explosion of interest in single-layer carbon has also spilled over into synthetic pore fabrication methods. For example, Ito et. al. [36] carried out extensive RPS experiments using 132 nm multi-walled carbon nanotubes (MWNTs) embedded in membranes of Si/Si_3N_4 and PDMS. Graphene pores, which are currently the subject of much research interest [25], could have wide-ranging applications due to the minimal thick-

ness of the membrane. They are typically 5 - 10 nm in diameter, pass through several layers of graphene, and are sculpted using the electron beam of a TEM. Graphene pores show particular promise for rapid DNA sequencing applications as simulations have shown that RPS resolution should be sufficient for detecting and differentiating between single nucleotides. As well as difficulties associated with handling such thin membranes, graphene pore technology may be limited by slight permeability of the thin membrane to the conducting electrolyte, and direct molecular interactions [16].

Nanopores have also been made in many different types of polymer membrane [16]. The track-etching fabrication method is commonly used, whereby energetic heavy ions are fired into polymer membranes as thick as 100 μm, creating damage tracks [37]. Chemical etching of the membrane preferentially erodes material along the damage track, creating pores with geometry that can be controlled by parameters such as temperature, etchant and etching duration. Track-etched polycarbonate pores were used by DeBlois *et al.* [11], and the technique has also been used to fabricate nanopores in poly(ethylene terephthalate) (PET), polyimide and mica [24]. Asymmetric etching produces conical nanopores which can have lower electrical resistance than equivalent cylindrical pores, can exhibit non-Ohmic behaviour, and tend to generate event peaks rather than square pulses characteristic of cylindrical pores [24]. Photolithography and micromolding of polymers such as polydimethylsiloxane (PDMS) can be used for rela-

tively rapid, cheap, reproducible pore production. Saleh and Sohn used this method for RPS detection of λ-phage DNA molecules using a 200 nm nanopore [38]. As a final example, laser heating can be used to make pores in both plastic [39] and glass [40] membranes.

Nanopore sensing finds application in a variety of fields far beyond sequencing and single molecules, from cell and virus detection to agglomeration analysis [41]. Several applications for pores have already been experimentally realised, most using solid state nanopores because of stability considerations. These include, but are not limited to: force spectroscopy, nucleic acid sorting, protein analysis, molecular sieving, molecular sensing, viral sensing and ion selection [16].

2.2 Tuneable Resistive Pulse Sensing (TRPS)

2.2.1 Pore Manufacture and Geometry

Fabrication of tuneable pores (TPs) was first reported by Sowerby *et al.* [3], who described how a chemically-etched tungsten needle can be used to mechanically puncture an elastomeric membrane with sufficient control to produce a conical nanopore. As the needle is pushed through the membrane, a voltage is applied between the needle and a conducting electrolyte in contact with the opposite membrane surface. The resistance between these elements is monitored and used to control the final pore size (Figure 2.1). The degree of penetration, and thus the size of the result-

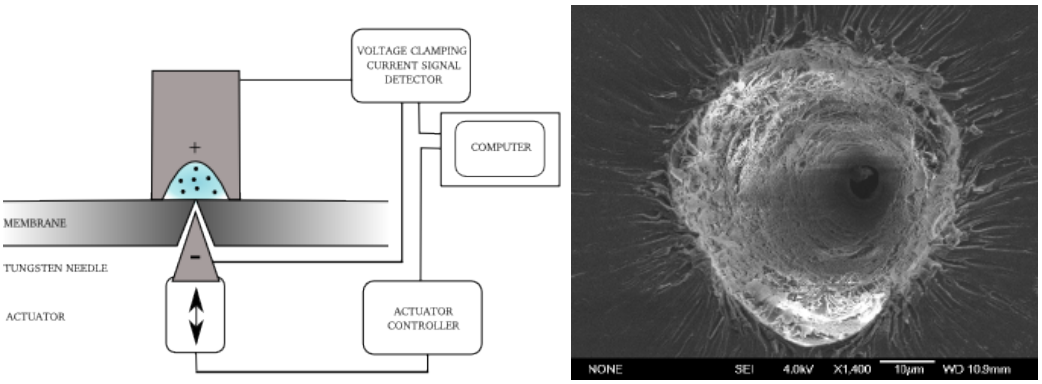

(a) (b)

Figure 2.1: Tuneable pores in thermoplastic polyurethane. a) Schematic control system for mechanical membrane penetration with a conical tungsten tip. b) SEM image of the larger opening of a conical pore at ∼20% strain. Reproduced from [42].

ing pore [3], is controlled by monitoring the membrane resistance, via the electrodes. The membrane resistance spikes when contact is made with the pocket of electrolyte. The position of the needle is controlled electronically by a piezo-electric actuator. The simplicity of this technique lends itself to a rapid fabrication process, which has been developed commercially by Izon Science (Christchurch, [7]) in the production of TPs for the qNano TRPS system. TPs have been made with constriction diameters small enough to resolve dsDNA [3], and are currently manufactured for detecting particles from ∼50 nm up to several microns.

The distinctive feature of TPs is that their geometry can be tuned on the nanoscale by stretching and relaxing the elastomeric membrane on macroscopic scales. The usual membrane material is thermoplastic polyurethane (TPU), a stable, inexpensive elastomer which can be extended to high

strains without causing large plastic deformations or breakage [43]. Stretch is applied by pulling the arms of a cross-shaped specimen, with a nanopore located at the intersection of the arms (Figure 2.2) [42]. When the arms are extended symmetrically in two directions (as indicated by displacements X in Figure 2.2), the membrane strain around the pore is near-isotropic and radial [8]. A key practical advantage of membrane stretching is modulation of pore diameter *in situ* to control the event to noise ratio, and hence change the precision, of an RPS measurement [17]. When the size of the nanopore is similar to that of particles being detected, tuning can screen measurements of larger particles or maximise the resistive pulse for smaller particles [17]. Stretching has also been used to gate dsDNA [3], and applications involving particle trapping, nanoscale confinement and fast actuation [44] can be envisaged. The elastomeric membranes do exhibit some plastic deformation, so most RPS experiments with TPs use standard particles sets for calibration. However, near-reproducible actuation can be obtained by stretch-cycling the membrane prior to use, invoking the Mullins effect [43].

TPs have been imaged using atomic force microscopy, SEM, optical, confocal and fluorescence microscopy [8, 17, 42, 43, 45]. Confocal microscopy [17, 42, 45] has been used to characterise the sectional profile of TPs at varying membrane stretch. Profiles are near-conical, but with slight curvature similar to that of a wine glass [42]. SEM images have characterised pore openings [8, 18, 42, 46], also at varying stretch, reveal-

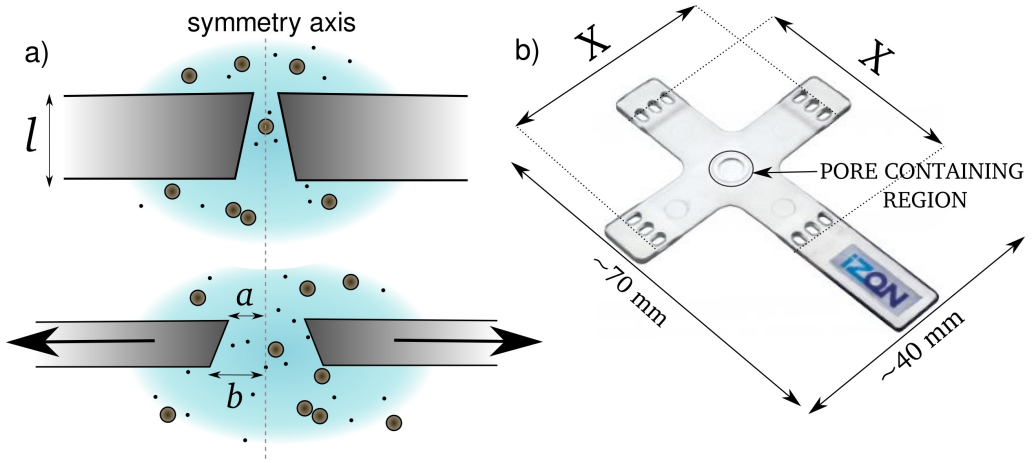

Figure 2.2: a) Schematic membrane sections showing how the membrane thins and the pore size increases upon application of radial strain. b) A cross-shaped TP specimen. Actuation is carried out by pegs placed in the holes on the specimen arms. Image courtesy of Izon Science [7].

ing radial striations which are formed adjacent to larger pore openings during pore manufacture (Figure 2.1 b), [42]). With no stretch applied, a typical pore extends through a membrane of thickness ~200 μm (see Section 4.2.4), joining a near-circular larger ('*cis*') opening of diameter ~20 μm to the submicron smaller ('*trans*') opening. In an electric field, conical pores create a localised region of concentrated field lines, and therefore heightened sensitivity, near the *trans* pore opening. The asymmetry of the conical profile also causes asymmetry in event profiles (Figure 1.1 b), [18]).

The geometry and elastomeric properties of nanopores produced using mechanical puncturing method have been extensively modelled [8, 18, 47, 47, 48], imaged [3, 8, 17, 42, 47] and characterised [3, 8, 17], yet the surface properties of the elastomer under the conditions necessary to make TRPS

measurements are less well known [49].

2.2.2 TRPS Development for Measurement

RPS measurements using TPs can be carried out at physiologically relevant pH, ionic strength and temperature, without any need for chemical labelling. Experiments to date have typically used a standard aqueous solution of 0.1 M KCl, with the minimum salt content used equivalent to 0.01 M KCl [50]. The typical particle concentration to obtain a fast measurement rate while avoiding overlapping events is around 10^8-10^{10} particles ml^{-1}. Solutions are regularly filtered to remove contaminants and ultrasonicated to limit particle aggregation.

Standard data analysis techniques have been developed for measurement of particle size, concentration and charge using TPs in RPS experiments. Here, we briefly recount these methods, while noting that more detail regarding assumptions and analytic methods have been detailed elsewhere [42, 45, 46, 51, 52] and in Chapter 4.

Sizing of nanoparticles using TPs was established by Vogel *et al.* [46] who compared standard sets of 100, 200, 400 and 780 nm carboxylated polystyrene nanospheres. Complementary DLS and TEM size measurements were compared, and a population of adenovirus particles was sized. For the standard particles, the accuracy of size measurements was better than 6%. Peak blockade heights were extracted algorithmically from the current trace, and the mean peak magnitude (ΔI) normalised by the

baseline current (I) provided comparison between calibration particle sets at any given stretch. The calibration step could be removed with precise knowledge of the pore geometry, but in practice it is more precise to use the standard particles due to high uncertainty around pore geometry.

Particle dispersity can be important for applications, whether caused by aggregation or the size distribution of individual particles. Measurements of a bimodal mixture of 84 nm and 150 nm polystyrene spheres have been reported [43], while Roberts *et al.* [17] studied a trimodal solution containing 100 nm, 220 nm and 400 nm particles. They were able to distinguish between the three populations at constant stretch settings. They also demonstrated changes in the resistive pulse distribution due to changing pore size by varying the macroscopic stretch applied to the TP membrane, and used stretch to gate 80 nm particles from a mixture of 50 and 80 nm polystyrene nanospheres.

Vogel *et. al* quantitatively sized 200, 400 and 780 nm particles and reproduced these results across a range of pores and compared the accuracy to size measurements obtained using TEM sizing and DLS sizing. Monodisperse populations of 200 to 780 nm particle dispersions showed linear relationships between particle volume and relative blockade magnitude ($\Delta I/I$), and whose sensitivity could be 'tuned' via adjustment of the pore size [46]. This agrees with calculations of blockade magnitude assuming a simple conical pore shape (discussed in Chapter 3), that indicated linearity for a wide range of particle sizes. Experimentally, the

linear relationship between particle and pore volumes breaks down when the particle size approaches that of the small pore opening. The linear expression suggested by Maxwell [53] and Rayleigh [54] fails to accurately predict occlusion volumes under these conditions.

In a suspension of monodisperse 100, 220 and 400 nm carboxylated polystyrene spheres Roberts *et. al* demonstrated that adjusting the nanopore size allowed them to select for specific particle sizes [17]. As strain was applied to the membrane, blockade magnitudes decreased as the 'relative occlusion volume' of the particle in the pore decreased correspondingly. Ultimately, Roberts *et al.* were able to 'gate' the passage of the larger particles by decreasing the pore size until it was too small to permit the 400 nm particles. This gating had previously been observed for DNA [3], however this was using a pore of much smaller dimensions, and re-sealing of the pore may have played a factor in the gating. In this example however, the pore remained clearly open as the <400 nm particles continued to pass through it unimpeded. Roberts *et. al*'s results provided an indicator that the qNano apparatus could be used for particle sizing [46] in disperse suspensions of mixed particles which prove problematic for competing techniques such as dynamic light scattering.

Transport of nanoparticles through a pore can be described by the Nernst-Planck equation, which can be written as a summation of (from left to right) diffusive, electroosmotic, electrophoretic, dielectrophoretic and pressure effects:

$$\mathbf{J} = J_{diff} + J_{eo} + J_{eph} + J_{dep} + J_{pd}. \tag{2.2}$$

Detailed consideration of each mechanism can be found in Chapter 3.

In typical TRPS experiments, diffusion is not significant because nanoparticles are relatively large compared to the pore opening [42]. The electrokinetic mechanisms depend on the surface charges of the particle and the pore, as quantified by the ζ-potential, and are typically considered in the 'high-salt' (small Debye length) limit for TP experiments. Pressure-driven flow can be influenced by fluid menisci and gravitational heads in fluid cells containing a nanopore membrane. The qNano system can include a manometer system, to control the pressure across the membrane, enabling charge [52] and concentration [42, 51, 55] measurements. Willmott *et al.* present a detailed comparison of transport mechanisms relevant to TRPS in [56].

In some RPS regimes, pressure-driven flow dominates transport to the extent that other mechanisms can be neglected. When this is the case, experiments using TPs have verified that the event rate is a linear function of both concentration and pressure, even when particles are of different sizes and types [42, 43, 51, 55], enabling measurement of particle concentration to $\sim$3% precision. The concentration of an unknown particle set (C_2) is most easily determined by comparison with a standard particle set of known concentration (C_1). A plot of particle count against applied pressure yields a line with a gradient proportional to concentra-

tion. Comparing the gradients for an unknown particle solution (g_2) with the corresponding gradient of a known standard (g_1),

$$C_2 = \frac{g_2}{g_1} C_1. \tag{2.3}$$

Concentration can also be calculated directly from Equation 2.2 when the pressure and pore geometry are known to high precision.

In 2010 Willmott *et al.* used the qNano system to investigate the blockade rate dependence on pH [57]. The particles in question were 500 nm carboxylic-acid-modified silica particles (pI = 4.0) and 200 nm amine-modified silica particles (pI = 5.5), and hence the protonation (or de-protonation) at differing pH controlled the surface charge and thus ζ-potential of these particles. For both particle sets, no translocations were observed at each particle set's isoelectric point, presumably as their low charge meant that the applied electric field magnitude was insufficient to drive them through the pore. However, particle aggregation is also known to occur at such low ζ-potential, as it directly controls colloidal stability, so this may also account for the low numbers of observed translocations [18, 58]. These results, although preliminary, indicated TRPS's potential as a surface charge measurement device, in addition to a nanoparticle concentration and particle sizing technique.

2.2.3 Charge Measurement

For nanoparticle ζ-potential measurements, TRPS has the key benefit of eliminating the size bias and contamination effects known to be important in widely used light scattering techniques (Section 2.3). TRPS measurements can be carried out in under 10 minutes in relatively high concentration (0.1 M) electrolyte [52].

When a high-precision manometer is used, the pressure across the membrane can be used to isolate the electrokinetic (electrophoretic and electro-osmotic) components of Equation 2.2. At a certain applied pressure, particle fluxes due to pressure and electrokinetic flow components exactly balance so that $J = 0$. If electro-osmotic effects are not significant, or are characterised (e.g. by measuring ζ_{pore}), the electrophoretic mobility of nanoparticles can then be isolated, allowing calculation of $\zeta_{particle}$ to characterise surface charge. Charge measurement with a TP has been demonstrated in practice [52], with the zero flux point identified by continuously varying the applied pressure over time and locating the pressure at which growth of cumulative event count was minimised. In this study, $\zeta_{particle}$ values between -14 and -39 mV were determined for a range of polystyrene nanoparticle types, with experimental uncertainty of $\sim$25% or less arising from geometric considerations and determination of electro-osmotic effects. Results were in good agreement with values obtained from titration calculations and phase analysis light scattering (PALS). However, the impact of additional experimental considerations, for example

the importance of analysis method or the reproducibility of the measured values across pores and particle types, was not yet known [52].

Ito *et al.* [36] previously compared RPS measurements of nanoparticle size and electrophoretic mobility with DLS and PALS respectively. This work used 28-90 nm carboxylated polystyrene nanoparticles with multi-wall carbon nanotubes, and reported greater accuracy when using RPS than with light scattering methods. The authors noted the complexity of RPS charge measurements due to the presence of both electrophoretic and electro-osmotic effects. The work described above using TPs has effectively met this challenge by isolating the electrophoretic component using precise application of pressure. In an earlier TP study [18], the influence of solution pH on the translocation rate of electrophoretically-driven silica particles was demonstrated. Both carboxylate and amine surface modification were used, and the observed transport trends were broadly consistent with values of $\zeta_{particle}$ measured independently using light scattering. The duration of each translocation could reveal charge information on a particle-by-particle basis [47].

Pulse Shape

Roberts *et al.* reported the first TRPS analysis of individual events in an attempt to yield more information than simply studying at the average properties of the dispersion as a whole [17]. They used tuneable nanopores to differentiate between silica particles functionalised with car-

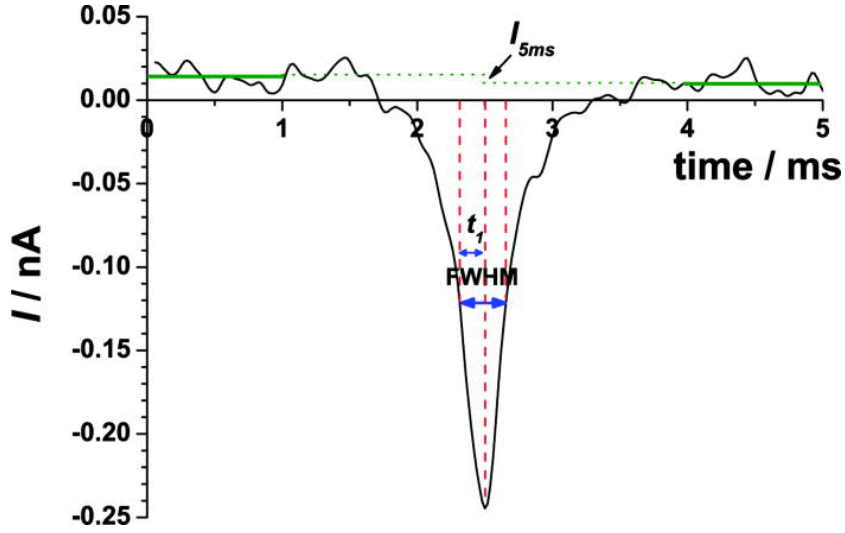

Figure 2.3: Typical event observed in RPS characterised by asymmetry measures F and I_{5ms} [18]

boxyl groups, strepdavidin or DNA by monitoring both relative blockade magnitude and blockade duration, under the hypothesis that the larger functional groups would lead to larger blockade rates and longer pore occupation times. Differentiation between functional groups was not possible on the basis of blockade duration, even with a small pore stretch. The authors observed an increased duration for the translocations of the DNA-functionalised particles. However, the cause of the increase is unclear as it may be size related, drag related or due to interactions between the pore surface and the DNA (both of which have net negative charges), or possibly even an artifact of the duration detection algorithm [17]. Hence, characteristics of individual resistive pulses provide additional metrics for generic development of future nanoparticle characterisation methods.

In order to gain more information from the individual events, Willmott

and Parry [18] investigated the peak shape, reproducibility, FWHM, and asymmetry. Asymmetry was categorised as either 'short term' or 'long term'. 'Short term' asymmetry, f_{factor}, was calculated from the ratio of t_1 to FWHM (Figure 2.3). 'Long term' asymmetry, I_{5ms}, was the difference between the average baseline current 2.5 ms before and after the event peak. Peak asymmetry [18] allows identification of the translocation direction, enabling study of transport mechanisms near the zero flux point [48].

Willmott *et al.* have also shown that more detailed analysis of events may also prove useful for determining nanoparticle shapes [48]. Examining the asymmetry of events at different pH and thus surface charge yielded different peak heights [42]. It was also noted that whilst there was little relationship between FWHM and particle size, larger particles tended to exhibit greater asymmetry than their smaller counterparts. Their most striking observation however was that at a pH of 7.0, particle mobility (as measured via reciprocal translocation rate) was consistently higher than at a pH of 8.0. This was contradictory to what was expected given the carboxyl functionalisation of the polystyrene particles that would suggest higher charge and thus higher mobility at higher pH due to deprotonation. The authors note that this may a specific interaction at these pH values, a property of the buffers used, or due to uncontrolled pressure as contradictory results have been reported over a wider (but less detailed) pH range in the past [42].

2.2.4 Applications of TRPS

The ability to accurately and rapidly characterise nanoparticles using RPS is clearly of interest for particle-based applications such as medical diagnostics and drug delivery. Standard measurement techniques are mostly developed using polystyrene sphere particle sets, but TPs have also been used to measure a plethora of different particle types, ranging from 2700 base pair dsDNA [3] to microscale viruses and bacteria [51]. Following Sowerby *et al.*'s work with DNA, TPs were used to detect λ-phage particles, with results suggesting that the head and tail of the phage could be distinguished in the resistive pulse [43]. Subsequently, Vogel *et al.* [46] studied a population of adenovirus particles, which are near-spherical, 70-90 nm in diameter and often used as gene vectors. This study reported that pore tuning could increase the resolution of size measurements by as much as 60%.

TRPS concentration measurements have been demonstrated using both $\sim$1 μm baculovirus in buffered electrolyte and $\sim$600 nm *Prochlorococcus* cyanobacteria in seawater [51]. The reported accuracy was equal to or greater than cytometry and microscopy techniques, when using the variable applied pressure technique (described above) over the range 0 - 1 kPa. Particle size distribution was measured at the same time as the concentration measurement, allowing simultaneous confirmation of data reliability and demonstrating the efficiency of TRPS experiments. The benefits of small sample requirements (compared with cytometry) and low time con-

sumption (compared with microscopy) were also apparent in this study.

Garza-Licudine *et al.* [59] have used TPs to detect synthesised unilamellar 200 nm liposomes, a type of capsule commonly used for drug delivery. This study demonstrated that non-rigid, biological particles can be characterised using TRPS. Characterisation or detection of modified surfaces on synthetic nanoparticles plays an important role in nanoparticle characterisation. Key functions include detection of binding in an assay, and quality control of particles manufactured with a functionalised surface. Roberts *et. al* [17] have shown that size measurements using a TRPS have sufficient resolution to differentiate between bare carboxyl-stabilised 220 nm organosilica spheres, and the same particles biofunctionalised with either streptavidin or λ-DNA. They also noted a 68% increase in event duration between bare particles and those functionalised with 48 kbp λ-DNA. These effects were attributed to the increased hydrodynamic radius of the particles, as the coiled λ-DNA has a radius of gyration of $\sim$1 μm.

Aggregation, a key mechanism for assays and particle stability, was studied in TRPS experiments using 1 μm superparamagnetic nanospheres [48]. The study was able to follow magnet-induced aggregation over the course of $\sim$1 minute, and used simulations to distinguish between resistive pulses caused by individual particles and dimers. Competition between magnetic, pressure-driven and electrokinetic transport was explored, and evidence suggested that pressure-driven flow at the pore constriction forced separation of aggregates formed outside of the pore. Mag-

netic beads are widely used in sub-cellular diagnostics and medicine [60], because their motion in magnetic fields is independent from other fluidic and biological transport. Their versatility and efficiency has resulted in many assay, separation and biological handling applications, and they are particularly suitable for studying aggregation because they are known to aggregate in an applied field.

Low *et al.* [61] used TRPS to investigate a bio-assay aggregation based on the interaction between a mixed base 22-mer peptide nucleic acid (PNA) and 50 nm citrate-capped gold nanoparticles. The presence of the PNA, which binds to nanoparticle surfaces and reduces their surface charge, caused the nanoparticles to aggregate in a concentration-dependent manner. Aggregation was monitored using TRPS, DLS and UV-vis spectrophotometry. TRPS reportedly gave the best resolution of these techniques, and was sensitive to size changes at PNA concentrations as low as 5 nM. This work aimed to produce an assay for detecting a target DNA molecule, which prevents aggregation when bound to PNA on the surface of the gold nanoparticles. In another recent aggregation study using TRPS [62], templated Au-Ni rods (approximate diameter 1 μm and length 2 or 4 μm) were used to demonstrate two assays. The first was the model biotin-avidin system, while the second used an aptameric capture probe to detect a platelet derived growth factor (PDGF) protein. PDGF is a growth factor overexpressed in cancer patients, particularly those with lung and pleural tumours. The shape of dimer aggregates was controlled by localising cap-

ture probes on the Ni surfaces of the rods using a histidine-modified peptide. End-to-end and side-on orientations were distinguishable based on the resistive pulse size and duration. In the aptamer assay, PDGF was detected at fM levels within approximately 10 minutes, and specificity was verified using a control. This study was also notable for an experimental comparison between resistive pulses caused by individual rod-shaped particles and spheres of similar size [63].

The recent explosion of interest in the field has generated a significant quantity of novel literature in the last two years, particularly in the area of microvesicle and exosome detection. We direct the interested reader to [64] and [65] for more detailed information on these areas.

Figure 2.4: Diagram of nanoparticle characterisation techniques comparable to RPS. From the top left: dynamic light scattering (DLS) and laser doppler electrophoresis (LDE), nanoparticle tracking analysis (NTA), dynamic centrifugation sedimentation (DCS), flow cytometry (FCM), suspended microchannel resonator (SMR), electron microscopy (EM).

Table 2.2: Summary of common nanoparticle characterisation techniques. Values are indicative, based on information in the references provided.

Technique	Used to Measure			Measured Quantity	Size Range	Ensemble or Individual	Sample Volume	Indicative Concentration	References
	Size	Charge	Conc		nm		μl	particles ml^{-1}	
DLS	✓			Brownian motion	<1 - 6000	Ensemble	2- 3000	$<10^{10}$-10^{13}	[67–69]
PALS/LDE		✓		Electrophoretic mobility	<1 - 6000	Ensemble	2 - 3000	10^{8}	[70]
NTA	✓		✓	Brownian motion	10 - 8000	Individual	∼300	10^{8}-10^{9}	[68]
DCS	✓			Sedimentation velocity	2 - 80	Ensemble	∼100	10^{11}-10^{13}	[69, 71]
FCM	✓		✓	Light scattering properties	>500	Individual	>50	$> 10^{6}$	[72]
EM	✓			Electron scattering	>0.05	Individual	negligible	$\sim10^{8}$ (n.i)	[73, 74]
SMR	✓	✓	✓	Cantilever resonance	∼50 - 10000	Individual	<20	$< 10^{8}$	[75–77]
TRPS	✓	✓	✓	Occluded ionic current	> 50	Individual	∼40	10^{5} - 10^{12}	[51, 52]

2.3 Comparable Characterisation Techniques

Whilst the majority of the work in this thesis concerns the use and development of TRPS, other comparable nanoparticle characterisation techniques are in use commercially. In this section we briefly discuss the fundamental concepts behind a selection of major modern nanoparticle characterisation techniques and consider their advantages and limitations in comparison to TRPS.

The techniques we have chosen to discuss are: dynamic light scattering (DLS), nanoparticle tracking analysis (NTA), differential centrifugal sedimentation (DCS), flow cytometry (FCM), suspended microchannel resonators (SMRs), and electron microscopy (EM), shown diagrammatically in Figure 2.4. All of these methods can be limited by requirements for monodispersity, sample preparation, and by lack of versatility. Furthermore, these are not intended to provide a comprehensive list of all comparable techniques, but rather highlight those that are in common use, exhibit a similar sensitivity, or enable similar measurements of particle size, concentration and charge as TRPS. Reviewed techniques are summarised in Table 2.2. Of particular note are dynamics light scattering and electron microscopy, both of which are employed to determine particle ζ-potential and pore geometry respectively during this thesis.

A range of dynamic light scattering (DLS)-based techniques are presently finding widespread use for nanoparticle size and charge measurements. The capabilities and limitations of these systems are broadly summarised

and compared with other particle characterisation methods in Table 2.2 and Figure 2.4. In DLS [66, 67], electromagnetic radiation is scattered by small moving particles, in a regime where particle dimensions are much smaller than the wavelength of the radiation. With the best equipment, DLS is reportedly able to size particles down to 0.6 nm in diameter [67].

The theory behind this measurement technique is based on the well-known phenomenon that small particles scatter electromagnetic radiation whose intensity fluctuates in a manner dependent on their size, due to interference. This scattering has been characterised by Rayleigh [54] for particles in different size regimes compared to the wavelength of the scattered light. In dynamic light scattering, the intensity of the scattered light at a certain angle to the incident wave changes with time, due to the thermally-induced Brownian motion of the particles. However, as particles following Brownian motion exhibit random walk characteristics, it is possible to derive a probability distribution function for them that depends only on their radius, time, and the diffusion constant D. Coupling this with the Einstein-Stokes relation for the motion of spherical particles through a fluid in low Reynolds number systems gives:

$$D = \frac{k_B T}{6\pi\eta r_H} \tag{2.4}$$

where r_H is the hydrodynamic radius of the particle, η is the viscosity of the fluid, k_B is the Boltzmann constant and T is the fluid temperature. By using a light source of a known intensity (in most systems a coher-

ent, monochrome laser) we can calculate the particle's size based on their change of position with time.

High dispersity, aggregation and the presence of large contaminants are key limitations for DLS techniques [66, 68] as the analysis assumptions rely on each photon undergoing only a single scattering event before detection - a condition which becomes implausible in high concentration solutions. The scattering model is only accurate for spherical particles and the reliance on an autocorrelation function is dependent on the assumption that the particles themselves are monodisperse.

This technique ultimately generates a size distribution for the particles, but such a technique has a resolution of $>$10 nm. This is a consequence of the Rayleigh approximation that indicates that the intensity of the scattered light (I) is proportional to r^6/λ^4 (applicable when $\frac{2\pi r}{\lambda} << 1$), meaning that the intensity generated by large particles is able to dwarf the light scattered by smaller particles by virtue of their size alone. For example, the intensity of scattered light produced by one 400 nm particle is matched by the light from 64 similar 200 nm particles. Data relating to an underlying distribution of small particles can therefore be swamped or skewed by light scattered from a comparatively low concentration of large particles. More modern DLS technologies include Mie theory to allow measurement of larger particles as well, and attempt to minimise scattering from contaminants such as dust by detecting backscatter as larger particles scatter light preferentially forwards [78]. In addition, accurate

DLS measurements are only possible in suspensions where thermal (convection), electronic and agglomerative effects have been minimised, in order to limit the signal generated by the interactions between particles rather than from the particles themselves. The quality of DLS data is enhanced when the nanoparticle shape and refractive index are known, and the electrolyte concentration (e.g. $<$0.1 w/v%) is relatively low [67, 68]. Shape and refractive index are used in calculations, while low concentration electrolyte screens electronic interactions between particles. Alternatively, DLS can be coupled to microfluidic flow field fractionation in order to separate particles based on size prior to light-scattering, reducing size bias effects [72].

DLS is an example of an ensemble characterisation method: the data describe a large population of particles. Ensemble methods provide the statistical benefits of examining a large population, providing an intensity-weighted average in the case of DLS. Alternative particle-by-particle measuring techniques, such as TRPS, can provide more precise information regarding the nature of individual particles in solution, and are not so susceptible to skewing of the data by outliers.

Similar techniques to DLS (such as laser Doppler electrophoresis (LDE) and phase analysis light scattering (PALS)) are used to determine the surface charge of nanoparticles, usually quantified as the ζ-potential ($\zeta_{particle}$). Surface charge is important for determining the stability and agglomeration potential of nanoparticles and emulsions, and is a key indicator of

surface functionality under varying environmental conditions [70]. LDE follows the same principles as described above, of wave vector scattering and autocorrelation. The particle-containing solution is placed in an oscillating electric field of sufficient strength so that electrokinetic behaviour dominates Brownian motion. This electrokinetic motion causes a Doppler shift in the scattered light frequency which allows calculation of the particle velocity. High resolution charge measurements can be obtained by detecting the phase shift between the incident and scattered radiation, rather than the direct shift in frequency. To compensate for electro-osmotic effects at the sample walls, the frequency of the oscillating field can be varied. Shorter oscillatory periods do not provide sufficient time for electro-osmotic flow to stabilise, whilst the long oscillatory periods allow direct measurement of electro-osmotic flow at the container wall [67]. As with sizing light-scattering techniques, large particles can dominate and reduce the accuracy of light-scattering charge measurements.

DLS is widely used as a generic size and charge measurement tool for nano- and microparticles, including those used in nanomedicine. However, the size effect described above can lead to inaccuracies when DLS is used as a quick, quality-control tool. For example, mixtures of drug delivery capsules made using bulk synthesis, a popular technique due to simplicity and scalability, are commonly polydisperse [66]. DLS is also used to monitor particle dynamics in processes such as aggregation, where polydispersity is again an important factor that can affect the accuracy and

consistency of the results.

2.3.1 Nanoparticle Tracking Analysis (NTA)

Nanoparticle tracking analysis (NTA) is a generally-applicable technique for size and concentration measurements. NTA is tolerant of low level impurities (unlike DLS) and is particularly suitable for particles dispersed in non-aqueous solvents such as toluene and heptane. In NTA, individual nanoparticles are identified and tracked in the optical field of an ultramicroscope. The diffracted light patterns produced by the nanoparticles are projected onto a CCD (charge coupled device) camera, and particle motion is tracked algorithmically by video processing software [79, 80]. As with DLS, characterisation of the Brownian motion enables calculation of the particle hydrodynamic radius. NTA requires that the particle refractive index differs sufficiently from that of the solution, and that the ultramicroscope is isolated from mechanical vibration [80].

NTA can accurately characterise polydisperse specimens, and is able to resolve populations with less than 40 nm difference in their radii[79]. Concentration measurements can be carried out by simply counting the total number of particles producing diffraction patterns in a known fluid volume. NTA is limited by some selection bias towards larger particles, which block smaller particles from the view of the CCD [68]. The technique is also dependent on user-defined adjustments to the algorithmic detection parameters, which can alter the minimum particle size detected

and thus affect the particle sampling process. The number of individual particles that can be measured in a practical time frame is limited, and typically ∼1000 sampled particles are required to effectively describe an assumed log-normal distributed population [68].

2.3.2 Differential Centrifugal Sedimentation (DCS)

Gravitational sedimentation has long been a staple technique for separating particles based on size. However, its use is typically restricted to particles larger than 1 μm, as the settling times for smaller particles are prohibitively long. With centrifuge technology however, it is possible to separate particles in the 2 nm - 80 μm size range, with resolution down to 2% of particle diameter [71, 81]. In a differential centrifugal sedimentation (DCS) experiment, suspended particles are introduced to the centre of a transparent rotating disc with a radial fluid density gradient. Rotational motion causes the (assumed spherical) particles to migrate at a well-defined speed v, as defined by sedimentation under centripetal acceleration α, from Stokes' law,

$$v = \frac{2r^3(\rho_p - \rho_f)\alpha}{9\eta} \tag{2.5}$$

[82] where ρ_p and ρ_f are particle and fluid densities respectively, r is the particle radius and η is the fluid viscosity [71]. An accurate particle size distribution can be determined from the velocity of the particle ensemble. Velocities are calculated (using Raleigh or Mie scattering theory) from

absorbance measurements obtained from a monochromatic light source and detector, positioned perpendicular to the plane of rotation towards the edge of the disc. Typically, short wavelength (400-500 nm) radiation is used for detection of <100 nm particles. DCS is an ensemble method, which can efficiently produce data that is reproducible and resistant to size bias, although it requires the use of standard calibration particles, as well as knowledge of the solution viscosity and density. DCS can reliably characterise particles with neutral buoyancy and lower densities, which are otherwise difficult to measure [71].

2.3.3 Flow Cytometry (FCM)

Flow cytometry (FCM), which is used for detecting and sorting microscopic particles (>500 nm), has been commercially available since the late 1960s. The FCM technique uses light emitted or scattered by microstructures suspended in a hydrodynamically focused stream of fluid to determine a range of properties. These can include the size and refractive index of individual particles, and the internal structure of cells, depending on the location of the collected light [72]. Cells or particles can be simultaneously categorised on the basis of fluorescent or radioactive expression markers or tags. Although FCM relies on detection of individual particles, results are algorithmically sorted to enable categorisation of thousands of cells or microparticles per second. This high throughput ensures relatively low uncertainty in population characteristics. For best quality results, FCM

requires high purity samples and low particle concentration to minimise coincident events. FCM is often included as part of integrated systems for cell sorting, optoacoustic and microfluidic applications [72].

2.3.4 Suspended Microchannel Resonator (SMR)

Suspended microchannel resonators (SMRs) measure the mass of individual particles. Solutions containing particles are passed through a microchannel embedded within a resonating cantilever in a vacuum. Resonant cantilever oscillations are driven by an electrical signal, and optically monitored by a laser focussed on the reflecting cantilever surface. When a particle passes through the channel, a shift in the resonant frequency is observed. The system's resonant frequency is

$$f = \frac{1}{2\pi}\sqrt{\frac{k}{m^* + \beta\Delta m}} \tag{2.6}$$

where k is the spring constant, m^* is the effective cantilever mass, β is a geometric factor and Δm is the change in mass [75].

SMR is reportedly able to detect mass changes with a precision of 300 attograms, over six orders of magnitude more precise than high-end quartz-crystal microbalances or surface plasmon resonance based systems [76]. Mass measurements can be used to calculate (assumed spherical) particle diameter, to monitor size changes in real time, and to study particles bound to the microchannel walls. SMRs have been used to characterise

a wide range of particle types, including polystyrene (1.5 μm) and gold (100 nm) particles, *Escherichia coli* (0.8 x 2 μm), *Bacillus subtilis* (1 x 2.5 μm), human red blood cells ($\sim$6 x 2 μm) and to monitor antibody binding at concentrations as low as 1 nM [76]. By applying an oscillating electric field to the resonator, electrophoretic mobility and thus zeta potential can be measured [77], and concentration can be determined by counting particles, given knowledge of the volume flow rate in the microchannel. The technique is limited by the need for low particle concentrations to prevent multiple particles concurrently occupying the cantilever resonator, and the associated low sampling rate.

2.3.5 Electron Microscopy (EM)

For imaging of any submicron structure, use of EM is standard practice and ubiquitous. To create an EM image, a beam of electrons is focussed on to a substrate, and the pattern of the deflected electrons is detected and analysed to reconstruct the substrate structure. Scanning electron microscopy (SEM) collects low energy ($<$ 10 keV) electrons backscattered from the substrate, and is suitable for imaging objects from $\sim$1 nm - 2 μm [74]. Transmission electron microscopy (TEM) utilises electron energies up to 100 keV to penetrate a thin substrate, affording imaging resolution down to 0.05 nm [73].

For nanoparticle characterisation, the greatest drawback of these techniques is sample preparation. Imaging is carried out in a near-vacuum,

with particles deposited on a dry solid surface. Coatings are applied to non-conducting specimens, and specialised preparation techniques are required for TEM in particular. Consequently, the number of particles that can be observed is restricted by time and cost, thereby limiting the statistical significance of quantitative measurements. Particles may undergo size changes or surface modification during sample preparation, and there can be errors associated with observation of a 2D projection of 3D particles. Recently developed techniques, such as Wet-STEM (scanning tunnelling electron microscopy), show promise for imaging particles in solution, but can also induce undesirable image noise. Overall, EM is best suited for accurate observation of small collections of particles. Aside from size measurements, EM provides clear advantages such as visualisation of contaminants or aggregation, and will remain important for nanoparticle characterisation.

2.4 Conclusion

This Chapter has presented a history of the development and application of RPS since its initial use in Coulter Counters during the 1950s. We have described RPS experiments performed using both biological and synthetic nanopores, and summarise common synthetic nanopore production techniques and the approximate sizes of nanopores produced by them. The history of TRPS developed using the qNano is also discussed in detail including the TPU pore fabrication process, TRPS's development as a par-

ticle size and concentration measurement technique, early nanoparticle charge measurements and additional application of TRPS to a wide variety of particles. Finally a short description of several common comparable nanoparticle characterisation techniques was also presented, that includes dynamic light scattering, nanoparticle tracking analysis, differential centrifugation sedimentation, flow cytometry, suspended microchannel resonators and electron microscopy.

Chapter 3

Theory

3.1 Introduction

In this Chapter, we develop theoretical ideas that are useful for analysing TRPS. These ideas originate from diverse areas of physics, chemistry, and materials science including fluid behaviour and the chemical and electrical properties of surfaces and electrolytes in solution. We begin by describing the generation of resistive pulses caused by particles moving through a nano- or micro-scale aperture. We then discuss transport mechanisms, such as laminar pressure-driven and electro-osmotic flows, and discuss the relationship to the surface properties of the aperture and the specific composition of the electrolyte. We then describe the theoretical treatment of other transport mechanisms, such as streaming currents and potentials, that could form in our system (although they are likely of negligible magnitude in our specific case [56]). We provide a brief overview of each topic

and then describe the specifics related to the TRPS system described in Chapter 4.

3.2 Resistive Pulses

3.2.1 Pore Resistance

The resistance (R) of a pore can be calculated using the electrical resistance of a cylindrical pore of diameter, a, and length, d, (Figure 3.1 a)) when filled with a conducting fluid of resistivity, ρ_e [10]:

$$R_{cylinder} = \int_0^d dR = \frac{\rho_e d}{\pi a^2} \tag{3.1}$$

assuming uniform electric field and homogeneous resistivity across the cylinder. These assumptions are most valid when surface charge is negligible, and when d $\gg$ a. It has been shown that the space between the end of such a cylinder and a large, distant electrode imparts a non-negligible electrical resistance, referred to as access resistance or end-effects [10]. Each end of the cylinder contributes $R_{end} = \rho_e 2\pi a$ to the total pore resistance, calculated by Hall [30].

The total cylinder resistance can then be expressed as [18]:

$$R = R_{cylinder} + 2R_{end} = \frac{\rho_e}{\pi a}\left(\frac{d}{a} + 1\right). \tag{3.2}$$

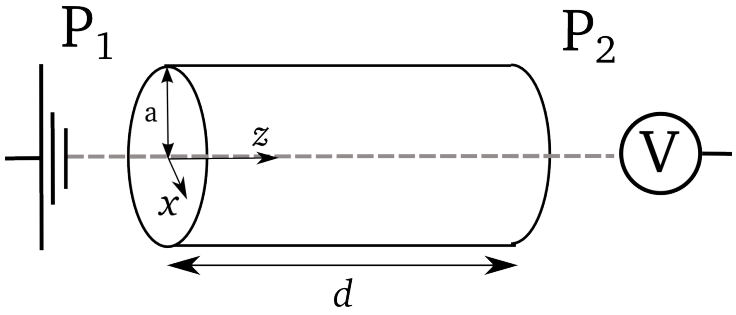

(a) Schematic view of a cylindrical pore used in theoretical analysis of flow. a indicates the pore radius and z the central axis with $z = 0$ at the left entrance of the pore.

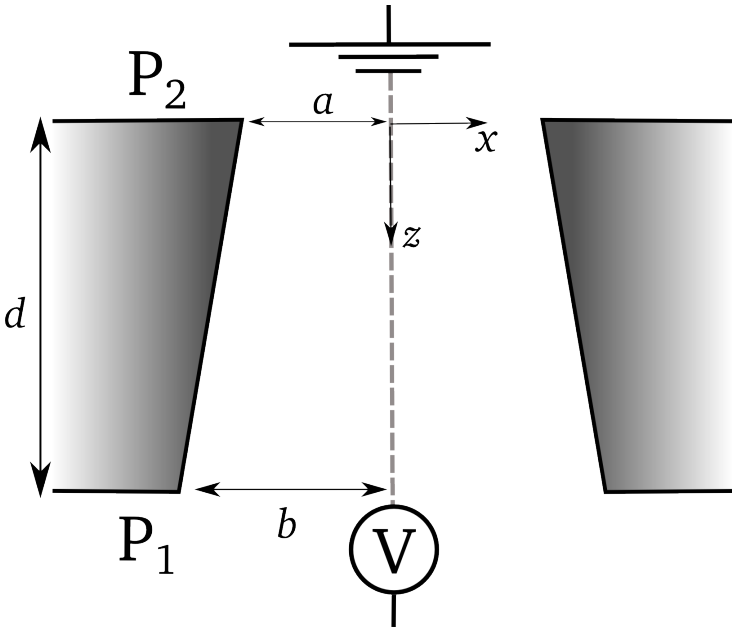

(b) Truncated cone geometry defined by small and large pore radii a and b and pore length d. z describes the central axis of the pore with $z = 0$ at the small pore opening.

Figure 3.1

Non-cylindrical Pores

For a pore with varying radius as a function of z the same general approach can be used to calculate the resistance of a non-uniform, electrolyte-filled pore:

$$R_{pore} = \rho_e \int \frac{dz}{A(z)}. \tag{3.3}$$

This again neglects end effects and as such provides a lower limit for the resistance of the pore. If we assume that the pore radius only changes slowly and smoothly with z, then each increment can be considered a specific radius case of the cylindrical pore, where current flow is parallel to the z-axis [18].

Now we consider the linear, conical profile shown in Figure 3.1 b). We can describe the internal radius of the pore as a function of depth as $\lambda(z)$, where we define $z = 0$ at the small pore opening and b as the radius of the large pore opening:

$$\lambda(z) = b - \frac{b-a}{d}z. \tag{3.4}$$

The requirement that λ varies slowly with z can be stated as $\frac{b-a}{d} << 1$.

Heins *et al.* [83] solved Equation 3.3 for the slowly-varying conical pore geometry described in Equation 3.4 showing

$$R_{pore} = \frac{4\rho_e d}{\pi a b}, \tag{3.5}$$

where a and b are respectively the smaller and larger pore opening radii

and d is the membrane thickness. Willmott *et al.* calculated the total resistance of a conical pore including end effects to be:

$$R = \frac{4\rho_e[d + 0.4(a + b)]}{\pi ab}. \tag{3.6}$$

This resistance is calculated for current flowing parallel to the central pore axis, integrated over cylindrical increments, and including the access resistance between the pore openings and a semi-infinite half space [18, 45].

A key assumption, that the electrolyte resistivity ρ is constant throughout the system, is typically justified because TRPS experiments take place in the high-salt limit, where the Debye length at the pore walls ($\sim$1 nm) is much smaller than the pore dimensions, explained in more detail in Section 3.3.2. This assumption is also consistent with the characteristic Ohmic response of TPs [84].

3.2.2 Resistive Pulse Magnitudes

The presence of an insulating spherical particle in the cylinder will increase the net resistance of the pore. Early work predicting the resistive pulse magnitude (ΔR) of insulating particles within an electrolyte-filled cylindrical pore held that the dominant cause of the change in resistance was due to the occlusion of electrolyte by the presence of the particle itself. The volume of conductive electrolyte occluded from the pore (equal to the volume of the particle) was then proportional to ΔR. Experimental measurements of ΔR for an unknown particle set can be compared with

those for calibration particles in order to accurately, rapidly measure particle size [46].

Maxwell [53] noted that the effective resistivity of an electrolyte containing insulating spheres was:

$$\rho_{\text{eff}} = \rho_e(1 + 3H/2 + ...), \tag{3.7}$$

where H is the volume fraction occupied by an insulating particle. In a cylindrical pore, $H = (4r^3)/(3a^2d)$ where r is the radius of a spherical particle. Then the change in resistance due to a particle being localised within a cylindrical pore, from Equation 3.1, is proportional to particle volume [10]:

$$\Delta R_{cylinder} = \frac{32\rho_e r^3}{\pi a^4}. \tag{3.8}$$

Equation 3.8 also demonstrates that fractional peak magnitude ($\frac{\Delta R}{R}$) can be controlled by altering the pore size, allowing tuning of the signal resolution when using a resizable nanopore. This result was incorporated into RPS work and compared with other approaches by DeBlois [11]. This approach has limitations, requiring that $r \ll a$, and that the electric field be homogeneous across the width and length of the pore. It neglects end effects (Equation 3.6) and has no relationship to the local pore geometry. As such, this approach is unsuitable for particles in pores of more complex geometries than cylinders.

Gregg and Steidley created an additional expression for ΔR [10, 20]

that attempted to allow for particles and pores of different shapes. Their approach was to integrate across the particle axis (Equation 3.1), ignoring the slope of the electric field at the particle's surface, calculating $A(z)$ as a ring of electrolyte between the centrally-located particle and pore wall at each step. They derived an expression for ΔR by taking the difference between the occupied and unoccupied pore. Their method was developed to allow for the capacitive and internal conductivity of biological cells and yields a minimum expected value of ΔR because of neglecting the electric field deviations caused by the particle. This error is greater the smaller the particle becomes as deviations from the z-parallel electric field assumption becomes greater. Whilst this method fails to account for end effects, it is generally applicable to any particle and pore geometry [85]. Building on work from Kubitschek [86] and Gregg and Steidley [20] DeBlois was able to demonstrate, using an inverse sine expansion on powers of the sphere diameter, [10] that

$$\Delta R \approx \frac{4\rho_e r^3}{3\pi a^4}\left(1+\frac{4}{5}\left(\frac{r}{a}\right)^2+\frac{24}{35}\left(\frac{r}{a}\right)^4+\frac{169}{280}\left(\frac{r}{a}\right)^6+...\right). \tag{3.9}$$

Outside the $a << d/2$ limit there is no simple analytic solution for ΔR. Using numerical calculations from Smythe [87] and Cooke [88], DeBlois [11] showed that for particles up to $r/a = 0.95$, ΔR can be accurately approximated by:

$$\Delta R = \frac{2\rho_e r^3}{\pi a^4} S(r/a) \tag{3.10}$$

with

$$S(r/a) = [1 - 0.8(r/a)^3]^{-1}$$

which does not vary from the numerical result more than 2%. S is a correction factor due to the non-linearity between pore and particle volumes that only becomes significant when the particle size is very close to the pore size.

More generally, Equation 3.10 can be re-stated to allow for the presence of non-spherical particles and more complex pore geometries [45]:

$$\frac{\Delta R}{R} = f\frac{V_{particle}}{V_{pore}}S\left(\frac{r}{a}\right) \tag{3.11}$$

where $V_{particle}$ and V_{pore} are the particle and pore volumes, and f is a structure factor (equal to 3/2 for spherical particles). This has been shown to produce values broadly consistent with several methods of analytically determining ΔR [11].

When using conical pores, ΔR can be analytically determined by integrating resistance along the pore, in a similar manner to the derivation of Equation 3.6, but with a sphere present [83]. This approach has been extended for conical pores using a more comprehensive semi-analytic model [18, 46], in which sphere position can be varied, with the key outcome being that ΔR is largely proportional to $V_{particle}$ (as in Equation (3.11)) [46]. Heins *et al.* also noted that with conical nanopores, the electric field is focused to the tip of the pore. In such a situation the current flow through a conical nanopore can be an order of magnitude larger than the current

through a cylindrical nanopore with opening radius equal to the tip of the cone [83].

3.3 Pore Transport Phenomena

The total flux of particles through the pore $\mathbf{J}$ can be described by the Nernst-Planck equation:

$$\mathbf{J} = \sum_{i=1} \mathbf{J_i} \tag{3.12}$$

where $\mathbf{J_i}$ is the transport for individual microfluidic phenomena such as diffusion, pressure, electrophoresis, dielectrophoresis and electro-osmosis [42, 56, 89]. In the sections below we describe each relevant flow component.

3.3.1 Pressure-driven Flow

Generally the flow of Newtonian fluids is described by the Navier-Stokes equation derived from the conservation of momentum in a fluid

$$\rho \left(\frac{\partial \mathbf{v}}{\partial t} + \mathbf{v}.\nabla \mathbf{v} \right) = -\nabla P + \eta \nabla^2 \mathbf{v} + \mathbf{f} \tag{3.13}$$

where ρ is density, $\mathbf{v}$ is velocity, η is dynamic viscosity, ∇P is the pressure gradient and $\mathbf{f}$ describes any other body forces. In essence, Equation 3.13 states that the motion of a fluid will be described by the balance between inertial, viscous and body forces present within and applied to the fluid.

Typically, it is combined with the equation for the conservation of mass (this is a requirement for most simple solutions)

$$\frac{\partial \rho}{\partial t} + \nabla.(\rho \mathbf{v}) = 0 \tag{3.14}$$

which simplifies to $\nabla.\mathbf{v} = 0$ when the fluid is incompressible.

Equation 3.13 is capable of yielding complex, non-linear motion, commonly referred to as turbulence, particularly when viscosity is low or inertial effects begin to dominate the system. The onset of phenomena is described by the ratio of inertial to viscous forces, the Reynolds number (R_e) which can be stated as

$$R_e = \frac{\rho v l_c}{\eta} \tag{3.15}$$

for fluid moving at a velocity (v) and dynamic viscosity η, in a system with characteristic length scale l_c. The persistence of non-turbulent (or laminar) flow is then directly related to the dimensionality of the confinement of the fluid with purely laminar flow typically occurring at $R_e < 0.1$. Hence passing fluids through micro- or nano-scale apertures minimises inertial effects yielding predicable, time-reversible motion of the fluid exhibiting exclusively laminar behaviour and simplifying Equation 3.13 to [90]:

$$\rho \frac{\partial \mathbf{v}}{\partial t} = -\nabla P + \eta \nabla^2 \mathbf{v} + \mathbf{f} \tag{3.16}$$

A well known solution to the Navier-Stokes equation describes motion of fluid moving through a cylinder of radius a when a pressure differential

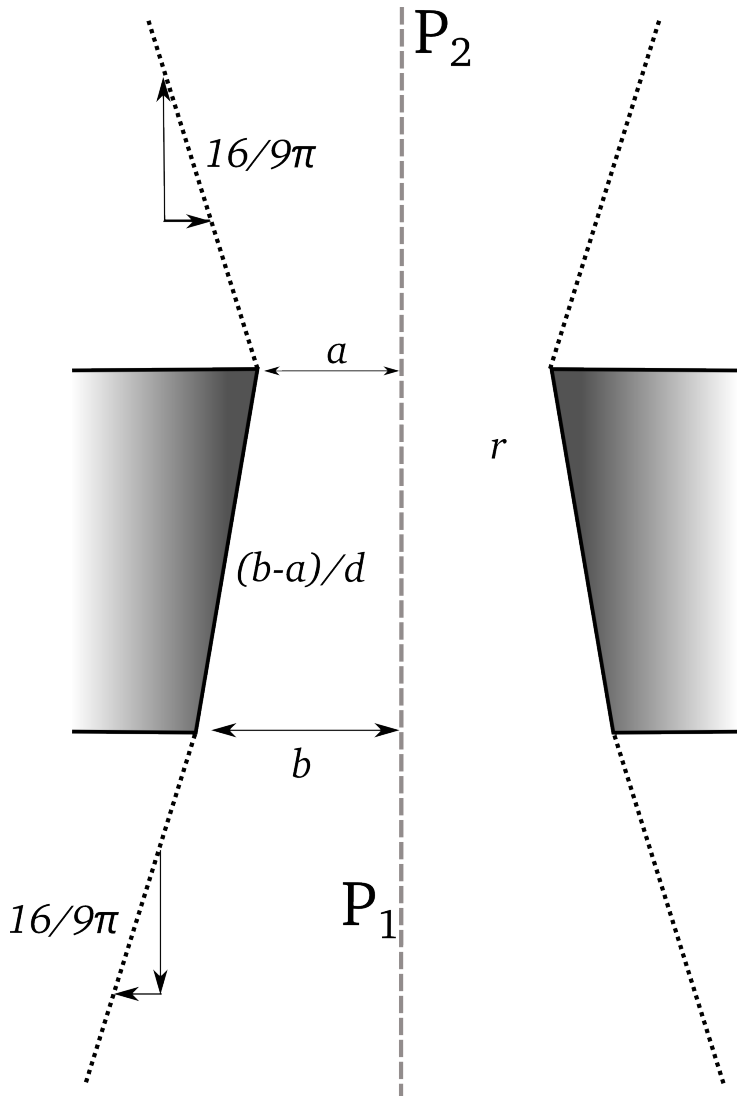

Figure 3.2: Truncated cone geometry showing artificial pressure cones used to approximate the pore access resistance at either end of the pore. The access cone gradient $16/9\pi$, is selected to match the known flow resistance between an infinite half-space and a circular opening. The internal pore gradient is dictated by the large and small pore openings and is required to vary slowly and smoothly down the length of the pore.

is applied across it with magnitude ΔP. This can be derived directly from Equation 3.16 when examining a steady state solution, hence $\rho\frac{\delta v}{\delta t} = 0$, and when flow is not divergent ($\mathbf{v}.\nabla\mathbf{v} = 0$). If pressure is the only external body force applied, the force balance on the fluid becomes:

$$\nabla P = \frac{\Delta P}{\Delta z} = \frac{\partial P}{\partial z} = \eta\nabla^2\mathbf{v}. \tag{3.17}$$

The solution, requiring the no-slip boundary condition that the velocity parallel to the cylinder (v_z) is zero at the wall of the cylinder (where $x = a$), is then:

$$v_z = -\frac{1}{4\eta}\frac{\partial P}{\partial z}(a^2 - x^2) \tag{3.18}$$

where x is the radial distance from the central cylindrical axis. If the pressure decreases linearly down the axis of the pore then this can be simplified further with $-\frac{\delta P}{\delta z} = \frac{\Delta P}{d}$ where d is the length of the cylinder. This is known as Hagen-Poiseuille flow and describes a parabolic flow profile across the diameter of the cylinder, with the faster fluid moving parallel to the central axis of the cylinder at the centre of the cylinder [91].

The pressure-driven volumetric flow rate parallel to the central axis of a pore (Q_p) is calculated from the net applied pressure, P, and the resistance to fluid flow T_r generated by the geometry of the pore, giving a fluidic analogue of Ohm's Law:

$$P = Q_P T_r. \tag{3.19}$$

If the resistance of pore is integrated over a series of thin cylinders, T_r is

the sum of resistance terms from the pore itself T_i and the access resistance T_a [30].

Parry and Willmott described the access resistance generated by the pressure drop between an infinite half space and a circular opening of diameter a as $3\eta/2a^3$ [18]. This analytic expression is derived for infinitely thin pores. Numerical results [18, 85] indicate this expression is also accurate for the access flow resistance to a half-space. Accounting for both ends of the cylinder:

$$T_a = \frac{3\eta}{a^3}. \tag{3.20}$$

For thin cylindrical pores ($d \sim a$) the internal flow resistance is negligible so $T_r \approx T_a$. However, for pores with more complicated geometry, the internal flow resistance of the pore is also significant. For a pore with the internal geometry of a truncated cone, as indicated in Figure 3.2, the access resistance is now the sum of the access resistance for each end with diameters a and b respectively:

$$T_a = \frac{3\eta}{2}\left(\frac{1}{a^3} + \frac{1}{b^3}\right). \tag{3.21}$$

The internal resistance of a truncated cone, T_i, can be calculated using the integral of the incremental resistance along the axis of the pore. For long, slowly varying ($(b-a) \ll d$) pores we can assume local cylindrical flow giving

$$\frac{dT_i}{dz} = \frac{8\eta}{\pi\lambda(z)^4}. \tag{3.22}$$

Integrating down the length of the pore yields an expression for the total internal flow resistance of the pore:

$$T_i = \int_0^d \frac{8\eta}{\pi\lambda(z)^4} dz = \frac{8\eta d\left(\frac{1}{a^3} - \frac{1}{b^3}\right)}{3\pi(b-a)} \tag{3.23}$$

for pores that vary smoothly with z so that for increments of dz, the pore is cylindrical. This also assumes a smooth transition from flow inside the pore to the access flow. We can estimate the pressure driven flow velocity $v(z)$ outside of the pore using artificial cones with gradients $(16/9\pi)$ (Figure 3.2). This value matches the analytical half-space resistance (Equation 3.20) with the integrated value of the cone resistance from the pore opening to an infinite distance. For the truncated pore the volumetric flow rate $\mathbf{Q_P}$ is:

$$\mathbf{Q_P} = \frac{\Delta P}{\eta} \frac{a^3 b^3}{\frac{3}{2}(a^3+b^3) + \frac{8d}{3\pi}(a^2+ab+b^2)}. \tag{3.24}$$

Equation 3.24 predicts that the rate of events should be simply proportional to the particle concentration and pressure, as long as the pore geometry is unchanged. Hence:

$$J_{pd} = C\frac{\mathbf{Q_P}}{A} \tag{3.25}$$

3.3.2 Electrokinetic Phenomena

Electric Field

The electric field within the pore is dictated by the applied voltage and pore geometry, analogous to the pressure-driven flow. The electric field due to a static potential is:

$$\mathbf{E} = -\nabla V. \tag{3.26}$$

This can be related to resistance using Ohm's law via a constant current, I so that we can express the electric field parallel to the central axis of the pore as:

$$E_z = -\frac{\partial V}{\partial z} = -I\frac{\partial R}{\partial z} = -\frac{V}{R}\frac{\partial R}{\partial z} \tag{3.27}$$

where I is the constant current through the pore, V is the total voltage applied between electrodes and R is the total resistance between electrodes.

If the electric field is assumed to be homogeneous across the pore width, within a truncated cone pore (i.e. $d < z < 0$) it is then expressed as:

$$\begin{aligned} E_z(z) &= -\frac{V}{R}\left(\frac{\rho_e}{\pi\lambda(z)^2}\right) \\ &= -\frac{Vab}{(d+0.4(a+b))(a-\frac{(b-a)}{d}z)^2} \end{aligned} \tag{3.28}$$

for a pore where $z = 0$ at the small pore opening, and R and $\lambda(z)$ are from Equations 3.4 and 3.6. Outside of the pore the electric field can be modelled as a cone with gradient matched to the resistance between a circular opening and an infinite half-space (1.25) as with the pressure driven flow

calculation described previously in Section 3.3.1. Hence above the pore ($z < 0$):

$$E_z(z) = -\frac{Vab}{(d + 0.4(a + b))(a + 1.25z)^2}, \tag{3.29}$$

and below the pore ($z > d$):

$$E_z(z) = \frac{Vab}{(d + 0.4(a + b))(b - 1.25(z + d))^2}. \tag{3.30}$$

In both these cases the electric field is still assumed to be homogeneous across the width of the artificial cone, and as such is less accurate than the same assumption made within the pore.

Electrical Double Layer

Fluid motion can also be achieved by the application of an electric potential across the cylinder with magnitude V when the surface of the cylinder exhibits a non-zero surface charge, σ. The presence of surface charges at the cylinder wall attracts counter-ions, repels co-ions and establishes a Boltzmann distribution of charges that decays into the channel and is known as the Debye layer or electrical double layer (EDL) [89], as shown in Figure 3.3.

The charge density of ions in a fluid σ_e can be quantitively described at a distance y from a charged surface as

$$\sigma_e = \sum_i z_i e n_i(y) \tag{3.31}$$

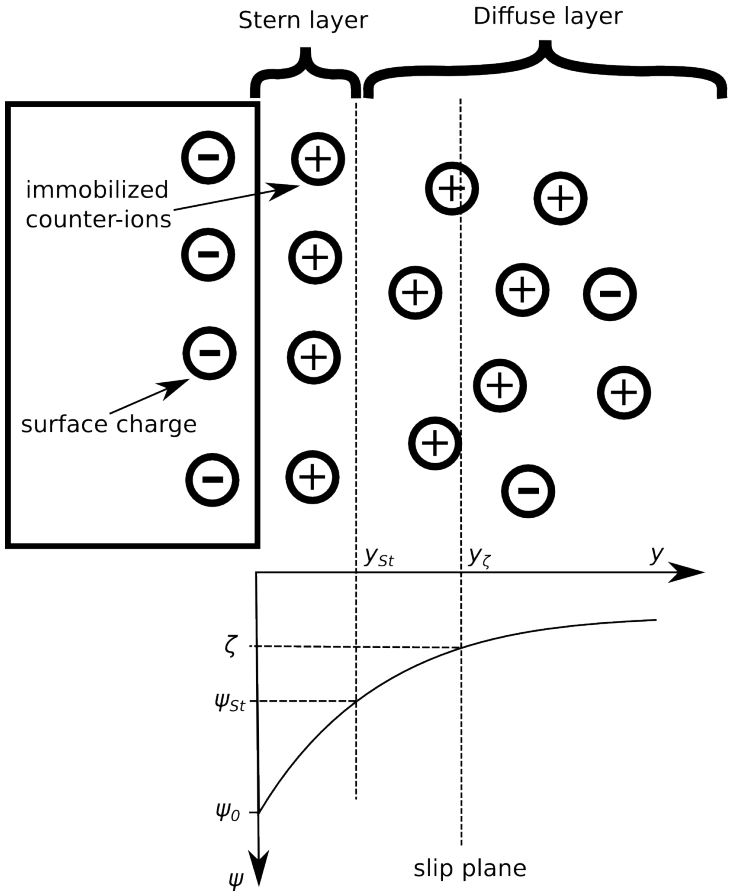

Figure 3.3: EDL diagram showing constituent layers, adapted from [89]. Electrolyte ions are either attracted to or repelled from the surface depending on their charge, creating a depletion (or enrichment) region adjacent to the surface. The ζ potential is defined as the potential at the slip plane, ψ at y_ζ - where the electrostatic attraction of the surface is equal to the viscous forces within the bulk fluid.

where e, z_i and n_i are the charge of an electron, ion valency and the number of ions of type i per unit volume at distance y. The composition of charges in the EDL is controlled by competing electrostatic forces between ions and charges on the surface and Brownian motion. In a solution with bulk ion concentration of n_0 at large distances from the charged surface, this generates a Boltzmann distribution of ions

$$n_i(y) = n_0 exp\left(\frac{-z_i e\psi(y)}{k_B T}\right) \tag{3.32}$$

where k_B and T are the Boltzmann constant and temperature, respectively and ψ is the electrostatic potential at y.

Combining Equations 3.31 and 3.32, the exponential term in Equation 3.32 can be approximated as a first-order Taylor expansion ($e^x \approx 1 + x$) if 0 $< ez_i\psi << kT$. This assumption is known as the Debye-Hückel limit, and holds when $\psi <<$ 26mV at room temperature. This yields:

$$\sigma_e(y) = \sum_i \left(z_i e n_0 - \frac{z_i^2 e^2 n_0 \psi(y)}{k_B T}\right). \tag{3.33}$$

The electroneutrality requirement of the bulk electrolyte causes the first term to cancel leaving the relationship between electrostatic potential and charge density as:

$$\sigma_e(y) = \sum_i \frac{z_i^2 e^2 n_0}{k_B T}\psi(y). \tag{3.34}$$

The electrostatic potential as a function of charge density σ can also be

described by the Poisson Equation:

$$\nabla^2\psi = \frac{\sigma}{\varepsilon} \tag{3.35}$$

if the surface charge per unit area is constant. By equating σ and σ_e and reducing Equation 3.35 to a 1D version we can obtain:

$$\frac{d^2\psi}{dy^2} = e^2 \sum_i \frac{z_i^2 n_0}{\varepsilon k_B T}\psi(y) = \kappa^2\psi(y) \tag{3.36}$$

where ε is the electrolyte permittivity. In this expression the influence of the specific electrolyte is captured within the κ^2 term. For a monionic, symmetric solution of electrolyte, $\kappa = (2n_o e^2 z_i^2/k_B T)^{1/2}$.

Using the boundary conditions $\psi = \psi_0$ at $y = 0$ and $\psi = 0$ at $y = \infty$, Equation 3.36 can be solved by integration giving:

$$\psi = \psi_0 exp(-\kappa y). \tag{3.37}$$

The electrostatic potential in this solution decays with increasing distance into the electrolyte, y, with the ions adopting a Boltzmann distribution and the decay scale described by the Debye length, $\lambda_D = \kappa^{-1}$, as indicated in Figure 3.3. Finally this can be explicitly related to charge by:

$$\sigma_e(y) = \varepsilon\kappa^2\psi_0 exp(-\kappa y) \tag{3.38}$$

Using a similar method as above but neglecting the Debye-Hückel limit,

which is only valid for low potential ($\psi_0 < 26$ mV) [89], we obtain a general analytic expression for which no complete analytic solutions exist:

$$\nabla^2\psi = \kappa^2 sinh\left(\frac{z_i e\psi(y)}{k_B T}\right). \tag{3.39}$$

At high electrolyte concentrations and close ($y << \lambda_D$) to the surface, the Debye-Hückel solution fails to accurately describe the potential. An alternative model is used known as the Gouy-Chapman equation which yields solutions for idealised surfaces only for a symmetric (both ion and counter-ion have the same valency) electrolyte. For more complex cases, involving electrolyte asymmetry, Equation 3.39 can only be solved numerically [89].

ζ-potential

The effect of the EDL is most commonly quantified via study of the ζ-potential as shown in Figure 3.3. In the Gouy-Chapman-Stern model [92] the EDL is deconstructed into specific regions dependent on the kinetic properties of the ions occupying them. The Stern layer is defined as the 'immobilised' layer of counter ions bound to the surface and extends into the channel some distance (y_{St}) dictated by the diameter of the counter ion. Outside the Stern layer exists a diffuse layer of a Boltzmann distribution of mobile ions, described in Equation 3.37. At some distance into this diffuse layer (y_ζ) a 'shear plane' exists where the viscosity forces of the bulk fluid balance the electrostatic forces immobilizing ions to the surface. For $y > y_\zeta$

there will be hydrodynamic motion parallel to the surface (due to the bulk fluid movement), resulting in ions exhibiting a distribution of velocities, **v**, parallel to the bulk fluid flow. The potential at this interface is defined as the ζ-potential, although the distance of the slip plane from the surface depends on the specifics of surface charge, geometry and viscosity of the electrolyte. The net effect of the Stern and diffuse EDL layers is to screen the surface charge from the bulk electrolyte fluid.

The reason ζ-potential measurements are used to characterize the EDL in the place of ψ_0 measurements from 3.37 is due to this division of the EDL. Due to the Stern layer screening, ψ_0 is experimentally problematic to measure. Instead, if the EDL is small, Equation 3.36 can be integrated only to the slip plane allowing Equation 3.38 to be approximated as a function of ζ-potential [89]:

$$\sigma_d(y) = \varepsilon\kappa^2\zeta exp(-\kappa y). \tag{3.40}$$

Electro-osmosis

Due to the localisation of charged counter-ions in the EDL, the superimposition of an external electric field perpendicular to the decay axis of the EDL can cause the net migration of charged species parallel to the cylinder wall as indicated in Figure 3.4, in a manner dependent on the sign and magnitude of the surface charge. The motion of the mobile ions in the EDL draws the bulk fluid viscously parallel to the surface, even when the Debye length is much smaller than the width of the channel. The resulting

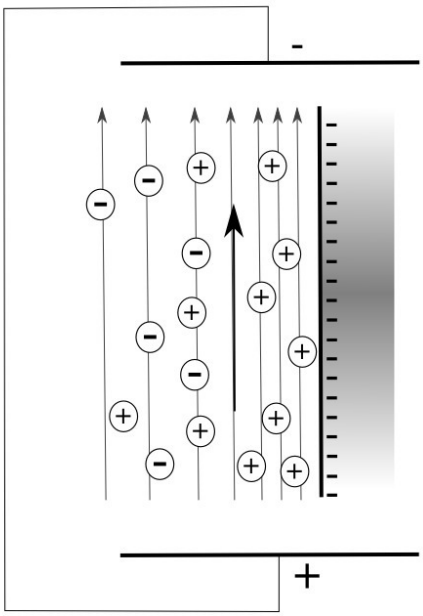

Figure 3.4: Electro-osmosis: charge in the electrical double layer adjacent to the pore wall moves in an applied electric field, causing the bulk electrolyte to flow.

fluid motion is known as electro-osmosis.

From the Navier-Stokes equation, if the only external body force is due to the applied electric field

$$\nabla^2 \mathbf{v} = \left(\frac{\varepsilon}{\eta}\right) \nabla^2 \psi \mathbf{E}. \tag{3.41}$$

A quantitative theoretical analysis was published by Rice and Whitehead [93] for flow in cylindrical capillaries beginning with the 1D equation of

motion parallel to a flat surface balancing viscous and electric forces:

$$\eta \frac{d^2 v_z(y)}{dy^2} E_z \sigma_e(y), \tag{3.42}$$

which has the solution, with the boundary conditions $dv/dy = 0$ at $y = \infty$ and zero slip length ($v_z = 0$ at $y = 0$):

$$v_z(y) = \frac{-E\varepsilon\psi_0}{\eta}(1 - exp(-\kappa y)). \tag{3.43}$$

However, for many common electrolytes and concentrations (for instance 0.1 M KCl), $\kappa^{-1} \approx 1$ nm and so the exponential term becomes negligible in a system whose dimensions, $y \gg \kappa^{-1}$. For these conditions it is also common to replace ψ_0 with ζ, thereby reducing Equation 3.43 to the Smoluchowski equation [89, 94] calculating the electro-osmotic velocity (v_{eo}) as:

$$v_{eo} = -\mu_{eo} E_z = -\frac{\varepsilon \zeta E_z}{\eta}. \tag{3.44}$$

Here E_z is the electric field component parallel to the surface and we define the 'electro-osmotic mobility' (μ_{eo}). Hence, electro-osmosis generates a uniform or 'plug' flow profile across the cylinder width apart from extremely close to the wall.

In Figure 3.5, the electro-osmotic flow shows a uniform velocity across the pore width apart from close to the walls where $\kappa y \sim 1$. The parabolic flow profile for pressure driven flow shows the non-slip boundary condition with maximum velocity at the centre of the cylinder. The net v_z

from the sum of these two effects reverses sign at approximately 50 nm from the pore wall, suggesting large changes in velocity as a function of position in the pore due to the competing effects of pressure driven and electro-osmotic flows.

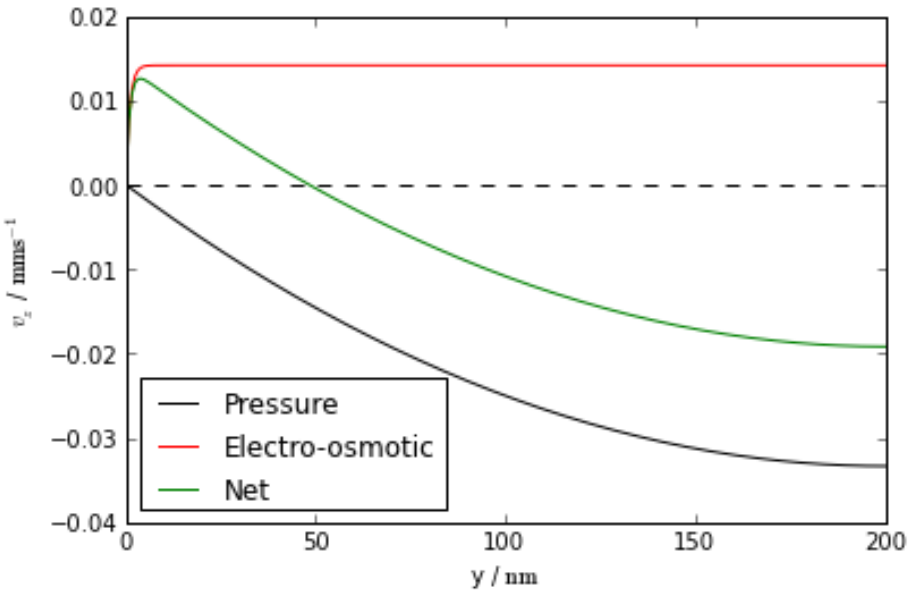

Figure 3.5: Plot of pressure driven and electro-osmotic flow velocities, v_z calculated across the radius of a 400 nm diameter cylinder. These flows are calculated for a cylinder of $d = 150\ \mu m$ in 0.1 M KCl with ΔP = 500 Pa, η = 0.001 Ns/m^2, ε = 7.08 x 10^{-10}, ζ_{wall} = -13 mV under a potential applied across the cylinder of 0.5 V. The opposing electro-osmotic flow (red) and pressure driven flow (black) are summarised by net v_z (green).

In smaller systems or in low electrolyte concentrations that extend the EDL, the electric potential from opposite surfaces can overlap at the centre of the channel leading to variation in v_{eo} across the pore width. Implicit in both Equation 3.41 and 3.44 are the assumptions that the electric field lines and hydrodynamic field lines are parallel (as would be the case in

a long, straight cylinder) and that application of the field does not alter the structure of the EDL. This is of particular importance in small dimension systems as it allows permanent localisation (or separation) of species dependent only on their electrical properties. In this case,

$$J_{eo} = -\frac{\varepsilon}{\eta} C\mathbf{E}\zeta_{pore}. \tag{3.45}$$

Streaming Currents

An additional complication can be generated by the combination of pressure driven flow and the presence of an EDL. Migration of the mobile charged counter-ions in the EDL upon application of a pressure differential, generates a "streaming current", I_s. In a uniform channel I_s can be calculated as:

$$I_s = -\int_A \rho_e \mathbf{v} \cdot d\mathbf{A} \approx -\frac{\varepsilon\zeta}{\eta}\frac{\Delta P}{L}A \tag{3.46}$$

where A is the channel's constant cross-sectional area. A/L can be experimentally estimated for complex geometries [95], can be numerically solved or can be solved analytically under certain specific geometries [93]. This net movement of charged species produces an electric potential due to the excess of ions at one end of the channel that generates an opposing current, I_c, referred to as the conduction current that runs anti-parallel to I_s. For the system to be in a steady state, $I_s + I_c = 0$ with the potential required for this state referred to as the "streaming potential", V_s.

In TRPS we hold the potential constant across the membrane and so

$V_s = 0$. However, recent experiments from Weatherall and Willmott have shown that even under a constant potential regions of charge build-up can occur adjacent to the pore ends [50]. The baseline current through the pore will include some component due to the streaming current, but for TRPS this is typically much smaller than the background current. Using the same values used to calculate electro-osmotic flow in Figure 3.5, we can calculate V_s to be on the order of 0.1 μV and as such is negligible compared to the typically applied voltages of 0.1-0.5 V.

Electrophoresis

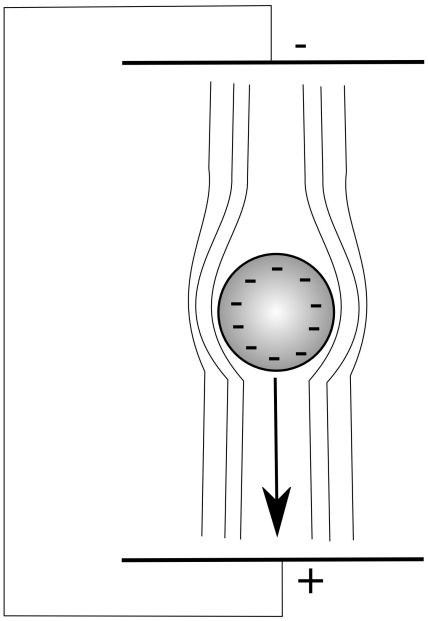

Figure 3.6: Electrophoresis: migration of charged particles against the fluid background due to non-zero surface charge. The field lines indicate the Stokes drag experienced by the particle against the direction of motion.

In addition to the motion of the background fluid, charged particles will also move due the presence of the external electric field, known as electrophoresis. In a static, electrolytic fluid a charged particle will become surrounded by an EDL in a manner akin to the formation of an EDL adjacent to a flat, charged surface, shown in Figure 3.3. The particle EDL screens the surface charge making the particle and its local region of the fluid electro-neutral [89]. The EDL increases the effective radius of the particle, because of the layer of immobile charges surrounding it, to the hydrodynamic radius, r_H: the sum of the particle radius and the distance of the new slip plane, y_ζ, above the surface of the particle.

The motion of the particle in an electric field is then due to the electro-osmotic movement of counter-ions in the EDL. The migration of these ions moves the fluid around the particle due to viscosity, resulting in the particle moving in the opposite direction to the flow of counter-ions. The specific electrophoretic motion of the particle depends on both the particle surface charge and the electrolyte, and analysis of this phenomena is typically split into a thin EDL regime ($\kappa r \gg 1$), a thick EDL regime ($\kappa r \ll 1$) and an intervening regime described by Henry's equation, if $\zeta_{particle} \leq 50$ mV [89]. Whilst for the majority of TRPS experiments the thin EDL regime is valid, we include the other regimes for completeness.

Most theoretical treatments of this system assume that the immobile layer is electrokinetically inactive and plays no part in the conductivity of the diffuse layer. For an insulating particle with uniform surface charge

such that at the particle surface, $\frac{\partial \psi}{\partial r} = 0$ and $\mathbf{v} = 0$ at the slip plane, the system is commonly simplified to one of two limits based on the conductivity of the diffuse layer relative to that of the electrolyte: the thin EDL regime that uses the Helmholtz-Smoluchowski limit and the thick EDL regime that utilises the Hückel-Onsager limit [89].

In the thin EDL regime, when $\kappa r \gg 1$, the particle surface is treated as a flat surface and electrophoresis becomes the exact opposite of electo-osmosis (Equation 3.44) and we define the 'electro**phoretic** mobility', μ_{eph} as

$$\mu_{eph} = \frac{\varepsilon \zeta_{particle}}{\eta}. \tag{3.47}$$

When converted to a particle electrophoresis term this becomes:

$$J_{ep} = \frac{\varepsilon}{\eta} C \mathbf{E} \zeta_{particle} \tag{3.48}$$

Whilst the majority of TRPS experiments occur in the thin EDL regime, it is also useful to consider other EDL regimes. The thick EDL regime, when $\kappa r \ll 1$, the increased radius of the particle due to the EDL become significant, with the mobility then arising from the balance of Stokes drag, the drag force experienced by a particle moving through a viscous fluid,

$$F_d = 6\pi\eta r_H v \tag{3.49}$$

and the Coulombic forces, $F_c = q\mathbf{E}$. Equating these forces, we obtain:

$$\mu_{eph} = \frac{q}{6\pi\eta r_H} = \frac{2\varepsilon\zeta_{point}}{3\eta} \tag{3.50}$$

where the ζ-potential is that due to a point charge, $\zeta_{point} = \frac{r_H q}{4\pi\varepsilon}$.

The intervening regime can be approximated via Henry's equation if particles are weakly charged ($\zeta_{particle} \leq 50$ mV)

$$\mu_{eph} \approx -\frac{\varepsilon\zeta_{particle}}{6\pi\eta} f(\kappa r) \tag{3.51}$$

$$f(\kappa r) = 1 + \frac{1}{2}\left(1 + \left(\frac{2.5}{\kappa r(1 + 2exp(-\kappa r))}\right)\right)^{-3}$$

where $f(\kappa r)$ varies smoothly from 1 to 3/2 at the $\kappa r \ll 1$ (Hückel-Onsager) and $\kappa r \gg 1$ (Helmholtz-Smouchowski) limits respectively [96]. Outside of the regime accurately described by Henry's assumption (weakly charged particles) there exist other methods available to account for the effects of the surface conductivity as described in [95, 97].

Alternately an approximate expression for mobility, ζ-potential and surface charge density (σ) was derived by Ohshima [97] such that:

$$\sigma = \frac{\varepsilon\kappa kT}{e}\left(exp\left(\frac{e\zeta}{2kT}\right) - exp\left(-\frac{e\zeta}{2kT}\right) + \frac{4}{\kappa r}.\frac{exp(e\zeta/2kT) - 1}{exp(e\zeta/2kT) + 1}\right). \tag{3.52}$$

Kirby [98] obtained another expression via substitution into the Guoy-

Chapman-Stern non-linear model, giving:

$$\sinh\left(\frac{-e\zeta}{2kT}\right) = \frac{\sigma\lambda_D e}{2\varepsilon kT} \tag{3.53}$$

Both Equations 3.52 and 3.53 simplify in strong electrolyte solutions [97, 98] to

$$\sigma \approx \varepsilon\kappa\zeta. \tag{3.54}$$

Note that outside of these limits, particularly that of low magnitude potential, the ion cloud surrounding the particle is distorted, further impeding the motion of the particle through the electrolyte [89, 97]. The counter-intuitive property that a particle's electrophoretic mobility is independent of its size is also of note. This has important implications for experiments sorting particles based on both particle size and ζ potential characteristics [90].

DC Dielectophoresis

Insulating particles in an electric field will also be subject to a dielectrophoretic force as they approach the cylinder and as they leave it. The constriction of the electric field lines at the cylinder openings causes polarisation of the particle, with the region of the particle immersed in the stronger electric field becoming more polarised than the other, leading to a net dielectrophoretic force.

For a spherical particle the dielectrophoretic force due to the spatial

gradient of a DC electric field can be calculated as [99]:

$$F_{dep} = 2\pi r^3 \varepsilon_m f_{CM} \nabla |\mathbf{E}|^2 \tag{3.55}$$

where ε_m indicates the electrical permittivity of the electrolyte and f_{CM} is the Clausius-Mosotti factor, accounting for the difference in complex permittivities between the electrolyte and the particle. For an insulating particle in an electrolyte f_{CM} becomes $-1/2$ indicating that the direction of F_{del} will always be towards the direction of the local electric field minimum [99]. The electric field is increased at the pore mouth, because of the constriction of the electric field, as described in Equations 3.29 and 3.30. A particle moving through the pore will be both decelerated on approach the cylinder mouth and then accelerated as it leaves the cylinder, whilst also experiencing a force towards the centre of the cylinder [99]. This is summarised as:

$$J_{dep} = -\frac{Cr^2}{6\eta} \epsilon \nabla \mathbf{E}^2. \tag{3.56}$$

For conducting particles, low conductivity electrolytes or in the presence of large spatial variations in electric field the above simplification of f_{CM} does not hold and must be calculated explicitly from:

$$f_{CM} = \frac{\varepsilon_p^* - \varepsilon_m^*}{\varepsilon_p^* + 2\varepsilon_m^*} \tag{3.57}$$

where ε^* indicates a complex permittivity of the form $\varepsilon^* = \varepsilon + \frac{\sigma}{i\omega}$.

3.3.3 Diffusion

Diffusive behaviour for both ions and particles is described by Fick's first law of diffusion:

$$\mathbf{J}_{\text{diff}} = -D\nabla C \tag{3.58}$$

where D is the diffusion constant and C is the concentration of the species in question. It follows that $\frac{\partial C}{\partial t} = D\nabla^2 C$.

If a concentration gradient exists across the pore then the relevant direction of diffusion is the pore axis, z. The relative importance of diffusion is dependent on the competing processes. Brownian motion is expected to cause particles to move through the pore, but equal numbers of transitions are expected in both directions. Electrophoresis or pressure driven flow typically dominate diffusion effects even at small length scales as calculated by Willmott *et. al* [56]. However, depending on the specific nature of the particle and electrolyte ions, diffusion can become significant when velocities are low, or pores are very short [58]. For particles the diffusivity can be approximated by the balance between the thermal motion of the particle and the Stokes drag [90]:

$$D \sim \frac{k_B T}{6\pi\eta r_H}. \tag{3.59}$$

For the analysis in Chapter 6, we are required to calculate D for non-spherical particles, which are modelled as ellipsoids. We define a particle's deviation from sphericity by the ratio of its radii r_z and r_{xy}. Particles

with $r_z < r_{xy}$ are oblate spheroids whose eccentricity e_o is:

$$e_o = \sqrt{1 - \frac{r_z^2}{r_{xy}^2}}. \tag{3.60}$$

Particles with $r_z > r_{xy}$ are prolate spheroids with eccentricity e_p:

$$e_p = \sqrt{1 - \frac{r_{xy}^2}{r_z^2}}. \tag{3.61}$$

The diffusive Brownian motion of particles in solution is described by the Einstein relation:

$$D = \frac{k_B T}{\gamma} \tag{3.62}$$

where γ is the drag coefficient of the particle. Deviating from spherical symmetry introduces complications into γ as particles now exhibit separate rotational and translational diffusion parallel to and perpendicular to the major axis of the particle (shown in Figure 3.7). The translational drag coefficient of spheroidal particles parallel to the pore axis can be calculated, as

$$\gamma_{t,para} = 16\pi\eta \frac{r_z^2 - r_{xy}^2}{(2r_z^2 - r_{xy}^2)s - 2r_z}. \tag{3.63}$$

and

$$\gamma_{t,perp} = 32\pi\eta \frac{r_z^2 - r_{xy}^2}{(2r_z^2 - 3r_{xy}^2)s + 2r_z}. \tag{3.64}$$

with s defined uniquely for oblate and prolate spheroids by [100]. For

oblate particles $s = s_o$ is:

$$s_o = \frac{2}{\sqrt{(r_{xy}^2 - r_z^2)}} \arctan\left(\frac{\sqrt{r_{xy}^2 - r_z^2}}{r_{xy}}\right) \tag{3.65}$$

and for prolate particles $s = s_p$ is:

$$s_p = \frac{2}{\sqrt{(r_z^2 - r_{xy}^2)}} \log\left(\frac{r_z + \sqrt{r_z^2 - r_{xy}^2}}{r_{xy}}\right). \tag{3.66}$$

For near-spherical (aspect ratio $r_z/r_{xy} > 0.99$) 500 nm diameter nanoparticles, the translational drag coefficients are around 11 orders of magnitude larger than the rotational coefficients. Additionally, the translational drag coefficient parallel to the minor axis of the spheroid is $\sim$60% of the perpendicular coefficient [100]. Hence only translational drag coefficients are considered in this analysis.

Conservative body forces

Whilst gravitational effects are typically weak in low dimension systems they, along with any conservative body force applied to the fluid, can be expressed explicitly as a modification of the pressure term in Equation 3.13. Conservative forces can be expressed as the gradient of a scalar quantity F such that $\mathbf{f} = \nabla F$. This effect is included by defining a modified pressure term P^* such that $P^* = P - F$. The pressure term of Equation

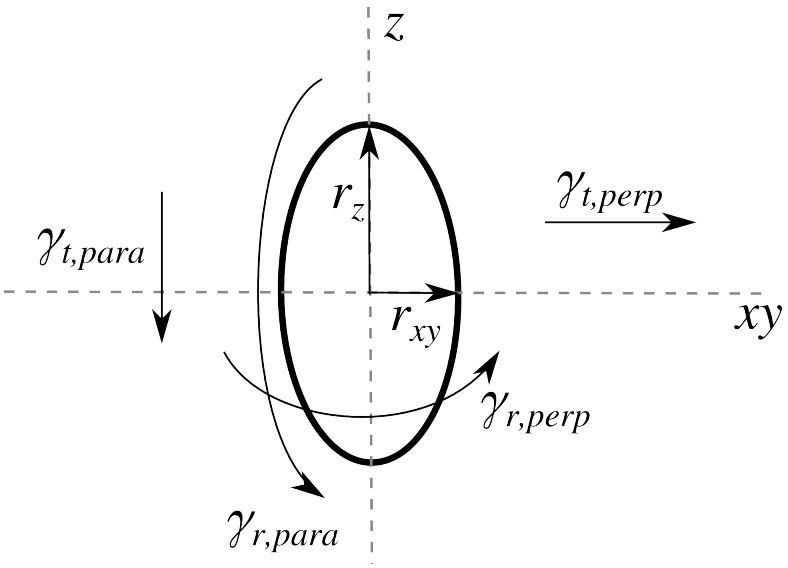

Figure 3.7: Spheroidal particle indicating rotational drag coefficients γ

3.13 then becomes:

$$-\nabla P + \mathbf{f} = -\nabla(P - F) = -\nabla P^*. \tag{3.67}$$

In the gravitational case $F = -\rho g z$. For the analysis of TRPS systems this allows gravitational effects to be included by the modification of P as appropriate. This approach is used to account for the gravitational pressure head in the fluid cell for TRPS.

3.3.4 Other Transport Phenomena

Due to the large number of other possible physical transport mechanisms, this thesis omits a detailed discussion of many common phenomena. For an in-depth discussion of many currently studied microfluidic phenomena

we direct the reader to [90] and [89]. In general, these are of negligible magnitude compared to the previously described phenomena for pores $>$ 100 nm in diameter and $>$ 100 μm in length [56].

3.4 Semi-analytic Model

3.4.1 Overview

The semi-analytic approach used to model resistive pulse events is that developed by Willmott *et. al* in [18] with some extensions. The model was implemented for the first time in the Python programming language (2.7) using the Scipy and Numpy calculation libraries (versions 0.13.3 and 1.9.1 respectively) for numerical simulation and integrating ordinary differential equations. Table 3.1 describes the constants used during model calculations. When the transport phenomena described in the previous

Table 3.1: Summary of constants used for calculating pore model, following [18].

Constant	Symbol	Value	Unit
Boltzmann Constant	k_B	1.38 x 10^{-23}	J K^{-1}
Temperature	T	293	K
Permittivity	ε	7.1 x 10^{-10}	C^2 N^{-1} m^{-1}
Viscosity	η	0.001002	Pa s
Resistivity	ρ	0.75	Ω m

section are stated explicitly for micro- and nanoscale systems, Equation

3.12 becomes:

$$\begin{aligned}\mathbf{J} &= J_{diff} + J_{ep} + J_{eo} + J_{dep} + J_{pd} \\ &= -D\nabla C + \frac{\varepsilon}{\eta} C\mathbf{E}(\zeta_{particle} - \zeta_{pore}) - \frac{Cr^2}{6\eta}\epsilon\nabla\mathbf{E}^2 + C\frac{\mathbf{Q_p}}{A}.\end{aligned} \tag{3.68}$$

The contribution to motion due to individual forces on a particle (J_{pd}, J_{eo}, J_{eph}, J_{dep} and J_{diff}) are computed from the theoretical background, Equations 3.25, 3.45, 3.48, 3.56 and 3.58 respectively. These can be summed to give an equation of motion, $\frac{\delta z}{\delta t}$, for a particle either above, within or below the pore, if the pore is on axis and the area $A(z)$ is known. At length scales below 10 μm typically electrokinetic and pressure driven flows dominate behaviour, with diffusion and dielectrophoresis only becoming relevant in the presence of high concentration or electric field gradients [56]. Even so, we must know the electric field $\mathbf{E}$ and the volumetric pressure-driven flow rate $\mathbf{Q_p}$, both of which are linked to the particular geometry of the system. Model inputs include the constants in Table 3.1, $V, P, \zeta_{particle}, \zeta_{pore}$ and the pore geometry.

A 4th order Runge-Kutta method is used to obtain a numerical solution in the form $z(t)$. Simulations typically start with particles at 10 μm above the small pore opening. At each step in the solution, the total resistance of the particle and the pore is calculated by integrating across both the particle and the pore. Finally ΔR is calculated from the difference between the calculated current and that computed for the pore in the absence of a particle from Equations 3.6 and 3.10.

For necessity all of these calculations assume surfaces are smooth to a length smaller than the Debye length. Experimentally, this can be tuned through the choice of a specific composition and concentration of electrolyte (see Section 3.3.2). We assume all surfaces have randomly distributed charge and hence treat them as homogeneous. Furthermore, we assume the size of the particle has little effect on the ζ-potential, but this is only true in the two extreme regimes, when the product of κr is very small or very large (see Section 3.3.2) [89]. Our calculation of electric field assumes that the conductivity of the diffuse layer is negligible compared to that of the electrolyte, which is only reasonable if surface ζ-potential < 50 mV, which appears the case for both TPU and polystyrene [97]. For non-spherical particles, revised expressions for diffusion and ΔR were used to extend the model as described in Section 3.3.3 and Equation 3.11 respectively. These assume that non-spherical particles have uniform surface charge, and behave identically to spherical particles in Poiseuille flow.

3.4.2 Non-spherical Particles

Effective Particle Charge

By comparing Equations 3.47 and 3.50 we can define the effective charge of a particle by balancing the applied electric force with the retarding force described by Stokes drag for a sphere:

$$q\mathbf{E} = 6\pi\eta r_{\text{eff}}\mathbf{v}. \tag{3.69}$$

Calculating the radius of an equivalent volume sphere for our particles yields $r_{\text{eff}} = ((3V_{particle})/(4\pi))^{1/3}$. r_{eff} is often referred to in similar formulations as the hydrodynamic radius of the particle. Using the Smoluchowshi equation in the Debye-Hückel limit gives:

$$q_{\text{eff}} = \frac{3\varepsilon\zeta_{particle}}{2r_{\text{eff}}}. \tag{3.70}$$

Particle Rotation

Non-spherical particles can take any rotational conformation as they move through the pore. Golibersuch attempted to calculate the fractional occupation of rotational conformation of non-spherical particles [101]. Our model assumes particles retain one orientation throughout their passage through the pore, hence we neglect the rotational diffusion of the particle and the translational diffusion of the particle perpendicular to the pore axis. We investigate the effect of rotation on pulse characteristics by simulating an on-axis particle rotated through some angle θ to the pore axis. To calculate the occlusion volume for each particle, R is integrated through the pore, as with non-rotated particles. However, a new particle radius r' is calculated as the radius of a circle with area equivalent to that of a cross-sectional ellipse through the xy plane at some z position through the particle, h. The centre of the cross-sectional ellipse is then C_x:

$$C_x = \frac{2h\cos\theta\sin\theta(r_{xy}^2 - r_z^2)}{2\beta} \tag{3.71}$$

with $\beta = (r_{xy}^2 \sin^2\theta + r_z^2 \cos^2\theta)$. The radius of the equivalent circle to that ellipse is then:

$$r' = \sqrt{\frac{\Omega}{\sqrt{r_z^2 \beta}}} \tag{3.72}$$

with

$$\Omega = r_z^2 r_{xy}^2 + (r_{xy}^2 - r_z^2)(2C_x h \sin\theta\cos\theta) - h^2(r_z^2 \sin^2\theta + r_{xy}^2 \cos^2\theta) - C_x^2\beta. \tag{3.73}$$

This allows calculation of R by integrating through the pore calculating the fractional areas of particle and pore, as for on-axis spherical particles. The issue of particle rotation is an area where this model could be extended in future work.

3.4.3 Alternative Pore Geometries

The truncated cone model provides a framework for calculating particle shape and charge, modelling the internal pore geometry whilst requiring only measurements of a, b and d. It is unlikely however, that the interior of the pore is as regular as this geometry may suggest. Furthermore, when examining resistive pulse shapes, the truncated cone model is insufficient to accurately reproduce pulses observed for all pore sizes. Willmott *et al.* have examined the actual interior pore geometry previously using SEM imaging and confocal microscopy [57]. Their results indicated that pores appear to resemble a 'wineglass' shape that could be approximated using a cubic function if the pore was assumed cylindrically symmetric. However,

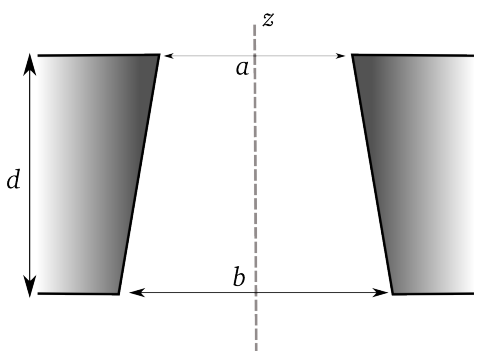

(a) Truncated Cone (a, b, d).

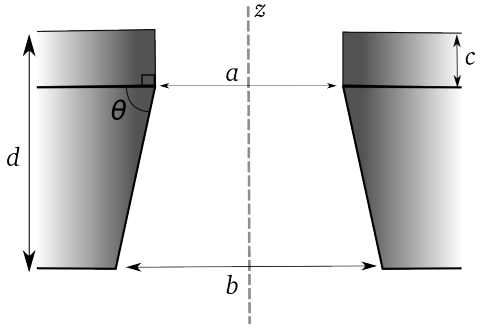

(b) Cylinder+Truncated Cone (a, b, c, d)

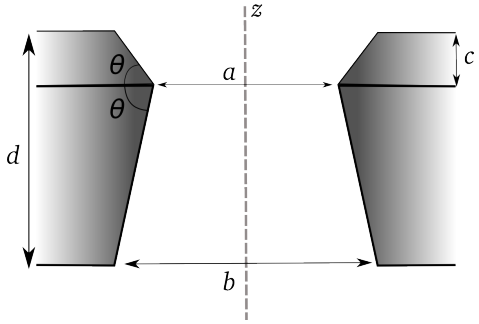

(c) Constricted Symmetric Cone (a, b, c, d)

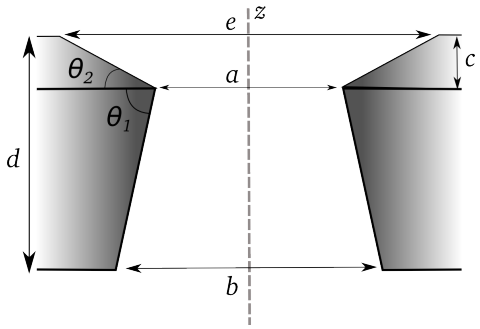

(d) Constricted Asymmetric Cone (a, b, c, d, e)

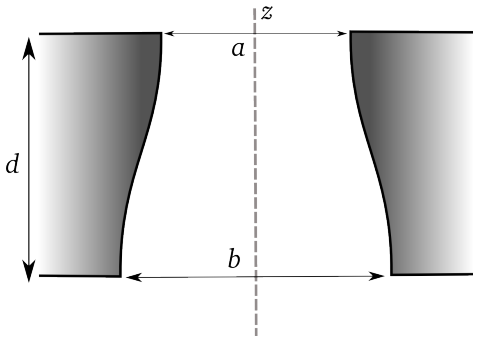

(e) Wineglass $(a, b, d, \lambda(z))$

Figure 3.8: Alternative internal pore geometries for nanopores and the parameters required to describe them. e) requires $\lambda(z)$ as an input function over the curved 'wineglass' section of the pore.

this was only possible due to the detailed data available for the internal geometry of the specific pore they examined. They have also shown that the internal geometry of a pore can significantly change the shape and magnitude of resistive pulses. In particular, the portion of an event prior to the minimum current being reached is closely tied to the pore opening geometry [18].

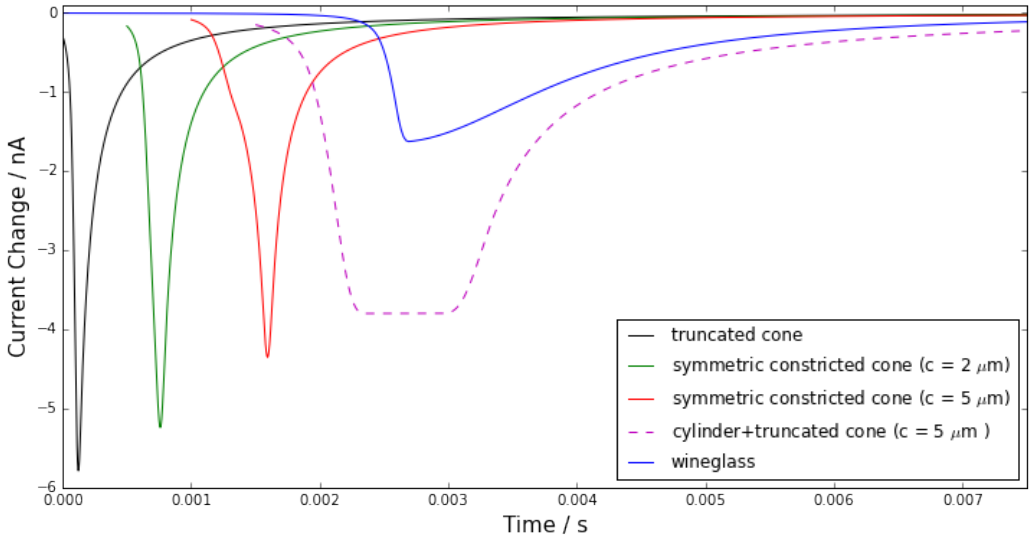

Figure 3.9: Resistive pulses generated from the semi-analytic model showing spherical particles traversing various pore geometries. For visual clarity each event has been plotted with an artificial separation of 0.5 ms. Events correspond to Figure 3.8 geometries a), c), c), b) and e) respectively. Pulses calculated for 1 μm diameter spheres passing through a 200 μm length pore, with P = 50 Pa, V = 0.15 V, a = 2.0μm, b = 40 μm, ζ_{pore} = -13 mV and $\zeta_{particle}$ = 20 mV.

A variety of pore geometries are plausible for the TPU nanopore fabrication method described in Chapter 2. Figure 3.8 summarises some of the previously used geometries and the dimensions required to charac-

terise them. For each model there is a trade-off between the accuracy of the model and the number of measurements required to characterise the geometry. To generate the geometry presented in Figure 3.8 a), a previous method for conical geometries is used [57] by defining a $\lambda(z)$ such that if $z = 0$ at a:

$$\lambda(z) = a + \frac{(b-a)}{d}z. \tag{3.74}$$

For more complex geometries we include a depth c that describes the distance below the upper pore opening over which the pore diameter is at its minimum, which also requires assumptions of $\lambda(z)$ about the constriction. This allows us to generate additional geometries in Figure 3.8 b), c) and d). For c) the pore gradient is assumed to be symmetric about the constriction. Figure 3.8 d) describes perhaps the most likely geometry because of the pore fabrication method and the $\sim$10 μm characteristic deformation length of TPU noted in both literature and in SEM images of the interior of the pore (see Chapter 4). However, it is also difficult to constrain because of the large number of experimental variables. Willmott *et al.* describe a 'wineglass' geometry by using a polynomial function fitted to confocal microscopy data [57]. We present an alternative requiring less constraints by using a cosine function:

$$\lambda(z_{wineglass}) = a + \frac{(b-a)}{2}(1 + cos(\frac{\pi z}{d})). \tag{3.75}$$

Figure 3.9 compares the pulses produced from some of the geometries

described above, with the translocation produced by spherical particles. Figure 3.9 indicates the close relationship between pulse shape and pore geometry that will be discussed further in Chapter 6.

3.5 Conclusion

This chapter has detailed approaches to pore resistivity and RPS calculations for several pore geometries. The major particle and fluid transport phenomena (pressure-driven flow, electrophoresis and electro-osmosis) are also presented and effects summed using the Nernst-Planck equation. Additional transport phenomena, including diffusion and dielectrophoresis, were also discussed but these are not expected to be present at sufficient magnitude to warrant inclusion in the semi-analytic model [56]. The implementation of this theory in the semi-analytic model for predicting resistive pulses was also presented, as were the extensions of it to allow for rotated, non-spherical particles and alternative geometry pores.

Chapter 4

Materials and Methods

This Chapter details the materials, experimental set-up and analytical procedures used to produce the results presented and discussed in Chapters 5, 6 and 7. Section 4.1 reports the composition and characterisation of electrolyte buffers, thermoplastic polyurethane (TPU) and all particles and preparation procedures used; including carboxylate polystyrene spheres, Au-nanorods, *Rattus* blood, *Shewanella marintestina* bacteria and bacterial polyhydroxyalkanoate particles. Section 4.2 describes the qNano system used for all TRPS experiments, characterises the nanopores used for all measurements, describes the variable pressure manometer (VPM) and presents the standard operating procedures used to collect all data presented in this thesis. Section 4.3 presents how data generated by either Izon Control Suite, or custom written software characterises resistive pulses. We also present our methodology for data filtering and pulse characterisation.

4.1 Materials

4.1.1 Buffers

Standard Electrolyte Buffer (SEB)

Most experiments with the qNano are performed by dispersing particles in standard electrolyte buffer (SEB) that consists of an electrolyte, buffering agent, surfactant to assist with pore wetting, and a chelating agent dispersed in 18.2 $M\Omega\,cm^{-1}$ deionised water supplied by a Barnstead easypure RoDI system, with the proportions noted in Table 4.1. All mass measurements were made using a Sartorius Basic analyical balance. The pH is set to 8.0 by the addition of HCl or KOH, confirmed by measurements using a calibrated PCS Testr35 pH meter. pH readings were taken after the pH meter held the same value in the solution for more than 20 seconds. Before use, SEB was filtered through a 0.2 μm Minisart filter (Sartorius Stedim Biotech, Goettingen) and degassed using a sonicator for 10 minutes. The deionised water and KCl solution was made up and stored at 4°C, with the rest of the SEB preparation being carried out on the same day experiments were performed.

Phosphate Buffered Saline (PBS)

Phosphate buffered saline (PBS) used for experiments was made up shortly before experiments from stock PBS tablets obtained from Sigma Aldrich (P4417) and dissolved in deionised H_2O. This provides PBS with 0.01 M

Table 4.1: Composition of standard electrolyte buffer (SEB) used for experiments

Component	Concentration	Action	Supplier
18.2 MΩ Deionised water	–	solvent	
KCl	7.45 g/L (0.1 M)	electrolyte	BDH Chemicals Ltd
2-Amino-2-hydroxymethyl -propane-1,3-diol (Tris)	1.21 g/L (0.01M)	buffer (pKa = 8.07)	Sigma Aldrich
ethylene glycol-bis (2-aminoethylether)-N,N,N,N -tetraacetic acid (EGTA)	1.1 g/L (3 mM)	chelating agent	Sigma Aldrich
polyethylene glycol p-(1,1,3,3-tetramethylbutyl) -phenyl ether (Triton-X)	0.01% v/v	surfactant	BDH Chemicals Ltd (England)
0.1 M HCl	dropwise	pH control (set to pH=8.0)	

phosphate buffer, 0.0027 M potassium chloride and 0.137 M sodium chloride, pH 7.4, at 25°C. Before use, PBS solutions were filtered through a 0.2 μm Minisart filter (Sartorius Stedim Biotech, Goettingen) and degassed using a sonicator. No extra surfactant was added to PBS solution unless expressly noted in experimental protocols.

4.1.2 Electrolyte Conductivity

The conductivity of SEB was measured with a Denver Instruments (Model 220) pH and conductivity meter at all stages of buffer preparation. As expected, measurements indicate that the only significant contribution to net electrolyte conductivity (within experimental error) is due to the KCl concentration for electrolyte concentrations greater than 10 mM KCl, as shown in Table 4.2. All changes in SEB conductivity measured during each synthesis step corresponded to $<$1 mS/cm, hence they are smaller than experimental uncertainties reported in 100mM KCl in Figure 4.1, once

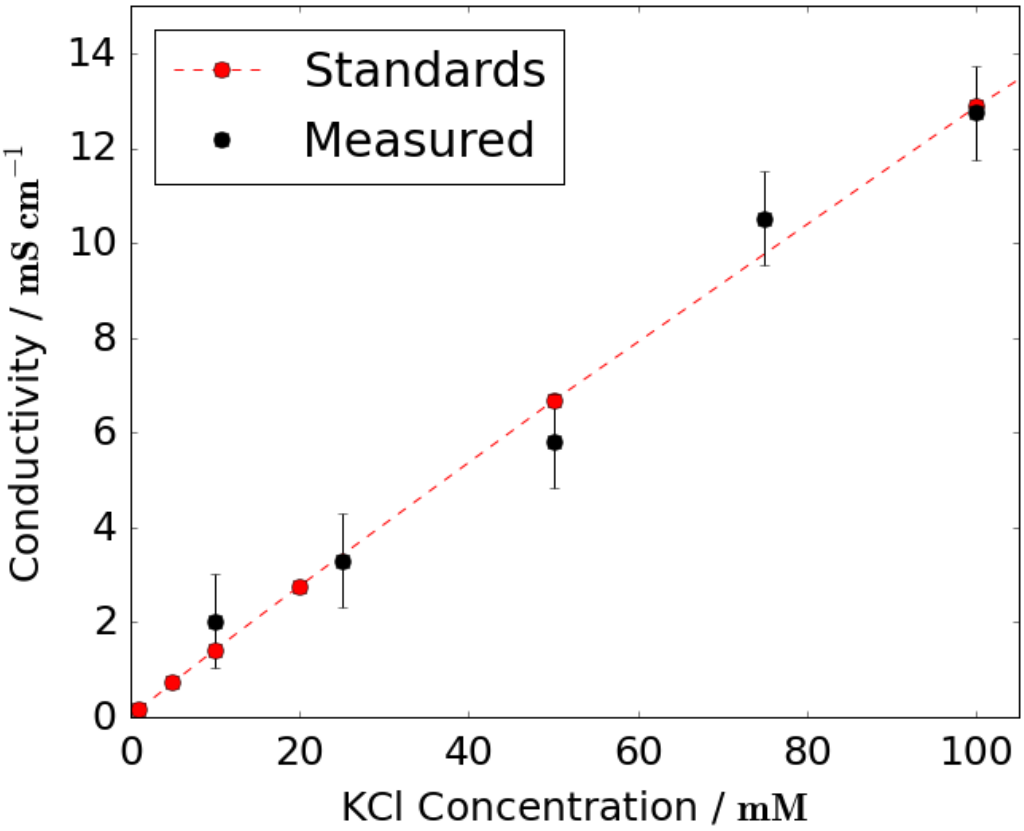

Figure 4.1: Measurements of SEB conductivity for different KCl compositions. Red datapoints and line indicate conductivities reported for electrolyte standard concentrations of KCl from [102]. Deviations from the red line may be due to differences in measurement apparatus, temperature and error in electrolyte composition. Error bars indicate standard error in the mean over repeated measurements.

variations in temperature (caused by sonication) are corrected for.

Table 4.2: Sequential conductivity changes measured during 0.1 M KCl SEB manufacture, measured at 21°C with n = 5 repeats. The initial value measured for 0.1 M KCl was 12 mS/cm.

Component	Conductivity Change mS/cm	Standard Error mS/cm
0.1 M KCl	–	–
0.01 M Tris	0.62	0.16
pH adjustment with HCl	-0.26	0.38
Triton-X (0.01% v/v)	-0.12	0.09
EGTA	0.06	0.06
Filtration	-0.40	0.24
Sonication	-0.20	0.25

Conductivities measured for 0.1 M KCl SEB solutions sealed at room temperature over a period of 1 month did not show conductivity variations beyond experimental error when re-measured. Solutions frozen overnight however, showed a mean reduction in conductivity, when re-heated to room temperature, of 30% when compared to a control sample kept at room temperature for the same duration. It is assumed that this change in conductivity is due to electrolyte precipitation from the freezing process and thus frozen SEB was not used in any experiments.

4.1.3 Thermoplastic Polyurethane (TPU)

The thermoplastic polyurethane used to fabricate the nanopore membranes is Elastollan 1160D (BASF, Germany). The material's elastomeric properties are a consequence of the mixture of long (flexible) and short (rigid)

chain polymers, and the specific conditions used for TPU synthesis [43]. The Elastollan 1100 class are composed of polyether-based polyols (long chain diols) and short chain diols crosslinked though reaction with diisocyanates to create linear polyurethane. The specific reaction mechanism for 1160D is proprietary and so the functional groups and hence surface charge of the polymer are not documented [103]. As such, electro-osmotic flow measurements were used to determine a value for ζ_{pore} for TPU in SEB.

ζ_{pore} Measurements

In order to determine ζ_{pore}, electro-osmotic flow (EOF) measurements were performed in TPU microchannels. These channels were custom-synthesized using soft lithography in 1 cm x 4 cm x 0.5 cm pieces of TPU. A laser direct writer (Microtech 405A) produced a master in SU-8 2015 Permanent Epoxy Negative Photoresist (MicroChem (Newton, MA), as described in [104]), consisting of an (inverted) channel of dimensions 0.022 mm x 0.1 mm x 30 mm. A piece of TPU was rinsed with ethanol, dried in a stream of nitrogen and placed between the master and a flat SU-8 master. This arrangement was held in a vice and heated at 100°C for 10 minutes, then further compressed and baked for another 15 minutes at 100°C. The sample was cooled to room temperature, and the embossed surface placed against a smooth TPU sheet (both having been rinsed with ethanol), clasped lightly in the press and baked again for 20 minutes at 120°C to form a seal. Fi-

nally the channel was cooled slowly in the oven for a minimum of two hours to prevent separation due to asymmetric thermal contraction. This thermal embossing process does not require a bonding agent (as used in [52]) which may chemically react with the polymer surface and thus alter the measured surface charge of unmodified TPU. It is also noteworthy that the actual membranes used in TRPS experiments are formed by injection moulding, which may alter the surface charge from the value measured for the TPU sheets, which were obtained directly from BASF.

EOF measurements were performed using the current monitoring method [52, 89] that involves filling the channel with an electrolyte only (typically between 10 and 200 mM KCl), applying 500 V across it using silver electrodes, as indicated in Figure 4.2 a), and measuring the current produced. Once the current has stabilised (less than 1% drift over 30 s), the fluid in one well is replaced with fluid of slightly lower conductivity (2% was used for these experiments) and the electric field re-applied. Due to the induced EOF, the lower conductivity fluid is driven down the channel, displacing the higher conductivity fluid and causing an overall drop in current through the channel. Once the channel has become entirely filled with the low conductivity electrolyte the current stabilises again and the fluid transit time ($t_{transition}$) is the interval during which the current is decreasing (Figure 4.2 c)). As the dimensions of the channel are known (channels are

3 cm in length = $L_{channel}$), the average v_{EOF} can be calculated directly from:

$$v_{EOF} = \frac{L_{channel}}{t_{transition}}. \tag{4.1}$$

Small differences in conductivity are used to minimise the effect of diffusion on the system. Fluid is replaced after each measurement to limit any Joule heating effects. All ζ_{pore} data points in Figure 4.2 b) represent at least 10 repeated EOF measurements performed with the same microchannel. The ζ_{pore} of TPU in SEB (100 mM KCl) used for all calculations in this thesis is -12 mV $\pm$ 2.5 mV.

Pore H_2O Absorption

Thermoplastic polyurethanes are well known to be hygroscopic to varying degrees. This hygroscopic behaviour can result in swelling, lowering of the polymer's glass transition temperature and premature aging [105]. This behaviour could potentially also account for the observed difference between the expected baseline current observed in pores characterised with SEM images and that measured (see Table 4.5).

Table 4.3: H_2O absorption measurements for pore A11486 (NP200) at 25°C.

Treatment	Mass(g) $\pm$0.0001	Change from dry (%)
Dry	1.2189	-
15 minute soak	1.2195	+0.05%
60 minute soak	1.2211	+0.18%
Dessicated	1.2200	+0.09%
20 minute heat at 60°C	1.2156	-0.27%

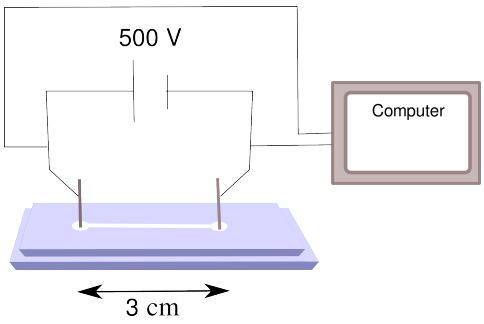

(a) EOF apparatus schematic showing the channel shape used to make EOF measurements.

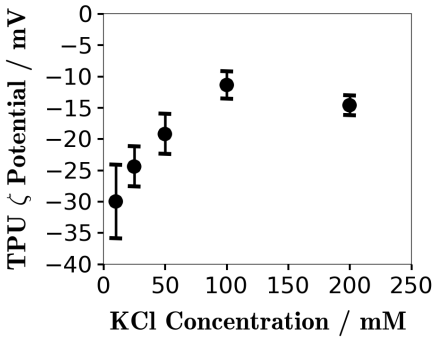

(b) The ζ-potential of TPU, the material used to make tuneable pores. Each data point is the mean of at least 10 individual electro-osmotic flow measurements, with error bars indicating the standard deviation of repeat measurements.

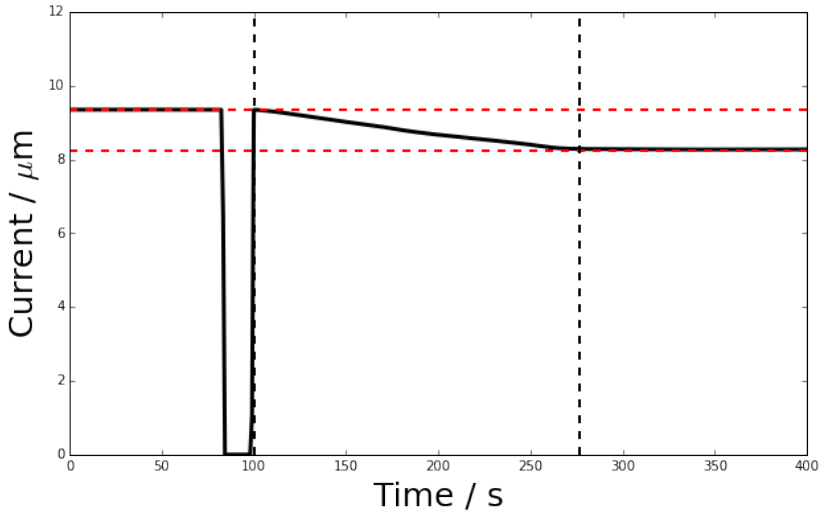

(c) An example EOF measurement showing current passing through the channel as lower conductivity fluid displaces higher conductivity fluid via electro-osmotic flow. In this example the electrolyte is changed at 100s and $t_{transition}$ indicated by vertical dashed black lines. The current upper and lower limits are indicated by dashed red lines.

Figure 4.2

Table 4.3 shows the masses for a TPU cruciform under different wetting conditions. The 'Dry' condition indicates the pore's state under normal laboratory conditions (i.e. exposed to air at 20-25°C). For both the 15 and 60 minute soak, the pore was left submerged in 0.1 M KCl at room temperature for the time indicated. Prior to the mass measurement each pore was blown dry using a stream of compressed nitrogen until no moisture was visible on the surface of the cruciform (Figure 2.2). After the 60 minute soak measurement the cruciform was dessicated (held under low pressure using an Emerson vacuum pump) for 30 minutes to attempt to return the cruciform to its original 'Dry' state. Finally the pore was placed in an oven and held at 60°C (lower than the softening point of TPU which is ∼80°C) for 20 minutes and weighed again. The measured percentage change in membrane mass is consistent with the expected hygroscopic nature of TPU. Therefore, during experiments, hygroscopic pore swelling may change internal pore diameters slightly from the internal pore diameters measured using SEM and add to the uncertainties in pore geometry.

At each of the 15 and 60 minute soak steps the large diameter of the pore was photographed using a Nikon Diaphot 300 optical microscope, between 41 and 48 mm applied stretch, with results presented in Figure 4.3. Pore diameters observed at each stretch are presented in Figure 4.4. Within the resolution of this method there is no evidence for a relationship between H_2O absorption and changes in pore diameter.

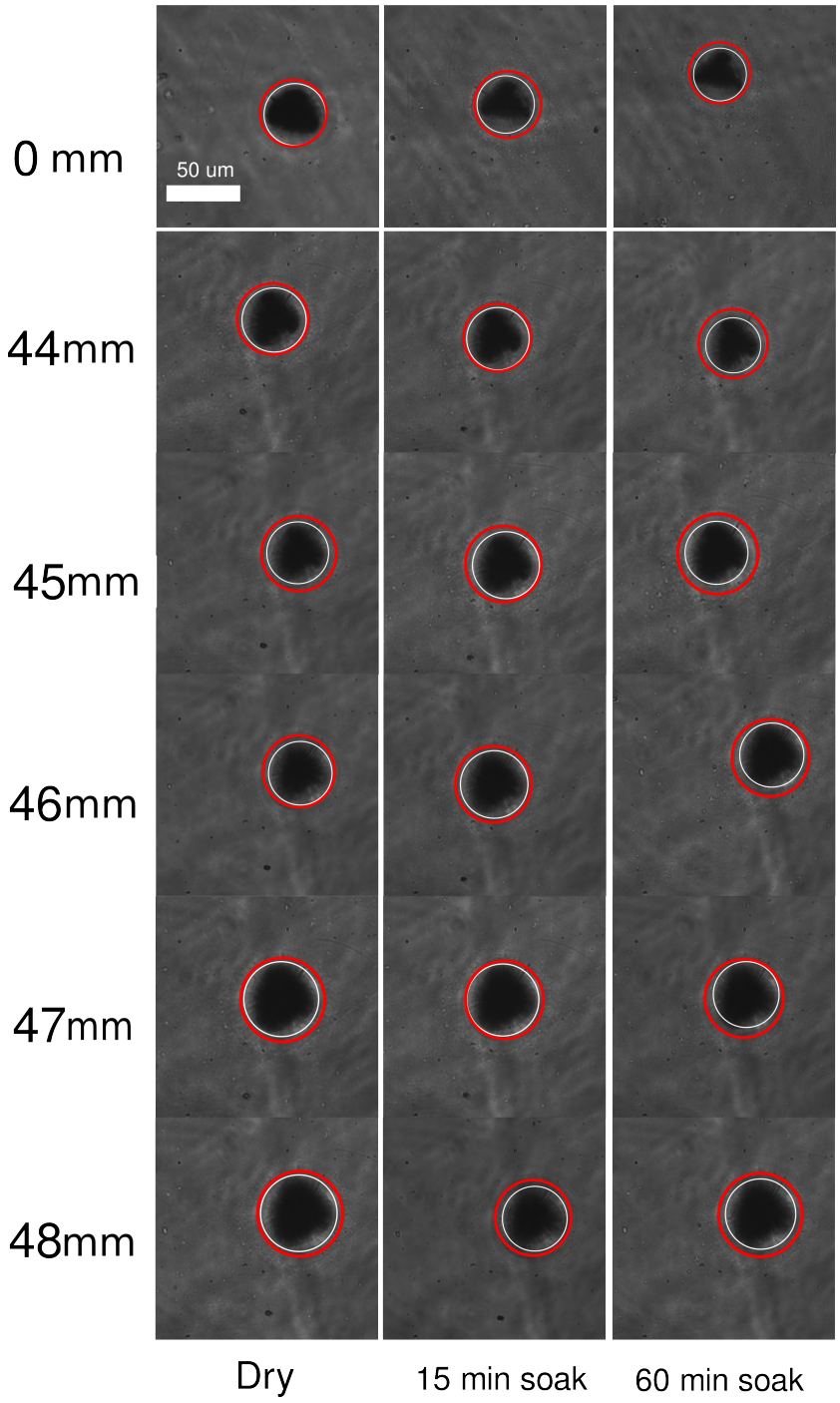

Figure 4.3: Optical microscopy images of the large pore opening under varying wetting and stretch conditions. Estimated maximum and minimum pore sizes are indicated by the red and white circles respectively to provide an estimate of the error associated with each measurement due to differences in focal length between images.

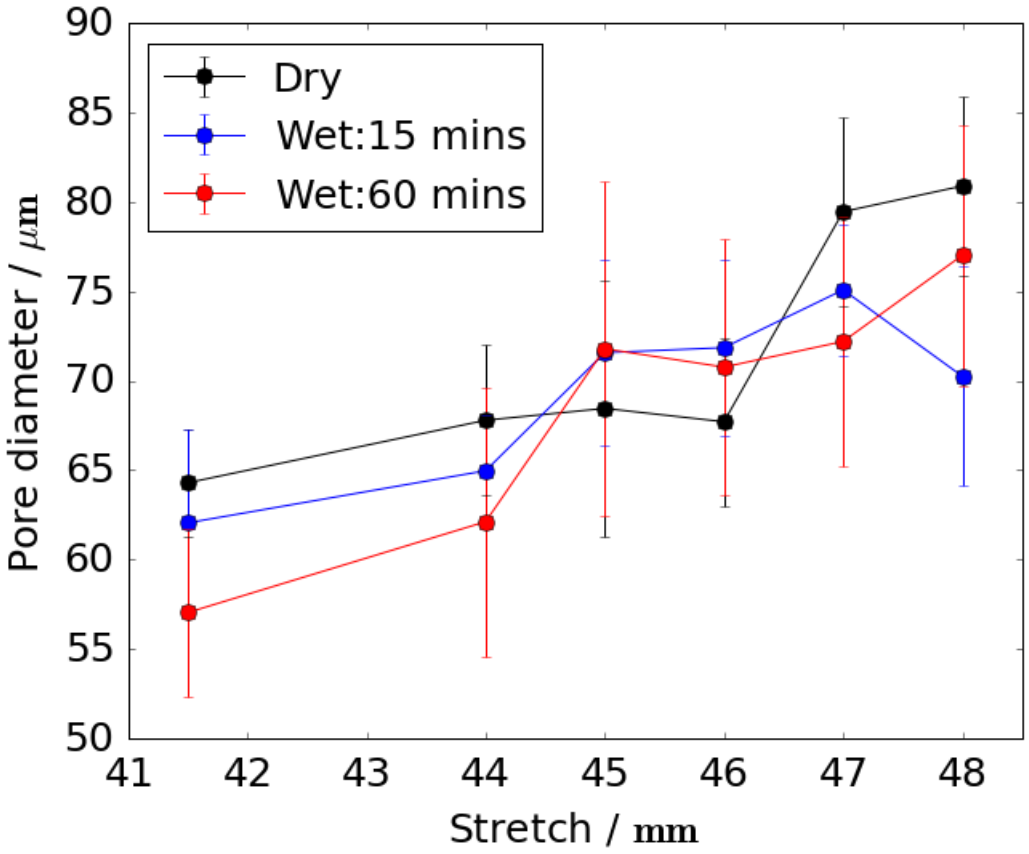

Figure 4.4: Large pore opening diameter measurements from optical microscopy for various hygroscopic conditions. 41.5 mm value corresponds to the 0 mm images in Figure 4.3. Error bars for each data point indicate the half-range between red and white circles (different estimates of pore diameter) shown in Figure 4.3.

4.1.4 Particles

Prior to TRPS measurements all particles are added to the electrolyte used, then dispersed by vortexing for at least 5 s and sonicating at high power for 30 minutes. Particles with diameters below 400 nm were additionally passed through a 0.45 μm syringe filter (Minisart, purchased from Sigma-Aldrich) to remove any remaining aggregates before use.

Table 4.4: Summary of particles used.

Type	Source	Relevant Chapters	Approximate Shape	Nominal Dimensions
Carboxylate Polystyrene	Bangs	5	Spherical	100 nm diameter
Carboxylate Polystyrene	Bangs	5	Spherical	200 nm diameter
Carboxylate Polystyrene	Bangs	5	Spherical	400 nm diameter
Carboxylate Polystyrene	Thermo-Fisher	5	Spherical	400 nm diameter
Carboxylate Polystyrene	Thermo-Fisher	6	Spherical	780 nm diameter
Carboxylate Polystyrene	Bangs	6	Spherical	1000 nm diameter
PEG-coated Gold Nanorods	Platt (see Chapter 6)	6	Cylindrical	500 nm Diameter 1-1.5 μm length
PolyBind Z, PHA Biobeads	Polybatics	7	Spherical	300-600 nm diameter
Shewanella marintestina Bacteria	Callaghan Innovation (see Chapter 7)	7	Cylindrical	0.4-0.7 μm diameter 2-3 μm length
Rattus Rattus Whole Blood	Trinity Bioactives	7	Disc	6.5 μm diameter, 1.2 μm width

Carboxylate Polystyrene

Additionally, the five spherical calibration particle sets used for charge experiments (Chapter 5, see Table 5.1) consisted of four sets of carboxylated polystyrene (CO-psty) beads obtained from Bangs Laboratories (IN, USA) and a set of uncharged NIST traceable standards obtained from Polysciences (PA, USA). All have diameters close to 200 nm, but the surface charge

varies. Particles were suspended at concentrations of 10^9-10^{10} mL^{-1} in SEB.

Gold Nanorods

Gold nanorods (Au-rods) were obtained from a collaborator (Mark Platt, Loughborough University), synthesised using the method outlined in [106]. In brief, high aspect nanorods are produced via the electroplating of Au onto a Ag-coated, porous alumina membrane. Both the Ag and alumima layers were etched away using a solution of methanol, ammonium hydroxide and hydrogen peroxide, and NaOH respectively. The resulting Au-rods were then collected via centrifugation and washed with H_2O and ethanol in which they were provided. The aspect ratio of the particles is controlled by the geometry of the alumina membrane and the thickness of the Ag coating. Au-rods used for our experiments were suggested (from SEM images) to exhibit lengths of approximately 2.1 μm and 4.7 μm and widths of 325 nm and 290 nm, respectively [106]. Additional SEM of the Au-rods used is presented in Chapter 6.

To increase the Au-rods solubility, a coating of mPEG-SH (Polyethylene glycol, 1k [PLS-606] purchased from creative PEG works) was applied to the surface. To coat, the Au-rods were pelleted via centrifugation at 10,000 rpm for 5 minutes and washed with PBS. Particles were then suspended in a solution of 4 g/L mPEG-SH in PBS, sonicated for 5 minutes, and incubated on a rotating wheel for a minimum of 2 hours. Finally, particles

were collected again via centrifugation and washed twice with a solution of PBS with <0.01% v/v of Triton-X. SEM images of the PEG-coated Au-rods used for experiments are included and discussed in Chapter 6.

Preparation protocols for *Rattus rattus* blood, *Shewanella marintestina* bacteria and Bacterial PHA particles are included in Chapter 7.

4.2 Experimental Equipment

4.2.1 Zetasizer Nano

Comparative ζ-potential measurements were made for calibration charge particles in Chapter 5 using phase analysis light scattering (PALS) with a Zetasizer Nano (Malvern). Immediately prior to PALS measurements, particles suspended in SEB were sonicated for 5 min and passed through a 0.45 μm syringe filter to remove aggregates. Each measurement was the mean value of 5 consecutive ζ-potential readings. Following each set of 5 readings, the fluid cell was rinsed with deionised water and reloaded with suspended particles. 3 of these measurements (15 readings) were completed for each particle set. To prevent electrode oxidation, each disposable fluid cell was replaced after 5 measurements (25 readings).

4.2.2 TRPS Apparatus: The qNano

The qNano system (Figure 4.5 a)) includes a fluid cell encapsulating the TPU membrane, covered with a Faraday cage to limit electrical interfer-

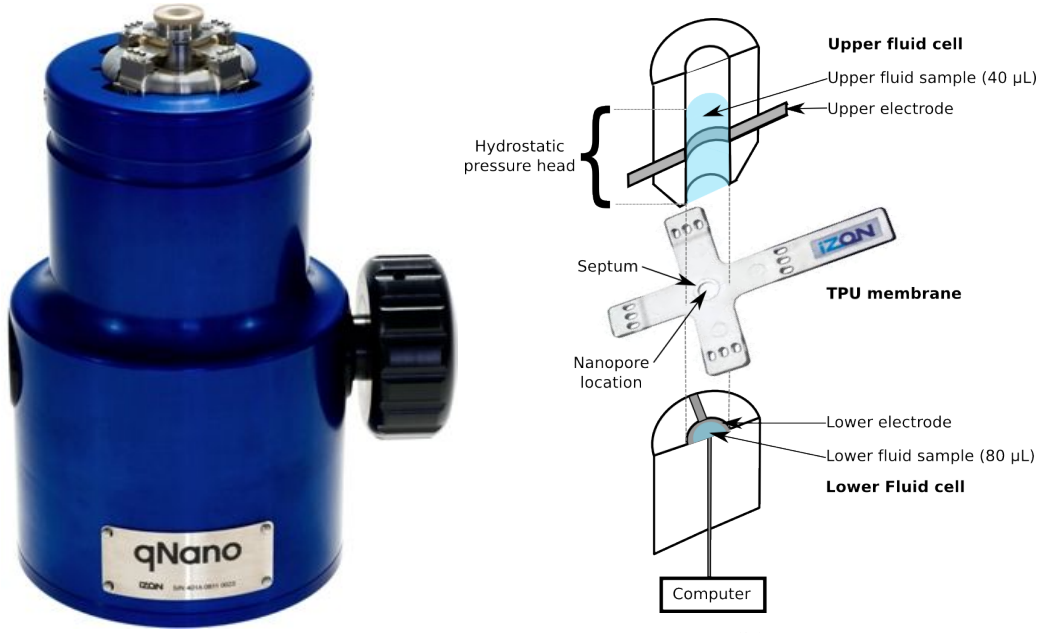

Figure 4.5: a) qNano with fluid cell and membrane mounted at top (without Faraday cage), courtesy of Izon Science [7]. b) Schematic cross section of the electrode set-up in the fluid cell with a membrane in place. Electrodes are positioned >1 mm away from the membrane surface. Diagram is not to scale.

ence, shown diagrammatically in Figure 4.5 b). When in operation, the bottom half of the cell is typically filled with 80 μL of electrolyte and the top with 40 μL, which results in a small 'pressure head' on the pore leading to translocations downwards through the pore, even without an applied voltage. The TPU cruciform containing the pore is held taut by four mechanically adjustable arms whose 'teeth' lock into corresponding holes on the membrane. Rotation of the large black dial causes uniform expansion of the teeth in the perpendicular directions simultaneously. We define the 'stretch' applied to the membrane as the distance measured (using Vernier calipers) between the outer edges of the teeth on which the cruciform is set at the time of measurement.

Once a voltage is applied, through Ag/AgCl electrodes, particle translocations become visible as the movement of the electrolyte though the pore is blocked by particles occupying the 'sensing zone' located at the apex of the conical pore. The current trace left by a typical translocation is shown in Figure 1.1 exhibiting a characteristic of peak height (ΔI), Full Width Half Maximum (FWHM) and Full Width Quarter Maximum (FWQM) that have been shown to depend upon particle size, charge, shape, pore stretch and applied electric field and pressure [3, 8, 17, 42, 47, 52].

Software (e.g. the ICS) can be used to identify events algorithmically, to view them whilst collecting data, and to find defining statistics of the translocations. Its graphical user interface (GUI) allows for simple display and editing of the sample set, which is crucial to ensure the accuracy of the

accumulated data as the algorithm is prone to assigning single event status to multiple peaks situated close together. However, the Izon standard operating procedures (SOPs) perform well at minimising pulse errors if followed correctly. Previous applications of TRPS using the qNano are reviewed in detail in Chapter 2.

Standard Operating Procedures (SOPs)

Except where explicitly noted, all experiments performed using the qNano follow SOPs to maximise the quality of data obtained from each run. A standard particle measurement consists of at least 500 resistive pulses with a minimum measurement time of 30 s. 40 μL of aqueous solution is placed in the top of the fluid cell and 80 μL in the lower fluid cell. In optimal sensing conditions, particles are run at concentrations of approximately 5 x 10^9 particles per mL, utilising centrifugation or dilutions to modify the particle concentration. Measurements at significantly higher concentrations suffer from particle-particle interactions, resulting in pore blockages and atypical pulse shapes. To ensure pulses are measured in a steady fluid flow state (as opposed to in evolving flow), the pulse rate **J** is monitored during the data collection period and only measurements that yield a near constant rate are used for data analysis. Examples of used and discarded rate characteristics are included in Figure 4.6. The linear rate requirement is relaxed for pulse rates that are not expected to be linear (as seen in the S-curve measurements reported in Chapter 5).

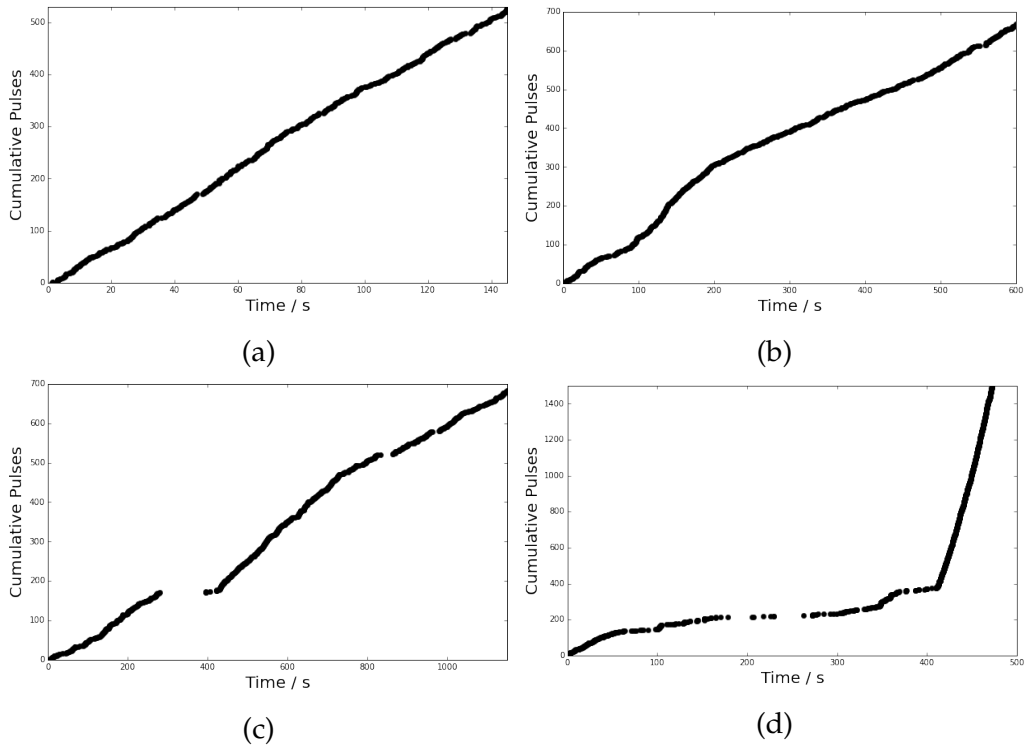

Figure 4.6: a) Example of an ideal TRPS pulse collection measurement exhibiting a near constant rate. b) TRPS pulse collection measurement exhibiting a near constant rate but some early rate stabilisation. c) TRPS pulse collection measurement exhibiting a near constant rate showing a 'gap' due to transient pore blockage. d) TRPS pulse collection measurement discarded due to clear deviation from constant rate. Examples a)-c) are deemed fit for further use. d) was rejected from further analysis.

If the pressure is not controlled by the manometer (see below) during a measurement, then fluid in the upper fluid cell is replaced after each measurement to minimise the impact of evaporation, which may lower the inherent pressure head and alter particle concentration. The baseline current measured in a pore completely wet with electrolyte is a further indicator of data quality. If a pore is geometrically deforming, or only partially

wet, background current will either drift or oscillate significantly. A requirement that the baseline current did not vary more than 1% in less than 1 s was met by all TRPS data presented during this thesis, except where specifically noted. Variations greater than this are common indicators that the pore is not yet in a stable state suitable for collecting data. Similarly, reversing the polarity of the voltage applied across the pore will, in a stable, fully-wet pore, reproduce a similar baseline current. Small variations due to rectification are expected as reported in [8].

Oscillating baselines can also indicate a complete or partial blockage of the pore. In these instances, and for partially wet pores, a rapid mechanical shock applied to the Faraday cage can clear the blockage or assist with wetting the pore. However, these shocks can also block or de-wet the pore (particularly for pore diameters $<$200 nm), and hence a pore is only assumed to be 'cleared' if the baseline current has returned to a value no more than $\pm$ 1% of the stable baseline current previously recorded for the same pore at that stretch. Pulse blockade magnitude normalized by baseline current through the pore is used to compare datasets for reproducibility over extended periods where the pore geometry may have deformed with time, age or repeated application of stretch. Over time, most pores will exhibit growth in baseline current as the pore relaxation is not perfectly elastic. The baseline current monitoring suggests when pores should no longer be used.

4.2.3 Nanopores

Nanopore membranes were provided pre-characterised by Izon Science with a rating indicating the optimal particle size for that pore, calculated from the baseline current through the pore [7]. This rating takes the form of 'NP' followed by the optimal particle diameter in nm that the pore should be used to examine. This is referred to as the 'NP rating' of the pore, and was first implemented systemically in 2012. Pores produced prior to this will not have an NP rating. Prior to use each new pore is 'matured' by repeated stretching and relaxation cycles from no applied stretch to maximal stretch (as defined by the pore manufacturer) and then back again, a minimum of 10 times. Willmott *et al.* showed that this is sufficient to reduce the variation in pore resistance to within 3% [84]. The characteristics of all nanopores used to obtain data are summarised in Table 4.5. The listed voltage and stretches are those used to find the baseline current for that particular pore. Specific values for pore geometries are included where possible from imaging. Nanopores can be placed on the qNano in two possible orientations, with the small pore opening placed at the top of the membrane or with the large pore at the top of the membrane. This is not be expected to significantly alter the baseline properties of the system (although it will influence the specifics of pulse shape).

Table 4.5: Summary of nanopores used.

Pore	NP rating	Baseline Current	Voltage	Stretch	a (SEM)	b (SEM)	d (callipers)	Experiments
A5959	not rated	45-50 nA	0.3 V	43 mm	—	—	—	Stretch
A5959	not rated	100-105 nA	0.3 V	45 mm	—	—	—	Stretch
A5959	not rated	150-175 nA	0.3 V	47 mm	—	—	—	Stretch
A8437	NP100	—	0.3 V	46 mm	—	—	—	Pressure change
A5961	NP200	120-125 nA	0.5 V	45 mm	—	—	—	Initial charge, buffer
A4002	not rated	—	0.3 V	44 mm	—	—	—	J vs P experiments
A4003	not rated	—	0.3 V	44 mm	—	—	—	J vs P experiments
A11204	NP100	70-80 nA	0.5 V	44mm	—	—	—	Bias, pH
A13208	NP100	70-80 nA	0.25 V	46mm	590 nm	—	—	Charge
A13208	NP100	100 nA	0.5 V	47mm	590 nm	—	—	Charge
A11485	NP200	75-80 nA	0.5 V	47mm	—	—	—	Charge
A11486	NP200	50-65 nA	0.5 V	47mm	—	40 μm	—	Charge
A11487	NP200	30 nA	0.5 V	46mm	—	—	—	Charge
A11487	NP200	90 nA	0.5 V	47mm	—	—	—	Charge
A09173	NP400	83 nA	0.1 V	44mm	3.45 μm	25 μm	167 μm	400 nm CO pSty
A09173	NP400	100 nA	0.1 V	45mm	3.45 μm	30 μm	150 μm	400 nm CO pSty
A09173	NP400	145 nA	0.3 V	45mm	3.45 μm	30 μm	150 μm	400 nm CO pSty
A09175	NP400	50 nA	0.12 V	44mm	—	—	—	
A09174	NP400	140 nA	0.4 V	44mm	—	25 μm	169 μm	Charge, Rat blood, BPHA, Au-rods
A09174	NP400	145-153 nA	0.3 V	47mm	—	33 μm	133 μm	Charge, Rat blood, BPHA, Au-rods
A17635	NP1000	145-150 nA	0.15 V	44mm	2.93 μm	39 μm	197 μm	*Shewanella*, Rat blood
A17636	NP1000	120-135 nA	0.2 V	44mm	1.5 μm	40 μm	207 μm	*Shewanella*

Pore Stretch Calibration

Individual pore geometries were characterised using a combination of SEM imaging, optical microscope imaging and calliper measurement of the membrane thickness at a variety of membrane stretches. Pores were imaged, after being used for TRPS measurements, using a Quanta SEM (Callaghan Innovation) at 20 kV at 2500x magnification under low vacuum (130 Pa) conditions. Such pores had been previously matured for use, and were mounted on a custom-fabricated stretching stage using the cruciform teeth, and carbon tape was applied around the pore opening to minimise charging effects. The location of the large pore opening was approximately determined using optical microscopy prior to SEM, and the cruciforms marked with a needle to enable location of the large and small pore openings under SEM. The SEM stretching stage consists of a ring of aluminium, with 4 locations for insertable teeth, at separations of 41 mm, 45 mm, 47 mm and 51 mm respectively. As most pores are listed as having a 'maximum stretch' by the manufacturer of 50 mm, pores were not imaged at 51 mm stretch. Cruciforms are mounted on the teeth manually using pliers (rather than having the stretch continuously adjusted by the qNano dial). Membrane stretch (X) was measured using 150 mm electronic Vernier calipers, measuring the distance between the outer edges of the qNano mounting teeth sharing the same arm of the cruciform.

Figures 4.7, 4.8 and 4.9 show SEM images of the large and small openings of pores A17636 and A17635. Pore opening sizes were calculated by

tracing the edges of the pores (shown as red lines in Figures 4.7-4.12) and using the calculate enclosed area function in Inkscape, which yields an estimate of the cross sectional area of the pore opening in pixels. We then calculate the radius of a circle of equivalent area to the measured pore opening, and convert the radius from pixels to microns using the scale bar shown in Figures 4.7-4.12. The same method was applied to images of all pores shown in Figures 4.7-4.12. Results for each imaged pore are summarised in Table 4.5.

For pores A09173, A09174 and A11486, no images of the small pore openings were able to be obtained as the small pore could not be either located or imaged at sufficient resolution to provide an area measurement. As such, Figures 4.10, 4.11 and 4.12 only show SEM of the large pore openings at different stretches. Two important trends are clear from Figures 4.7 to 4.12: that large pore openings are not circular and that increased applied stretch causes the large pore openings to become more circular. Hence we expect the semi-analytic model to more accurately approximate pore geometry at higher stretches, due to the assumed truncated conical geometry.

Figure 4.13 summarises pore geometry measurements using both optical microscopy and SEM data for NP200 (Figure 4.13 a)), NP400 (Figure 4.13 b)) and NP1000 (Figure 4.13) pores. Figure 4.13 a), b) and c) show discrepancies between the large pore opening measurements made using optical microscopy and SEM that is largest with the smallest (NP200) pore.

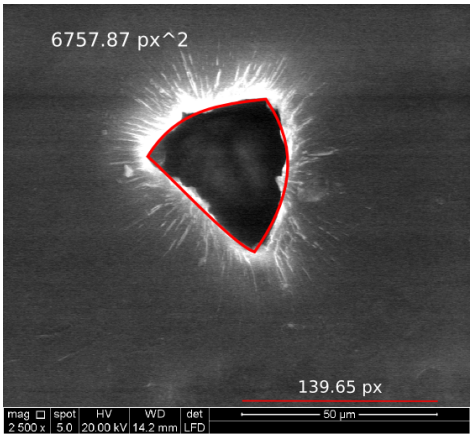

(a) A17636 Large pore opening at 41 mm stretch.

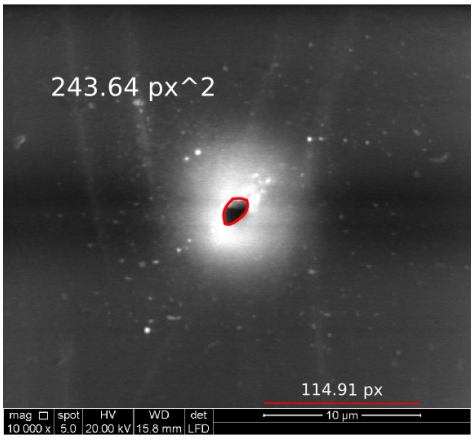

(b) A17636 Small pore opening at 41 mm stretch.

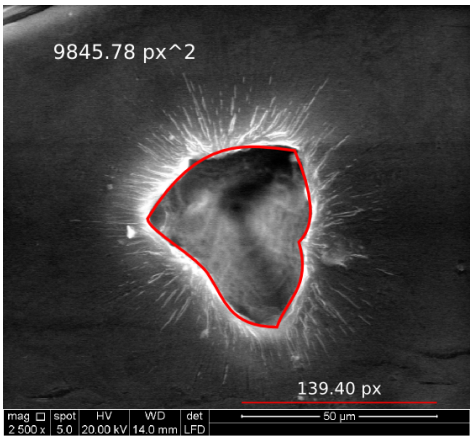

(c) A17636 Large pore opening at 45 mm stretch.

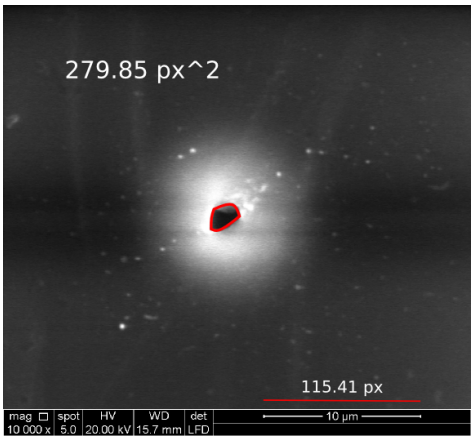

(d) A17636 Small pore opening at 45 mm stretch.

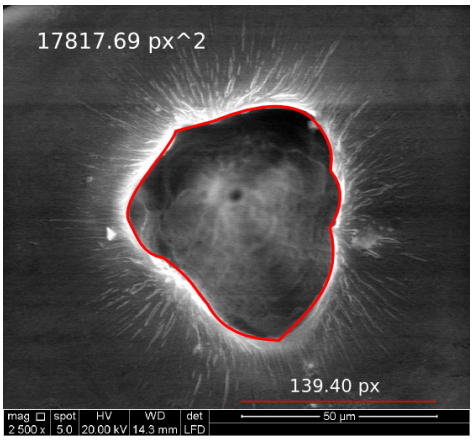

(e) A17636 Large pore opening at 47 mm stretch.

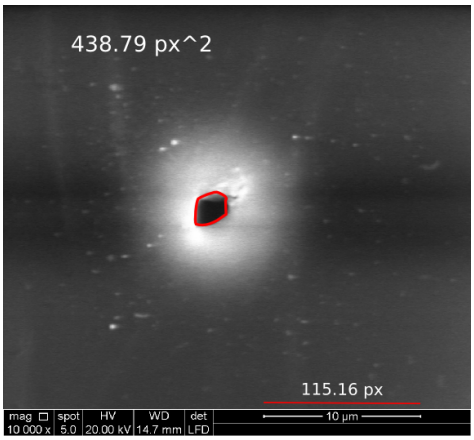

(f) A17636 Small pore opening at 47 mm stretch.

Figure 4.7: SEM images of large and small pore openings of A17636 and calculated areas.

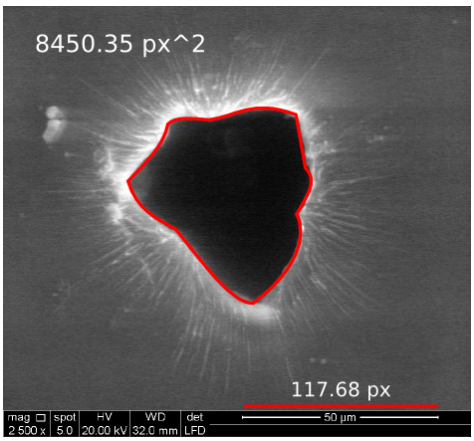

(a) A17635 Large pore opening at 41 mm stretch.

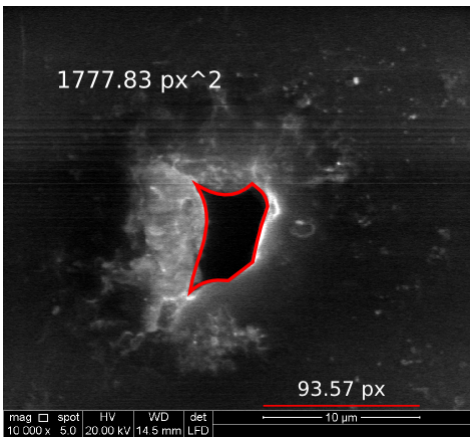

(b) A17635 Small pore opening at 41 mm stretch.

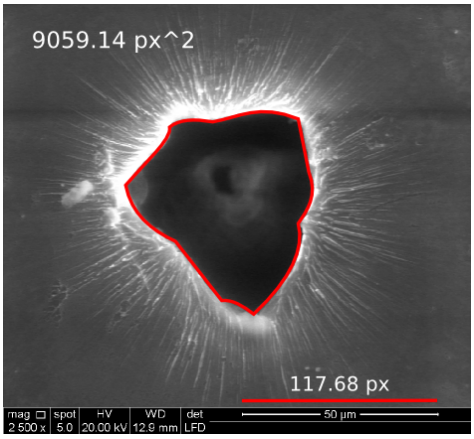

(c) A17635 Large pore opening at 45 mm stretch.

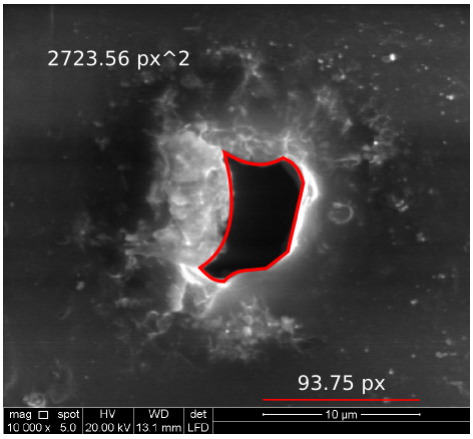

(d) A17635 Small pore opening at 45 mm stretch.

Figure 4.8: SEM images of large and small pore openings of A17635 and calculated areas at 41 and 45 mm stretch.

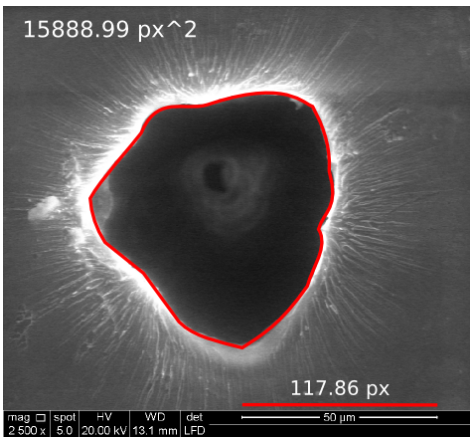

(a) A17635 Large pore opening at 47 mm stretch.

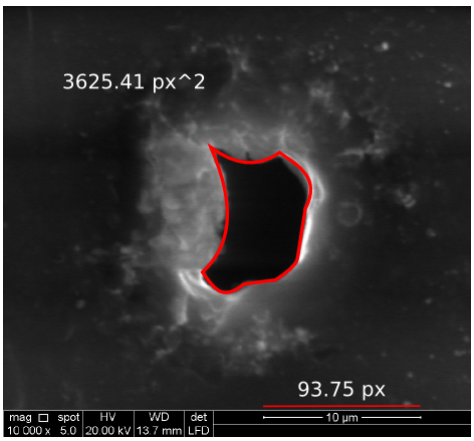

(b) A17635 Small pore opening at 47 mm stretch.

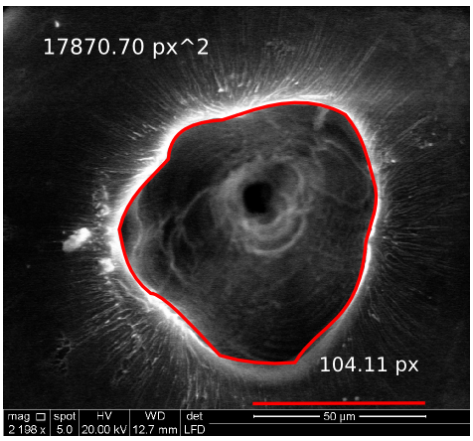

(c) A17635 Large pore opening at 50 mm stretch.

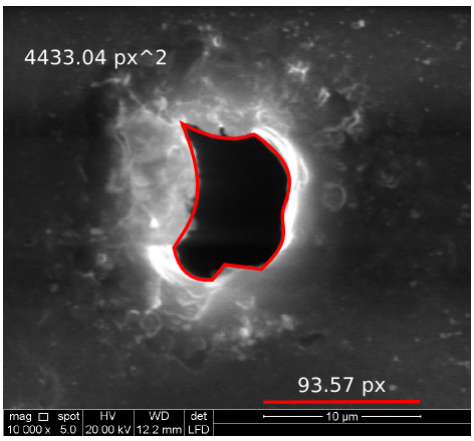

(d) A17635 Small pore opening at 50 mm stretch.

Figure 4.9: SEM images of large and small pore openings of A17635 and calculated areas at 47 and 50 mm stretch.

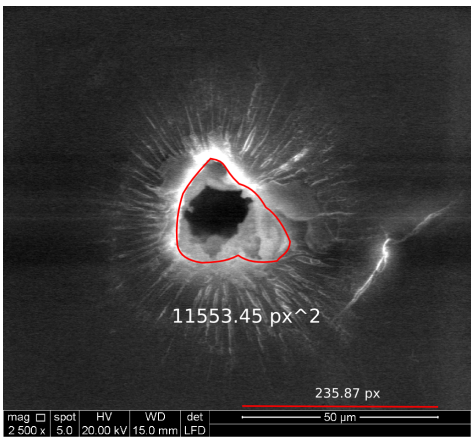

(a) A09173 Large pore opening at 41 mm stretch.

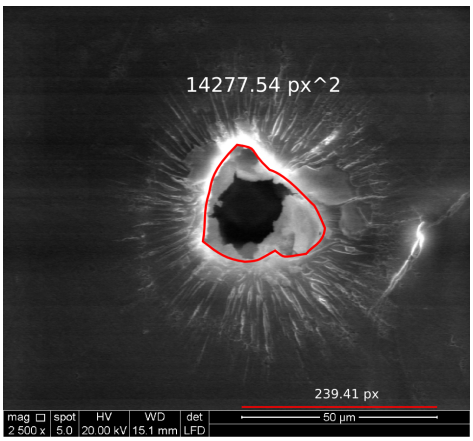

(b) A09173 Large pore opening at 45 mm stretch.

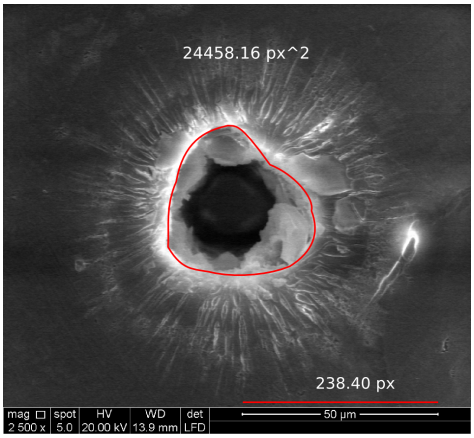

(c) A09173 Large pore opening at 47 mm stretch.

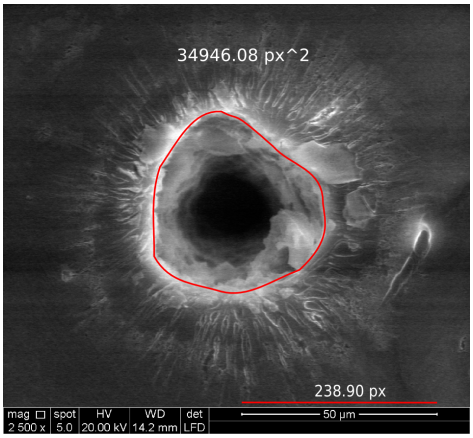

(d) A09173 Large pore opening at 50 mm stretch.

Figure 4.10: SEM images of large pore openings of A09173 and calculated areas.

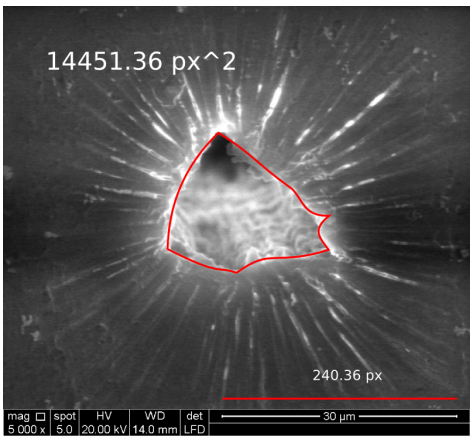

(a) A09174 Large pore opening at 41 mm stretch.

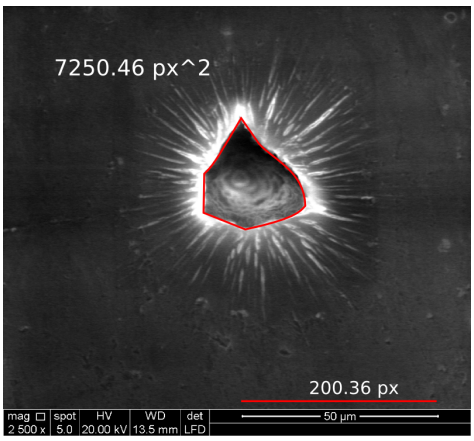

(b) A09174 Large pore opening at 45 mm stretch.

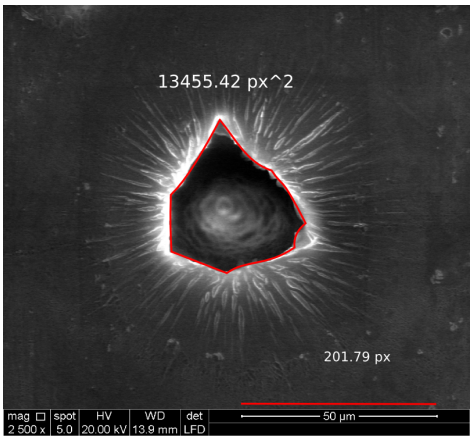

(c) A09174 Large pore opening at 47 mm stretch.

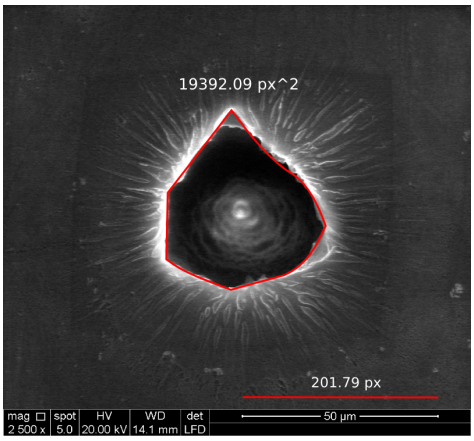

(d) A09174 Large pore opening at 50 mm stretch.

Figure 4.11: SEM images of large pore openings of A09174 and calculated areas.

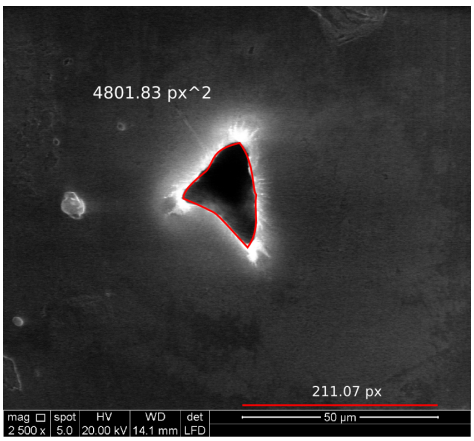

(a) A11486 Large pore opening at 41 mm stretch.

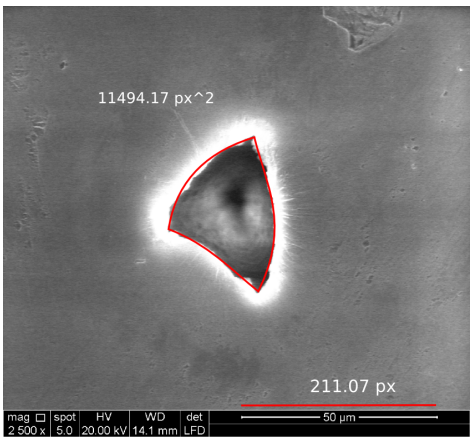

(b) A11486 Large pore opening at 45 mm stretch.

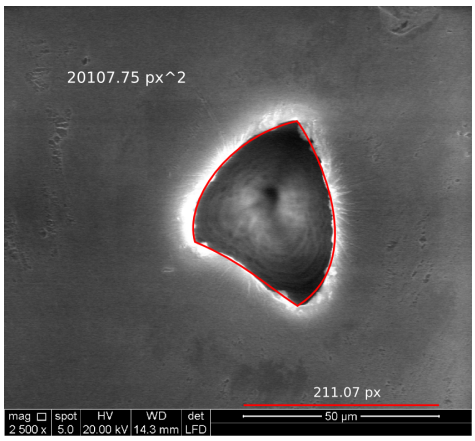

(c) A11486 Large pore opening at 47 mm stretch.

Figure 4.12: SEM images of large pore openings of A11486 and calculated areas.

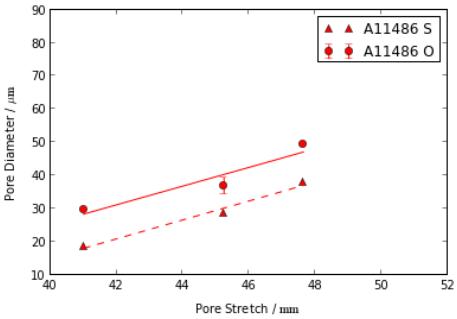

(a) Large pore opening diameter for an NP200 pore.

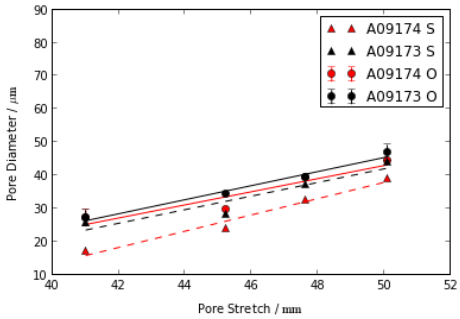

(b) Large pore opening diameter for NP400 pores.

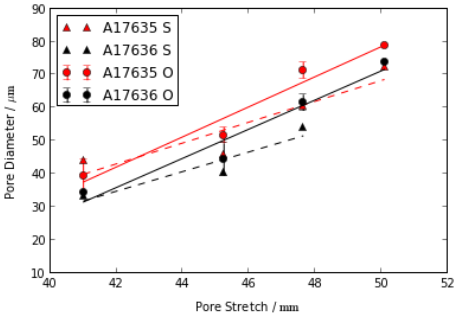

(c) Large pore opening diameter for NP1000 pores.

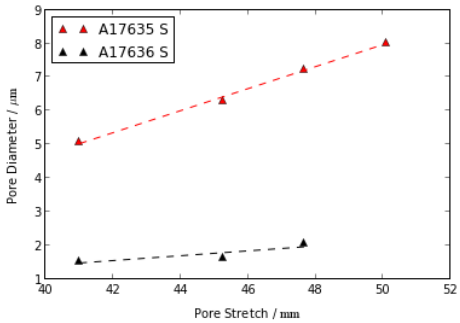

(d) Small pore opening diameter for NP1000 pores.

Figure 4.13: Measured pore diameters from both SEM (S) and optical microscopy (O) measurements. Solid and dashed lines are linear best fits to optical data and electron microscopy measurements respectively. Optical measurements represent the average of two separate diameter measurements of the pore made in perpendicular directions. Error bars indicate the half range of these measurements.

A larger uncertainty is expected for optical microcopy images due to the diffraction limit of the microscope. It is also noted that the specific shape of the small pore opening will have an effect on the resolution of the diameter measurement from the SEM image. Whilst optical microscopy measurements for NP400 and NP1000 pores are within 50% of the SEM values, it is clear that optical microscopy is insufficiently precise to provide inputs for the semi-analytic model, even for the largest tested pores. Reducing uncertainty in pore geometry measurement is particularly important as it also contributes the largest amount of uncertainty to the semi-analytic model. Small pore opening measurements for A17635 and A17636 are presented in Figure 4.13 d), showing that even sequentially produced pores (as these are) can vary in small opening diameter by almost half an order of magnitude. For semi-analytic model inputs, we use the linear fitted SEM data to calculate the large and small pore openings at a specific stretch. For pores where measurement of the small pore opening was not possible, we use small pore measurements obtained for pores from the same batch and NP rating.

4.2.4 Membrane Thickness

Membrane widths were measured using a TradeQuip (Melbourne) 25 mm micrometer, with pincers modified with flattened screws (tip diameter 2 mm) to reduce the surface area in contact. Width was measured by tightening the micrometer with the screw tips rested firmly on the membrane.

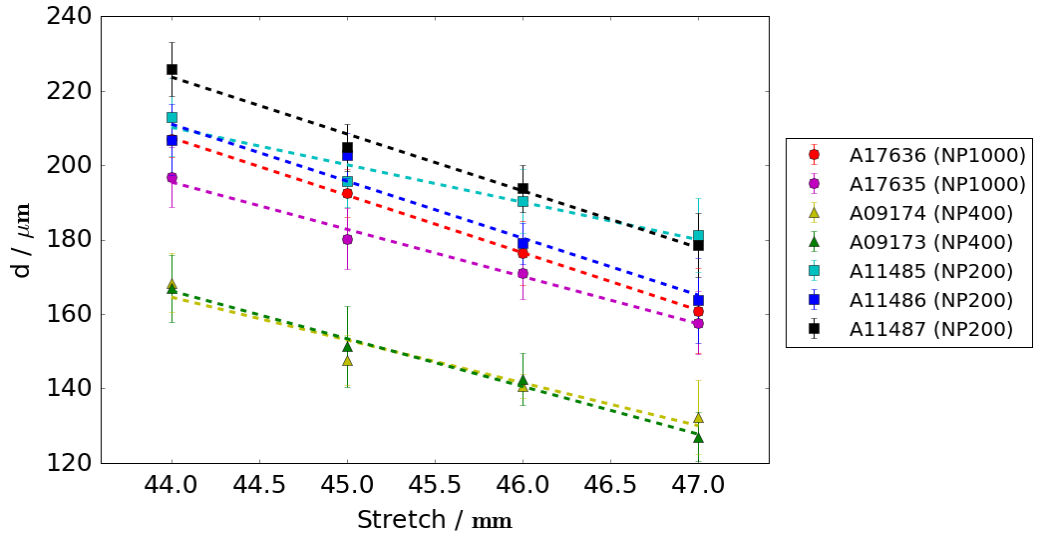

Figure 4.14: Pore length (d) measurements as a function of the stretch applied to the membrane. Values and errors are summarised in Table 4.6.

Due to the elastomeric nature of the material and likely variations in surface roughness, the reported membrane widths are the mean of 10 consecutive width measurements, and the errors bars are the standard deviations of these measurements, shown in Figure 4.14. Whilst a linear fit is used to describe the varying pore width, the detailed behaviour is expected to be non-linear due to the elastomeric pore material [84].

The strain, α applied to the membrane at a given stretch X can be calculated, if a consistent initial stretch (X_0) is defined:

$$\alpha = \frac{X - X_0}{X_0}. \tag{4.2}$$

In these experiments we consistently define X_0 as 44 mm stretch. This differs from previously used X_0 values (which are typically between 41 and

Table 4.6: Summary of pore d measurements.

Pore	NP Rating	d at X_0 (μm)	Standard Error (μm)	Fit Gradient (d/α)x10^3	R^2
A11485	NP200	213	3.3	-10.1	0.947
A11486	NP200	207	3.0	-15.3	0.944
A11487	NP200	226	2.3	-15.3	0.984
A09173	NP400	167	2.9	-12.8	0.989
A09174	NP400	168	2.5	-11.5	0.928
A17635	NP1000	197	2.5	-12.7	0.989
A17636	NP1000	207	1.5	-15.5	1.000

43 mm [18]) because of the range of pores investigated. For some pores 43 mm is insufficient to apply tensile strain to the membrane (meaning the membrane is not held taut), either due to age or variations in the injection moulding manufacturing process. For all pores investigated 44 mm stretch was sufficient to ensure that some strain was applied to the membrane.

4.2.5 Variable Pressure Manometer (VPM)

The net pressure across the membrane is controlled by using a consistent volume of fluid in the upper fluid cell (40 μL), generating the hydrostatic pressure head (as shown previously in Figure 4.5). We define the $P_{applied}$ as the pressure applied by the manometer, $P_{inherent}$ as the hydrostatic pressure head and P as the total pressure applied across the fluid cell such that $P = P_{applied} + P_{inherent}$.

An additional pressure differential ($P_{applied}$) can be applied by sealing the upper fluid cell to a variable pressure manometer (VPM) via tubing. Early versions, Figure 4.15 a), connected the upper fluid cell to a fixed

(a) The original gas-based model with a resolution of 5 mm H_2O

(b) The more recent version with reported resolution of 0.5 mm H_2O

Figure 4.15: Izon Science variable pressure manometers [7].

amount of air and H_2O, which was then pressurised by varying the volume of the chamber by raising or lower the stopper. The reported precision of this device was 5 mm H_2O, but it was prone to inaccuracies due to ambient thermal fluctuations. The more recent commercial VPM, Figure 4.15 b), uses the same principle but connects the upper fluid cell to an insulated reservoir of water. The thermal reservoir minimises variations in pressure due to thermal fluctuations in ambient temperature. The claimed precision of the new VPM is 0.5 mm H_2O. Except where noted, pressure is re-applied at the beginning of each TRPS measurement in case of a slow manometer leak.

Prior to the release of these VPMs, two laboratory systems were developed in collaboration with Vogel [52], to allow stable, high resolution ($<$1 mm H_2O) application of pressure to the system - shown schematically in Figure 4.16 a) and Figure 4.17.

In Figure 4.16, $P_{applied}$ is controlled by the relative height of the liquid in the beaker and within the glass cylinder connected to the upper fluid cell. The system is connected with the valve (Label f) opened and the system is allowed to equilibrate to atmospheric pressure. The valve is then closed and the pressure applied to the upper fluid cell can be increased by increasing the volume of water in the beaker, or reduced by removing it. A large (2 L) beaker is used so that small changes in relative height can be achieved without precise control over the volume of liquid added or removed (although further improvements are described below).

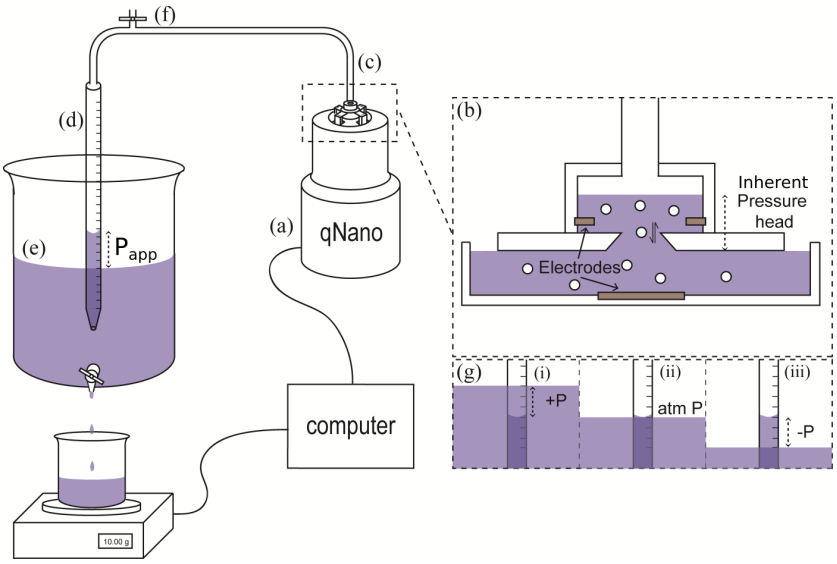

(a) Diagram showing the system used to construct the high-resolution variable pressure manometer (VPM) in [52] using hydrostatic flow to constantly adjust the applied pressure $P_{applied}$.

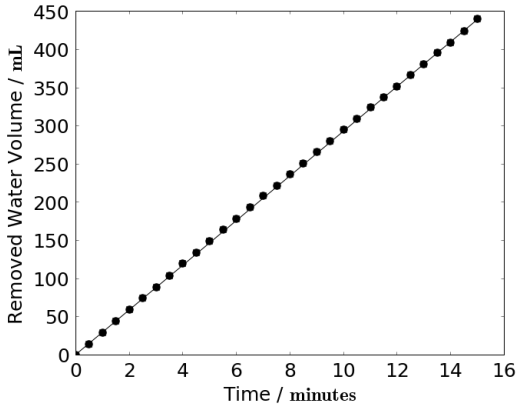

(b) Outflow rate from the beaker used in a). The black line in the figure is a least-squares linear fit to the data. Pressure change varies linearly with time within 1% over 10 minutes. R^2 of the linear fit is 0.99.

Figure 4.16

In a typical experiment, after sealing, liquid was allowed to drain from the beaker into a collection beaker on a mass balance. As the volume of water in the beaker drains, the hydrostatic pressure will reduce, leading to a reduction in fluid flow rate through the draining valve. To minimise this effect, the outflow pipe was situated at the bottom of the beaker and the mass balance was placed >1 m below the level of rest of the experimental apparatus. The mass of the water on the balance was recorded over time, generating a calibration curve for $P_{applied}$, shown in Figure 4.16 b). Whilst volume flow is expected to be parabolic with time due to the change in hydrostatic pressure head as the water level lowers, the black line in the figure is a least-squares linear fit to the data. The average flow rate for repeated experiments was 30 mL/min.

Figure 4.17 shows the VPM improved via the addition of a controlled flow syringe pump. Two 25 mL syringes were used to add or remove water from the beaker at a programmed rate of 6 mL/min per syringe (12 mL/min in total). This precise control of the relative water level allowed optimisation of the pressure change rate in order to minimise blockages (which occur more commonly at lower pressures) whilst ensuring sufficient numbers of pulses were collected at low particle translocation rates. Pressure variation experiments can be repeated with particles moving either direction through the pore to ensure gravitational or pore orientation effects are not influencing the measurements made using the system.

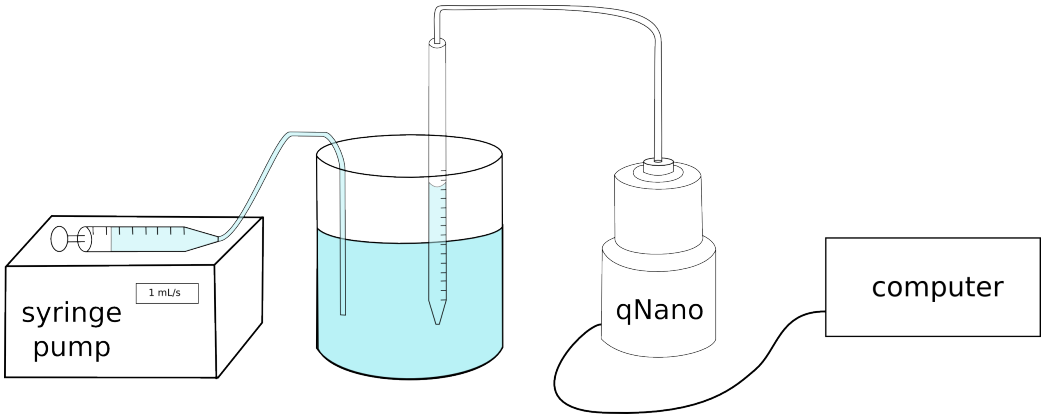

Figure 4.17: Diagram showing the system used to construct the high-resolution variable pressure manometer (VPM) with the addition of the syringe pump to allow tighter control of pressure. Adapted from [52].

4.3 Analytic Methods

4.3.1 Izon Control Suite (ICS)

Figure 4.18 a) shows an example trace recorded for 200 nm carboxylate polystyrene particle pulses through an NP200 pore. Pulse analysis can be performed using the proprietary analysis algorithm developed by Izon Science made available through the ICS software. Current trace information is recorded at 50 kHz as a binary '.irbd' file (which can be unpacked directly using the linux octaldump utility command *od -A d -t f8 -w32*) with columns recording time (s), current (nA), bias (V) and applied stretch (mm) respectively, and an associated .xml file that records the experimental specifics entered by the user such as pore, buffer and dilution. Trace analysis consists of generating a running average of the current (baseline current) across a time window (typically 100 ms although this can be set

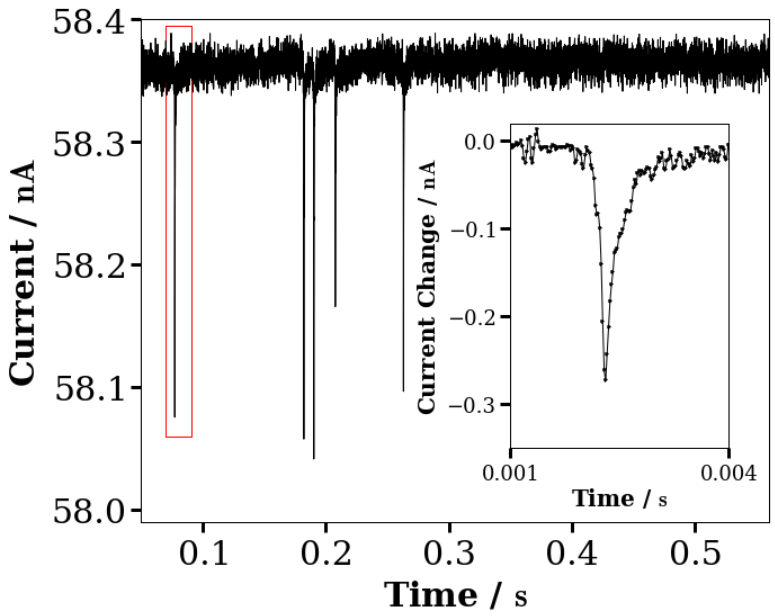

(a) Example pulses produced by the passage of 200 nm carboxylate polystyrene particles through an NP200 pore (46 mm stretch at 0.5 V). Inset is a scaled version of the event indicated by the red rectangle.

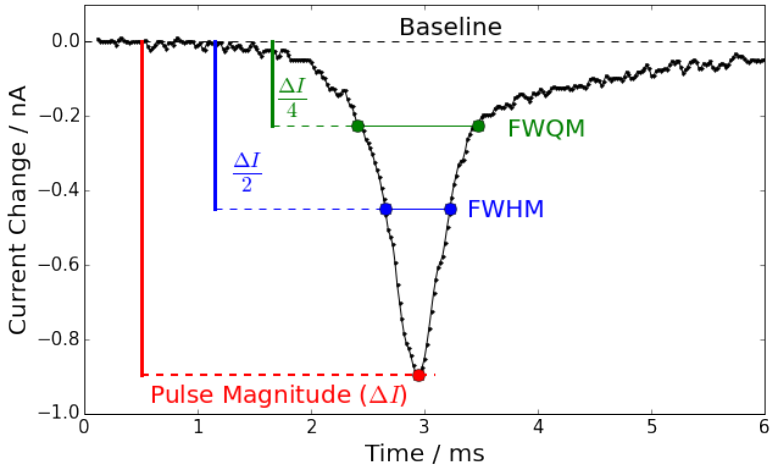

(b) A single pulse with metrics: Pulse magnitude, baseline, FWHM and FWQM. Black dots indicate sampled data points at 50kHz. Example event from 400 nm spheres in A17636.

Figure 4.18

by the user in later versions of ICS). The trace is then scanned for multiple consecutive data points that deviate from the baseline current by more than a set amount (the default threshold value is a change in 0.05% of the baseline current, but this is able to be set in later versions). 'Durations' of these deviations are the time difference between the initial datapoint that crosses the variation threshold and the first recorded value that returns to within the threshold value for the baseline. Durations are compared to another set minimum threshold value (the default is 0.2 ms). Any pulses below this minimum are discarded as noise and any larger are recorded.

Recent versions of the software (versions >2.2) impose a maximum sampling time on each collection period of 10 min to limit the output file size. Longer sampling periods generate files >2 GB in size which are loaded into RAM in their entirety before the analysis is performed, effectively placing an upper limit on the size of files that is dictated by the RAM capabilities and accessibility of the specific computer. It is noteworthy that for modern operating systems (such as Windows 7) there is often a limit (1 GB) to the amount of memory accessible to single programs without explicit permission changing. This can limit the processing ability of the Izon software even on hardware that has ample physical memory. As much of the memory requirement for the Control Suite software is associated with the GUI rather that the algorithm itself, large individual files or large quantities of files can also be analysed by an alpha command line version of the software provided by Izon Science, *sioscmd.exe*.

Pulses are characterised by the metrics shown in Figure 4.18 b), Full Width Half Maximum (FWHM), Full Width Quarter Maximum (FWQM), blockade height (the difference between the pulse minimum and the baseline current) and the times corresponding to each of these. ICS software users are limited to FWHM, duration and blockade magnitude data but the *sioscmd.exe* tool also includes pulse FWQM measurements. The resultant event characteristic data can be analysed within ICS or exported to a .csv file of individual pulse characteristics for external analysis. ICS software reports some basic statistics at the end of each run. As the specific calculations behind these are embedded in the proprietary software, all statistics reported in this thesis have been computed externally to the Izon software except where noted. All pulse characterisation has been performed using the *sioscmd.exe* software except where noted.

4.3.2 Pulse Filtering

Standard use of the qNano also involves a pulse filtering step separate to the algorithm analysis. The purpose of this is to remove any events that may skew the analysis, such as events with multiple peaks or those generated by pore blockages. This is performed by visually assessing a scatter plot of the blockade magnitudes with the duration or FWHM measurements to identify clear outliers. The ICS offers the ability to inspect a reduced resolution trace for each event, allowing the user to assess which events generating outlier data merit exclusion. Under typical settings this

filtering removes $< 5\%$ of data points and, if this reduces the number of pulses to < 500, users are encouraged to re-collect data such that after this filtration >500 pulses are still available for analysis. For complex samples filtration by pulse inspection is not always possible and outliers may have significant effects on means or averages recorded for a run, particularly for highly disperse samples. Data exclusion based on magnitude and FWHM lower thresholds is automatic within the ICS and *sioscmd.exe* software, whereas other filtration based on observed outliers must be performed manually. As the manual exclusion is subjective, and depends on identifying whether a pulse is 'characteristic' of a particle set or not, manual filtration of data was not performed on any TRPS pulses presented in Chapters 5, 6 and 7. Instead all data not excluded automatically by Izon software is included in data presented, unless explicitly noted.

4.3.3 Pulse Characteristics

Figure 4.18 b) shows diagrammatically how the ICS algorithm characterises each pulse. Two additional data points are actually reported for each event, referred to as the pulse 'duration'. These occur when the baseline current varies more than a maximum threshold value, set as a fraction of the baseline current by the user. However, as this method of characterising pulse duration is prone to sampling and noise errors, we omit these data from our characteristic events. Threshold duration data points are omitted from gradient fits. The remaining 5 points plus knowledge of the

baseline current prior to the pulse allows measurement of the pulse magnitude, full width half maximum and full width quarter maximum. Further notes on measurement of metrics to characterise pulses follow. New metrics regarding pulse asymmetry are introduced and discussed in detail in Chapter 6 but we outline them briefly here.

Pulse Magnitude

Whilst pulse magnitudes are produced by the ICS software, we also use a different method to determine the magnitude of individually inspected pulses, or pulses produced by the semi-analytic model. This method will not produce an identical magnitude measurement to the ICS software, as it simply finds the difference between the maximum and minimum values of the current trace over a $<$2 ms period. However values obtained typically agree within 1% of ΔI.

Pulse Rate

The pulse rates reported for measurements are the mean event rate over the duration of the collection period. Due to the adherence of the SOPs to obtaining linear pulse rates, large variations in rate are not expected within each run.

FWHM and FWQM

Because the aforementioned issues with baseline duration measurements, all 'durations' reported in this thesis (except where explicitly noted) are FWHMs. FWHM is simply the time between a pulse's half magnitude values. The FWQM is defined similarly.

Asymmetry

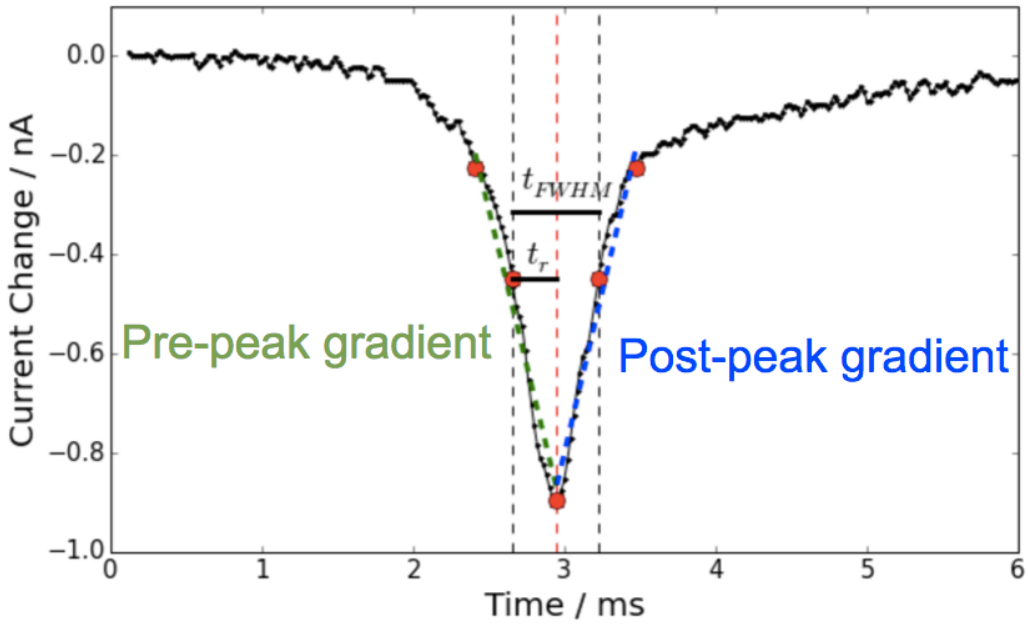

Figure 4.19: Pulse from Figure 4.18 labeled showing asymmetry and gradient measurements.

For event asymmetry analysis we use a previously [18] defined asymmetry measurement, f_{factor}, the ratio of the FWHM prior to the pulse minimum (t_r) to the total FWHM (t_{FWHM}). This is indicated diagrammatically

by the ratio of Figure 4.19.

$$f_{factor} = \frac{t_r}{t_{FWHM}}. \tag{4.3}$$

Unlike the gradient analysis discussed below this does not require normalisation for comparison to alternate sized particles as normalisation in already implicit in the definition of the FWHM and FWQM.

Gradient

Pulse pre-minimum G_r and post-minimum G_f gradients are calculated by performing linear fits to the data points indicated in Figure 4.19 for each side of the minimum of the pulse. For gradient comparison between particles of alternative sizes the gradients are normalised against the blockade magnitude of the event. Finally we define the gradient ratio R_g used to assess the asymmetry of pulse gradients about the event minimum as $R_g = \frac{G_r}{G_f}$. Whilst observation and the semi-analytic model predict non-linear behaviour about the pulse minimum for data close to the event minima, linear fits provide simple approximations to the behaviour observed. More complicated fits can be performed using the full data from each event, however limitations on computing power and algorithm design cause this to be unpractical for large pulse numbers without adding significantly to the analysis time.

4.4 Conclusion

In addition to describing the details of the experimental apparatus we also performed characterisation measurements on SEB and the nanopores used for TRPS in Chapters 5, 6 and 7. The conductivity of 0.1 M KCl SEB was measured as 12 $\pm$ 1 mS/cm. The ζ-potential of TPU in 0.1 M KCl was measured as -12 $\pm$ 2.5 mV. SEM measurements of both the large and small pore openings across a range of pore sizes show large variations in pore sizes, even between sequentially produced pores with the same manufacturer's NP rating. As such, inputs for the semi-analytic model in subsequent Chapters use these SEM data rather than the manufacturer's rating for pore size. Membrane width as a function of applied stretch was also measured for each pore and the results used as inputs to the semi-analytic model. The SOPs used in the collection of all TRPS data presented in this thesis and the analytic methods used to characterise pulses were also discussed. These are further discussed during their application in subsequent Chapters.

Chapter 5

ζ-potential Measurements

5.1 Introduction

In this Chapter we describe and compare several similar but distinct methods for measuring ζ-potential. Using both TRPS and Dynamic Light Scattering (DLS) we study measurement consistency across different experimental conditions, apparatus and analysis methods. We present a detailed study and comparison of TRPS-based ζ-potential measurement methods in which the rate or duration of resistive pulses are measured as a function of applied pressure, with the intent of optimising such techniques.

As has been discussed previously in Chapter 2, TRPS can be used to measure the charge of nanoparticles in addition to their size, when calibrated with spherical particles of known charge or when the pore geometry is well-known [47]. The ζ-potential of nanoparticles in solution is crucial for understanding and predicting the long-term stability of sus-

pensions, yet it is difficult to accurately predict the ζ-potential from first principles [107], even in a well-characterised solution. Existing techniques for ζ-potential measurement draw upon either electrokinetic phenomena, such as electrophoretic light scattering or microelectrophoresis [95], or electroacoustic phenomena [108]. ζ-potential measurements are not trivial, particularly for high dispersity particle distributions.

ζ-potential measurement has been attempted previously using RPS in Coulter counters [2] and DeBlois and Bean [11] measured the electrophoretic velocity of virus particles passing through polycarbonate pores. Nanoparticle ζ-potentials have since been inferred from individual duration measurements [36, 109]. More recent RPS ζ-potential measurements [47, 52, 110, 111] have considered resistive pulses in detail, accounting for multiple particle transport mechanisms and conical pore geometry with end effects.

Whilst TRPS ζ-potential measurements have been demonstrated, little is known about the reproducibility and experimental uncertainty of ζ-potential measurements made using these techniques. The nanoparticle size limitations of TRPS ζ-potential measurements is also unknown. This Chapter compares four methods for determining the ζ-potential of nanoparticles by balancing the pressure and electrokinetic forces within the nanopore, specifically discussing reproducibility, consistency and comparison to the current comparable standard technique, DLS.

Much of the material in this Chapter has been published in [112]. All

experiments and analysis were performed by Eldridge. Anderson and Vogel first developed the 'S-curve' balance point measurement technique and the continuous pressure experimental apparatus [52]. Willmott provided the semi-analytic model used for charge calculations, discussion and suggestions on the writing style and content of the paper.

5.2 Theory

We measure the ζ-potential of a particle ($\zeta_{particle}$) by determining its electrophoretic mobility in the Smoluchowski approximation, in which particle size is much greater than the Debye length. Based on the Nernst-Planck equation, and the assumption that electrokinetic and pressure driven flow are the dominant particle transport phenomena for these experimental conditions, particle flux through a pore $\mathbf{J}$ can be summed as [46]

$$\frac{\mathbf{J}}{C} = \left(\frac{\varepsilon(\zeta_{particle} - \zeta_{pore})}{\eta} \right) \mathbf{E} + \frac{\mathbf{Q_p}}{A} \tag{5.1}$$

Here C is the volume concentration of particles, ε and η are the fluid permittivity and viscosity respectively, and ζ_{pore} is the ζ-potential of the pore wall. $\mathbf{E}$ is the applied electric field, A is the cross-sectional area of the pore, and $\mathbf{Q_p}$ is the volumetric rate of pressure driven flow through the pore. Here we assume dieletrophoresis and diffusion processes are negligible because of the low applied voltages (between 0.5 and 1 V), and because the applied pressure magnitudes typically mean diffusion is neg-

ligible for TRPS [42]. It is assumed that the gradient of the pore wall is shallow enough (on the length scale of a particle) that the internal pore geometry can be considered locally cylindrical.

In the scenario described above, by applying pressure across the pore ($P_{applied}$) and monitoring the particle flow rate by TRPS, a pressure (P_0) can be determined at which there is no net motion of particles through the pore ($\mathbf{J}$ = 0). At P_0 particle transport mechanisms must by balanced and hence Equation 5.1 can be re-written as

$$\zeta_{particle} = -\frac{\eta \mathbf{Q_p}}{\varepsilon \mathbf{E} A} - \zeta_{pore}. \tag{5.2}$$

To calculate $\zeta_{particle}$, the semi-analytic model was used (Chapter 4). SEM measurements of specific pore geometry were used to compute $\mathbf{E}$ and $\mathbf{Q_p}$ in terms of $P_{applied}$, the inherent pressure within the fluid cell ($P_{inherent}$), and applied voltage (V). To obtain a value for ζ_{pore} electro-osmotic flow measurements were performed in channels constructed of TPU as described in Chapter 4. These returned a value of -12 mV $\pm$ 2.5 mV for ζ_{pore} when using 0.1 M KCl.

Pores used for TRPS exhibit conical geometry, which is modelled as indicated in Chapter 4. The small opening radius a, large opening radius b and length d are model inputs. Vogel *et al.* [52] applied this method to a range of carboxylate polystyrene nanoparticles, using TRPS with a custom built manometer to allow precise control of $P_{applied}$. Somerville et al.[110] used the same technique to measure the ζ-potential of a water-in-

oil emulsion. We aim to study the precision and accuracy of the method used previously [52, 110], as well as three further methods which identify P_0. The particles used are described in Table 5.1 and the standard TRPS operating procedures used are those described in detail in Chapter 4.

Table 5.1: Particle sets used in the present study. Diameters and surface charge details are as specified by the suppliers. Bangs Laboratories calculates charge densities as described in [113]. 'CO-psty' indicates carboxylated polystyrene. [a] Particles are not carboxylated. [b] Surface groups include both carboxylic and polyacrylic acids.

Particle set	Material	Manufacturer	Diameter (nm)	Charge density (σ) (C m^{-2})
A	Polystyrene	Polysciences	200	n/a[a]
B	CO-psty	Bangs	226	-0.181
C	CO-psty	Bangs	217	-0.318
D	CO-psty	Bangs	194	-0.400
E	CO-psty[b]	Bangs	160	-0.666

5.3 Preliminary Experiments

Previous experiments [18] had indicated a relationship between carboxylate polystyrene particle surface charge, particle aggregation and pH of the electrolyte. Figure 5.1 shows the predicted behaviour of surface charge groups on carboxylate polystyrene particles at a pH between 2 and 10. Deprotonation of charged species is expected between pH of 4 and 6, above which the deprotonation (and thus the predicted surface charge of the particles) is expected to remain comparatively constant.

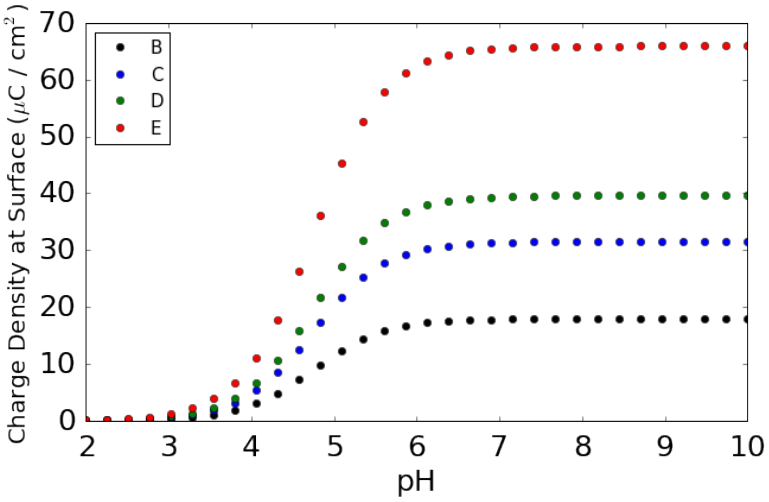

Figure 5.1: Calculated values for the resultant charge density for 200 nm carboxylated polystyrene particles across a range of pH from manufacturer (Bangs) information [113]. Labels correspond to particles B, C, D and E described in Table 5.1.

5.3.1 Fluid Cell Volume

As discussed in Section 4.2.2, the upper fluid cell typically contains 40 μL of electrolyte which produces a small but significant hydrostatic pressure $P_{inherent}$ across the membrane. This was noted by Vogel *et. al* previously in [52] and reported as a static figure of 4.7 mm H_2O. However, evaporation during experiments or errors in the measurement or addition of the electrolyte may cause this volume to change, altering $P_{inherent}$ from this value. Whilst small volume errors may not be expected to alter $P_{inherent}$ significantly (especially compared to the $P_{applied}$ across the membrane in many experiments), the exact change in $P_{inherent}$ due to volume changes depends on the internal geometry of the upper fluid cell which is not well

known.

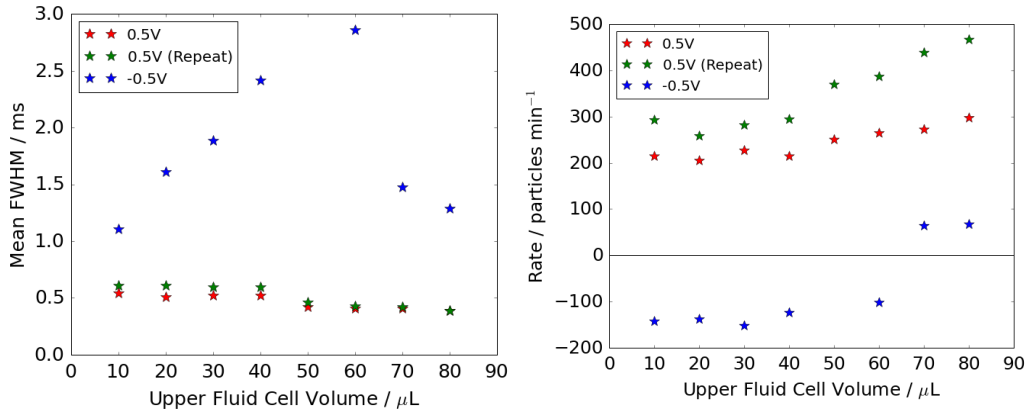

(a) (b)

Figure 5.2: Change in FWHM a) and Rate b) due to change in volume of fluid in the upper fluid cell increasing the hydrostatic pressure applied to the pore. Data obtained for particle set C from Table 5.1 in A11487 at 46mm stretch at 0.5 V.

As such we vary the volume of the upper fluid cell, about the typical 40 μL value, and measure the resultant change in ensemble FWHM and particle rate for $\sim$200 nm spherical carboxylate polystyrene particles, with results shown in Figure 5.2. From the data we can see that at positive voltages, reducing the upper fluid cell volume by 10 μL does not change the FWHM or rate by more than 6% on the 40μL value. However increasing the volume by the same amount changes the rate by between 16 and 27%. Furthermore, experiments performed at negative voltage show changes of between 18 and 22%, for both FWHM and rates, to to both increases and decreases in the volume. Whilst these uncertainties are small compared to the $P_{applied}$ values commonly used in experiments, uncertainty in $P_{inherent}$

will add to the overall uncertainty in $\zeta_{particle}$ measurements.

5.4 Methods for Finding the ζ-potential

Four methods were used to analyse TRPS data for particle ζ-potential measurement, with example results from each method presented in Figure 5.3. In all methods, the strategy is to identify P_0 by collecting resistive pulse data while controlling $P_{applied}$, which can be varied continuously or in discrete steps. The four methods involve measurement of a) continuous rate, b) discrete rate, c) continuous duration and d) discrete duration.

5.4.1 Continuous Rate

The continuous rate method has been described and used previously [52, 110]. $P_{applied}$ was continuously varied, at a rate of 1.5 Pa s^{-1}, between +500 Pa and -500 Pa. This pressure range was selected to ensure that resistive pulses were recorded in regimes dominated by either pressure-driven flow or by electrokinetics. The rate was chosen to ensure that a high number of pulses were counted and the chance of a pore blockage during a measurement remained low. In this method P_0 is identified as the pressure at which the net flow of particles through the pore is at a minimum. Figure 5.3 a) shows the cumulative pulse count with decreasing $P_{applied}$, producing an 'S'-shaped curve, with the dashed vertical lines indicating P_0, determined by calculating the point of inflection of a least-squares cubic fit

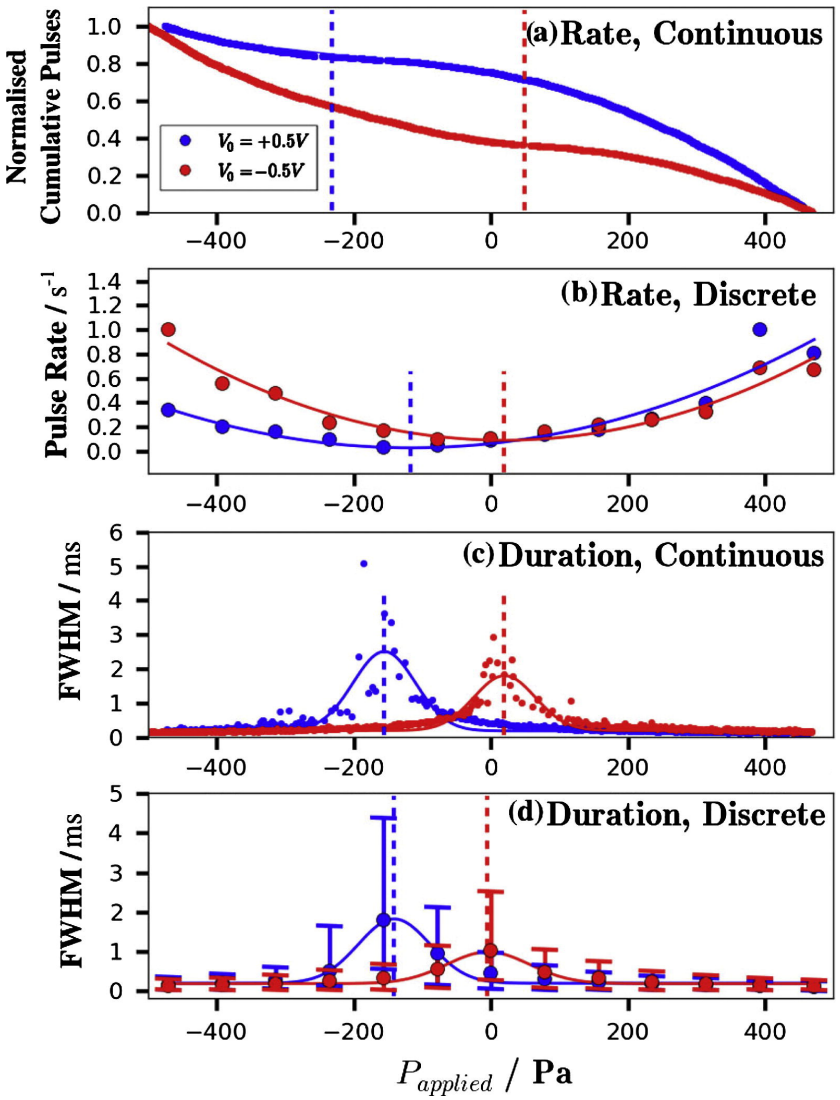

Figure 5.3: Indicative results for particle set C (Table 5.1), demonstrating analysis methods. Vertical dotted lines indicate derived values of P_0. a) and b) Data obtained from continuous and discrete particle rate measurements respectively. Cumulative data in a) are normalised by the total pulse count in each run. c) and d) Data from continuous and discrete measurements of full width half maximum (FWHM) duration respectively. Each data point for 'discrete' cases is the average of at least 500 pulses. Error bars in d) indicate the interquartile range around the median FWHM.

to this curve. When the polarity of the applied voltage is reversed, indicated by a change in colour in Figure 5.3, P_0 changes because the sign of $\mathbf{E}$ changes in Eq. 5.2. Each 'S'-curve represents data collected over a period of approximately 15 minutes, and curves with evidence of a partial or complete pore blockage (indicated by sharp deviations from the expected smooth curve) are discarded. Additional experiments were performed determining P_0 using both continuously increasing and decreasing $P_{applied}$ as indicated by the error bars in Figure 5.4 a).

5.4.2 Discrete Rate

The discrete rate method (Figure 5.3 b)) also identifies P_0 as the pressure at which the minimum pulse rate occurs. In this case an average pulse rate is recorded at between +500 Pa and -500 Pa in steps of 49 Pa (5 mm H_2O). The minimum indicating P_0 is determined by fitting a parabola to discrete rate data, using least-squares fitting, and calculating the minimum. Over 500 events were recorded at each $P_{applied}$ over a period of at least 30 s. Each measurement was visually inspected to ensure that the rate was near-constant throughout the collection period, as large deviations typically indicate a pore blockage. The impact of possible pore blockages and the required measurement time are both reduced in comparison to the continuous rate method.

5.4.3 Continuous Duration

The continuous duration method uses the full width half maximum (FWHM) duration of pulse peaks to indicate the speed at which particles move through the pore. P_0 is identified as the pressure at which the average FWHM is maximised due to the balance between the electrokinetic and pressure-driven transport. The maximum duration is calculated by least squares fitting a Gaussian function to FWHM data, obtained with pressure varied in the same way as for the continuous rate method (above). A Gaussian function is used because it is simple, symmetric about P_0, and appears to represent the single-peak data obtained. Due to outliers (discussed further below), each data point in Figure 5.3 c) represents the mean of 5 consecutive FWHM measurements.

5.4.4 Discrete Duration

In the discrete duration method (Figure 5.3 d)), data are collected at discrete $P_{applied}$ values using the same experimental regime as the discrete rate method. As with the continuous duration method, the mean of a Gaussian fitted to the data yields a measurement of P_0.

5.5 Results and Discussion

5.5.1 Pulse Rate Methods

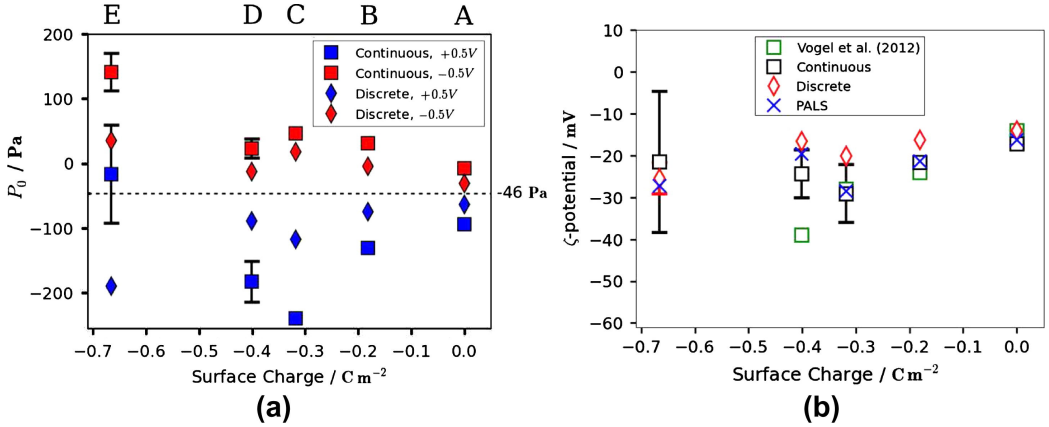

Figure 5.4: Data obtained using rate methods for particle sets A-E (Table 5.1). Particle set labels appear directly above the relevant data in a), which plots applied pressure at minimum pulse rate (P_0) as a function of nominal surface charge density (σ). The horizontal black dotted line indicates -$P_{inherent}$. Error bars for continuous experiments indicate the range spanned in cases of increasing and decreasing pressure. b) ζ-potentials calculated from the rate data. For continuous experiments, error bars indicate the standard deviation of four contributing data points; for discrete experiments, error bars indicate the range spanned by the two values at +0.5 V and -0.5 V (see Figure 5.3 a)). Data from Vogel *et al.* [52] (green squares) were obtained using the continuous rate method. Mean values obtained using PALS are plotted in b), with error bars (±5 mV maximum) omitted for clarity. In both a) and b), error bars smaller than symbol size are omitted.

Figure 5.4 a) shows P_0 data obtained using the continuous and discrete rate methods. Measurements were performed at both V_0 = +0.5 and -0.5 V, and corresponding values of P_0 are separated by the horizontal line corresponding to -$P_{inherent}$, equivalent to $P_{net} = 0$. When positive voltages

are applied across the pore, particles are electrophoretically driven in the same direction as $P_{inherent}$, so the opposing pressure required for **J** = 0 is negative. For values of $\zeta_{particle}$ and ζ_{pore} used in these experiments, the electro-osmotic and electrophoretic transport mechanisms drive particles in opposite directions, but electrophoresis is larger. In the continuous case, each data point represents two experiments, in which P_0 was either increased or decreased over time. The typical variation in P_0 between these cases was less than 5%, and the range of the two values is indicated by the error bars shown in Figure 5.4. Systematic variation is removed by plotting the average of the two values.

All data show a monotonic trend with respect to surface charge for particles A, B and C (i.e. less negative than -0.32 C m^{-2}). The trend extends more weakly to particle set D (σ = -0.40 C m^{-2}). Particle set E (σ = -0.67 C m^{-2}) is exceptional, generating widely varied P_0 measurements and resulting ζ-potential values. These observations, further discussed in Section 5.7, can be partly attributed to the use of polyacrylic acid (in addition to carboxylate groups) to functionalise set E. Comparing continuous and discrete rate measurements, the trend with respect to surface charge is identical for $\sigma \geq$ -0.40 C m^{-2}. However, absolute values of P_0 - $P_{inherent}$ are consistently smaller for the discrete rate measurements.

Figure 5.4 b) plots ζ-potentials calculated from P_0 measurements in Figure 5.4 a) using Equation 5.2 and experimental inputs from Chapter 4. The calculation accounts for the polarity of V_0, so measurements at opposing

polarities ($\pm$0.5 V) are treated as repeats. Particle set E, with the highest magnitude surface charge, shows the greatest variability, indicating unreliable data. Particle sets A and B indicate the least variability in ζ-potential measurement. Consistent with Figure 5.4 a), discrete measurements give lower absolute values of $\zeta_{particle}$.

Data obtained using PALS (Figure 5.4 b)) broadly agree with the TRPS data. Experimental PALS details are included in Section 4.2.1. Ignoring particle set E, the average PALS value is close to the discrete and continuous results, and consistently lies between them. The continuous rate data are within experimental uncertainty of the PALS data, with maximum differences of 4.6 mV (absolute) and 24% (fractional) across sets A-D. The equivalent maximum differences for the discrete rate data are 8.3 mV and 29%. It is notable that $|\zeta_{particle}|$ is lower for particle set D than for set C in three of the four data sets plotted. The exception to this trend is from an earlier experiment [52] which used the same particle sets (A-D) in experiments.

The two key advantages of the rate methods are, firstly, that considerable data obtained over a wide range of conditions are brought to bear on the task of finding P_0, and secondly, that pulses do not need to be further analysed once they have been identified. The primary difficulty with rate methods is that pulses recorded within 50 Pa of P_0 are often non-ideal (further discussed in Section 5.7), and identification of P_0 is strongly dependent on these pulses. Previously [8] these issues have been partially

mitigated by discarding events within 50 Pa of P_0 prior to fitting. In general, the continuous rate method offers more precision than the discrete rate method. The latter method involves a trade-off between precision and time per measurement, which is dependent upon the discrete step size. The discrete raw data (Figure 5.3) are smoother near P_0, but the parabolic fit has uncertainty on a similar scale to the step size. The discrete method also has advantages, namely that it is less vulnerable to spurious pulses near P_0, it is not terminally interrupted when a pore blockage occurs, and it does not require pressure changes in chronological sequence. For the continuous case, the latter requirement can be mitigated by checking and averaging results for increasing and decreasing pressures.

5.5.2 Duration Methods

Measurements of P_0 using duration methods are summarised in Figure 5.5 a). There are broad similarities to data obtained using the rate methods, such as the division of P_0 values for different polarity of V_0 about the horizontal line equivalent to $P_{net} = 0$. Again, P_0 monotonically increases with σ at low absolute values, including particle set D (σ = -0.4 C m^{-2}), although data for set E are again inconsistent. In contrast with Figure 5.4 a), there is no clear systematic difference (and indeed there is very good agreement) between discrete and continuous data. Overall, $|P_0 - P_{inherent}|$ data are smaller than those produced by the rate methods, and it is notable that these values are greater at positive rather than negative values of V_0.

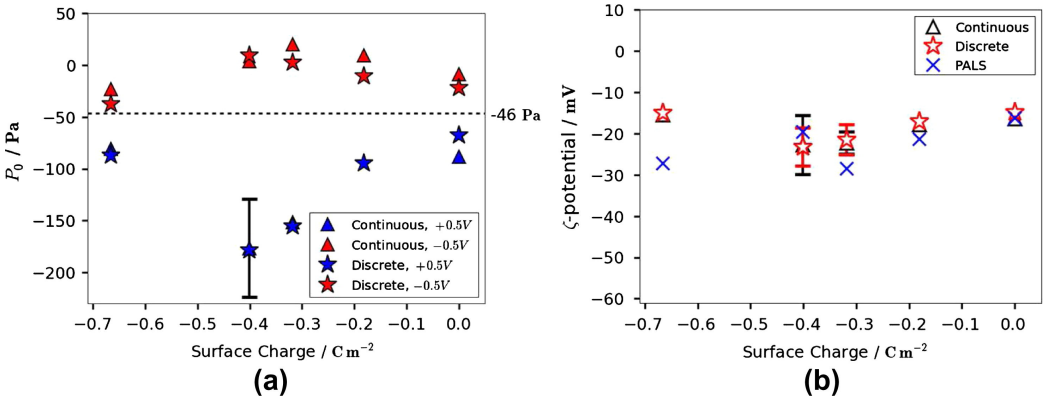

Figure 5.5: Data obtained using duration methods for particle sets A-E (Table 5.1). a) Applied pressure at maximum pulse duration (P_0) as a function of nominal surface charge density (σ). b) Corresponding ζ-potential data. Error bars and the horizontal black dotted line are as described for Figure 5.4, with error bars for PALS (±5 mV maximum) and those smaller than the symbol size omitted for clarity.

These trends are further explored in Section 5.7. Calculated ζ-potentials, with measurements at ±0.5 V treated as repeats (Figure 5.5 b)), yield a monotonic relationship between σ and $\zeta_{particle}$, other than for particle set E. The relatively large uncertainty in ζ-potentials for particle sets C and D relative to sets A and B is a feature of both Figures 5.4 b) and 5.5 b). For these particle sets, $\zeta_{particle}$ values may have high dispersity, or random measurement uncertainly may be relatively large for the specific measurement parameters (including σ) used here. The maximum difference between duration data and the corresponding PALS data is 7.0 mV (absolute) or 25% (fractional) for sets A-D. Across these four particle sets and all four methods (i.e. 16 measurements), the average difference between TRPS and PALS $\zeta_{particle}$ values was 3.4 mV (absolute) or 15% (fractional).

The average uncertainty attributed to repeated measurement was 10% for the TRPS methods and 11% for PALS. PALS and rate measurements (Figure 5.4 b)) indicated a higher absolute ζ-potential for particle set C than for set D, suggesting that values of σ (manufacturer-specified) and $\zeta_{particle}$ may not be monotonically related. This trend was not observed in Figure 5.5 b), although as with the rate data, PALS results are consistent with duration data for all particle sets A-D.

Overall, duration measurements of $\zeta_{particle}$ are more reproducible than measurements using pulse rates. Figures 5.4 b) and 5.5 b) each contain data for six individual measurements using each particle set (four measurements for set B). When each set of six is treated as repeats, all five particle sets have a lower coefficient of variation (equivalent to standard deviation as a fraction of the mean) in the case of duration measurements. As with the rate methods, the discrete duration method usually requires less measurement time than the continuous method, but affords less precision depending on the discretization. Although pulses close to P_0 are again problematic (naively, the FWHM tends to ∞ at P_0), each pulse is analysed more closely than for the rate methods, resulting in less uncertainty. Nevertheless, the Gaussian fit can be significantly affected by individual events, and indeed it is prudent to partially discretise the continuous data by averaging five consecutive individual events for each data point (Figure 5.3).

FWHM pulse durations do not change greatly with pulse magnitude,

the latter being proportional to particle volume [46]. For example, for a sample of set C particles the pulse FWHM varied by <14% between the largest (1.3 nA) and smallest (0.5 nA) pulses, corresponding to <30% variation in particle diameter. The range of mean particle diameters for the sets used here was 40% (Table 5.1). This could partly account for the low P_0 value for particle set E.

5.6 Comparison of Methods

Figure 5.6 summarizes ζ-potential measurements using TRPS, plotting the difference between the value for each method and the mean value over all methods. Raw data used to calculate the cross-methods ζ-potential for particles is summarized in Table 5.2. Duration measurements, both continuous and discrete, are always within $\pm$5 mV of the mean, further indicating that duration measurements produce more precise (self consistent) results than event rate methods. Occasional variations closer to 10 mV are obtained using the rate methods, especially for more highly charged particles. For particles of unknown charge, there is clear advantage in taking measurements using multiple TRPS techniques to check for self consistency, and to avoid measurements such as those found to be characteristic of highly charged particles here.

Some of the trends observed in Figures 5.4 and 5.5 are further evident in Figure 5.6. The continuous and discrete rate data lie either side of the mean in all cases, due to the consistently lower absolute values of $\zeta_{particle}$

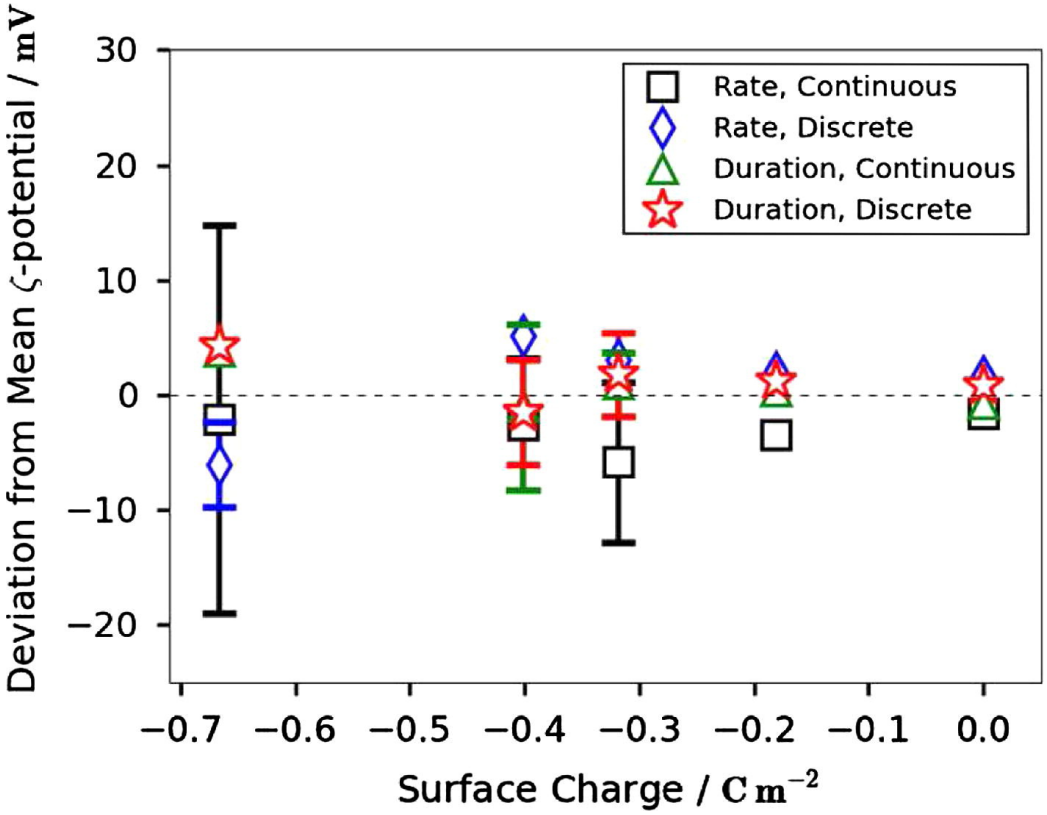

Figure 5.6: Summary of all ζ-potential data, plotted as a deviation from the mean over all methods for each particle set. Error bars correspond to those plotted in Figures 5.4 b) and 5.5 b), and are omitted if smaller than the symbol size.

Table 5.2: Summary of P_0 data and uncertainty obtained from all methods showing calculation of ζ-potentials presented in Figure 5.6. *Direction indicates whether pressure is being varied from positive pressure to negative (direct) or from negative to positive (return).

Particle Set	Method	Direction*	V	P_0	Average P_0	P_0 Half Range	ζ-particle (mV)	Average ζ-particle (mV)	ζ-particle Std. Dev. (mV)	ζ-particle Half Range (mV)	Cross-method ζ-particle (mV)	Cross-method ζ-particle Std. Dev. (mV)	Charge Density (C m^{-2})
A	Cont. Duration	direct	0.5	-86.92			-19.36						
A	Cont. Duration	return	0.5	-75.10	-81.01	5.91	-17.23						
A	Cont. Duration	direct	-0.5	-10.70			-18.34						
A	Cont. Duration	return	-0.5	-7.12	-8.91	1.79	-18.99	-18.48	0.93				
A	Cont. Rate	direct	0.5	-88.43			-19.63						
A	Cont. Rate	return	0.5	-100.50	-94.46	6.04	-21.80						
A	Cont. Rate	direct	-0.5	-13.99			-17.75						
A	Cont. Rate	return	-0.5	-0.31	-7.15	6.84	-20.21	-19.85	1.67				
A	Discrete Duration	n/a	0.5	-67.44			-15.85						
A	Discrete Duration	n/a	-0.5	-21.59			-16.39	-16.12		0.27			
A	Discrete Rate	n/a	0.5	-63.44			-15.14						
A	Discrete Rate	n/a	-0.5	-31.29			-14.64	-14.89		0.25	-17.33	2.24	-0.00341
B	Cont. Duration	direct	0.5	-88.17			-19.58						
B	Cont. Duration	direct	-0.5	9.22			-21.93	-20.75		1.17			
B	Cont. Rate	direct	0.5	-131.21			-27.32						
B	Cont. Rate	direct	-0.5	31.06			-25.85	-26.59		0.73			
B	Discrete Duration	n/a	0.5	-94.80			-20.77						
B	Discrete Duration	n/a	-0.5	-10.84			-18.32	-19.55		1.23			
B	Discrete Rate	n/a	0.5	-74.81			-17.18						
B	Discrete Rate	n/a	-0.5	-4.66			-19.43	-18.31		1.13	-21.30	3.66	-0.181
C	Cont. Duration	direct	0.5	-156.26			-31.82						
C	Cont. Duration	return	0.5	-147.79	-152.02	4.23	-30.30						
C	Cont. Duration	direct	-0.5	19.34			-23.75						
C	Cont. Duration	return	-0.5	21.32	20.33	0.99	-24.10	-27.49	4.17				
C	Cont. Rate	direct	0.5	-231.23			-45.30						
C	Cont. Rate	return	0.5	-248.12	-239.67	8.45	-48.33						
C	Cont. Rate	direct	-0.5	49.40			-29.15						
C	Cont. Rate	return	-0.5	44.41	46.91	2.50	-28.25	-37.76	10.54				
C	Discrete Duration	n/a	0.5	-155.69			-31.72						
C	Discrete Duration	n/a	-0.5	2.70			-20.76	-26.24		5.48			
C	Discrete Rate	n/a	0.5	-117.51			-24.85						
C	Discrete Rate	n/a	-0.5	18.36			-23.57	-24.21		0.64	-28.92	6.04	-0.318
D	Cont. Duration	direct	0.5	-224.07			-44.01						
D	Cont. Duration	return	0.5	-129.34	-176.70	47.36	-26.98						
D	Cont. Duration	direct	-0.5	-1.94			-19.92						
D	Cont. Duration	return	-0.5	9.27	3.67	5.60	-21.94	-28.21	10.94				
D	Cont. Rate	direct	0.5	-150.97			-30.87						
D	Cont. Rate	return	0.5	-214.68	-182.82	31.85	-42.32						
D	Cont. Rate	direct	-0.5	8.92			-21.87						
D	Cont. Rate	return	-0.5	38.07	23.49	14.57	-27.11	-30.54	8.68				
D	Discrete Duration	n/a	0.5	-178.79			-35.87						
D	Discrete Duration	n/a	-0.5	9.69			-22.01	-28.94		6.93			
D	Discrete Rate	n/a	0.5	-88.79			-19.69						
D	Discrete Rate	n/a	-0.5	-12.52			-18.02	-18.86		0.84	-26.64	5.28	-0.4
E	Cont. Duration	direct	0.5	-88.46			-19.63						
E	Cont. Duration	return	0.5	-73.77	-81.11	7.34	-16.99						
E	Cont. Duration	direct	-0.5	-23.33			-16.08						
E	Cont. Duration	return	-0.5	-23.02	-23.17	0.16	-16.13	-17.21	1.67				
E	Cont. Rate	direct	0.5	-92.33			-20.33						
E	Cont. Rate	return	0.5	59.68	-16.32	76.01	7.00						
E	Cont. Rate	direct	-0.5	170.98			-51.01						
E	Cont. Rate	return	-0.5	112.54	141.76	29.22	-40.50	-26.21	25.54				
E	Discrete Duration	n/a	0.5	-86.86			-19.35						
E	Discrete Duration	n/a	-0.5	-37.61			-13.51	-16.43		2.92			
E	Discrete Rate	n/a	0.5	-189.77			-37.84						
E	Discrete Rate	n/a	-0.5	35.13			-26.58	-32.21		5.63	-23.01	7.57	-0.666

derived from discrete measurements. The continuous rate data point for particle set C appears here to be an outlier with low reproducibility. This demonstrates how the inconsistent trend observed for sets C and D in Figure 5.4, discussed above and supported by PALS data, could originate from measurement uncertainty rather than from characteristics of the actual particle distribution. The possibility of error in the nominal charge densities (Table 5.1) should also be noted.

Although the rate methods depend on pulses near P_0 (Section 5.5.1), the analysis required for these methods is relatively facile, requiring only accurate identification of each event. In comparison, duration measurements employ a detailed analysis of each individual event. This provides advantages, such as the ability to discard individual events if they are considered to be outliers, and the possibility to extract more information from each individual event. Indeed, the ζ-potential can in principle be calculated from a single event, without variable pressure [47]. However, the model is designed for an ideal particle travelling smoothly along the central pore axis, and so for individual particle charge measurements factors such as off-axis trajectory, steric interactions and polydispersity should be considered. The comparison between continuous and discrete methods can be summarised by noting that the precision of discrete data is limited by the discrete step size, but that discretization allows flexibility over the step size as well as timing and quality control of measurements.

5.7 Highly Charged Particles

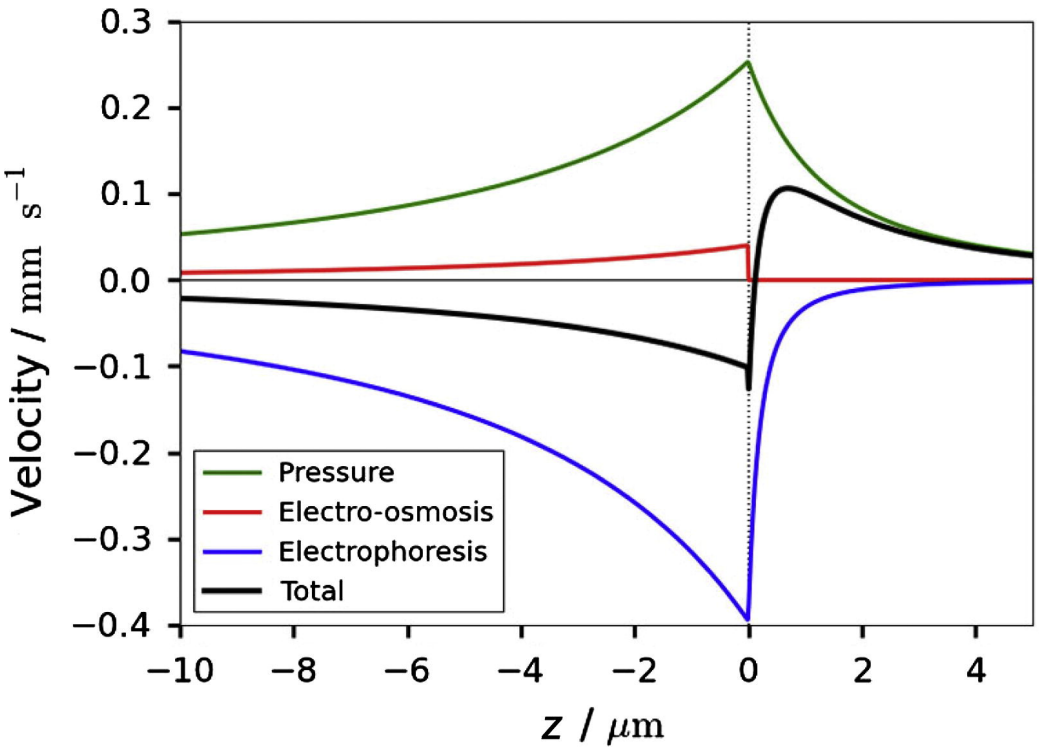

Figure 5.7: Example of simulated particle velocity components in which the direction of transport reverses at the pore constriction. The simulation is based on the semi-analytic model discussed in Chapter 4 using the following parameters: P_{net} = -30 Pa, V_0 = 0.5 V, particle radius 100 nm, a = 450 nm, b = 46 μm, ζ_{pore} = -12 mV,$\zeta_{particle}$ = -30 mV.

In Section 5.5.1, the high variability of P_0 data and derived ζ-potentials for particle set E (Figures 5.4 and 5.5) was partly attributed to differences in functional groups. In addition, set E has the highest nominal charge of the particle sets used (Table 5.1), which may give rise to complications due to competing flow effects near the pore constriction, at the smaller opening.

Figure 5.7 employs the semi-analytic model used above for ζ-potential calculations to plot the relative contributions to particle transport for a specific set of experimental parameters. Due to the differences between electrokinetic and pressure driven flows, the dominant transport mechanism can switch within (say) a few tens of nanometres of the geometric discontinuity at the pore opening, causing the particle flux to change sign. Additionally, particle transport varies across the width of the pore [56]. The pressure-driven flow profile is approximately parabolic (as in Poiseuille flow), while electro-osmosis is nearly a plug flow, and electrophoresis depends on the electric field geometry. This consideration of transport details reveals that complexities in particle transport will not be captured by Equations 5.1 and 5.2.

Figure 5.7 shows that particle transport can be asymmetric about the pore constriction. In this example, any on-axis particle near the small pore opening (on either side) will be transported away from the pore, potentially creating a region of depleted particle concentration around the pore opening. Particles approaching the constriction from above the membrane move differently to those moving from within the pore. This asymmetry could explain differences between P_0 magnitudes (relative to $P_{inherent}$) for positive and negative applied voltages, which are especially evident for duration method data. Perhaps more importantly, competing mechanisms produce a higher likelihood of abnormal resistive pulses near P_0 due to steric or Brownian mechanisms. Abnormal pulses can be generally

characterised as those caused by particle lingering near the pore, perhaps passing through multiple times, rather than cleanly passing through. In our experiments, competition between pressure-driven and electrokinetic transport is increased when particles have high charge.

For particle set E, there is also greater range of $P_{applied}$ at which abnormal pulses were observed, although this could also be caused by relatively high polydispersity. As demonstrated in Figure 5.8 a), fitting of a cubic to the continuous rate method can be uncertain under these conditions, with a range of possible inflection points observed. As a result, the accuracy of P_0 measurement is similarly uncertain for particle set E. Possible differences between P_0 for the cases of $\mathbf{J} = 0$ and maximised duration could explain why ζ-potentials are consistently smaller when obtained by the duration methods, in comparison with the rate methods. As identified in rate experiments, P_0 is the pressure at which the number of particles passing through the constriction is minimised. This may differ from the pressure at which the average particle flux is zero, because it is possible for particles to be moving through the pore in both directions, promoted by transport variation across the pore width. As for maximised duration, the dominant transport mechanism acting on a particle can vary as it moves along the z-axis on length scales comparable to the size of the particle.

This Section reveals clear directions for future improvement of TRPS-based particle charge measurement methods. A significant step would be to establish a process to identify (and discard) abnormal pulses, and draw

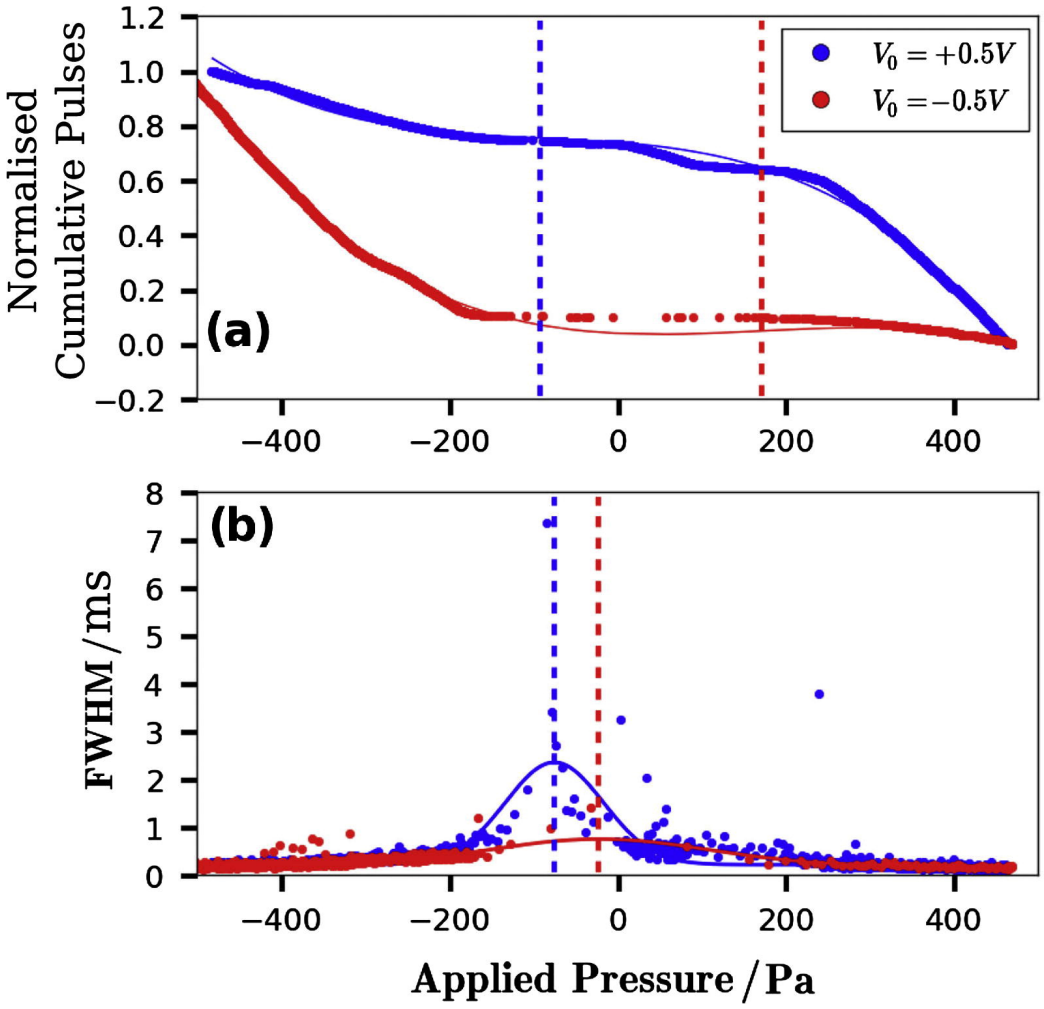

Figure 5.8: Example results using particle set E (Table 5.1). Vertical dotted lines indicate P_0, determined as described in Section 5.4. a) and b) show data obtained from continuous rate and continuous duration measurements respectively.

upon event asymmetry [18] to establish the direction of particle motion through the pore. Research into the importance of precise pore geometry and competition between transport mechanisms will be ongoing. The convergence of the electric field at the pore constriction may give rise to significant DC dielectrophoresis. Further work is required to establish the working range of particle charge measurements for pores of different sizes and in different electrolytes.

5.8 Conclusion

We have studied variable pressure methods for ζ-potential measurement using TRPS. Measurements are comparable to PALS data between zero surface charge and -0.4 C m^{-2}, both in terms of absolute values and repeatability. Use of tuneable pores enables multiple measurement and analysis methods, an advantage over light scattering. Key advances in this Chapter and other previous work include introduction and comparison of four relatively simple analysis techniques, improved experimental control, and more rigorous determination of ζ_{pore} (a key parameter for $\zeta_{particle}$ calculation). Our results are more reproducible when calculations are based on FWHM duration data than when rate data are used. Collection of data over a range of experimental conditions has ensured that uncertainties are clear. Uncertainty increased for more highly charged particles, probably due to competing electrokinetics and pressure about the pore opening. Future work should focus on measurement uncertainties due to pore ge-

ometry and surface charge parameters used in calculations. TRPS charge measurements could also be extended to a wider range of particles. Transport of larger particles is readily dominated by pressure-driven flows, so low-conductivity electrolyte and modified electronics should be used to allow the application of larger voltages necessary to measure electrokinetic transport.

Chapter 6

Shape

6.1 Introduction

The semi-analytic model described in Chapter 3 suggests that a number of factors are capable of producing variations in pulse shape. These include pore geometry, particle trajectory and velocity through the pore, as well as particle size and shape. Results from the previous Chapter describing ζ-potential measurements also indicate that some distribution of event metrics is generated during typical measurements made using the qNano, even with monodisperse, spherical particles. The hypothesis tested in this chapter is then: variations in particle shape can be detected by altered pulse shapes, beyond the variations inherent in the system.

In this Chapter we begin by looking at the predictions for pulse shapes of non-spherical particles using both the theoretical background and semi-analytic model discussed in Chapter 3. Prior experimentation and mod-

elling suggest that it will be difficult to disentangle the effects of particle shape, volume and polydispersity using standard TRPS metrics of pulse magnitude and FWHM. As such we discuss novel metrics for assessing pulse shape: pulse asymmetry (first presented by Willmott and Parry in [18]) and pulse gradients. We characterise the inherent variation in each of these metrics using a well-studied NP200 pore and calibration particles. We then apply these metrics to gold nanorods and calibration particles using a characterised NP400 pore. Finally we assess whether each metric is able to identify non-spherical shaped particles from pulse data.

6.2 Background

Prior experimentation performed with RPS suggests that some particle shape information can indeed be obtained using pores that are small relative to particle size [11, 101]. In early electrokinetic experiments DeBlois *et al.* [11] recorded numerous variations in pulse shape that were attributed to non-uniformity of the pore and resistivity changes within the pore itself. Measurements made on T4 bacteriophage showed multiple peaks in histograms of pulse height and width. The authors concluded these were of unknown origin whilst suggesting that they possibly indicated sample contamination, or else different conformations of the protein capsid, depending on occupation of the capsid by DNA. The T4 phage is an asymmetric particle with a polygonal head and tail, and DeBlois *et al.* noted that dimers of the phage could not explain the observed events using their RPS

model. In this model the T4 phage was simplified to be a prolate ellipsoid with an axial ratio of 1.4 to 1, and it was assumed that the particle long axis aligns to the pore axis during translocation. While the most likely explanation for these observations is contamination or populations of virioids with varying charge, data are also consistent with translocations of ellipsoids with different orientations [11].

Golibersuch also investigated the potential of Coulter counters for geometric measurements [101]. This study generated results of particular note because it used long, large pores and aspherical particles that minimized many potentially confounding electrokinetic effects. Using the metric of fractional resistance change during a translocation ($\Delta R/R$), and comparing with the volume fraction of the particle and pore ($V_{particle}/V_{pore}$), Golibersuch reported that the proportionality constant relating the two was a function of both particle shape and orientation under Poiseuille flow conditions. By examining individual traces and noting that resistance maxima did not occur immediately at the beginning of the pulse, Golibersuch suggested that this was evidence of preferential orientation of spheroids with their long axis parallel to the pore axis, due to the constricting flow fields at the pore entrance. Theoretical analysis of the system suggested that truly random orientations of spheroids during translocation would generate a bimodal distribution of blockade magnitudes, but this did not agree with experimental observations. Golibersuch ultimately predicted a distribution of pulse magnitudes for a population of randomly orientated

particles which depended on the specific particle's hydrodynamic shape factor, γ_H [101].

Golibersuch and Bean [101] noted that this shape factor, for spheroids, is directly related to their demagnetisation factors, the calculation and tabulation of which is described in detail by Osborn in [114]. That work described spheroids, amongst several other geometries including cylinders, as ellipsoids of revolution with semi-axes *a*, *b* and *c* (with particular axes defined by $a \geq b \geq c > 0$) and with corresponding demagnetisation factors denoted as D_a, D_b and D_c. Limiting spheroid geometries to only spheres, oblate and prolate spheroids, we can define prolate spheroids as spheroids where $b = c$ and oblate spheroids where $a = b$ as indicated in Figure 6.1.

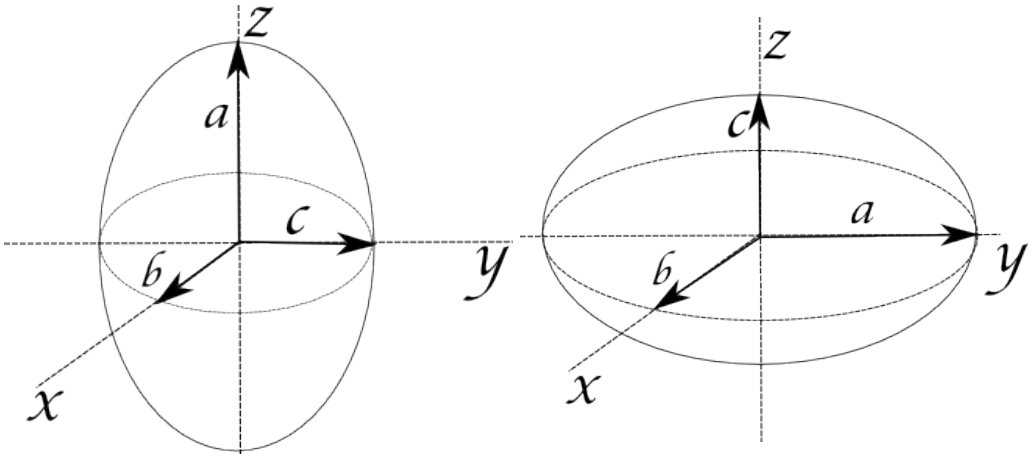

Figure 6.1: Diagram of a) prolate and b) oblate spheroids showing relevant semi-axes, using Osborn's convention of $a \geq b \geq c > 0$.

Defining the aspect ratio of a spheroid as $m = a/c$, the demagnetisation

factors for a prolate spheroid are then:

$$D_a = \frac{1}{m^2-1}\left[\frac{m}{2(m^2-1)^{\frac{1}{2}}}\ln\left(\frac{m+(m^2-1)^{\frac{1}{2}}}{m-(m^2-1)^{\frac{1}{2}}}\right)-1\right] \tag{6.1}$$

and

$$D_b = D_c = \frac{m}{2(m^2-1)}\left[m-\frac{1}{2(m^2-1)^{\frac{1}{2}}}\ln\left(\frac{m+(m^2-1)^{\frac{1}{2}}}{m-(m^2-1)^{\frac{1}{2}}}\right)\right]. \tag{6.2}$$

For an oblate spheroid demagnetisation factors are [114]:

$$D_a = D_b = \frac{1}{2(m^2-1)}\left[\frac{m^2}{(m^2-1)^{\frac{1}{2}}}\arcsin\left(\frac{(m^2-1)^{\frac{1}{2}}}{m}\right)-1\right] \tag{6.3}$$

and

$$D_c = \frac{m^2}{(m^2-1)}\left[1-\frac{1}{(m^2-1)^{\frac{1}{2}}}\arcsin\left(\frac{(m^2-1)^{\frac{1}{2}}}{m}\right)\right]. \tag{6.4}$$

From these, Golibersuch [101] was able to calculate shape factors for the particle both parallel ($f_{||}$) and perpendicular (f_{-}) to the particle's axis of revolution, with:

$$f_{||} = \frac{1}{1-D_{||}} \text{ and } f_{-} = \frac{1}{1-D_{-}}. \tag{6.5}$$

For spheroids with longest dimension less than $1/3$ of the pore diameter, $\Delta R/R$ can then be calculated from:

$$\frac{\Delta R}{R} = [f_{-} + (f_{||} - f_{-})cos^2\alpha]V_{particle}/V_{pore} \tag{6.6}$$

where α is the angle between the electric field and the axis of revolution.

Figures 6.2 a) and b) reproduce two plots from Golibersuch's paper [101] showing the relationships between parallel and perpendicular shape factors for oblate and prolate spheroids, calculated using Equation 6.5. Figure 6.2 c) shows the predicted changes in pulse magnitude due to the rotation of a spheroid. Resistive pulses for oblate spheroids will reduce in magnitude up to $\alpha = \pi/2$, whereas prolate spheroids are predicted to increase pulse magnitude over the same range.

Prior attempts have been made to extract information from pulse shape using TRPS, including Willmott and Parry's study of pulse asymmetry (f_{factor}) as defined by the ratio of FWHM prior to the blockade magnitude to the FWHM [18] as described in Chapter 4. Vogel *et al.* have, in addition, inferred particle position information from the trace data [52]. However, this approach is predicated on having highly characterized pores with transport operating under idealized conditions. This approach was refined by Kozak *et al.* as part of ζ-potential measurement for individual particles [47]. Additionally the semi-analytic model has been applied to particle dimers [48] and rod aggregates [106].

Using RPS, Pevarnik *et al.* have shown previously that the internal structure of a pore can be determined using polystyrene nanoparticles [115]. Menestrina *et al.* have shown that resistive pulse peaks are both a measure of local pore geometry and electrolyte concentration [116].

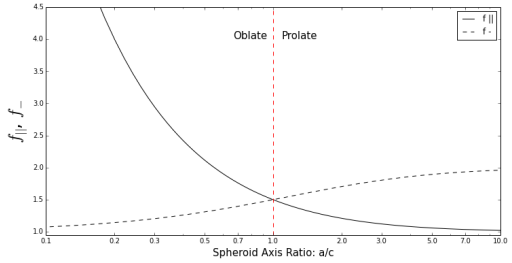

(a)

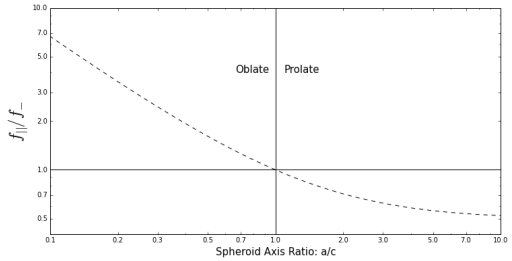

(b)

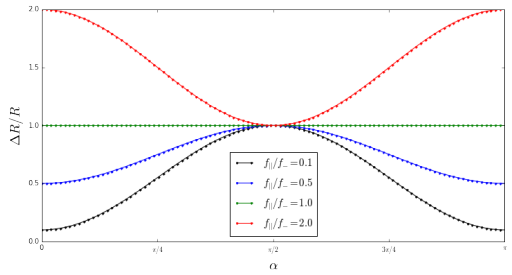

(c)

Figure 6.2: Relationships between parallel and perpendicular shape factors. a) shows the parallel ($f_{||}$) and perpendicular (f_{-}) factors separately whilst b) shows their ratio as a function of particle sphericity. Reproduced from [101] with demagnetisation factor calculations from [114]. c) Predicted $\Delta R/R$ variation for various spheroids rotated through angle α from Equation 6.6 with the electric field parallel to the z-axis.

6.3 Factors Affecting Pulse Shape

As has been described previously, factors that influence pulse shape include, but are not limited to: applied pressure, particle charge, pore geometry, and particle shape, orientation, and location with respect to the pore during translocation. Each factor, however, is expected to alter pulse shape in a unique way due to the specific physics of each phenomenon, suggesting that with appropriate selection of experimental conditions, particle shape information could potentially be extracted from pulse data.

The dominant in-pore effect in TRPS experiments is often the pressure applied across the pore, acting through the pressure driven flow. Spheroids whose longest axis is not parallel to the central pore axis will experience a torque due to the difference in fluid velocities from the centre to the edge of the pore. The magnitude of such a force is dependent on the fluid velocities which are themselves determined by the applied pressure and the specific position of the particle in the pore. The dependence of the radial shear (τ) on axial fluid velocity in Poiseuille flow is:

$$\tau(r) = \mu \frac{\delta v}{\delta r}. \tag{6.7}$$

A spheroidal particle with its centre of mass on the pore axis will not experience a net rotation.

Increasing the pressure applied across the pore is also known to produce a reduction in FWHM and FWQM [52] of the pulse whilst the block-

ade magnitude, at least for particles of identical orientation, should remain constant. The composite effect of shear alignment and increased particle velocity will be a reduction in both pulse duration and in the variation of both pulse duration and magnitude as the possible rotated states of the particles become constrained.

Recently Lan *et al.* have shown that applied voltage and surface charge can alter pulse shape both in simulations and experimental measurements using a 430 nm diameter glass nanopore. The experiments performed by Lan *et al.* showed they were able to control the formation of mono- or biphasic pulses by controlling the electrolyte concentration in this system [117]. Menestrina *et al.* [116] have also observed changes in pulse shape due to pH-mediated control of local ionic concentrations. Weatherall's recent work studying similar phenomena using TRPS [50] has established that such charge distribution effects should not be significant when using electrolyte concentrations $>$50 mM, as in our experiments.

As discussed in Chapter 5, variable ζ-potential will produce similar variations in pulse duration, with particles of increased surface charge exhibiting shorter durations and hence an increase in the rate of rise and fall from the pulse minimum. These variations however, are typically dominated by the pressure driven flow in all pores with a smaller opening diameter $>$400 nm, and careful pressure calibration is required to enable their detection [112]. We also expect particle charge to influence pulse shape. Initially it may seem that the effect of an increase in particle charge

would only reduce the pulse duration, whilst retaining its size and symmetry. However because particle velocity is not directly proportional to particle charge, as it depends on other phenomena which have a separate spatial dependance to **E**, the pulse symmetry is not necessarily preserved. Due to the asymmetric geometry of tuneable pores, there is some evidence that the geometry influences pulse shape [18, 43].

6.4 Modelling of Factors Affecting Pulse Shape

For our analysis in this section we use the semi-analytic model to examine pulses generated by oblate and prolate spheroids as a function of their orientation. In all simulations, particles are located with their centre of mass on the pore axis, and orientations are preserved during translocations. As demonstrated in Figure 6.3, pulses from spheroids with their symmetry axis aligned with that of the pore (solid lines) exhibit variations in blockade magnitude from a sphere even whilst their volumes are identical. This is due to the focusing of the volume either into (in the oblate case) or away from (in the prolate case) the small pore opening (sometimes referred to as the pore 'sensing zone' in literature) where the electric field is constricted. As particles become more prolate (i.e rod-like), with aspect ratios above 1, the blockade magnitude is reduced from the expected magnitude of a spherical particle of the same volume and the pulses become more symmetric about the pulse peak (Figure 6.3 b)). For particles that become more oblate (i.e. disc-like), the opposite is expected with blockade magnitude

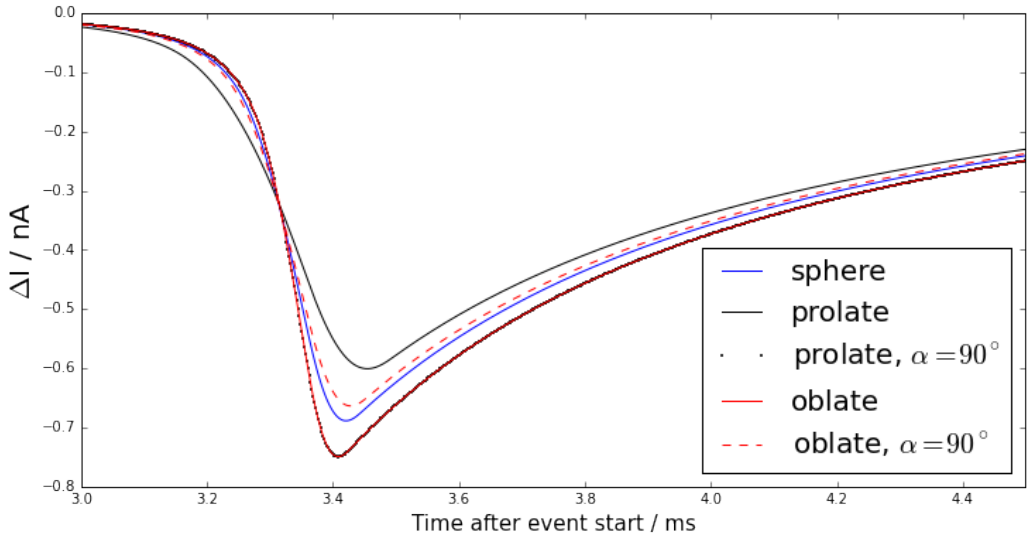

(a)

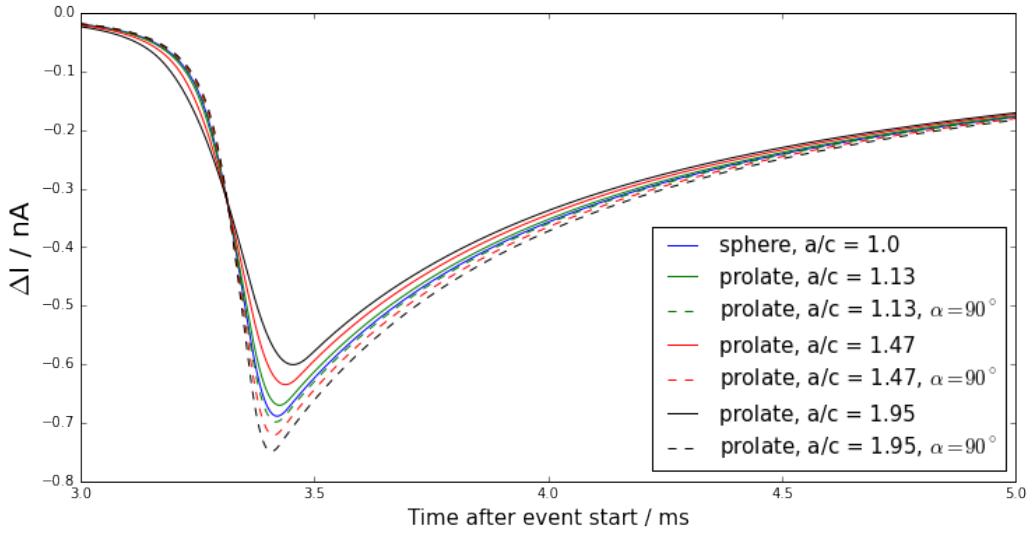

(b)

Figure 6.3: a) Model prediction for pulse characteristics of a sphere, oblate spheroid and prolate spheroid of equal volume with varying rotation relative to the central pore axis. Sphere radius is a = b = c = 250 nm. Oblate particle is c = 200 nm, a = b = 390 nm. Prolate particle is b = c = 200 nm, a = 280 nm. b) Model prediction for pulse characteristics of an equal volume sphere and prolate spheroids with varying aspect ratios. The model for both figures was calculated using a 160 μm long truncated cone shaped pore, with 500 nm small opening, 10 μm large opening, 10 Pa of applied pressure, ζ_{pore} = -13 mV and $\zeta_{particle}$ = -30 mV.

becoming larger and pulses becoming more asymmetric.

Figure 6.3 suggests that particle orientation plays a role in the formation of pulse shape. Whilst the shear force from the Poiseuille flow may align some particles with the pore, a population of orientations is still expected [101]. For prolate particles the effect of these different orientations is expected to be greater than for oblate particles. For oblate particles, whilst the rotation effect significantly alters pulse magnitudes, the size of this change (although dictated by the aspect ratio of the particle) is less than that caused by variations in particle shape (typically a decrease in pulse magnitude of $\sim$30%). The semi-analytic model predicts changes in pulse magnitude due to rotation of spheroidal particles that are similar to the trends predicted by Golibersuch. Whilst comparing pulse shape variation is possible for theoretical data, most populations of particles will not have identical volumes in practice. These volume variations will be a confounding factor when attempting to differentiate rotational variation from particles of different shapes.

Deviations in pore geometry from the truncated cone model described earlier (Chapter 5) generate events of varying symmetry for a spherical particle as indicated in Figure 6.4 a). These geometries either have the mouth of the cone below the surface of the membrane, or have a different internal pore shape. Specifically, the more cylindrical the internal pore profile becomes, the more symmetric pulses appear. The blockade magnitude, asymmetry, and rise and fall characteristics of the pulse are all

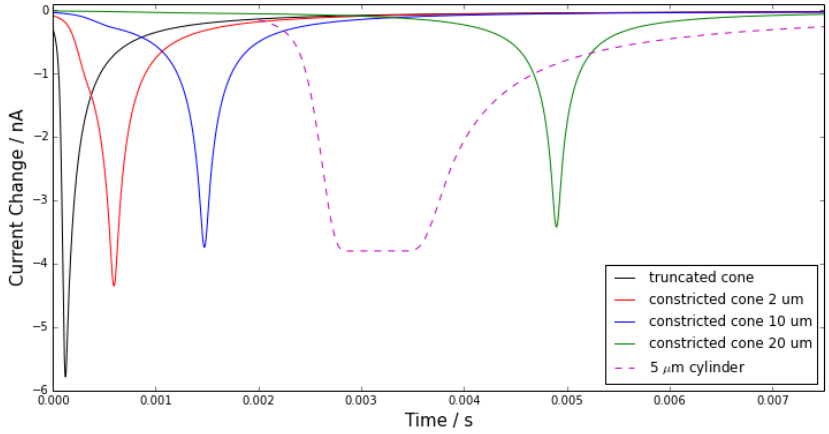

(a)

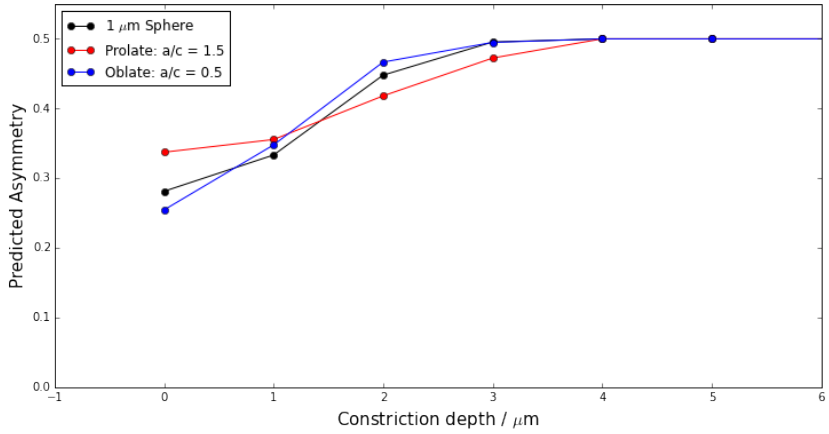

(b)

Figure 6.4: a) Model predicted pulse dependance on internal pore geometry (defined in Section 3.4.3). 'Constricted cone' refers to the symmetric cone described in Chapter 4 b) Model predicted asymmetry dependance on pore constriction depth from small pore opening. Asymmetry (f_{factor}) calculated as described in Chapter 4.

affected by the pore geometry. These trends are consistent with previous RPS studies in which pulse shape depended on pore geometry [115, 116].

To summarise, when studying the relationship between particle shape and pulse shape, the optimal experimental conditions are tightly constrained to using pores with constant geometry, where electrokinetic phenomena are negligible and pressure driven flow is sufficient to drive particle transport alone. The data least prone to sampling error will be those with the longest possible durations. Particles and pores with well-known geometries of >0.5 μm in diameter are then preferable for a study of particle shape using TRPS, yet will require comparison with particles of known geometry to assess inherent variation due to other experimental variables such as the internal geometry of any specific pore and the size dispersity of the particle set.

6.5 Metrics

In order to quantitatively investigate changes in pulse shape, several metrics were decided upon for investigation, indicated in Figures 4.18 and 4.19. Common TRPS metrics are pulse magnitude, and some measurement of event duration - typically either a FWHM, FWQM, or the duration between deviations from baseline current. For the latter an arbitrary threshold for duration is usually dictated by the current trace noise. For particle size and charge measurements these metrics are sufficient because the pulse peak occurs when the particle occupies a position immediately

adjacent to the small pore opening [18], and whichever duration measurement is used can be strongly influenced by electrophoretic effects. However, limiting an analysis to any single duration measurement risks discarding important pulse information.

All of the aforementioned pulse metrics (magnitude, FWHM and FWQM) exhibit variation between pulses, even for nominally monodisperse particle sets and well-characterized pores. This can be due to particle dispersity, changes in the trajectory of the particle through the pore or other factors including particle shape and orientation. In order to link duration measurements with pulse rise and fall rates, a novel method was defined and tested: linear fitting to the pulse leading towards and away from the pulse minimum as indicated in Figure 4.19, referred to as the pulse 'gradient'. The gradient method performs least squares fitting on datapoints at the FWQM, FWHM and maximum blockade magnitude to describe the average gradient each side of the blockade maximum. The ratio of these is then compared to the pulse's FWHM and FWQM measurements and asymmetry, giving considerable information about the overall event shape.

6.6 Results and Discussion

6.6.1 Metric Assessment

The metrics were first experimentally tested by comparing their ranges and variation using three populations of 200 nm monodisperse, spherical,

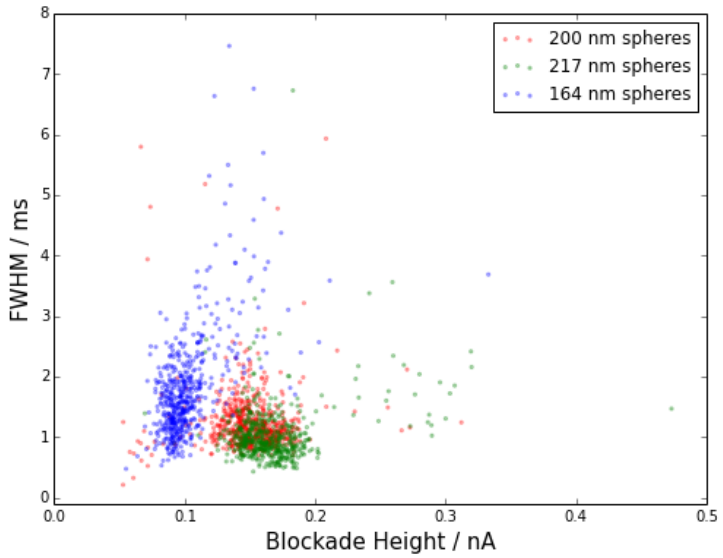

Figure 6.5: Experimental scatter plot for ∼200 nm particles of different charges as indicated in Table 6.1. Measurements are taken at 0 Pa applied pressure.

carboxylate polystyrene particles that have been thoroughly characterised previously [52], shown in Figure 6.5. Particles were driven through an NP200 pore (A11486), at the same stretch and applied voltage (46 mm, 0.5 V), that had been characterised previously (Chapter 4) under low pressures ($P_{applied}$ = 0 Pa). These data are expected to indicate the maximum variation across all metrics for monodisperse samples. Data from all three particle sets across a range of pressures are summarised in Table 6.1. Subsequently (Section 6.6.2), results for non-spherical particles will be compared with results from spherical particles.

The summary data provided by the ICS software for blockade height and duration typically includes mean and mode values for the pulse magnitude and FWHM, and summary D10 and D90 measurements. These

are insufficient to characterise a skewed distribution of pulse magnitudes that is expected for particles able to traverse the pore in multiple, distinct conformations. Hence we use an additional range measurement for all metrics, the Interquartile Range (IQR). The IQR is defined as the difference between the upper and lower quartiles of the population, which becomes a dimensionless range when normalised against the population median. Furthermore the IQR is more suitable for measurements of skewed or asymmetric distributions than the mean or standard deviation and is less prone to errors associated with outlier pulses.

As indicated in Figure 6.5, even nominally monodisperse samples exhibit variation in both blockade height and duration, with a typical dimensionless range of $\sim$20% for magnitude and between 35% and 60% for FWHM. Each value presented in Table 6.1 summarises a histogram of pulse data such as those demonstrated in Figure 6.6. Histogram binning in all plots is calculated using the Freedman-Diaconis rule [118] to limit the effect of outliers on bin size selection, which utilises the IQR and n, the total number of resistive pulses:

$$\text{Binsize} = \frac{2\text{IQR}(x)}{n^{1/3}}. \tag{6.8}$$

Table 6.1: Range data from nominally monodisperse, spherical particle sets measured using an NP200 pore. All data are generated from measurements of over 500 pulses collected over a period of >30 s. 'Range' here indicates the dimensionless range of the metric (i.e. the IQR/Median). A pore blockage prevented data for 200 nm, <0.01 C/m^3 particles being collected at $P_{applied}$ of 10 or 20 Pa.

	Magnitude (nA)			FWHM (ms)			FWQM (ms)		
$P_{applied}$ = 20 Pa	Median	IQR	Range	Median	IQR	Range	Median	IQR	Range
200 nm, <0.01 C/m^3	-	-	-	-	-	-	-	-	-
217 nm, 0.32 C/m^3	0.1683	0.0259	15%	0.4393	0.1593	36%	1.3775	0.4472	32%
164 nm, 0.89 C/m^3	0.082	0.0179	22%	0.5506	0.3153	57%	1.586	0.7773	49%
$P_{applied}$ = 10 Pa									
200 nm, <0.01 C/m^3	-	-	-	-	-	-	-	-	-
217 nm, 0.32 C/m^3	0.1565	0.0266	17%	0.6559	0.2376	36%	2.1337	0.8292	39%
164 nm, 0.89 C/m^3	0.0874	0.0184	21%	0.8515	0.4619	54%	2.3173	1.0709	46%
$P_{applied}$ = 0 Pa									
200 nm, <0.01 C/m^3	0.1495	0.0246	16%	1.1302	0.4089	36%	4.5099	1.7938	40%
217 nm, 0.32 C/m^3	0.1617	0.0263	16%	0.937	0.3897	42%	2.8957	1.128	39%
164 nm, 0.89 C/m^3	0.0973	0.018	18%	1.6403	0.9046	55%	4.2256	1.6507	39%
	Asymmetry			Post-peak Gradient (s^{-1})			Pre-peak Gradient (s^{-1})		
$P_{applied}$ = 20 Pa	Median	IQR	Range	Median	IQR	Range	Median	IQR	Range
200, nm <0.01 C/m^3	-	-	-	-	-	-	-	-	-
217 nm, 0.32 C/m^3	0.3802	0.1057	28%	2.3437	0.969	41%	-0.6321	0.2521	-40%
164 nm, 0.89 C/m^3	0.3824	0.1651	43%	1.8727	0.9483	51%	-0.572	0.3119	-55%
$P_{applied}$ = 10 Pa									
200 nm, <0.01 C/m^3	-	-	-	-	-	-	-	-	-
217 nm, 0.32 C/m^3	0.3951	0.1182	30%	1.643	0.6785	41%	-0.3911	0.201	-51%
164 nm, 0.89 C/m^3	0.3655	0.1502	41%	1.3183	0.6872	52%	-0.3952	0.2034	-51%
$P_{applied}$ = 0 Pa									
200 nm, <0.01 C/m^3	0.4047	0.1421	35%	0.9564	0.4021	42%	-0.1722	0.0913	-53%
217 nm, 0.32 C/m^3	0.3614	0.1082	30%	1.1632	0.4896	42%	-0.2986	0.1274	-43%
164 nm, 0.89 C/m^3	0.3489	0.144	41%	0.746	0.4918	66%	-0.2156	0.0934	-43%

Magnitude

The distribution of pulse magnitudes shown in Figure 6.6 a) is typical of a monodisperse, spherical particle set measured at an appropriate pore stretch (larger pore stretches can produce distributions truncated at lower magnitudes). The distribution could be approximated as symmetric and standard descriptors such as mean, mode and standard deviation are used to describe it. Magnitude consistently exhibits the smallest dimensionless range when compared to other metrics. Median pulse magnitude and IQR only change minimally under applied pressure, with the different sized particles being easily discernible at all three pressures tested (Figure 6.6 b)).

FWHM and FWQM

Figure 6.7 shows characteristic data for FWHM and FWQM. As expected both FWHM and FWQM duration averages show a strong negative relationship with pressure as has been discussed in Chapter 5. The duration IQRs also reduce with an increase in pressure, but the dimensionless range does not show a corresponding trend. There is also a link between particle charge and the amount of variation in both FWHM and FWQM, with more highly charged particles consistently exhibiting the same or larger IQRs than lower charged particles. This is expected because the electrophoretic force opposes the applied pressure in this configuration.

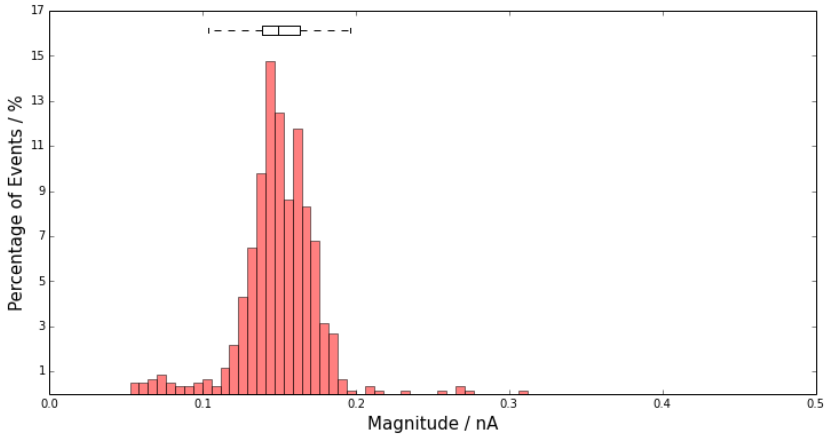

(a)

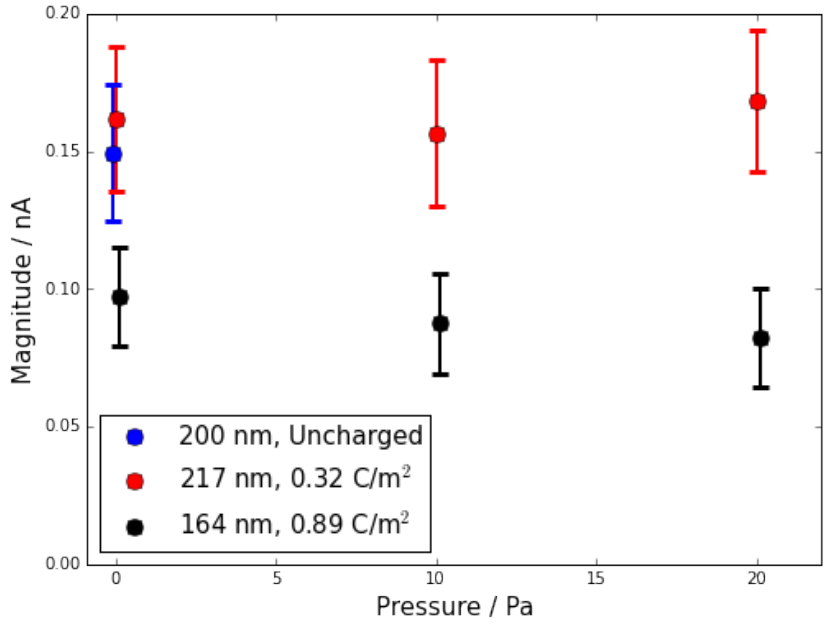

(b)

Figure 6.6: a) The histogram of pulse magnitudes for 200 nm spherical particles (< 0.1 C/m^2) at $P_{applied}$ = 0 Pa. Box and whisker overlay indicates the D10 and D90 points, the upper and lower quartiles, and the median of the data. b) shows summary data for all particles across a variety of pressures. Error bars indicate the IQR.

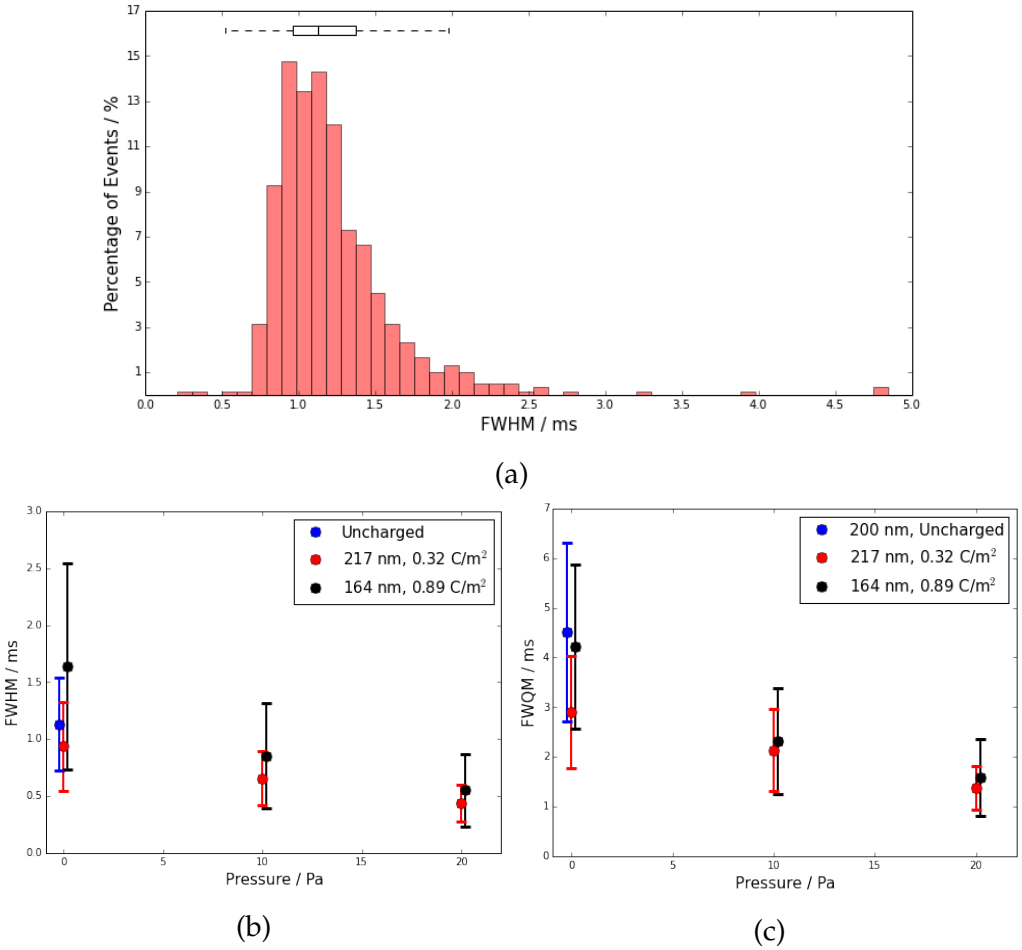

Figure 6.7: a) Histogram of pulse FWHMs for 200 nm spherical particles (< 0.1 C/m^3) at $P_{applied}$ = 0 Pa. Box and whisker overlay indicates the D10 and D90 points, the upper and lower quartiles, and the median of the data. b) and c) show summary data for a range of particles across different pressures. Error bars indicate the IQR.

Asymmetry

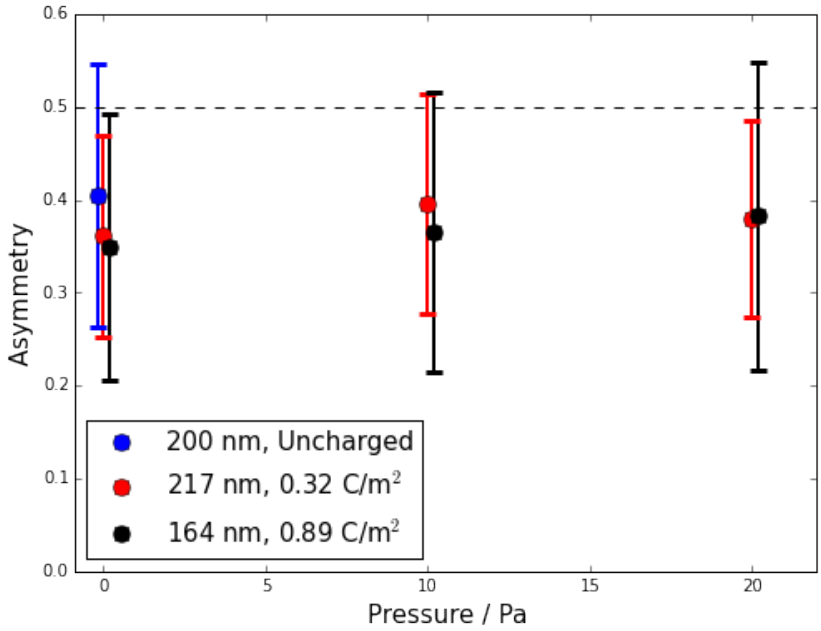

Figure 6.8: Asymmetry measurements for 200 nm spherical particles. Error bars indicate IQR of the data.

There is a weak correlation between increasing pulse symmetry and an increase in pressure, shown in Figure 6.8. However, over all pressure measurements, median asymmetry measures did not vary more than 11.5% from their values at 0 Pa. The dimensionless range does not change more then 2% over a pressure difference of 20 Pa. As with FWHM and FWQM, particle charge may be connected to the dimensionless range of the asymmetry as 217 nm particles and 164 nm particles maintain an asymmetry dimensionless range of 28-30% and 41-43% respectively.

Gradients

Figure 6.9 a) shows summary gradient data for 200 nm particles. Gradients, both pre- and post-peak, are strongly linked to the applied pressure. The ratio of gradients does not appear strongly linked to pressure (Figure 6.9 b)). Instead this ratio is linked to the inherent charge of the particle, with the mostly highly charged (and smallest) particles having the gradient ratios closest to -1 (indicated by the dashed black line in Figure 6.9 c)). The IQR of both gradients increases along with pressure, because pulses become shorter. The post-peak gradient of pulses is consistently greater than 3 times the pre-peak gradient, regardless of particle size. The IQRs of pre-peak gradients are correspondingly smaller as well, however the post-peak gradients dimensionless range is more consistently the same or smaller than that of the pre-peak gradient.

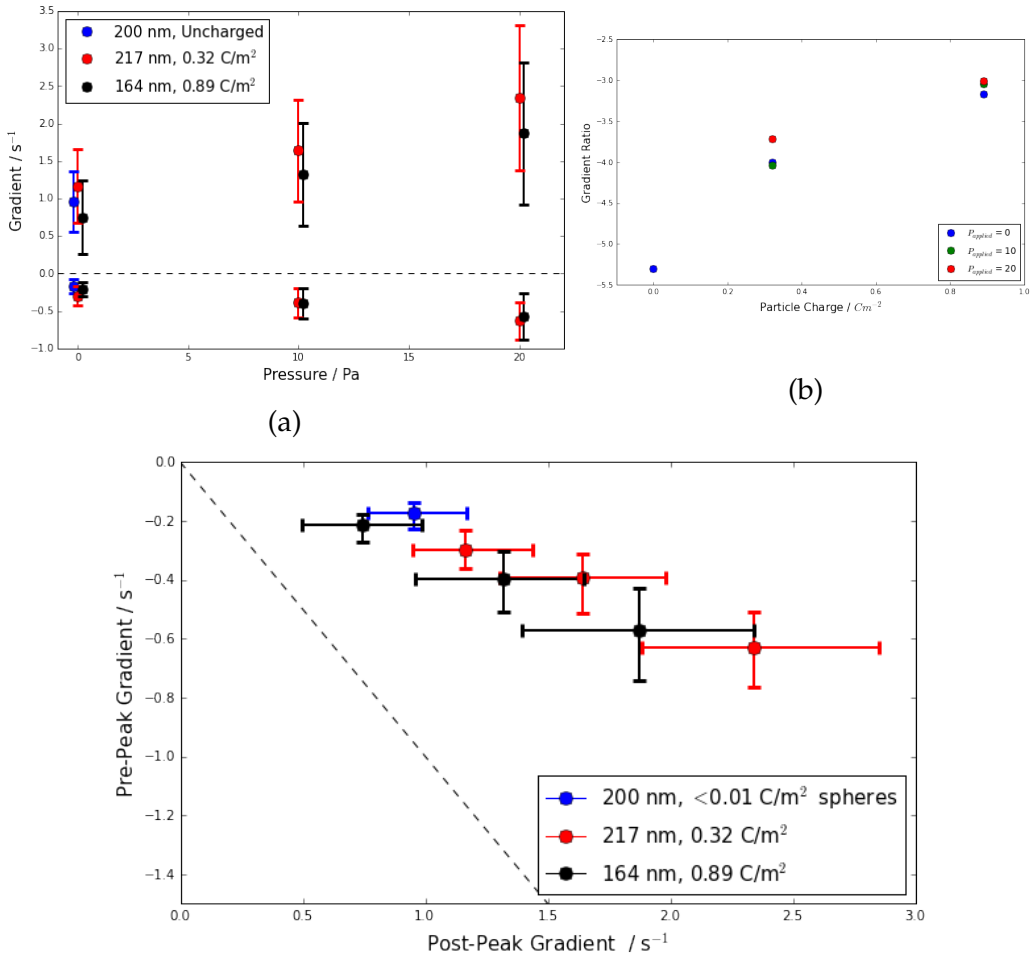

Figure 6.9: Gradient and gradient ratio data for calibration particles under varying pressures (0, 10 and 20 Pa applied). Gradients in a) are normalised by blockade magnitude, with error bars indicating the IQR for each gradient. Pre-peak gradients appear below the axis (are negative by convention of a resistive pulse). Gradient ratios from a) are plotted explicitly against particle charge in b). In c), post-peak gradient is plotted against pre-peak gradient.

6.6.2 Gold Nanorods (Au-rods)

To analyse particle shape a series of PEGylated gold nanorods (described in detail in Chapter 4) were analysed using TRPS. These particles were calibrated against two populations of spherical carboxylate polystyrene particles, with diameters of 400 nm and 780 nm. Measurements were performed using A09174 (NP400).

SEM of Au-rods

Au-rods were imaged using an FEI Nova Nano SEM 450 at ∼40 000 times magnification (Figure 6.10). The large clusters of rods observed under SEM are not expected in TRPS as samples were sonicated prior to TRPS measurements. SEM images were analysed using the open source software Inkscape and measurements of rod dimensions were rounded to the nearest nanometer. A high degree of variation was observed in the rod length whilst all observed rod widths were between 260 and 430 nm. Rods were observed to be mostly cylindrical, excepting sharp tips that were commonly observed and are due to the manufacturing process [119].

29 individual rods were measured, with characteristics summarised in Table 6.2. Whilst prior SEM of the particles suggested that their diameter was ∼300 nm and length 2.0-2.5 μm [106] (as suggested by Figure 6.10 a)), our SEM (Figure 6.10 b)) suggests that the rods have an average width of 260 $\pm$ 50 nm and a length of 1.5 $\pm$ 0.5 μm. A sphere of equivalent volume to an average rod is 536 nm in diameter.

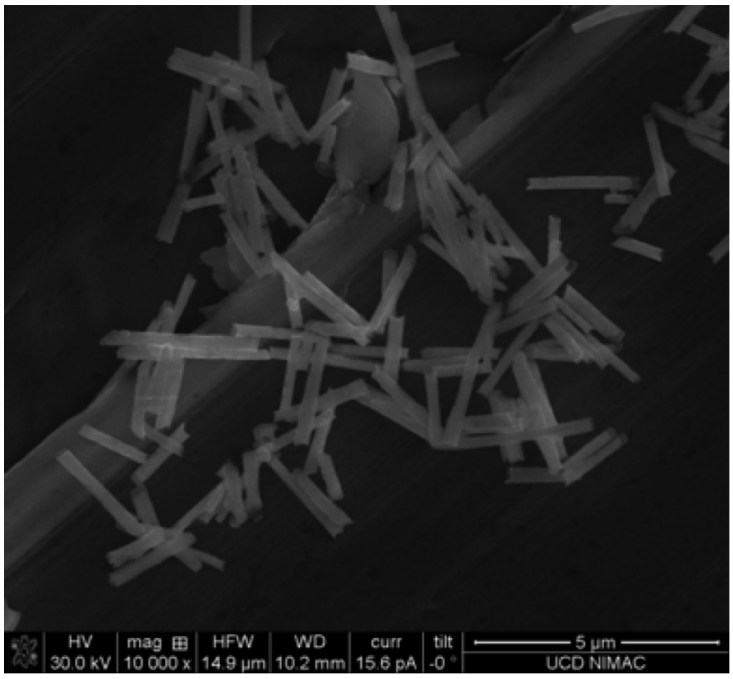

(a)

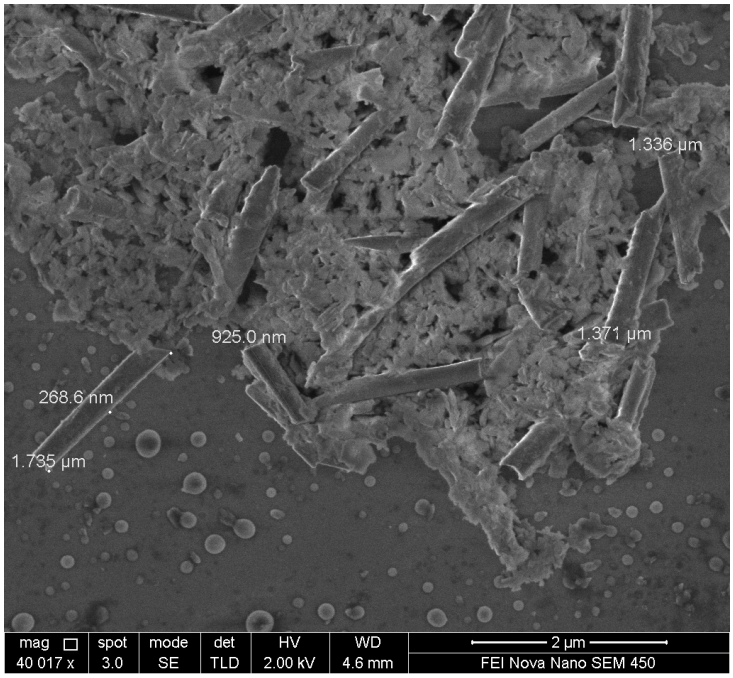

(b)

Figure 6.10: a) SEM of the rods prior to PEG coating obtained from Platt [106]. b) SEM images of Au-rods. Numbers in white represent the lengths and widths of the adjacent rods as measured by the Nova software.

Table 6.2: Summary of shape characteristics of Au-rods (n = 29) from our own SEM measurements.

	Width (nm)	Length (μm)
Mean	259	1.47
Standard Deviation	48	0.45
Max	431	2.76
Min	196	0.67
Median	262	1.37
Upper Quartile	282	1.68
Lower Quartile	226	1.24
Dimensionless Range	0.21	0.32

TRPS Magnitude

The estimated volumes of the particles are 0.081 μm^3, 0.036 μm^3 and 0.249 μm^3 for Au-rods, 400 nm and 780 nm diameter carboxylate polystyrene spheres, respectively. As such there is a risk of confounding particle volume effects with particle shape effects when interpreting the results of the TRPS experiments comparing spherical and non-spherical nanoparticles. Figure 6.11 demonstrates pulse magnitude histograms for all particles along with the median FWHM for each bin. Each of a), b) and c) show both magnitude and FWHM data, and similar plots will be used to characterise pulse distributions in this and later Chapters. The horizontal box and whisker overlay indicates the median, upper and lower quartile (shown by the box) and the D90 and D10 measurements (the whiskers) of the pulse magnitudes. The vertical box and whisker shows the same data for FWHM measurements for the same pulses. Overlaid 'x's indicate the median FWHM for all pulses in each magnitude bin.

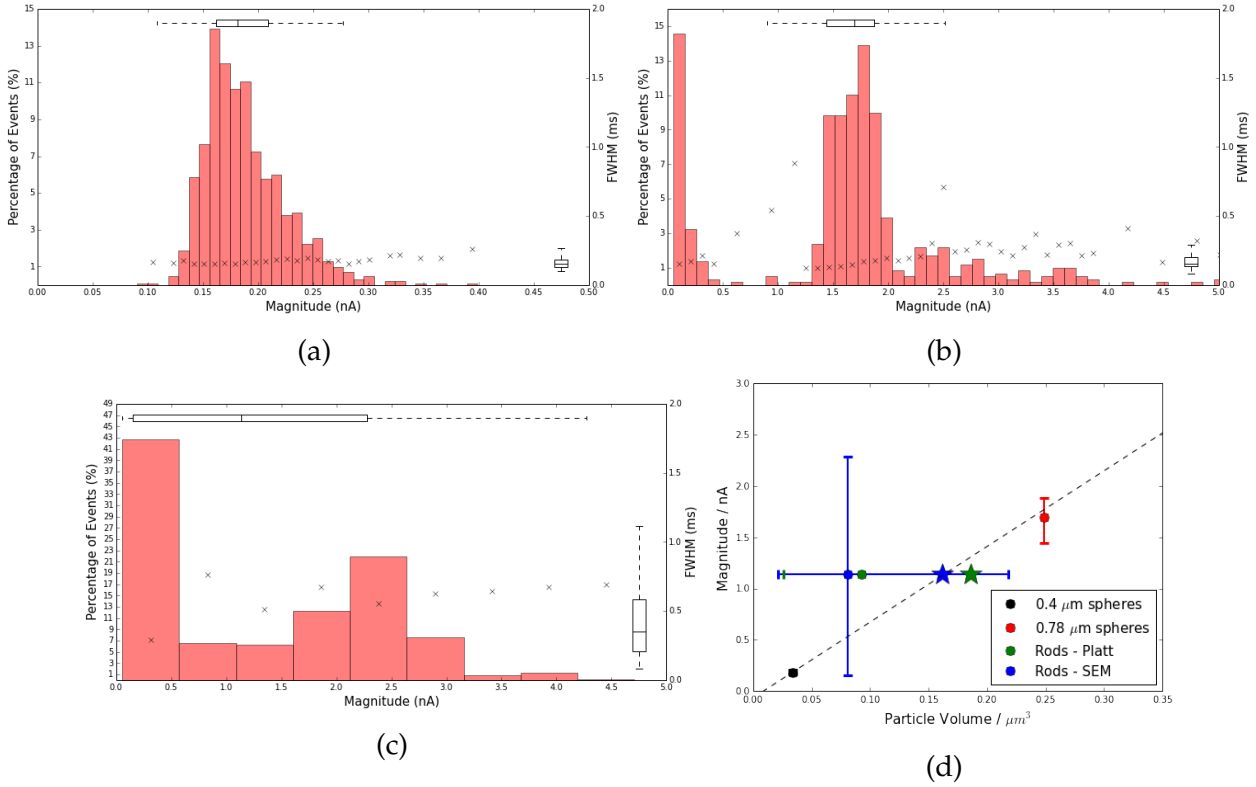

Figure 6.11: a) Population distribution of 0.4 μm calibration particle pulse magnitudes and mean FWHMs for each bin (black crosses). b) Population distribution of 0.78 μm calibration particle pulse magnitudes and FWHMs. c) Population distribution of Au-rods pulse magnitudes and FWHMs. Note the change of horizontal axis scale between the 0.4 μm diameter particles in a) and the larger particles in b) and c). d) plots the calculated particle volumes against median pulse magnitudes. The star points in d) indicates the expected volume of a rod-dimer. Error bars indicate the sample IQR. Horizontal error bars for rods in d) indicate standard error in mean from SEM data. Measurements taken at 20 Pa of applied pressure, 46 mm stretch, 0.25 V in A09174 (NP400).

Table 6.3: Range data from 0.4 μm, 0.78 μm and rod-shaped particle sets at two different pressures: 10 and 20 Pa. All data are generated from measurements of over 500 pulses collected over a period of $>$ 30s.

	Magnitude (nA)			FWHM (ms)			FWQM (ms)		
	Median	IQR	Range	Median	IQR	Range	Median	IQR	Range
$P_{applied}$ = 10 Pa									
0.4 μm spheres	0.191	0.053	28%	0.223	0.084	38%	0.434	0.164	38%
0.78 μm spheres	1.768	0.346	20%	0.396	0.114	29%	0.611	0.219	36%
Rods	2.279	0.935	41%	0.705	0.556	79%	1.266	0.937	74%
$P_{applied}$ = 20 Pa									
0.4 μm spheres	0.181	0.047	26%	0.152	0.055	36%	0.299	0.11	37%
0.78 μm spheres	1.696	0.435	26%	0.157	0.070	45%	0.326	0.144	44%
Rods	1.139	2.130	187%	0.354	0.376	106%	0.691	0.669	97%

	Asymmetry			Post-peak Gradient (s^{-1})			Pre-peak Gradient (s^{-1})		
	Median	IQR	Range	Median	IQR	Range	Median	IQR	Range
$P_{applied}$ = 10 Pa									
0.4 μm spheres	0.489	0.131	27%	4.367	2.033	47%	-2.911	1.176	-40%
0.78 μm spheres	0.460	0.076	17%	3.154	1.576	50%	-2.057	0.583	-28%
Rods	0.517	0.11	21%	1.41	1.297	92%	-1.043	0.719	-69%
$P_{applied}$ = 20 Pa									
0.4 μm spheres	0.475	0.136	29%	6.701	3.119	47%	-4.138	1.739	-42%
0.78 μm spheres	0.473	0.094	20%	5.814	3.21	55%	-3.776	1.169	-31%
Rods	0.495	0.123	25%	2.831	3.006	106%	-1.821	1.839	-101%

As shown in Figure 6.11 d), median pulse magnitudes are similar to calculated particle volumes for spherical particles, with rod shaped particle exhibiting smaller pulse magnitudes than expected for volumes calculated from SEM data. The dashed line in Figure 6.11 d) corresponds to a least squares fitting of the spherical particle points only. Spherical particles show levels of variation in pulse magnitude comparable to the 200 nm particles studied earlier, exhibiting a dimensionless range of 20-30% compared to 15-25%. However for the rod-shaped particles, the dimensionless range IQR in pulse magnitudes is almost an order of magnitude larger, consistent with observations of rods with multiple orientations traversing the pore. However, this is also consistent with a highly disperse sample of particles, as suggested by the SEM data which showed that rod length can vary by 0.5 μm or more. Data from all experiments with rods and particles are summarised in Table 6.3.

Figure 6.12 shows the data for the same particles but collected at $P_{applied}$ = 10 Pa. Spherical particle pulse magnitudes remain consistent to within 6% of their median value at $P_{applied}$ = 20 Pa. Spherical particle dimensionless range also remains broadly consistent over this pressure range. Notably both Figure 6.12 and Table 6.3 show both an increase in median magnitude and a decrease in the range of pulse magnitudes observed for rods. It is likely that the decrease in IQR is due mostly to the increased percentage of events detected near the lower detection threshold for the pore for the sample shown in Figure 6.11 .

As aggregates of the rods were observed in both visual inspection of the particles and under SEM, it is likely that these contribute to the increased range as rod dimers would be expected to produce dimers of double the blockage magnitude of the rods alone (Figure 6.11). Figure 6.11 c) also shows significantly larger histogram bin sizes for the rods than for either of the spherical particle samples. This is due to the histogram binning rule used (Equation 6.8) which calculates bin sizes based on the sample IQR.

Pressure-dependence was further investigated over a series of additional applied pressures. The combined results are plotted in Figure 6.13. Smaller 0.4 μm particles were included to calibrate the pressure behaviour of the pore showing that for this specific pore the 'balance point' used for charge measurement is at approximately -10 Pa. Whilst an increase in magnitude dimensionless range is observed at all pressures over 10 Pa, this appears to be due to a larger proportion of smaller pulses being observed. Hence this may be evidence of a pressure driven alignment effect which could generate a higher proportion of smaller magnitude pulses if prolate particles are aligned to the pore axis (Figure 6.3). It should also be noted that when compared to other pressure measurements (as in Figure 6.13 a)) the rod-shaped measurement made at 20 Pa appears to be an outlier. However as this was the experiment performed immediately after sonication (with experiments at other pressures immediately following it), the increased average pulse magnitude observed at other pressures may

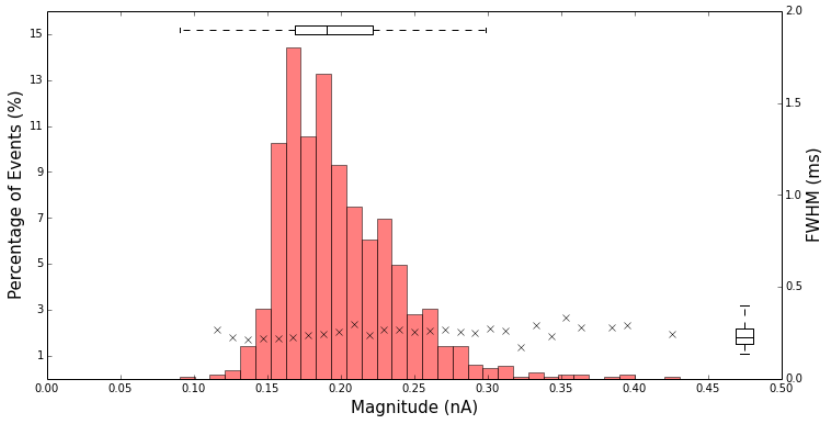

(a)

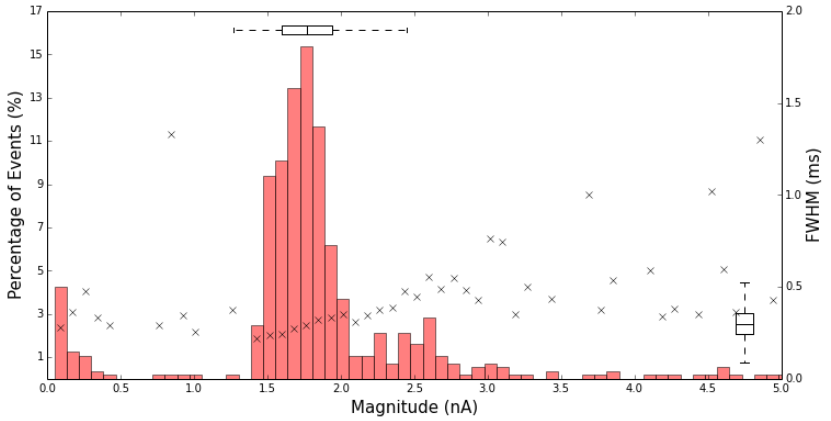

(b)

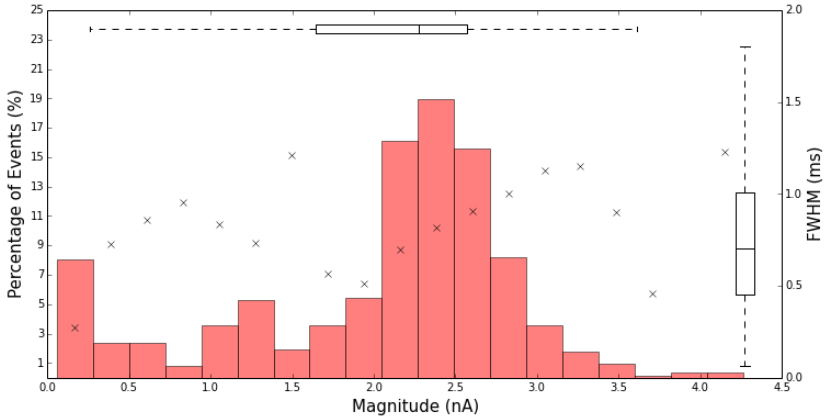

(c)

Figure 6.12: a) Population distribution of 0.4 μm calibration particle pulse magnitudes and FWHMs. b) Population distribution of 0.78 μm calibration particle pulse magnitudes and FWHMs. c) Population distribution of Au-rods pulse magnitudes and FWHMs. Note the change of horizontal axis scale between the 0.4 μm particles in a) and the larger particles in b) and c). Measurements taken at 10 Pa of applied pressure.

be due to an aggregation of particles over time (as was observed under SEM). Increased pressure also produced an expected reduction in pulse duration (Figure 6.13 b) and c)).

At all pressures in Figure 6.13 a), the IQR is particularly noteable for the rod-shaped particles as they have a more asymmetric distribution of pulse magnitudes than the spherical particles. Rod-shaped particles also exhibit a larger IQR despite the median blockade magnitude being only 40% larger than for 0.78 μm spheres at 10 Pa. Whilst this asymmetric distribution with a tail below the mean (discussed in more detail below) can be understood as evidence of non-sphericity, it could also be due to high dispersity. Also, an NP400 pore is expected to have an opening diameter of between 1 and 2 μm and hence larger particles and aggregates may simply be undetectable with this pore. The rod distributions are clearly different from spheres, but there is no clear trend pointing to non-sphericity over high dispersity.

Duration

Figure 6.13 b) shows the pulse FWHM for particles across a variety of pressures. Duration measurements are larger for the rod-shaped particles (see also Table 6.3), whereas even for spherical particles with volumes an order of magnitude different, durations did not change by more than $\pm$0.1 ms at the same pressure. Duration measurements for rods are therefore larger than would be expected for an equivalent volume sphere of the rod's vol-

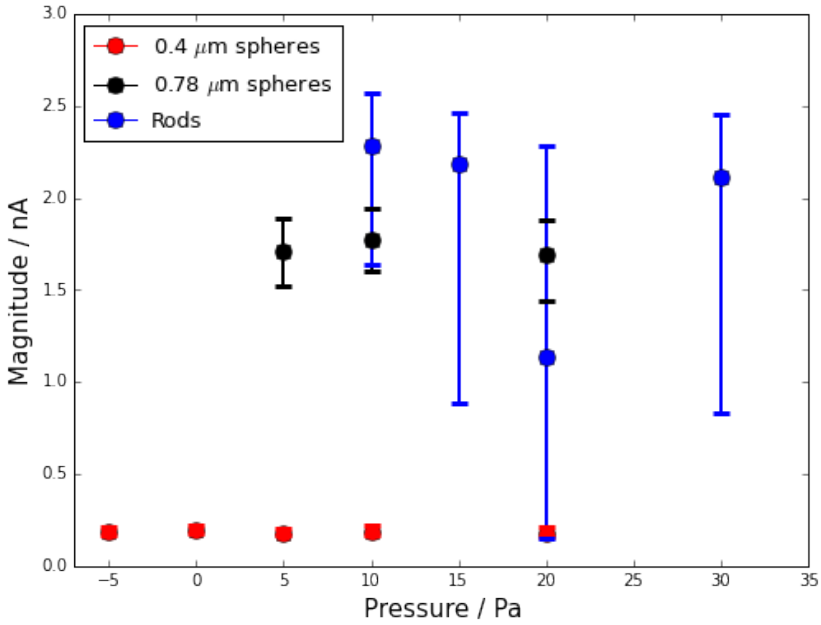

(a)

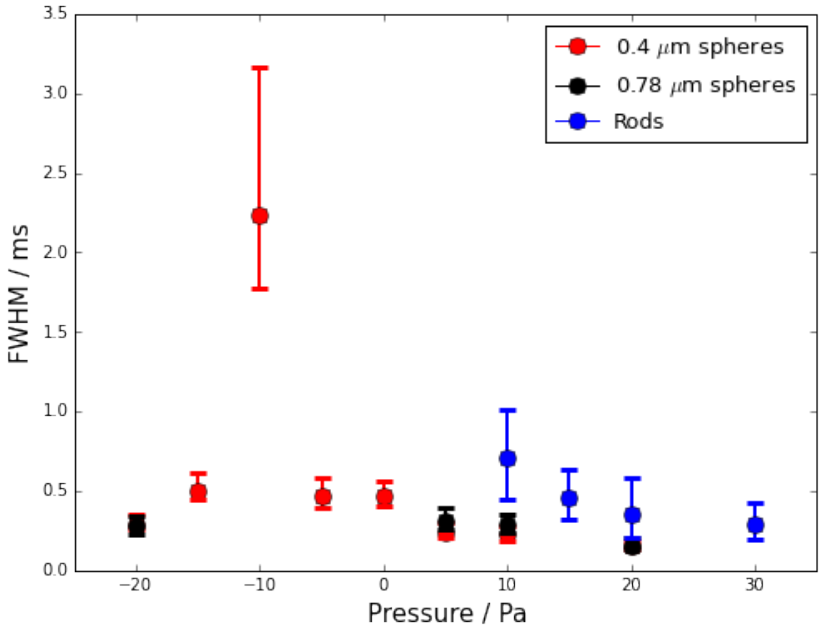

(b)

Figure 6.13: Median pulse metrics for two sets of spherical particles (0.4 and 0.78 μm spheres) and Au-rods across varying pressures. a) Magnitude b) FWHM. All datapoints represent the median of at least 500 pulses. Error bars indicate the IQR. Measurements made at 46 mm stretch in A09174 at 0.2 V.

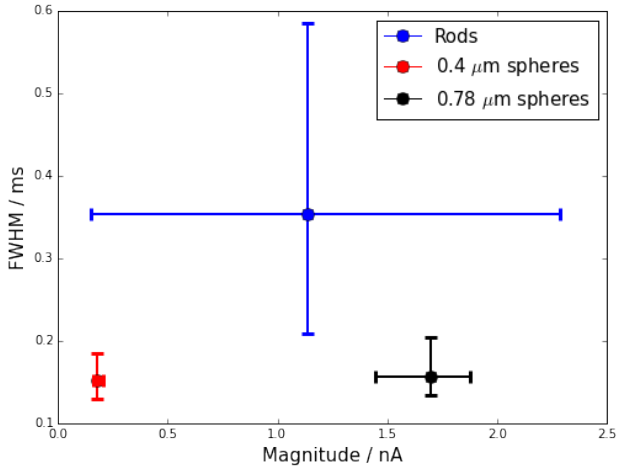

Figure 6.14: Plot indicating relationship between pulse magnitude and FWHM. All datapoints represent the median average for at least 500 pulses. Error bars indicate the IQR. Measurements made at 46 mm stretch in A09174 at 0.2 V at $P_{applied}$ = 20 Pa.

ume. At $P_{applied}$= -10 Pa, the increased FWHM duration is due to the pressure 'balance point' used to measure particle charge in Chapter 5. Figure 6.14 compares pulse magnitudes and FWHM data (a nearly identical plot is produced when performing the same comparison with FWQM data). The definition of FWHM (the width of a pulse at half magnitude) can be expected to be resistant to changes due to pulse height (and in this case particle volume) for spherical particles. However we can observe from Figure 6.14 that this is not the case for the rod-shaped particles.

Asymmetry

As shown in Figure 6.15, rods are consistently the most symmetric (i.e. have an asymmetry measurement closest to 0.5) particles across a range

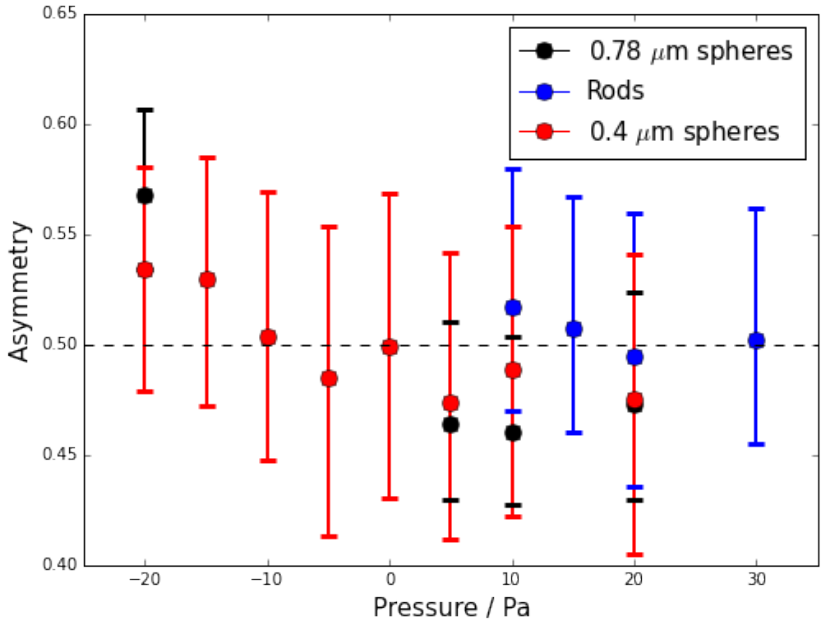

(a)

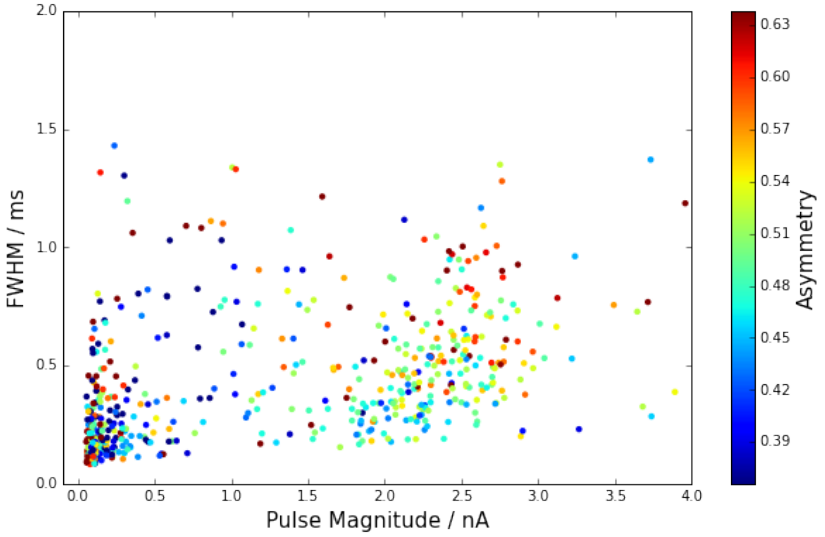

(b)

Figure 6.15: Asymmetry for 0.4 and 0.78 μm spheres and Au-rods. Data points represent the median average of at least 500 pulses. Error bars indicate the IQR. b) shows rod-shaped particles pulse magnitude and FWHM data coloured by the asymmetry measurement for each pulse. Data from measurements made at 46 mm stretch in A09174 at 0.2 V at $P_{applied}$ = 20 Pa.

of pressures with 0.78 μm particles being consistently the least symmetric (regardless of the direction of travel through the pore - see the 0.78 μm asymmetry measurement at $P_{applied}$ = -20 Pa). This pulse symmetry is consistent with pulses being generated by axially aligned rods, which is also consistent with the earlier observation that a larger proportion of smaller events are generated at higher pressures (Figure 6.13). Prolate spheroids, with their major axis axially aligned with the pore, are predicted to generate smaller magnitude pulses with longer FWHM and more asymmetry (Figure 6.3) than rods in other orientations. This postulated correlation between smaller pulse magnitudes, longer FWHMs and more symmetric pulses is not apparent for the individual pulse data shown in Figure 6.15 b) however.

Figure 6.15 documents the observed reversal in asymmetry of pulses, f_{factor}, as their direction through the pore changes at sufficient opposing pressure to counteract the inherent pressure head, for both sets of spherical particles. The asymmetry of spherical particles crosses the symmetry line at an applied pressure of -10 Pa. This corresponds with the maximum FWHM point shown in Figure 6.13 b). Spherical particles have similar median asymmetries, with 0.4 μm particles having a larger (27-29%) dimensionless range than the 0.78 μm particles (17-20%). Interestingly, asymmetry values for both particle sets are different from the asymmetries observed for the 200 nm particle examined earlier, with a median asymmetry of 0.47 for spherical particles compared to the earlier median

of 0.38 at 20 Pa. This disparity is likely due to the specific pores used and shows that asymmetry measurements are dependant on specific pore geometry. Asymmetry IQRs for 0.4 μm particles are comparable with those of the 0.32 C/m^2 200 nm particles earlier (between 27 and 30%). This is consistent with the interpretation that 200 nm 0.89 C/m^2 particles exhibit more variation in the IQRs due to the particle charge. As the calculation method for the asymmetry depends on FWHM measurements, it can be influenced by the sampling frequency when driven under high pressures. Rods and 0.78 μm particles show the smallest asymmetry IQRs of all particles studied. This suggests that pulse symmetry is either related to the pulse magnitudes, or that the rod-shaped particles are aligning with the pore and thus producing less asymmetry variation than expected for particles able to change orientation.

Gradients

Figure 6.16 a) shows median pulse gradient data across a variety of pressures. Rod-shaped particles exhibit consistently smaller absolute gradients than spherical particles at the same pressures. The smallest particles (0.4 μm) show the largest gradients, and gradients are highly dependent on pressure. Indeed, this could be used to provide an additional method for balance point determination as gradients tend towards 0.The gradient trend for rod-shaped particles suggests a higher balance point for the rods (between -6.8 and -4.3 Pa using a linear least squares fit to the positive

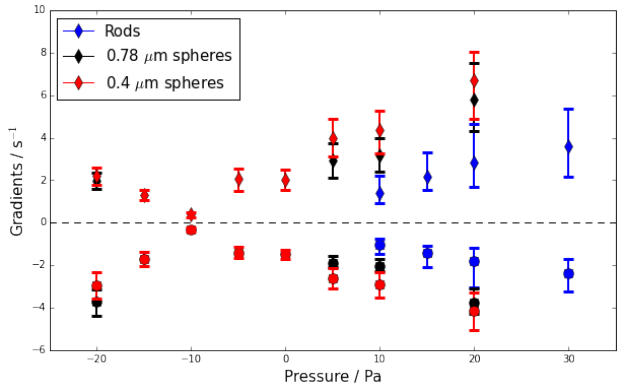

(a)

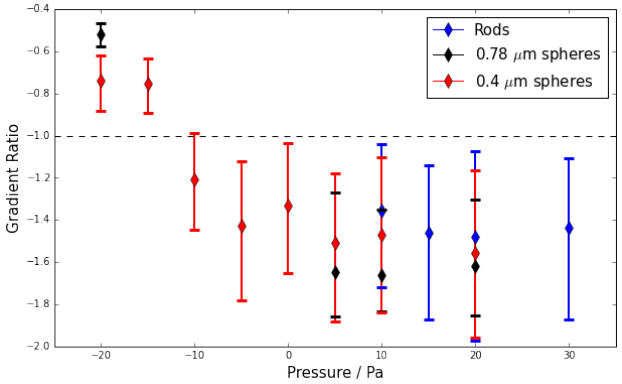

(b)

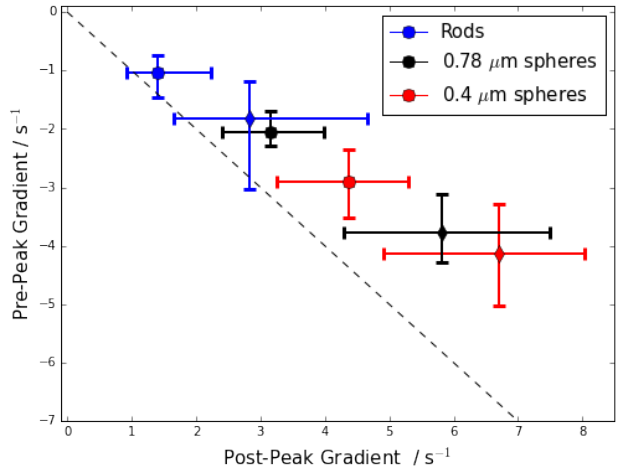

(c)

Figure 6.16: a) and b) show mean gradient data for 0.4 and 0.78 μm spheres and Au-rods. All datapoints represent the median average of at least 500 pulses. Error bars indicate the IQR. c) shows average gradient data at 10 Pa (squares) and 20 Pa (diamonds) of pressure, respectively. The black dashed line indicates a gradient ratio of -1 (i.e. a gradient-symmetric pulse about the peak).

and negative gradient data respectively) than for either of the spherical particles (-7.7 $\pm$ 0.1 Pa for the 0.78 μm particles).

It is notable that gradient measurements are so distinct between spherical particles and rods, and that IQRs do not overlap at any pressure (between 10 and 30 Pa). The lower rod gradients are consistent with earlier observations that pulses for rod-shaped particles have longer durations then those from spherical particles. A particularly interesting point is that, the median absolute gradient values for the two spherical particle sets never differ by more than 40% at the same pressure. For comparison the smallest difference between the median spherical and rod-shaped pulse gradient measurement is a decrease of 50%. This is despite the volumes of the 0.4 and 0.78 μm particles being separated by an order of magnitude.

Another notable trend is that the gradient dimensionless range for the rod-shaped particles is consistently almost double that for the spherical particles. The gradient IQRs for both spherical particles are comparable to those observed earlier for 200 nm particles, between 40 and 60% of the measured gradient. The gradient IQRs for the rods by comparison are 70-100% of the measured gradients. This is consistent with the greater ranges of pulse magnitude observed for rods above, and could be due to high dispersity or varying particle alignment.

As with the data for 200 nm spheres, the absolute post-peak gradient is consistently larger than the pre-peak gradient. For rod-shaped particles the gradient ratio is between -1.3 and -1.5, whereas for the comparable vol-

ume 0.78 μm particles the gradient ratio exhibits a consistent magnitude larger than -1.6. This difference is less clear than the individual gradient data. The trend is consistent with the asymmetry measurements above.

Large spherical particles are expected to show larger gradient ratios from the semi-analytic model, consistent to what is observed for the rod-shaped particles and 0.78 μm spheres. Figure 6.16 c) indicates the gradient ratios at 10 and 20 Pa. Specific gradient measurements are linked to the specific pore used, but comparison with calibration sets shows that different particle sets can be distinguished from each other on the basis of gradient data. Spherical particles deviate further from the symmetry line, as is expected for pulses produced by an asymmetric pore. The increased symmetry for rod-shaped particles can be accounted for by the length of particles extending beyond the pore 'sensing zone'.

Figure 6.17 examines the gradient ratio further by sorting individual pulses by pulse magnitude and pulse FWHM duration. As established above, shorter duration pulses generate larger gradients that are less symmetric and longer duration particles produce more symmetric pulses. A similar trend is observed for spherical particles (Figure 6.17 c). Figures 6.17 b) and d) however show that unlike for spherical particles, the gradient ratio of rod-shaped particles is not strongly linked to pulse magnitude. This gives an indication that particle orientation is playing a role, and that therefore the translocation of non-spherical particles is being observed.

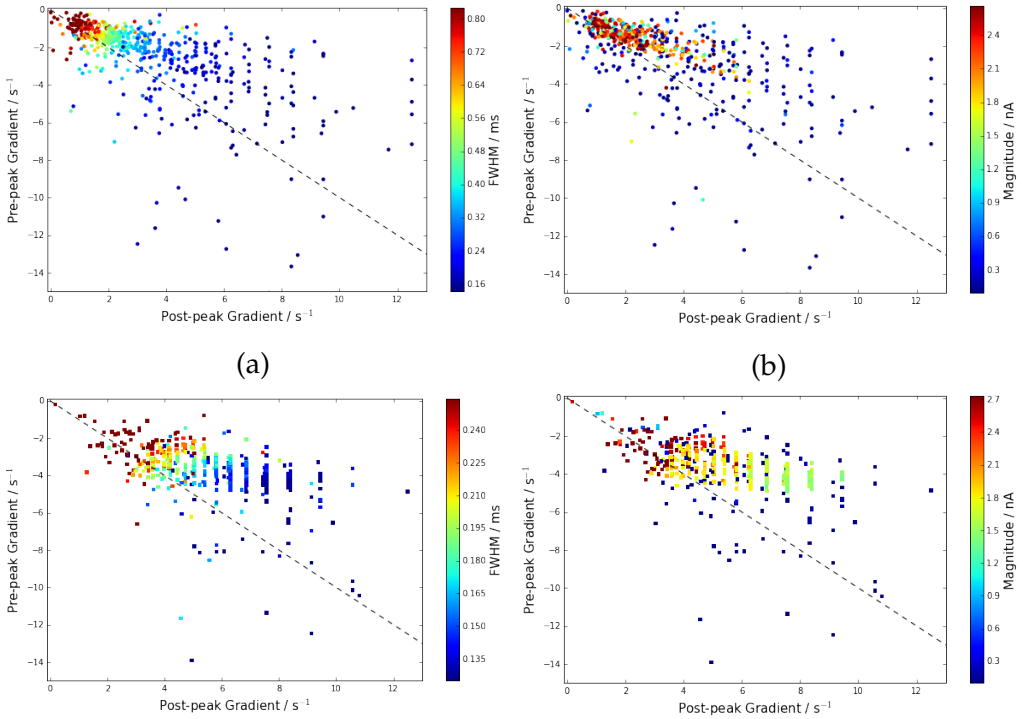

Figure 6.17: Scatter plotted data from individual Au-rod pulse gradients at 20 Pa coloured by a) FWHM duration and b) pulse magnitude. For visual clarity 3 events are not shown on these plots with pre-peak gradients between -15 and -20 s^{-1}. c) and d) display the same data for 0.78 μm spheres.

6.7 Conclusion

We have investigated whether TRPS measurements can differentiate between spheres and rods. Literature and the semi-analytic model suggest that pulse symmetry may indicate different particle shapes. However variation in pulse shape due to other factors, most notably pore geometry, must first be considered. To this end we measured the variation in pulse metrics using a well-characterised NP200 pore and spherical calibration particles. We find that for monodisperse, charged particles the IQR of pulse magnitudes is seldom over 20%. To quantitatively measure difference in pulse shape we define and use pulse metrics of pre- and post-peak gradients. Futhermore we observed that the ratio of these gradients (post-peak/pre-peak) appears linked to particle surface charge.

We have compared PEGylated gold nanorods and spherical calibration particles in an NP400 pore. We compare SEM images of the Au-rods with TRPS volume measurements and note that rod TRPS magnitudes are larger than expected from their SEM dimensions. We obtain size distributions for both rod and spherical particles at a range of pressures and note that rod-shaped particles consistently exhibit an IQR almost double that of the spherical particles (which remains approximately 20%). We have observed that pulse durations for rods are longer than those of spherical particles, despite the pulses sharing similar magnitudes. We have also observed that pulses generated by rod-shaped particles have a gradient ratio closer to 1 and have f_{factor} values closer to 0.5 than those from spherical

particles. Finally we noted that gradients for pulses from both rods and spherical particles are more closely linked to pulse duration than pulse magnitude. Whilst these metrics show promise for differentiating particle on the basis of pulse shape, these characteristics may also be a consequence of the high dispersity of the rods. Gold nanorods presented a challenging TRPS measurement due to their high dispersity, with pulse magnitudes and FWHM showing high levels of variation. However consistently low gradient data when compared to spherical calibration particles suggests that pulse gradient and asymmetry measurements may show promise for shape detection in highly disperse samples.

Chapter 7

TRPS of Complex Systems

7.1 Introduction

Many micro- and nanoparticle samples are obtained in non-ideal conditions for measurement. For example, they can be highly polydisperse, contained in a complex solution of a variety of particles and proteins (e.g. urine or blood), or in growth media. TRPS has been used to study a variety of particle types including exosomes, liposomes, membrane vesicles, viruses and bacteria [64], discussed previously in Chapter 2. However, many of these studies focus only on the well-characterised ability of TRPS to size large numbers of nanoparticles, due to the volume relationship between nanoparticle and pore volume and resistive pulse blockade magnitude as has been discussed previously in this thesis.

In this Chapter we selected and measured three samples containing interesting particle types that have yet to be studied using TRPS: whole

Rattus rattus red blood, a diluted solution of rod-shaped *Shewanella marintestina* bacteria and bacterially-produced polyhydroxyalkanoate (BPHA) particles commercially sold under the 'Polybatics' brand. These experiments investigate the utility of the shape metrics introduced and discussed in Chapter 6 in non-ideal samples, and examine the ability of the qNano to provide accurate measurements on complex samples.

Particles studied previously in Chapter 5 and Chapter 6 are comparatively simple in that the solution simply contains the particles to be measured, dispersed in an electrolyte. This allows tight control of parameters such as concentration and conductivity to achieve optimal TRPS resolution. The 'complex systems' examined in this Chapter contain either highly disperse particles, or multiple populations of particles across a wide range of sizes, and are often suspended in complex media that may contain aggregates, cellular debris and other potentially confounding factors.

Each sample was selected to test the ability of TRPS to yield quantitative measurements for a specific non-ideal condition, with a minimum of sample processing. Mammalian blood represents a well studied, yet highly complex medium including cells of a variety of sizes, from $\sim$10 μm leukocytes to protein aggregates, as well as exosomes and cell debris with diameters $\leq$100 nm [120]. The most common particulate constituents of *Rattus* whole blood are disc-shaped erythrocytes (red blood cells) [121]. *Shewanella* bacteria are rod-shaped, similar in dimension to the gold nanorods studied in Chapter 6. However, as they were not fixed prior

to measurement (as is typical when examining bacteria) this sample also represents a dynamic, non-spherical particle set. Finally spherical BPHA particles sold as Polybind-Z particles (Polybatics, Palmerston North) as potential drug delivery vectors were measured as they are thought to be highly disperse with an estimated particle size range of between 300 and 700 nm. The relative proportions of particle sizes within this range are not well known. In addition, the composition of all three complex particle sets is markedly different to both the carboxylate polystyrene particles commonly used for TRPS calibration experiments, and to the Au-nanorods studied earlier in Chapter 6. In this Chapter we compare all three samples described against spherical calibration particles and summarise the results of both TRPS ensemble and individual pulse analyses to assess the suitability of qNano TRPS for similar future work.

7.2 *Rattus rattus* Blood

Rat (*Rattus Rattus*) blood and its constituents have been extensively studied and characterised due to its common use across a variety of medical fields and its similarity to human blood. In particular, rat erythrocytes are only slightly smaller (to 6.5-7.5 x 1-2 μm concave discs) than human erythrocytes (8 x 1.8 μm concave discs [123]) whilst rat blood is a far safer, and more readily accessible medium in which to experiment. Note that the 6.5 μm diameter measurement for *Rattus* RBCs given in [121] is presented without any uncertainty, and other literature values range up to

Table 7.1: Reference values for (*Rattus rattus*) blood components. The packed volume of RBCs is 37.6 - 50.6%.

Cell Type	Concentration [121]	Dimensions
Red Blood Cells (RBC)	6.76 - 9.75 x $10^6/mm^3$	6.5 μm diameter,
White Blood Cells	6.6 - 12.6 x $10^3/mm^3$	12 μm diameter
Neutrophils	1.77 - 3.38 x $10^3/mm^3$	–
Lymphocytes	4.78 - 9.12 x $10^3/mm^3$	–
Eosinophils	0.03 - 0.08 x $10^3/mm^3$	–
Monocytes	0.01 - 0.04 x $10^3/mm^3$	–
Basophils	0.00 - 0.03 x $10^3/mm^3$	–
Platelets	150 - 460 x $10^6/mm^3$	$\sim$4 fL [120] or $\sim$2 μm diameter [122]

7.5 μm [123]. Whilst erythrocytes are routinely sized and counted in Coulter counters, we use TRPS to test the hypothesis that additional characterisation information is available from TRPS on RBCs, even in highly concentrated, complex, non-purified systems such as whole blood. The nominal concentration and dimensions of whole *Rattus* blood constituents are included in Table 7.1.

In this section we first use TRPS to analyse dilute whole *Rattus* blood, using an NP1000 pore, through several stages of centrifugal separation in order to isolate and measure separate blood constituents. Subsequently we examine the disc-shaped RBCs specifically to test if the metrics defined in the previous Chapter to study particle shape are able to detect the non-sphericity of these particles. We compare in detail representative pulses from RBCs and calibration particles using NP1000, NP400 and NP200 pores to further examine particle shape.

7.2.1 TRPS Measurements of Whole Blood

Rattus blood was provided by Trinity Bioactives (Lower Hutt) on the day of extraction from source in solution with the anticoagulant, EDTA (Ethylenediaminetetraacetic acid). Blood samples were either sampled immediately or rapidly refrigerated to prevent further degeneration or coagulation. Samples containing different particulate components of whole rat blood were then prepared as described in Table 7.2. Measurements were carried out in both the raw samples and after all subsequent purification steps, to analyse the components and to determine the degree of processing necessary in order to generate meaningful results.

Table 7.2: Type and isolation method of (*Rattus rattus*) blood particulates from whole blood

Sample	Name	Purification method	Contents
E2	Whole Blood	–	Whole Blood
E3	Diluted Whole Blood	–	E2 and PBS (1:1)
E4	(intermediate)	centrifuged at 200g for 20 min	E2
E5	Red Blood Cells	–	~125 μL E4 pellet in 1 mL PBS
E6	White Blood Cells	–	~250 μL E4 central layer in 1 mL PBS
E7	(intermediate)	centrifuged at 200g for 15 min	E4 supernatant
E8	(intermediate)	centrifuged at 800g for 20 min	E7 supernatant
E9	Plasma	–	E8 supernatant in 1 mL PBS
E10	Platelets	–	E8 pellet in 1 mL PBS

For all dilutions, fresh PBS was used as the diluent. Samples were analysed using 3 pores of differing radii: A17635, A09174 and A11486 (NP1000, NP400 and NP200 respectively) to ensure detection bias did not skew the collected data through omission or under-sampling of small events. All pores were calibrated using particles of known geometry.

Figure 7.1 a) shows data from TRPS for 2.8 μm calibration spherical

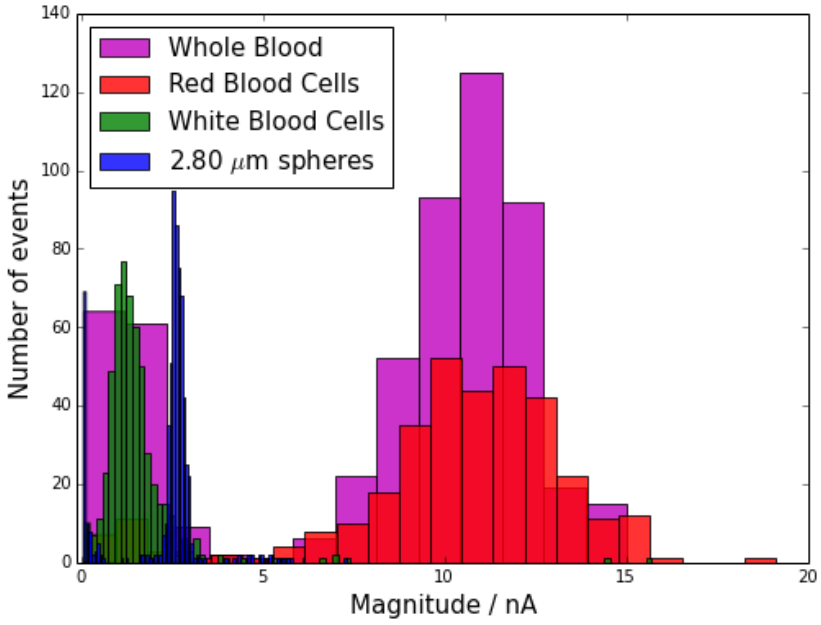

(a)

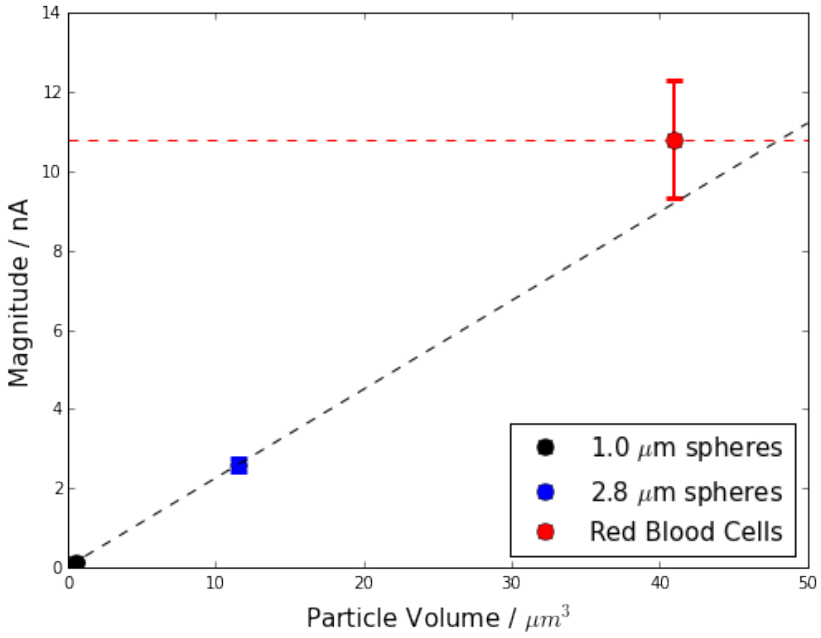

(b)

Figure 7.1: a) Pulse magnitude distributions for 2.8 μm calibration particles and rat whole blood constituents separated by centrifugation. b) Comparing nominal particle volume with median magnitude measurements for calibration particles and RBCs. Error bars indicate the IQR of the sample. The dashed black line indicates a linear fit to the calibration particles that would be used to calculate the radius of the RBCs sample if they were spherical. The intersection between the red and black dashed lines indicates the volume for a sphere producing the median pulse magnitude. Measurements were made at a pore stretch of 44mm using A17636 at 0.15V.

carboxylate polystyrene particles (Invitrogen) and *Rattus* blood after centrifugal purification to isolate named components, using an NP1000 pore. TRPS is able to differentiate between calibration particles and blood constituent particles, particularly for the RBC and whole blood samples. As centrifugation rather than filtration was used to separate RBCs from whole blood, a degree of shared constituent components is expected between samples. Complete white blood cells are not expected to be detectable in a pore of this size as their diameter ($\sim$10 μm) is significantly larger than the small pore opening [121]. The relative proportions of events show the large proportion of red-blood cell sized particles with pulse magnitudes between 5 and 17 nA, and their increased dispersity compared to the calibration particles peak at $\sim$2.5 nA. The reduction of the number of RBCs in the white blood cell sample, due to the centrifugation filtration process, increased the fraction of smaller events with magnitudes less than 2.5 nA. Experiments were repeated at a higher stretch and lower voltage to minimise the impact of the addition of small particles, indicated in Figure 7.2 b).

Both experiments in Figure 7.2 show a predominance of erythrocyte-sized cells in both the whole blood and re-suspended RBC samples, demonstrating a broad range of particle magnitudes. Of additional note are the populations of events with magnitudes below 1.5 nA that are broadly consistent across the RBCs, whole blood and white blood cells samples (illustrated in more detail below). These data are inconsistent with the expected

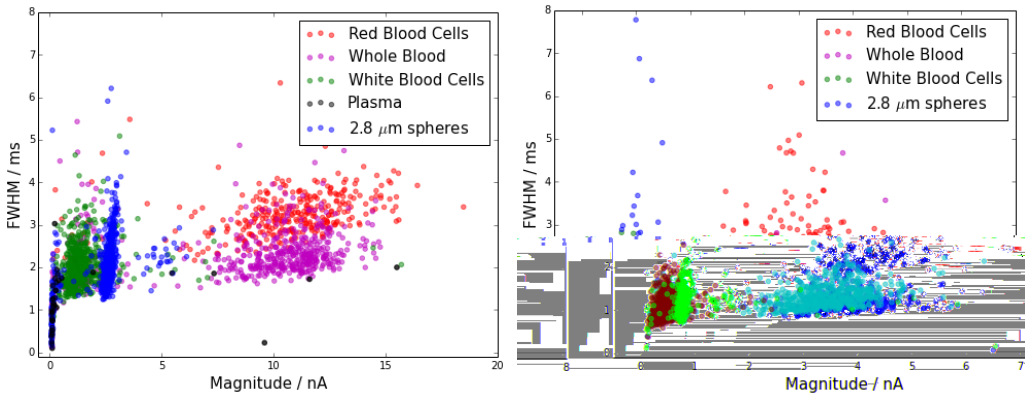

(a) (b)

Figure 7.2: Scatter plot of FWHM and pulse magnitude data from calibration particles and whole rat blood constituents. a) displays data obtained at a pore stretch of 44mm in A17636 at 0.15V. b) displays data obtained at a pore stretch of 46mm in A17636 at 0.05V.

TRPS signals from leukocytes (which typically have diameters on the order of 10 μm) and are likely coagulated cellular debris, plasma proteins, exosomes or micro vesicles.

The RBC sample exhibits a median pulse magnitude 4.15 times larger than that of the 2.8 μm calibration particles, compared with a 3.57 times increase in volume calculated from literature values, indicated in Figure 7.1 b). Median pulse magnitudes from the whole blood and RBC samples are of a volume consistent with the literature value of *Rattus* RBCs of 41 μm^3 (equivalent to a magnitude of 9.2 nA, Figure 7.1 b)) [123]. The measured median for RBCs, equivalent to a volume of 48.11 μm^3, is within 17% of this value. However, literature values are often presented with no uncertainties and so it is unclear how precise this value is expected to be. For comparison, one can find literature quoted values for the diameter of rat

erythrocytes from 6.3-7.5 μm^3, depending on the technique used for measurement [121, 123]. This would be equivalent to an uncertainty of 40% in the final calculated volume figure, placing our measurement well within experimental uncertainty.

The dimensionless range of pulse magnitudes for RBCs is also more than double that of the 2.8 μm calibration particles. This increase in range is indicative of either high dispersity or varying orientations of disc-shaped particles, an issue further investigated in Section 7.2.2. However the range is approximately equivalent (within 8%) to all the values reported for spherical particles in Chapter 6 and markedly lower (>13% less) than the values for rod-shaped particles. 2.8 μm calibration particle events with magnitudes below 1.5 nA were unexpected and may represent degradation or contamination of the calibration particles.

In summary, TRPS is able to differentiate between RBCs and non-RBC components of whole rat blood with a minimum of purification steps. If RBCs are removed as the dominant species using centrifugation, TRPS is able to detect additional populations of smaller particles that warrant further investigations in smaller pores (as presented in the following sections).

7.2.2 Shape Measurements for Red Blood Cells

This section examines specifically the RBC particle set shown in Figure 7.1, in particular evaluating the ability of TRPS to determine their shape dif-

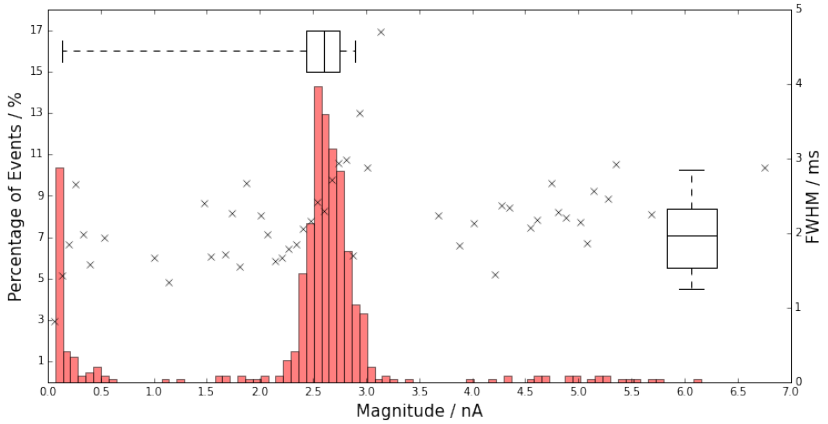

(a)

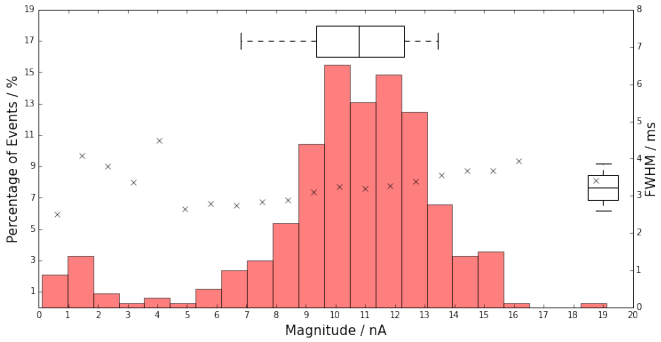

(b)

Figure 7.3: Summary histograms of ensemble magnitude and FWHM pulse data for 2.8 μm spherical calibration particles *a)* and the purified red blood cell particles *b)*. Each bin of the magnitude histograms is overlaid with an 'x' indicating the mean FWHM of pulses from that bin. Box and whisker plots are included to convey a measure of the dispersity of the sample. The box represents the median, upper and lower quartiles. The whiskers displayed represent the 10 and 90% quartiles respectively.

ference from spherical particles. The purification of the RBC sample will minimise the impact of both cells too large to fit through the pore, and the number of smaller events due to exosomes or other <500 nm particles present in the system (these are examined in more detail in Section 7.2.5). The nominal volumes for 2.8 μm diameter particles and RBCs are 11.49 μm^3 and 41 μm^3 [123] respectively. Metric data are presented in Table 7.3.

Table 7.3: Metric summary data for calibration particles and RBC samples. IQR indicates the metric interquartile range. Range indicates the dimensionless range defined in Chapter 6.

Particle Type	Magnitude (nA)			FWHM (ms)			FWQM (ms)		
	Median	IQR	Range	Median	IQR	Range	Median	IQR	Range
1.0 μm spheres	0.144	0.031	22%	1.314	0.674	51%	2.306	1.435	62%
2.8 μm spheres	2.598	0.313	12%	1.965	0.794	40%	3.272	1.255	38%
RBC	10.79	2.984	28%	3.21	0.673	21%	5.226	1.031	20%
	Asymmetry			Post-peak Gradient (nA s^{-1})			Pre-peak Gradient (nA s^{-1})		
	Median	IQR	Range	Median	IQR	Range	Median	IQR	Range
1.0 μm spheres	0.344	0.166	48%	1.081	0.587	54%	-0.447	0.28	-63%
2.8 μm spheres	0.291	0.066	23%	0.837	0.427	51%	-0.322	0.116	-36%
RBC	0.334	0.034	10%	0.475	0.128	27%	-0.209	0.037	-18%

Figure 7.3 shows summary histograms for 2.8 μm calibration particles and RBC pulses, expanding on the same data used in Figure 7.1. The RBC sample demonstrated a broad distribution of pulse magnitudes. Interestingly, the samples show markedly different relationships between pulse magnitude and FWHM. Spherical particles show a strong positive relationship (a gradient of approximately 0.9 ms/nA) between magnitude and FWHM for bins between 2.0 and 3.0 nA. For the RBC sample, the correlation between magnitude and FWHM is much weaker ($\sim$0.1 ms/nA) but still positive and over a much larger region (5 to 16 nA). Addition-

ally, whilst ranges for both FWHM and FWQM measurements for spherical particles are consistent with those observed in previous Chapters, the duration range measurements for RBCs is lower (a dimensionless IQR of $\sim$20%) than for all previously measured particles. This is despite the median FWHM being 66% higher for RBCs than for 2.8 μm particles.

The semi-analytic model (see Section 7.2.3, below) suggests that a larger range of pulse magnitudes and durations are to be expected for non-spherical particles because of the different possible rotated configurations of the particles as they traverse the pore. Specifically, if we model RBCs as 7.5 μm diameter, 1.4 μm wide oblate ellipsoids, simulations suggest 40% smaller pulse magnitudes with 71% longer FWHM would be observed if they traverse the pore with their shortest axis perpendicular to the pore axis (compared with an axially aligned spheroid). These predictions are consistent with the observed magnitude and magnitude range data. However, the observed median FWHM and FWQM duration for RBCs are lower that what would be expected for a spherical particle of the same volume.

Pulse Symmetry

Figures 7.4 a) and b) display the FWHM and asymmetry data (see Chapter 6) for spherical calibration particles and RBCs. All asymmetry measurements for all particle sets are similar, and within the IQR of each other. Notably, as with FWHM however, the RBC dimensionless range for asymmetry is less than 50% of that observed for spherical particles. Whilst the

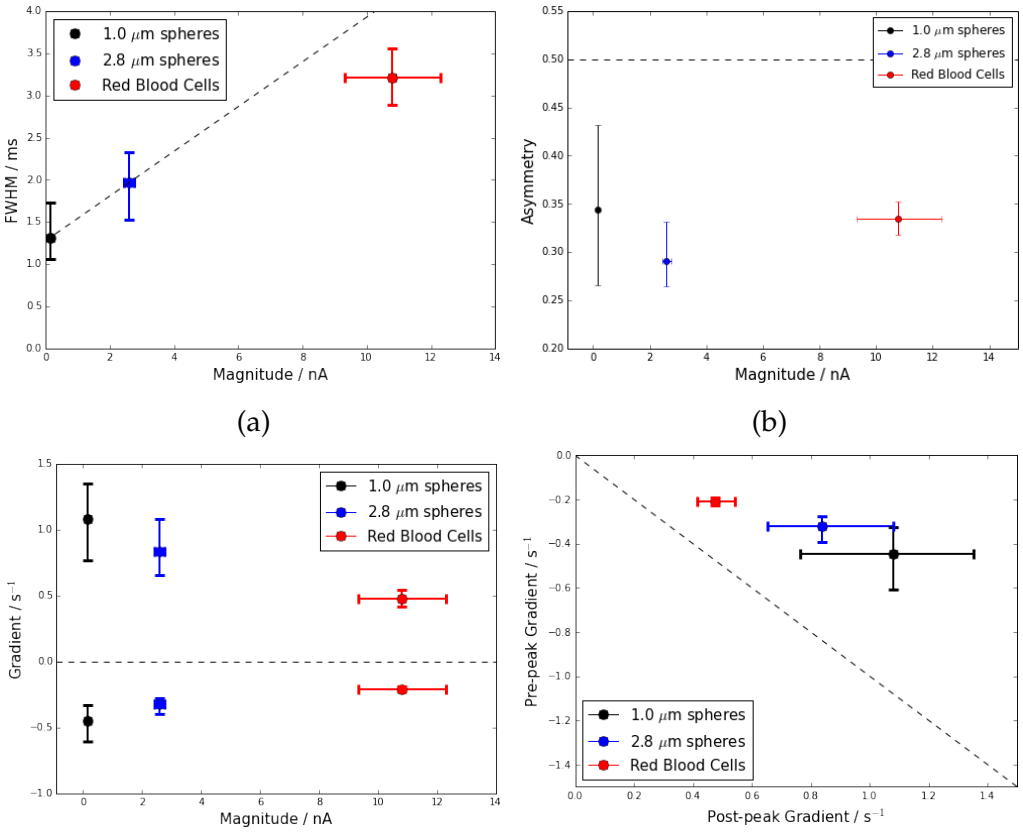

Figure 7.4: Comparative metrics (see Chapter 6) for the purified RBC sample and the spherical calibration particles. Error bars indicate the IQR for each data collection run. a) FWHM, b) asymmetry, c) gradients, d) gradient ratios.

asymmetry range for the 2.8 μm particles is comparable to what has been observed previously for spherical particles (see Table 6.3), the range for 1.0 μm spheres is larger than expected. This is likely due to the small particle size relative to the NP1000 pore used which has a lower limit of detection of $\sim$400 nm (shown and discussed in more detail in the following section, 7.2.3). It should be noted that whilst the axial aspect ratio for RBCs is between 5-6:1 which is similar to that for the Au-rods ($\sim$5:1), the former is similar to an oblate particle and the latter to a prolate particle. The pulse magnitude and FWHM effects of rotation (in pure volumetric terms) are then expected to be larger for the RBCs than for the rods (Figure 6.3).

Figures 7.4 c) and d) show data comparing the gradient and gradient ratio for RBCs and calibration particles. As with earlier observations, gradients are lower for the largest magnitude pulses, in this case the RBCs. Lower gradients overall are also consistent with non-spherical particle observations (see the rod-shaped particles section (6.6.2) in Chapter 6). RBCs still display a significant difference between gradients, unlike the earlier rods (Figure 7.4 d)). However the gradient ratio is consistently closer to 1 than for either of the spherical samples. The range of the gradient measurements is also lower for the RBC particles than for either of the two spherical samples. Again this range is only $\sim$50% of the expected range for spherical particles of this volume.

It is unclear whether the systematically lower gradients and gradient ratio measurements for non-spherical particles are indicative of par-

ticle shape or simply due to the relative size of the particles. Of the non-spherical particles measured thus far, RBCs have also exhibited the largest blockade magnitude events compared to their respective calibration particles. As gradients are normalised by their respective blockade magnitudes, pulses with markedly larger blockade magnitudes than the comparison spherical particles (as we have with RBCs here) may exhibit low apparent gradients. This will be further discussed in Section 7.3 below.

To summarise, the higher pulse magnitude range and the lower gradients and gradient ratios exhibited by RBCs in comparison with spherical particles are possible indicators of non-sphericity. The low FWHM, FWQM and their respective ranges and gradient range are unexpected for either spherical and non-spherical particles. Asymmetry measurements are insufficiently different to differentiate RBCs from calibration particles. As such, whilst we can assert with certainty that RBCs are larger than their calibration particles and that their size is approximately consistent with literature, we are unable to make definite conclusions regarding shape based on these TRPS data.

7.2.3 Individual Pulse Comparison

Ensemble data, whilst being the traditional way of understanding distributions of particles, can miss important information from individual pulses in the pursuit of broader trends. In this section we extract individual pulse data from each run and compare them between runs and particle

sets (Figure 7.5). The median magnitude blockade pulse for each experiment is used for this comparison (except where noted) as these pulses are expected to be representative of the most common pulses observed during a single TRPS measurement. All individual pulse comparisons however, will be prone to small sample biases. We guard against this by also including events at the upper and lower quartile magnitude in comparisons. In addition we also normalise events by their blockade magnitude in order to enable comparison of pulse shape alone. Finally, all pulses are compared visually against other pulses from the same run to ensure they are qualitatively similar (i.e. they do not include multiple pulse peaks or other unexpected behaviour).

Figure 7.5 a) indicates the magnitude disparity between the calibration particles and RBCs. The blockade normalised version in Figure 7.5 b) however demonstrates that normalisation does not appear to invalidate gradient comparisons, as the spherical particle trace clearly demonstrates higher pre- and post-peak gradients, even when normalised. Furthermore spherical particle pulses (Figure 7.5 c) and d)) have consistently larger gradients than comparable events from the RBC sample (Figure 7.5 e) and f)). Interestingly, the variation apparent between IQR events in f), which is unexpected given the gradient range data in Table 7.3, suggests that the high variation in spherical particle events is simply because the gradients are larger. Large gradients calculated using FWHM and FWQM data have much higher uncertainty than corresponding lower gradients exhibited by

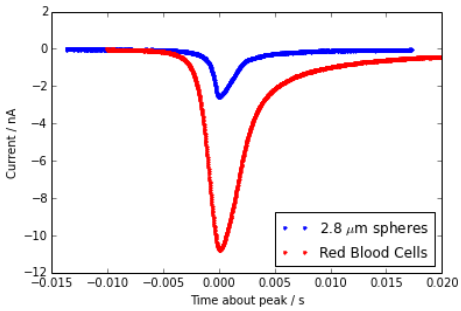

(a) Median blockade magnitude pulses for RBCs and calibration particles.

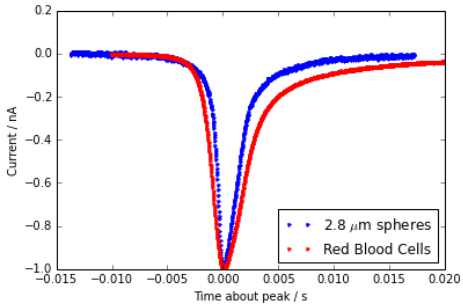

(b) Median pulses normalised by blockade magnitude.

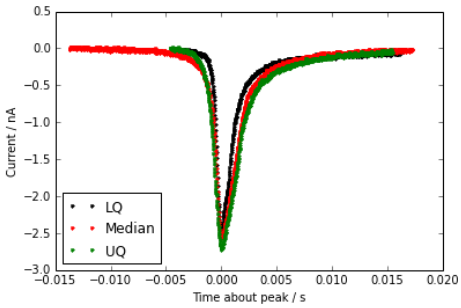

(c) 2.8 μm spheres.

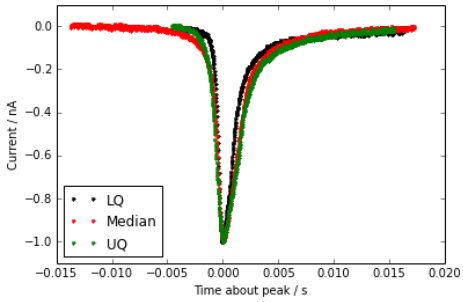

(d) 2.8 μm spheres, normalised by blockade magnitude.

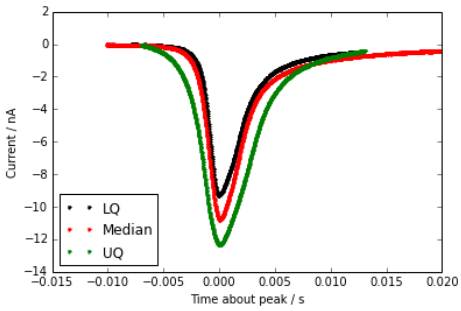

(e) Characteristic RBC pulses from upper quartile, median and lower quartile.

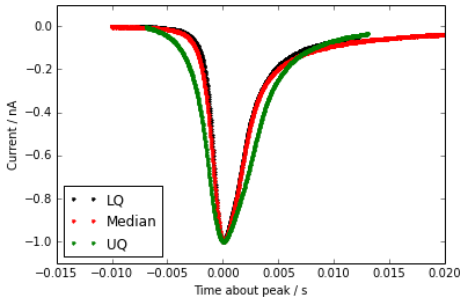

(f) Characteristic RBC pulses from upper quartile, median and lower quartile, normalised by blockade magnitude

Figure 7.5: Selected events for RBCs and calibration spheres with a), c) and e) displaying raw data and b), d) and f) displaying data normalised by blockade magnitude. Pulses are aligned by shifting the current minimum to time = 0. UQ, median and LQ represent the upper quartile, median and lower quartile events by pulse magnitude, except where otherwise noted.

the RBCs, for the reason that if FWHMs or FWQMs are smaller, then the normalised gradients must be correspondingly larger. As such, gradient range should not be taken as a good indicator of particle shape.

Of particular note in the pulse traces presented in Figure 7.5 is the increased FWHM for larger events. This is contrary to what the semi-analytic model predicts for rotated oblate spheroids passing through the pore (Section 7.2.4), where spheroids with long axis perpendicular to the pore axis are expected to produce relatively high magnitude, short duration events. This is most likely due to some dispersity in the volume of the particles, but also strongly suggests that little (if any) rotation of the particles occurs during translocation.

The most important result from this comparison however is that pulse shape is largely conserved over the magnitude IQR for these particles. Therefore the use of approximation metrics, such as asymmetry and gradient, appears to be a valid method for comparing populations of pulse shapes. It is not clear that this will generally be true, unless a similar comparison is be performed for each unique pore and particle set.

7.2.4 Comparison to Semi-analytic Model

We are able to use the semi-analytic model (Chapter 3) to predict the pulse for an oblate spheroid passing through a pore with the dimensions of A17636. An oblate spheroid model will provide an upper bound on the changes observed however, as modelling the cells as oblate spheroids ne-

glects the concavity of the erythrocytes and this will overestimate their volume. The results presented in Figure 7.6 show reasonable agreement with pulse magnitude but poor prediction of realistic FWHM, gradients or asymmetries. Interestingly, while this is commonly attributed to errors in the pore geometry, experimentation within the restrictions of the model suggest that the discrepancies observed in the FWHM measurements (and indeed in ANY of the metrics other than pulse magnitude) cannot be fully explained by geometric factors alone. Variations in model geometric input parameters are unable to unify theory and experiments suggesting that the disparity is due to an oversimplification in the model assumptions.

The ability of a particle to rotate can also alter the model prediction of the pulse shape. Table 7.4 shows the predicted values for the metrics of magnitude, FWHM and pulse asymmetry for a rotated oblate spheroid with the dimensions and volume of a RBC. The non-rotated particle yields the closest measurement to experiment when examining only blockade magnitudes. As shown in both Figure 7.6 and Table 7.4, the semi-analytic model systematically underestimates pulse FWHM and overestimates pulse asymmetry. The most significant result here is the discrepancy between the semi-analytic model and observed events for both spherical and non-spherical particles. This is clearly a direction for further refinement of the model. In particular the symmetry of the pulses is most likely related to the specific geometry of the pore used (see Section 6.4). In its current form the semi-analytic model is insufficiently accurate to be able

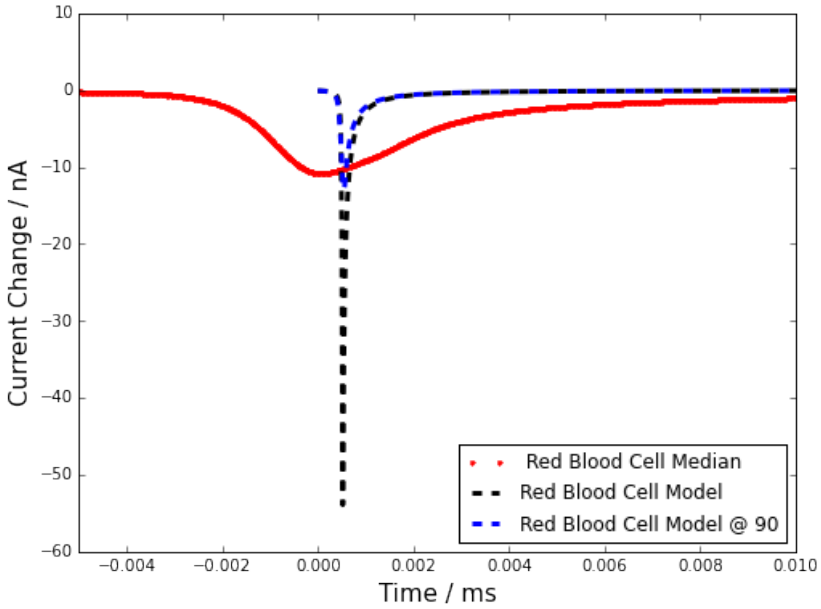

(a)

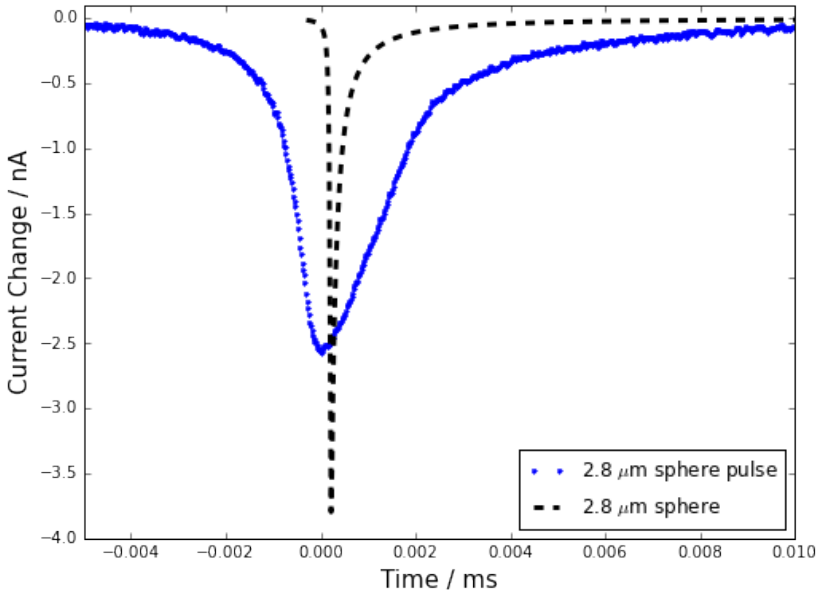

(b)

Figure 7.6: a) compares an event for a RBC modelled as an oblate spheroid (- -) with r_{xy} = 3.75 μm and r_z = 0.7 μm with trace data (red). The oblate spheroid is rotated through 90° to the pore axis. b) shows the same but for a spherical particle (blue).

to predict whether a given particle will be detectably non-spherical or not. However the model does reinforce the general trend of increased FWHM, lower magnitude and increased asymmetry.

Table 7.4: Predicted pulse magnitudes, FWHM and asymmetry for a oblate spheroid of the dimensions of an RBC at a variety of rotations about and axis perpendicular to the central pore axis.

Model Rotation	Magnitude (nA)	FWHM (ms)	Asymmetry
Experiment	10.79	3.21	0.334
0°	8.9	0.100	0.200
45°	5.51	0.140	0.286
90°	5.21	0.160	0.250

7.2.5 NP400 and NP200 Pore Measurements

Samples were also examined with pores A09174 (NP400) and A11486 (NP200) to assess particle size distribution upon screening of the larger samples, and to act as a control for the RBCs. Figure 7.7 presents the results of TRPS of calibration particles, RBC, plasma and platelet samples using the NP400 pore. Data show several separate particle populations, consistent with what is expected as a consequence of the centrifugal separation.

Figure 7.8 shows more detailed data for 0.4 μm spheres and the platelet sample. Calibration 0.4 μm spherical particles in Figure 7.8 a) show a clear peak of pulses at $\sim$1.0 nA. Figure 7.8 b) indicates a clear population of particles well below 400 nm in size (i.e. below 0.25 nA). These were common to all of the blood samples presented in Figure 7.7 suggesting that the filtration methodology used in separation was insufficient to screen them

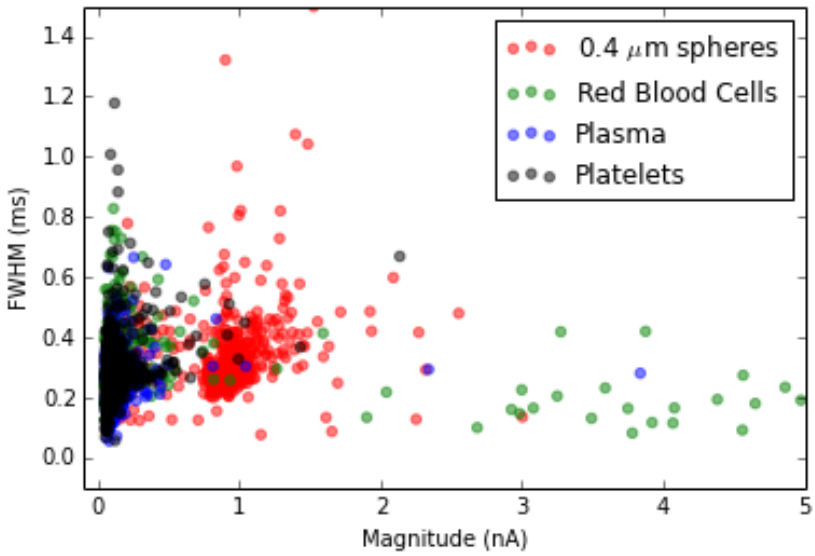

Figure 7.7: Summary data for NP400 TRPS of purified blood samples. Scatter plot of pulse magnitude and FWHM.

completely. These are assumed to be cellular debris as all these events are too small in magnitude to represent RBCs. It is likely that these particles extend below the minimum size detectable using this NP400 pore.

Data comparing metrics for NP400 data is summarised in Table 7.5. For RBC and platelet samples, median pulse magnitude and FWHM measurements and ranges indicate highly disperse populations of particles as they have the highest magnitude range of any particles measured in this Chapter. By contrast, 0.4 μm spheres show ranges for all metrics comparable to all spheres documented earlier. All particles show similar, very low levels of asymmetry (all are within 2% of the symmetric 0.5 value). The 0.4 μm particles produce the least symmetric pulses, both in terms of the asymmetry metric and the gradient ratio (-1.38 for the spheres compared

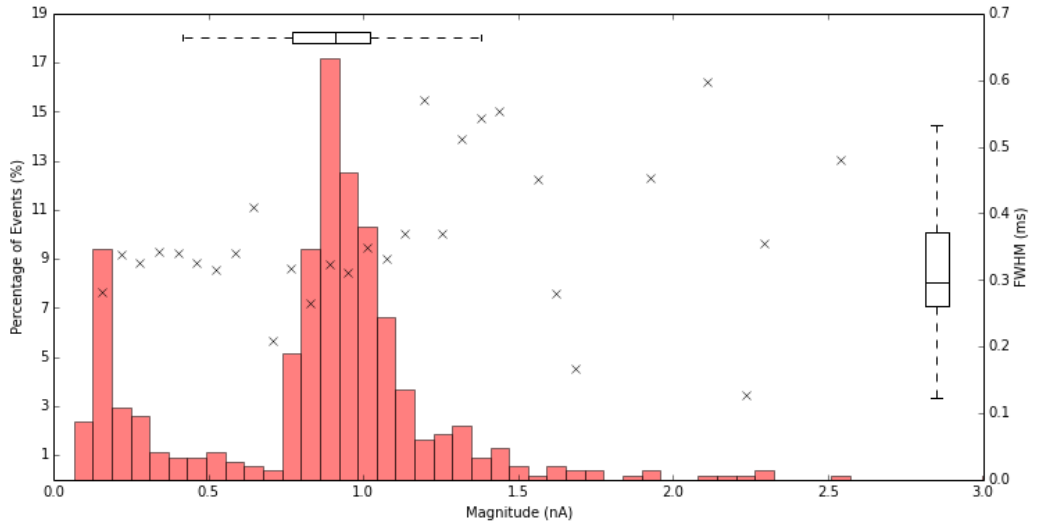

(a)

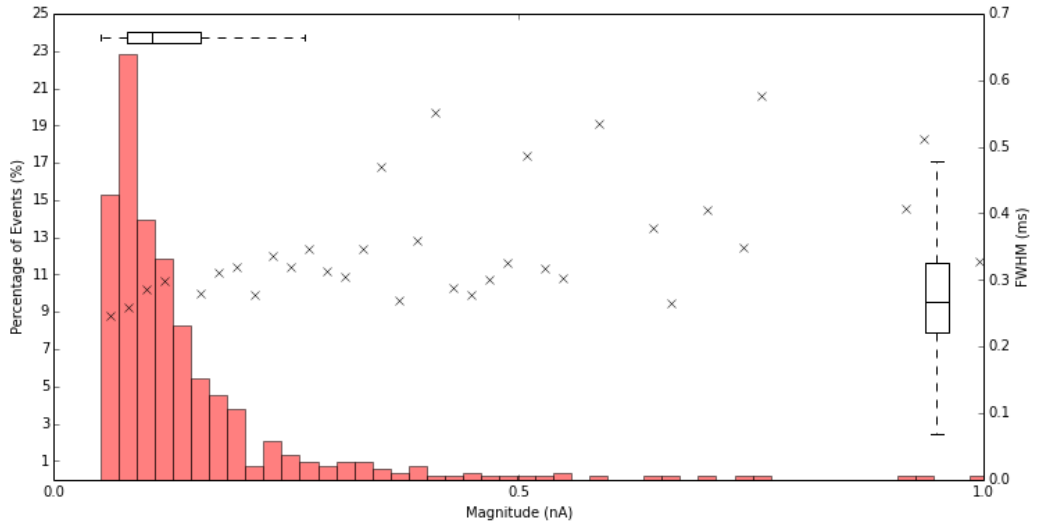

(b)

Figure 7.8: Summary histograms of data from the NP400 pore. a) shows data from NIST400 spherical calibration particles. b) displays pulses from the platelet sample.

Table 7.5: Metric summary data for calibration particles and RBC samples in an NP400 pore. IQR indicates the metric interquartile range. Range indicates the dimensionless range defined in Chapter 6.

Particle Type	Magnitude (nA)			FWHM (ms)			FWQM (ms)		
	Median	IQR	Range	Median	IQR	Range	Median	IQR	Range
0.4 μm sphere	0.908	0.249	27%	0.297	0.111	37%	0.618	0.231	37%
RBC	0.108	0.095	88%	0.268	0.126	47%	0.52	0.271	52%
Platelets	0.106	0.079	75%	0.266	0.105	39%	0.538	0.24	45%
	Asymmetry			Pre-peak Gradient (nA s^{-1})			Post-peak Gradient (nA s^{-1})		
	Median	IQR	Range	Median	IQR	Range	Median	IQR	Range
0.4 μm sphere	0.489	0.092	19%	2.801	1.127	40%	-2.027	0.648	32%
RBC	0.501	0.168	34%	3.259	1.792	55%	-2.532	1.632	64%
Platelets	0.496	0.167	34%	3.042	1.358	45%	-2.448	1.548	63%

to -1.24 to -1.29 for the RBC and platelet samples.) The platelet sample yielded the highest percentage population of the <400 nm particles. As a consequence the platelet sample was subsequently examined using an NP200 pore.

Figure 7.9 displays the results for the NP200 pore, including for 200 nm spheres. The NP200 pore used had an approximate lower limit of detection at 0.05 nA (equivalent to 140 nm diameter particles). Importantly, these data do not conform to the collection standard of over 500 events (excepting the calibration set) due to pore blockages during measurements. This is likely due to the presence of larger cells and aggregates in the blood samples. The modal peak in Figure 7.9 b) at $\sim$0.15 nA does qualitatively indicate the population of 150-200 nm particles that was observed across all samples (consistent with those observed in the NP400 sample) which could be composed of liposomes, microvesicles, platelets, cell debris and more. There were insufficient data to further support or refute the detection any of these specific sub-populations. It is likely that further purifica-

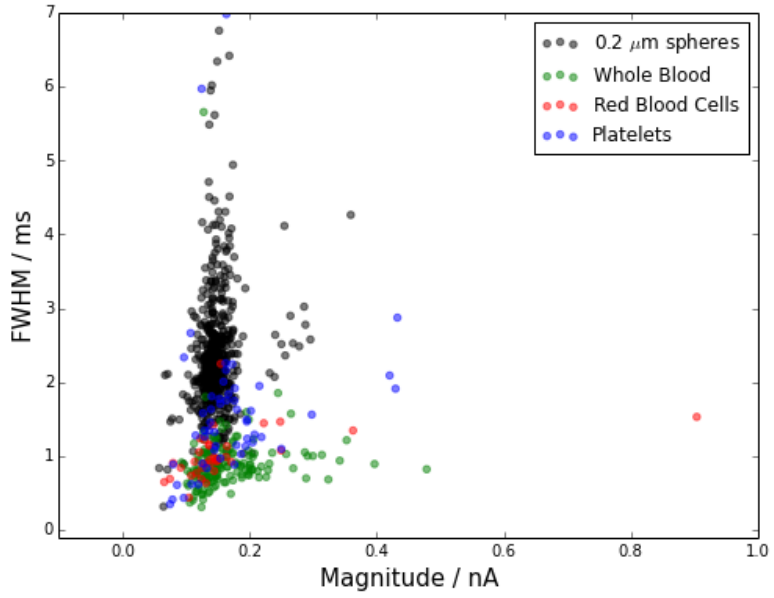

(a)

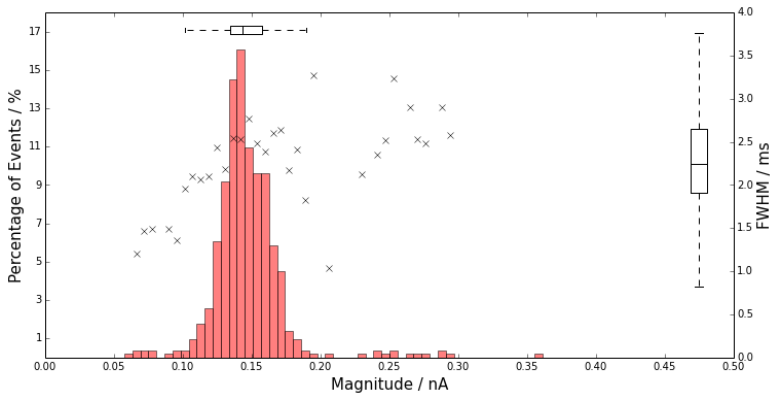

(b)

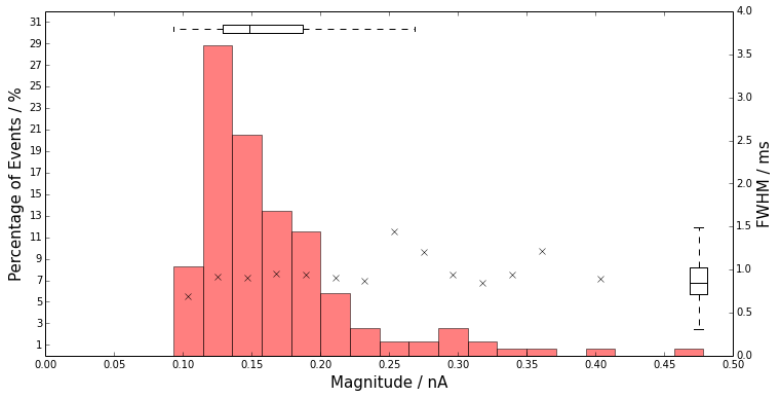

(c)

Figure 7.9: Summary data for TRPS of purified blood samples using a NP200 pore. a) Scatter plot of pulse magnitude vs FWHM. b) a summary histogram for 0.2 μm spherical calibration particles. c) RBC sample.

tion steps or alternation of the buffers used may be able to provide greater clarity around such size distributions in the future.

7.2.6 NP400 and NP200 Individual Pulses

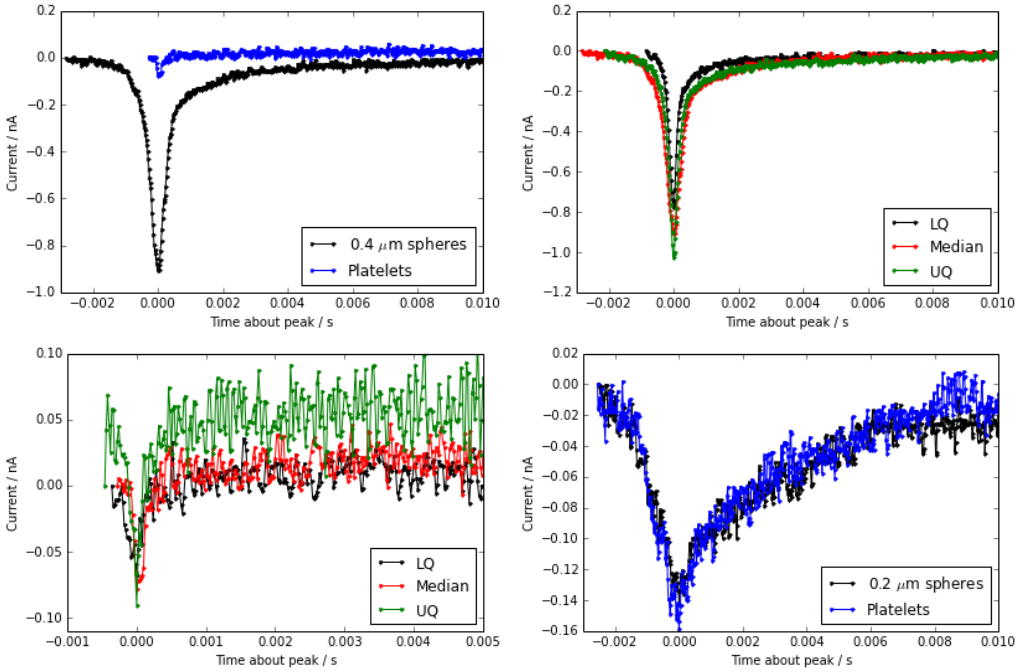

Figure 7.10: Individual events from NP400 and NP200 pores. a) compares median pulse events for calibration particles and the platelet samples in an NP400 pore. b) shows pulse data for pulse magnitude lower, middle and upper quartile events for 400 nm calibration particles. c) shows the same as b) but for the platelet sample. d) compares median pulse events for calibration particles and the platelet samples in an NP200 pore.

Figure 7.10 compares characteristic pulses for each data set in the previous Section. Figure 7.10 a) - c) indicate how different pulses for the 0.4 μm calibration particle and the platelet samples are, particularly in regards to the signal to noise ratio. The calibration particles in Figure 7.10 b) show lit-

tle variation between upper quartile and lower quartile magnitude events (as expected from the histogram in Figure 7.8 a)) and these characteristics are consistent with monodisperse particle sets at suitable size to be examined using an NP400 pore. Figure 7.10 c), showing the same data for the platelet sample, indicates that the precision of the platelet data collected will be affected by the low signal to noise ratio. Whilst the blockade magnitudes are sufficient to detect a resistive pulse, FWHM measurements approach the sampling limit of the qNano. 7.10 d) indicates how data quality improves with a pore matched more closely to the particle size, despite still showing clear background noise. However it is difficult to quantify these relationships further when pores block with sufficient regularity to hinder sample collection.

The important result here is that whilst it is possible to extract information from rat blood resistive pulses in NP1000, NP400 and NP200 pores, not all data are of the same quality and can be used for sample shape characterisation. Because of the high signal to noise ratio at NP400 and NP1000 and because of the well-known geometry of RBCs some shape information may be gleaned from TRPS whilst simultaneously measuring RBC size and concentration. However at NP200 length scales much more care is required when data processing and, unless a suitable pore is chosen, data may not be suitable for shape characterisation. To make precise measurements for these particle sizes a higher degree of filtration is needed than in NP400 and above.

7.2.7 *Rattus* Blood Summary

Whilst RBC counting and sizing has been possible with Coulter counters since the 1950s [2], the results presented in this section demonstrate that TRPS is capable, with minimal sample processing, of performing measurements on and detecting non-RBC components of *Rattus* blood. Whole mammalian blood is a complex medium containing a highly disperse mixture of particles (Figure 7.2). Erythrocytes, as the dominant cell population, can be simply measured using TRPS with an NP1000 pore. TRPS magnitudes return a volume for RBCs consistent with that expected from literature values, and may provide more accurate cell volume measurements than literature values calculated from optical microscopy measurements. Comparison of the RBC pulses with 2.8 μm calibration spheres (Figure 7.3) shows not only that RBCs exhibit larger median pulse magnitudes than the calibration particles, but also that they exhibit a broader range of pulse magnitudes and a shallower relationship between pulse magnitude and pulse FWHM. Both of these latter characteristics are consistent with a population of oblate spheroids traversing the pore at different orientations, although a broad range of pulse magnitudes is also consistent with a population of highly disperse particles.

Examination of ensemble pulse metrics indicates disparity between spherical particles and RBCs in FWHM, FWQM and gradient data that are consistent with earlier observations of non-sphericity. Pulse asymmetry and gradient metric data (Figure 7.4 and Table 7.3), indicate that the

RBC pulse magnitude range cannot be solely due to particle dispersity, as the RBC pulses are more symmetric than for spherical particles using the same pore. Pulse gradient data demonstrates that spherical particles exhibit larger pre- and post-peak gradients (and larger variation of those metrics) than the RBCs. Individual pulse data suggest this is not an effect of blockade magnitude normalisation. We are currently unable to explain FWHM and FWQM range data but note that the smaller ranges are consistent with oblate spheroids rotated at 90° to the pore axis and retaining their orientation as they traverse the pore.

The pulse height for both spherical particles and RBCs are predicted by our semi-analytic model to within 18% of their experimentally observed value. The same model underestimates the FWHM and over-estimates pulse asymmetry and gradients, despite using pore geometry data from an SEM calibrated pore (Figure 7.6). The semi-analytic model provides reasonable accuracy for known volume particles however these results suggest that a component of particle transport is currently being overestimated or neglected. Possible explanations for this were covered previously in Chapter 6. Without estimating the distribution of orientations of spheroids in the pore it is not currently possible to compare the IQR from the semi-analytic model with that obtained experimentally.

Centrifugal purification of the whole blood to separate the RBCs from the rest of the media (Figure 7.3) enabled TRPS analysis of non-RBC blood components in NP400 and NP200 pores (Figures 7.7, 7.8 and 7.9). TRPS

of the non-RBC components blood components <400 nm in diameter indicate a highly disperse population of particles with effective diameters 150-200 nm, consistent with that expected for exosomes and similar sized blood constituents. The limit of detection at ∼140 nm and regular blockages of the pore however hampered collection of detailed data, and do not preclude the presence of additional particles <140 nm in diameter.

7.3 *Shewanella marintestina*

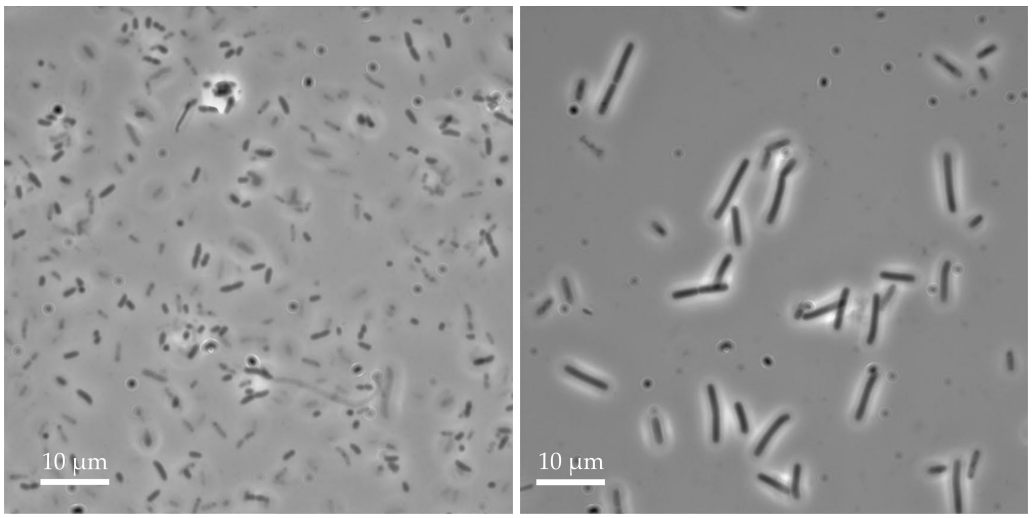

(a) (b)

Figure 7.11: a) Optical microscopy images of *Shewanella marintestina* taken immediately after isolation from growth media. b) Optical microscopy images of *Shewanella marintestina* 24 hours after the image in a). Optical microscope images were taken and provided by Dr. Mike Arnold [124].

In addition to synthetic particles and eukaryotic cells, interest in quantification of nanoparticles extends to microbes including viruses and bacte-

ria. A variety of these have been measured using TRPS previously as outlined in Chapter 2. Typical quantification techniques for these microbes include optical microscope observations, plating for concentration measurements or SEM analysis of relatively small sample sets. In several of these techniques pre-measurement treatments can cause changes in the geometry of the species under observation. The sheer variety in shapes, sizes and physical characteristics of microbes make them a challenge to accurately and efficiently characterise, particularly in fluid media. As such, a solution to this measurement is of interest in a variety of fields from medicine to food technology and environmental science. TRPS is well placed as a potential solution as it is significantly quicker than plating.

Shewanella are a genus of rod-shaped, marine bacteria. *Shewanella marinintestina* are a species of this genus which are gram-negative and motile utilising a single flagellum, and were originally isolated from the intestines of squid, scallops and goby acquired from oceans around Japan [125]. Phase-contrast microscopy has indicated these bacteria are 0.5-0.8 μm in diameter and 2-3 μm in length [125]. *Shewanella marinintestina* were cultured by Dr. Jason Ryan at Callaghan Innovation (Lower Hutt) at optimal growth conditions (20°C and pH = 7.0 in half strength seawater (300 mM NaCl)) and diluted by a factor of 200 in a solution of PBS.

Table 7.6: Summary of metric data obtained using TRPS for *Shewanella* samples and calibration particles.

Sample	$P_{applied}$	Pore	Magnitude (nA)			FWHM (ms)			FWQM (ms)		
			Median	IQR	Range	Median	IQR	Range	Median	IQR	Range
Shewanella	+10 Pa	A17636	1.126	0.935	83%	0.794	0.622	78%	1.776	1.348	76%
Shewanella	+20 Pa	A17636	1.078	1.016	94%	0.510	0.420	82%	1.154	0.870	75%
Shewanella+2hr	+20 Pa	A17636	0.995	1.138	114%	0.646	0.506	78%	1.409	1.073	76%
0.78 μm spheres	+10 Pa	A17636	0.483	0.121	25%	0.394	0.229	58%	0.940	0.476	51%
Shewanella	+20 Pa	A17635	0.209	0.242	116%	1.428	1.310	92%	2.564	2.229	87%
1.0 μm spheres	+20 Pa	A17635	0.127	0.048	38%	0.756	0.463	61%	1.303	0.819	63%
			Asymmetry			Post-Peak Gradient (nA s^{-1})			Pre-Peak Gradient (nA s^{-1})		
			Median	IQR	Range	Median	IQR	Range	Median	IQR	Range
Shewanella	+10 Pa	A17636	0.425	0.115	27%	1.464	1.169	80%	-0.584	0.503	-86%
Shewanella	+20 Pa	A17636	0.428	0.115	27%	2.229	1.810	81%	-0.883	0.751	-85%
Shewanella+2hr	+20 Pa	A17636	0.466	0.157	34%	1.759	1.415	80%	-0.731	0.649	-89%
0.78 μm spheres	+10 Pa	A17636	0.406	0.097	24%	2.795	1.606	57%	-1.068	0.499	-47%
Shewanella	+20 Pa	A17635	0.427	0.261	61%	0.776	0.735	95%	-0.449	0.369	-82%
1.0 μm spheres	+20 Pa	A17635	0.402	0.255	63%	1.562	0.946	61%	-0.829	0.552	-67%

Optical microscopy images of the same *Shewanella* culture were taken after similar preparation and are shown in Figure 7.11. *Shewanella* were not fixed prior to TRPS or optical microscopy measurements. Images are of the same *Shewanella* strain used for TRPS measurements. Figures 7.11 a) and b) indicate that this strain of *Shewanella* is expected to grow markedly over a 24 hour period and so a change in particle size over the duration of TRPS measurements can be expected. Attempts were also made to obtain SEM images of *Shewanella* microbes without success due to their organic nature. SEM images were attempted using a Quanta SEM (the same used for pore imaging in Chapter 4) under low vacuum (130 Pa) conditions, at approximately 10-20 kV.

In order to test TRPS's suitability for studies of asymmetric bacterial particles, rod-shaped *Shewanella* were examined using A17636 (the same NP1000 pore that was used for *Rattus* RBC analysis) and repeated using another NP1000 pore, A17635. For A17636, *Shewanella* were calibrated against 0.78 μm diameter, carboxylate polystyrene spheres. Figure 7.12 shows the pulse magnitude and FWHM data from TRPS *Shewanella* experiments. Experiments were repeated at several pressures over a 2 hour period. Data from experiments are summarised in Table 7.6.

7.3.1 Pulse Magnitude and Duration

All *Shewanella* data obtained using A17636 exhibit larger pulse median magnitudes and magnitude IQRs than the 0.78 μm spheres, independently

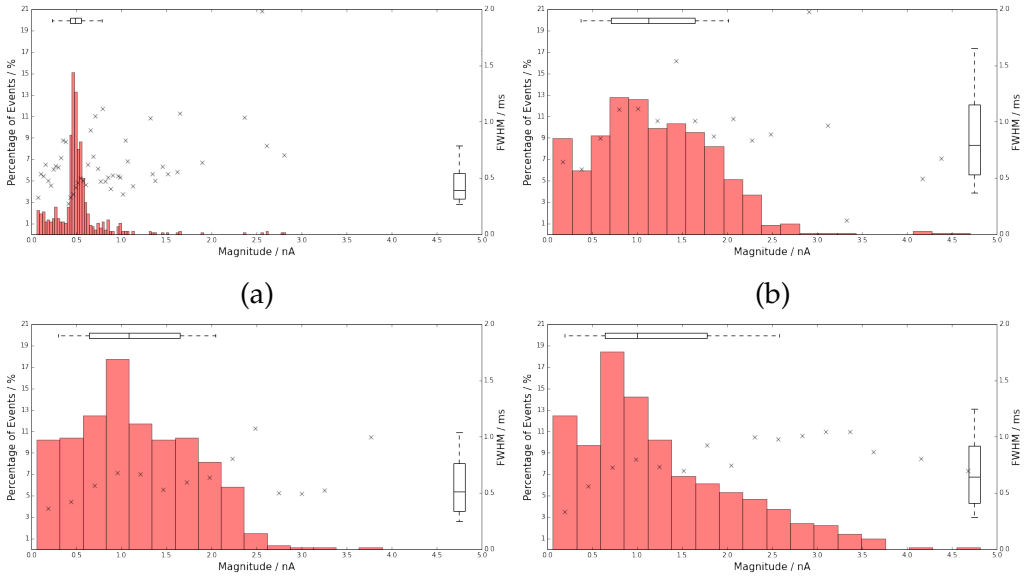

Figure 7.12: All measurements taken in A17636, at 44 mm stretch and 0.2 V. Figure a) shows a summary histogram for 0.78 μm calibration particles at +10 Pa pressure. b) - d) Displays TRPS pulse magnitude histogram data for *Shewanella* samples with different pressure conditions over time. Plot b) indicates TRPS data obtained directly after sample preparation at +10 Pa pressure. Plot c) indicates TRPS data obtained directly after sample preparation at +20 Pa pressure. Plot d) shows the same measurements as c) repeated 2 hours later.

of applied pressure or the time at which the measurements were taken. Calibration particles produce a clearly defined 'peak' about 0.5 nA imposed on background of outlying pulses with irregular FWHMs. The median pulse magnitude for the *Shewanella* sample in Figure 7.12 b) is consistent with the volume of a 1.034 μm diameter sphere (0.58 μm^3). However the broad distribution of pulse magnitudes indicated for all samples in Figure 7.12 b) - c) shows that the sizes of the bacteria are highly variable. For comparison, modelling a *Shewanella* particle as a 0.7 μm diameter, 3.0 μm length cylinder gives a particle volume of 1.155 μm^3 (almost double the measured volume) and 0.770 μm^3 for a prolate spheroid with the same dimensions as the cylinder. The semi-analytic model predicts a $\sim$58% increase in pulse magnitude due to a 90° rotation of a particle of that spheroidal geometry.

The *Shewanella* sample shows a 102% larger median FWHM and an 89% larger FWQM than the 0.78 μm spheres, whilst being linked to pressure as has been observed previously. The semi-analytic model suggests that this is a characteristic of non-spherical particles rather than due to high particle dispersity.

Shewanella particles also exhibit larger dimensionless ranges in both FWHM and FWQM (70-80% compared to 50-60% in the spherical sample). The semi-analytic model predicts changes in FWHM due to the rotation of particles, suggesting variations in FWHM of over 50% over a rotation of 90° for a prolate spheroid with the aspect ratio expected for a *Shewanella*

particle.

Histograms of pulse magnitude data obtained at $P_{applied}$ = 20 Pa (Figure 7.12 c)) show the same median magnitude and IQR as for those obtained at 10 Pa. Median FWHM and FWQM data are reduced by 35% due to the pressure increase. The semi-analytic model predicts a 53% increase over the same pressure. The reproducible nature of the magnitude measurements at different pressures, and the large FWHMs for *Shewanella*, both suggest the presence of rod-shaped particles rather than simply a disperse population of spherical particles.

Previous experimentation [124] has suggested rapid aggregation of *Shewanella* once removed from their growth matrix, as well as a disperse population of rods (shown in Figure 7.11). Consequently TRPS measurements were repeated in A17636, 2 hours after the initial experiments, with the results shown in Figure 7.12 d). If a large degree of aligned aggregation was occurring, either head-to-tail or side-by-side, then one would expect distinct volume populations in the *Shewanella* histogram plot in Figure 7.12. These would be centred around double the calculated particle volume (at approximately $\sim$1.5 μm^3, equivalent to a magnitude of 2.8 nA in A17636), which are not observed in the initial samples (Figures 7.12 b) and c)). Furthermore the previous double volume calculation assumes *Shewanella* are monodisperse prolate spheroids. However the high dispersity of the bacteria (Figures 7.11 and 7.12) suggests that two-particle aggregates would cover a large range of pulse sizes. After 2 hours the median pulse magni-

tude has reduced slightly, but the IQR has increased (Figure 7.12 d)). The lower quartile measurement is consistent across the samples however the broader upper tail shown in Figure 7.12 d) is the cause of this increase (the upper quartile has increased by 8%). This tail covers pulse magnitudes consistent with those expected from particle aggregation, over a range approximately equivalent to particle dimerisation given the high degree of uncertainty around the shape of *Shewanella* particles.

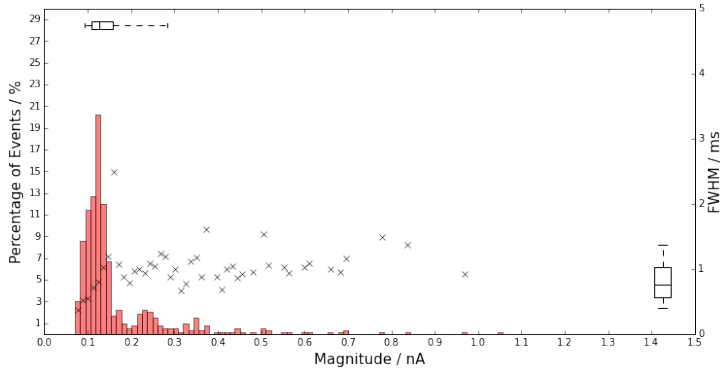

(a)

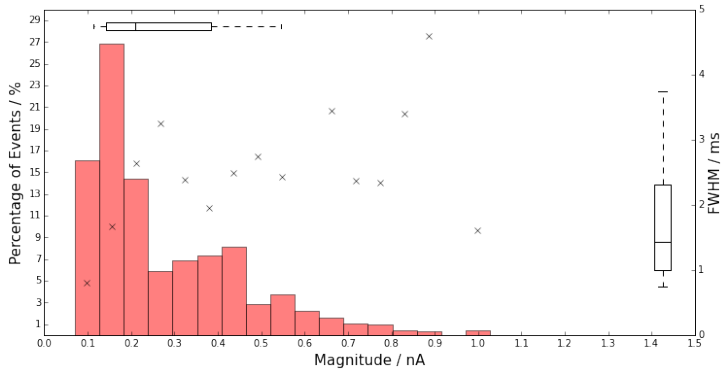

(b)

Figure 7.13: Summary TRPS measurements for 1 μm carboxylate polystyrene spheres a) and *Shewanella* particles b) for experiments performed using pore A17635.

Given the complex relationship between particle and pore geometry, *Shewanella* measurements were repeated using a sequentially manufactured pore. Despite having the same NP rating and being produced by the same needle in the same batch, both SEM and baseline current measurements indicate pore A17635 is larger than A17636. In A17635 *Shewanella* were calibrated against 1 μm diameter carboxylate polystyrene spheres, due to the increased pore diameter, with results presented in Figure 7.13. Calibration particles show a clearly defined modal peak at 0.13 nA. The *Shewanella* particles' pulse distribution (shown in Figure 7.13 b)) now exhibits a peak at magnitudes below 0.25 nA. Due to the larger size of the A17635 pore, this peak is consistent with the detection of the broad range of pulses observed in A17636, as they approach the lower limit of detection for this new pore. A17635 data also show a larger tail of particles at high magnitudes. The median *Shewanella* pulse detected in A17635 suggests a particle volume of 0.86 μm^3, greater than for A17636. The slight secondary peak at $\sim$0.4 nA could indicate aggregation. Experiments performed in A17635 were performed after those in A17636 but before the A17636 repeat shown in Figure 7.12 d).

1 μm particles show magnitude and duration dimensionless ranges similar to those observed for 0.78 μm spheres in the previous pore. The same data for the *Shewanella* sample are markedly higher and most similar to that from the 2hr sample from A17636. Notably A17635 and A17636 show large differences in the relationship between pulse magnitude and

FWHM, shown in Figure 7.14 a), explained by the variation in pressure between the two experiments. A17635 produces smaller pulse magnitudes, as is expected for a larger pore, however it also shows an increase in FWHM for the *Shewanella* sample. The presence of the larger FWHM for *Shewanella* compared to spherical particles in both pores suggests that this increase is not only due to steric interactions between the particle and pore, which would be expected to exhibit a larger effect in a smaller pore.

7.3.2 Pulse Symmetry

Asymmetry and gradient data for both A17636 and A17635 are displayed in Figures 7.14 b), c) and d) and summarised in Table 7.6. Both pores exhibit low levels ($>$0.4) of pulse asymmetry across all particles (when compared to data from NP400 and NP200 pores), however A17635 also exhibits an asymmetry dimensionless range of 60-65% compared to 25-35% for all particles in A17636. The semi-analytic model predicts that a single pulse produced by a spherical particle will be more asymmetric than that of a non-spherical particle. *Shewanella* particles consistently exhibit a 6% larger median asymmetry measurement than the spherical particles in both pores, with the +2hr sample showing the most symmetric pulses. Higher pulse symmetry could be expected for *Shewanella* particle dimers, particularly if they are end-to-end. *Shewanella* asymmetry dimensionless ranges are $>$12.5% larger than for 0.78 μm spheres, which is also consistent with the passage of non-spherical particles as has been discussed in

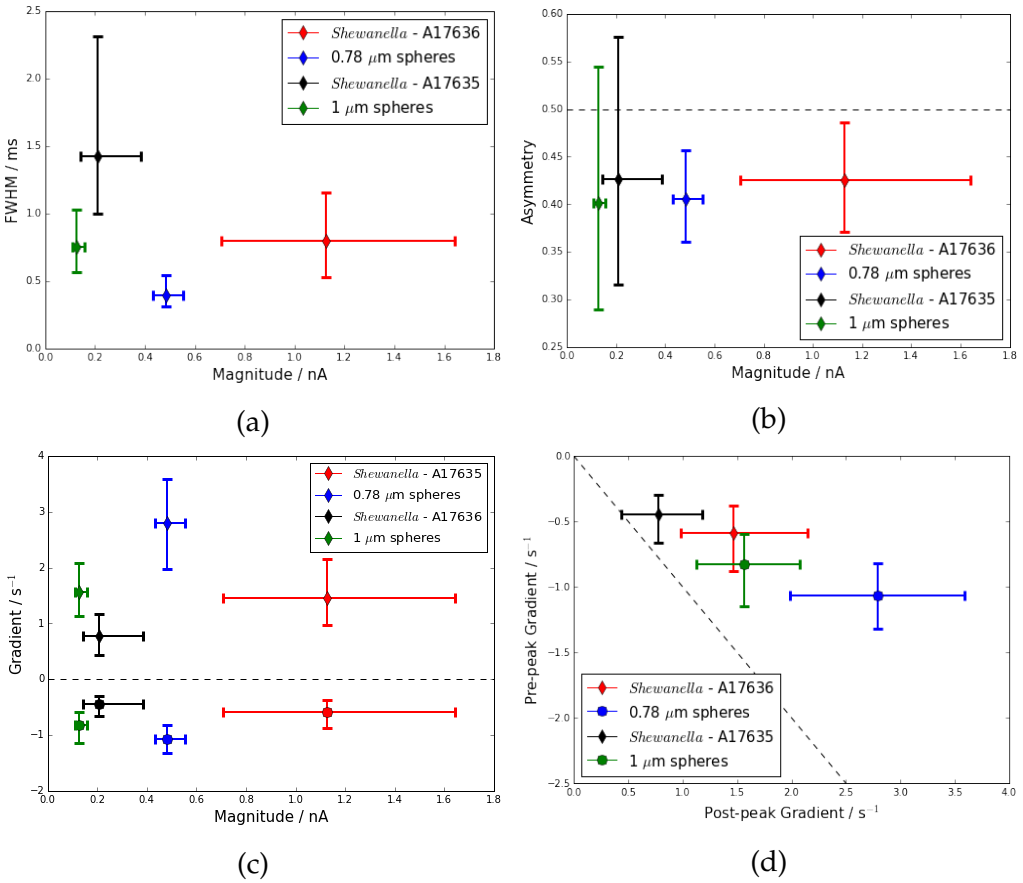

Figure 7.14: Data from TRPS *Shewanella* experiments. Data points indicate the medians and error bars indicate the measurement IQR. a) Plot of *Shewanella* and calibration spheres FWHM vs magnitudes. b), c) and d) show asymmetry, gradient and gradient ratio data for *Shewanella* and calibration particles obtained at 10 Pa in A17636 and 20 Pa in A17635 as shown in Table 7.6.

Chapter 6.

Shown in Figure 7.14 c) and d), particle gradients for *Shewanella* particles are smaller than those measured for spherical particles in both pores. Post-peak gradients for *Shewanella* particles are between 47 and 50% reduced compared to spherical particles, and pre-peak gradients are similarly reduced by 45 to 46%. The fact that both gradients are markedly lower than the spherical particle measurements for the same pore may indicate that non-spherical particles are being observed, or may simply be due to the increased FWHM observed for *Shewanella* particles. As with previous metrics, the gradient dimensionless ranges of *Shewanella* particles are also larger than for spherical particles.

Figure 7.14 d) compares gradient ratio data for *Shewanella* and spherical particles. In both A17636 and A17635, the gradient ratio for *Shewanella* particles is closer to the dashed pulse symmetry line than for spherical particles. This replicates the trend for non-spherical particles that has previously been identified using RBCs and the rod-shaped particles discussed in Chapter 6. The 1 μm particles in A17635 have a post-peak gradient ratio comparable to that of the *Shewanella* particles as measured in A17636. This is likely due to the differences in pore size and geometry.

7.3.3 Individual Events

Comparison of characteristic pulses from calibration particles and *Shewanella* in both pores yields further insight into the differences outlined by

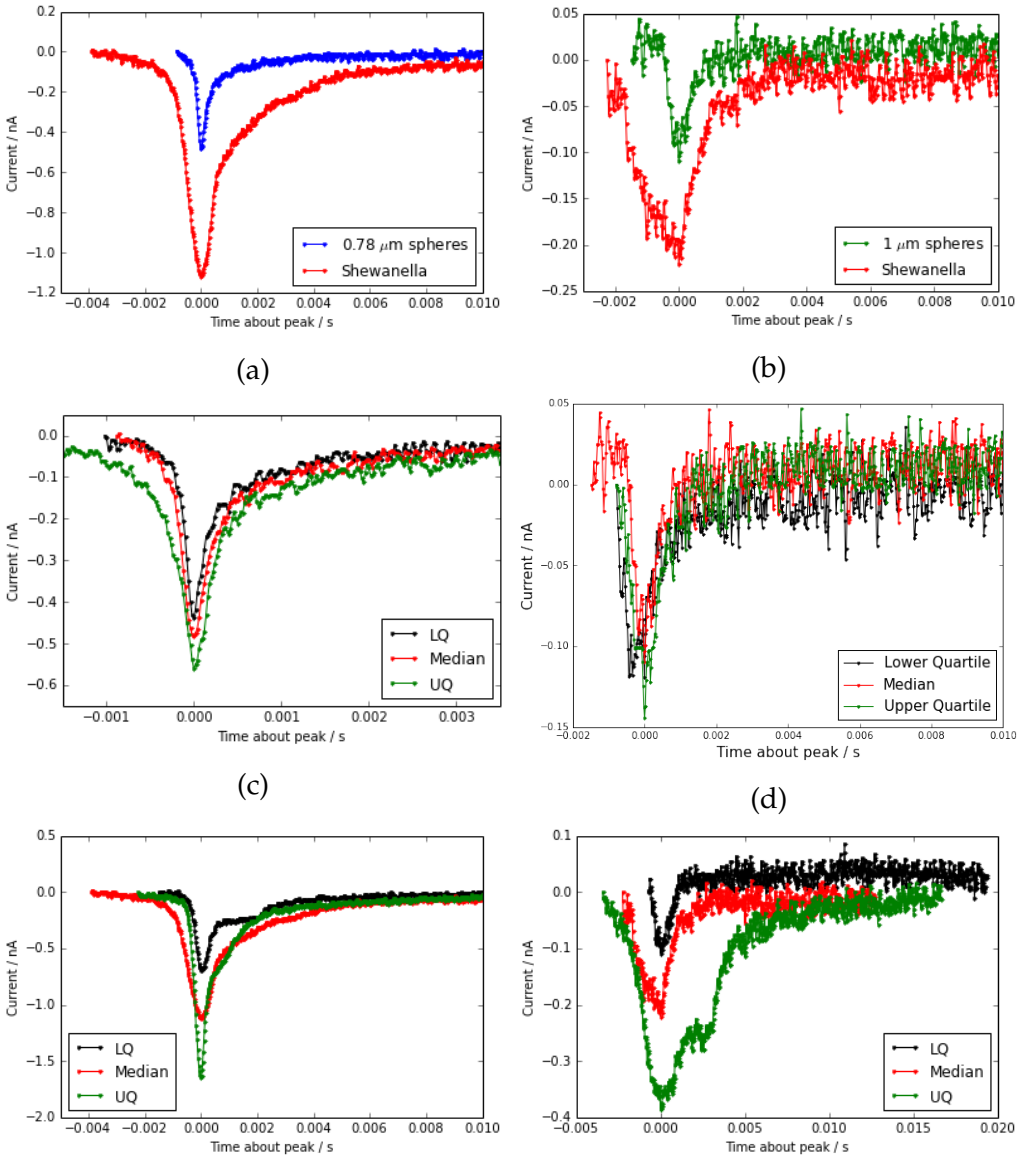

Figure 7.15: Comparison between pulse traces for spherical particles and for the *Shewanella* particles. Plots a) and b) show median pulse events for calibration and *Shewanella* particles in A17636 and A17635 respectively. c) and d) show quartile magnitude events for 0.78 and 1μm calibration spheres. e) and f) present the same data for the *Shewanella* samples in A17636 and A17635 respectively.

ensemble data. Figure 7.15 shows the median magnitude pulses obtained from spherical particles and *Shewanella* in both A17635 and A17636. Not only do *Shewanella* events have larger pulse magnitudes than the calibration particles, but they also exhibit much more variation in pulse shape across the IQR pulses. As shown in plots c) and d) in Figure 7.15, calibration particle pulse shape is consistent across the IQR, in particular the post-peak gradient. *Shewanella* events (plots e) and f)), show similar behaviour. The deviations from typical pulse shape shown in plots e) and f) are unique to these individual events and are not representative of all collected pulses. In A17636 the FWQM is 2.2-2.3 times that of the FWHM regardless of the specific particle, and in A17635 the ratio between FWHM and FWQM is 1.7-1.8 for all particles.

The effect of the increased pore size is immediately obvious in the decreased signal-to-noise ratio of the raw pulse data in A17635 plots (Figure 7.15 b), d) and f)). Unfortunately, given the high levels of noise in these pulses, we cannot say with confidence that this is significantly different from the A17636 events

The variations in *Shewanella* pulses observed could be explained by populations of rotated and non-rotated prolate particles traversing the pore as indicated by the rotated and non-rotated events produced by the semi-analytic model in Figure 7.16.

Plots a) and c) in Figure 7.16 show that there is some agreement between the semi-analytic model event and the spherical particle pulses ob-

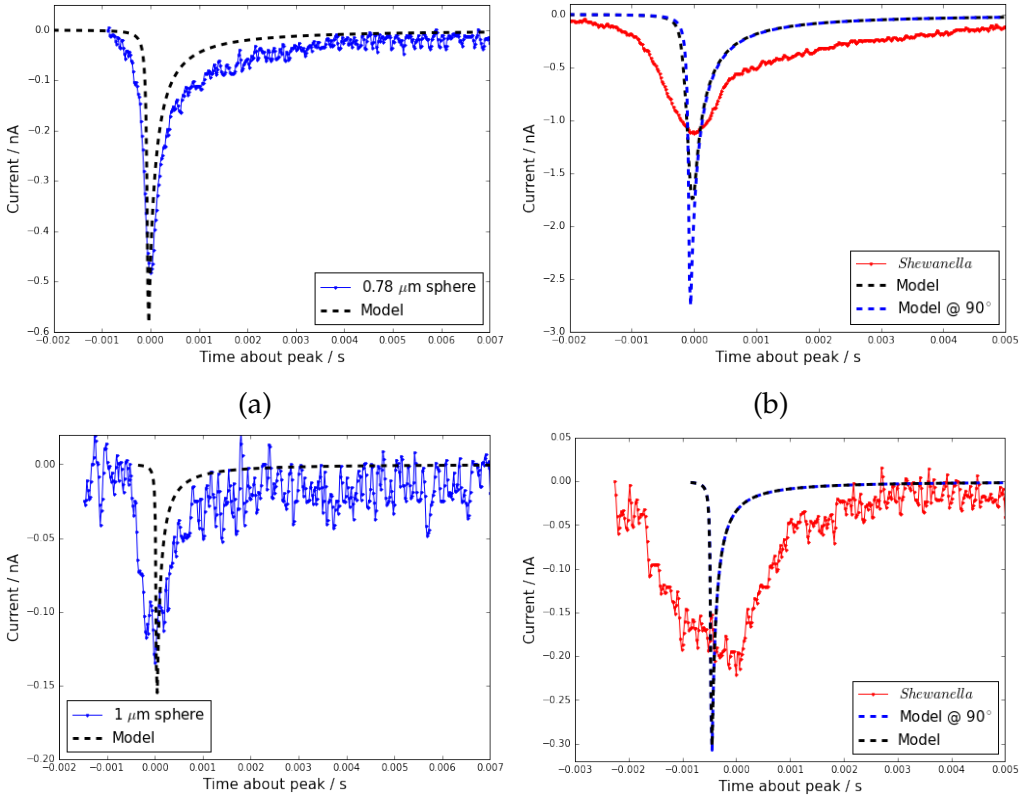

Figure 7.16: Comparison of median event with model. Plot a) compares median 0.78 μm calibration particles against model output for passage through A17636 under 10 Pa of pressure driven flow at 0.2 V. Plot b) uses the same experimental conditions and includes a *Shewanella* particle (modelled as a prolate spheroid) with a width of 0.7 μm and a length of 3 μm, compared with a median magnitude *Shewanella* pulse. Plots c) and d) show median magnitude pulses for 1 μm particles and *Shewanella* in A17635 at 0.2V and 20 Pa.

served from A17636 and A17635 using geometry data obtained from microscopy measurement as described in Chapter 4. Pulse magnitudes are predicted to within 20% of their observed values for spherical particles and FWHMs are predicted to within a factor of 2 of the experimentally observed value for A17636 and within a factor of 8 for A17635. *Shewanella* particles are less well predicted, as show in Figure 7.16 b) and d). Whilst allowing for rotation of the *Shewanella* particle modelled as a prolate spheroid does provide better agreement with the median pulses, the semi-analytic model still underestimates the FWHM and FWQM characteristics of the observed pulses.

Whilst this may suggest some unaccounted-for pressure effect (as pressure is the dominant flow phenomena under these conditions), the FWHM of pulses is also tightly linked to pulse geometry. For example a 10% increase in the model pore radius causes a 15% reduction in pulse magnitude and a 13% reduction in FWHM. However a similar reduction of pore radius will cause a proportionally larger increase in FWHM because of the reduction of pressure driven flow through the pore. As the diameter used for the semi-analytic model is an effective diameter calculated from area measurements from SEM images (linearly calibrated with pore stretch as described in Chapter 4), it is unlikely to be a precise measurement of actual pore radius. Furthermore the under-estimate of pulse FWHM by the semi-analytic model suggests a factor slowing down the transport of the rods.

7.3.4 *Shewanella* Summary

In summary, we have been able to detect and measure rod-shaped *Shewanella marintestina* particles using two NP1000 pores. We obtained a reproducible size measurement of a disperse population of *Shewanella* particles consistent with their expected size from literature values and optical microscopy. The distribution of blockade magnitudes detected suggests either a highly disperse mixture of particles, or the passage of rod-shaped particles traversing the pore with different orientations, or some combination of the two. Asymmetry data from both pores are unable to distinguish between *Shewanella* particles and spherical particles, but comparison of the gradients and gradient ratios of pulses clearly differentiates *Shewanella* from calibration particles. Examination of individual pulses shows further evidence of the passage of rotated *Shewanella* particles. Pulse magnitudes produced using the semi-analytic model are in reasonable agreement with pulses generated by spherical particles. The good agreement between the semi-analytic model and the predicted pulse magnitude and the relatively poor agreement with FWHM is similar to the RBCs discussed earlier. The FWHM and FWQM predicted for spheroids by the semi-analytic model are underestimated.

7.4 Bacterial Polyhydroxyalkanoate (BPHA)

7.4.1 Introduction

Whilst a body of work exists applying TRPS to known monodisperse particle sets (and combinations of monodisperse particle sets [126]) less has been reported regarding TRPS data from non-standard particle sets. Typical calibration particles are polystyrene latex made from colloidal suspensions. Bacterially produced bioester nano beads are spherical and have a similar polymer structure to calibration particles, but a unique synthesis method is used and therefore they are unlikely to be monodisperse. Bacterial polyhydroxyalkanoate (BPHA) particles, sold commercially as PolyBind-Z (Polybatics, Palmerston North) are bacterially produced polymer microparticles intended for protein functionalisation or vaccine delivery [127], with an estimated diameter of 100-500 nm [127], that are highly disperse compared to standard commercial micro- and nano-bead samples. The biogenic production of these BPHA particles is described in detail in [127]. In brief, PHA is produced within the cytoplasm of *E. coli* by the polymerisation of soluble (R)-3-hyroxyacyl-CoA monomers to insoluble PHA polymers. These high molecular weight chains ultimately aggregate into granules coated with a phospholipid membrane and various membrane associated proteins. 5-10 granules are produced per cell with diameters ranging from 100 to 500 nm, measured from TEM images [127]. The precise mechanism of granular formation is not yet known.

Plasmids are used to control the expression of proteins on the granule's surface and granules are then isolated and purified from other cell constituents by bonding the protein to an immoblizing matrix.

In this section we perform TRPS measurements on these highly disperse particles and compare results with collected SEM data. We determine the mean and median particle sizes, and also to attempt to establish the distribution of these particles throughout their known size range. We investigate how reproducible typical TRPS measurements are for highly disperse samples and further test the utility of our novel metrics (pulse asymmetry and gradients) in differentiating high dispersity from changes in particle geometry.

7.4.2 SEM of BPHA Particles

BPHA particles were imaged using an FEI Nona Nano SEM at both 40 000x and 80 000x magnification, after being deposited on carbon tape. Deposition was carried out by placing a droplet of high-concentration solution of BPHA suspended in SEB on carbon tape. The tape was then placed in a vacuum chamber and pumped down for 10 minutes. In order to preserve aggregate populations and minimise particle degradation prior to imaging, the suspension of particles in SEB was subjected to vortexing but not sonication. Figure 7.17 displays example SEM images showing a cluster of particles. Images used to generate particle SEM measurements showed mostly small clusters of 2-3 particles, with the large cluster shown

in Figure 7.17 being exceptional. 141 BPHA particles were imaged and measured, with the results summarised in Table 7.7, suggesting an average particle diameter of 257 $\pm$ 5.6 nm (from the standard error in the mean) with a standard deviation of 67 nm. Particle diameter measurements were performed by taking the mean of two perpendicular diameter measurements for each particle measured in pixels. Pixel values were then converted to nanometers using the 1 μm scaling line generated on each separate SEM image.

Table 7.7: Summary of SEM measurements of BPHA nanoparticles. n = 141.

	Diameter (nm)
Mean	257
Std Deviation	67
Max	443
Min	111
Median	256
Upper Quartile	305
Lower Quartile	202
IQR	103
Dimensionless Range	40%

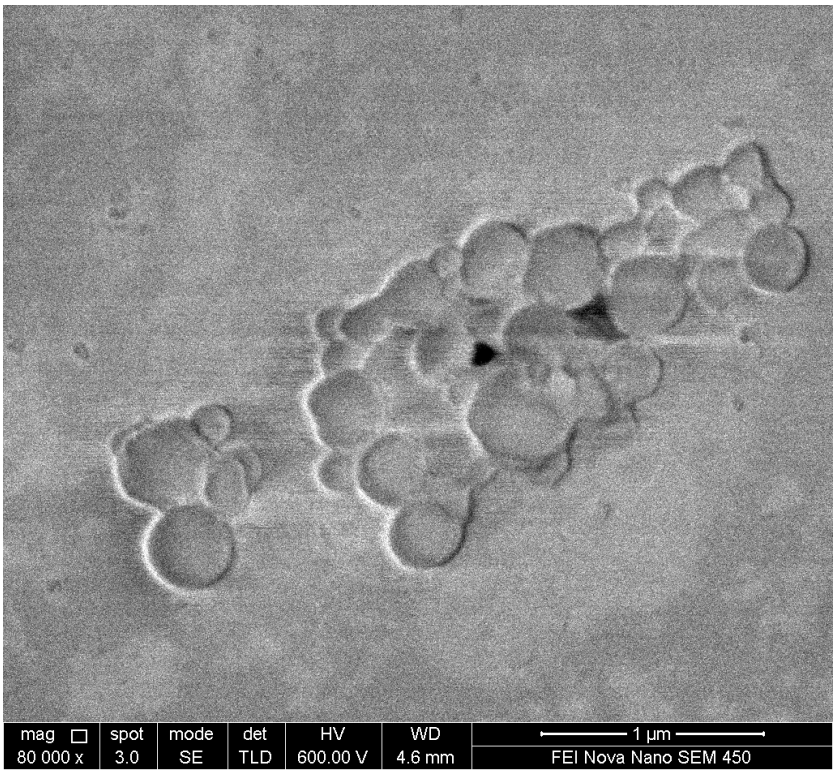

(a)

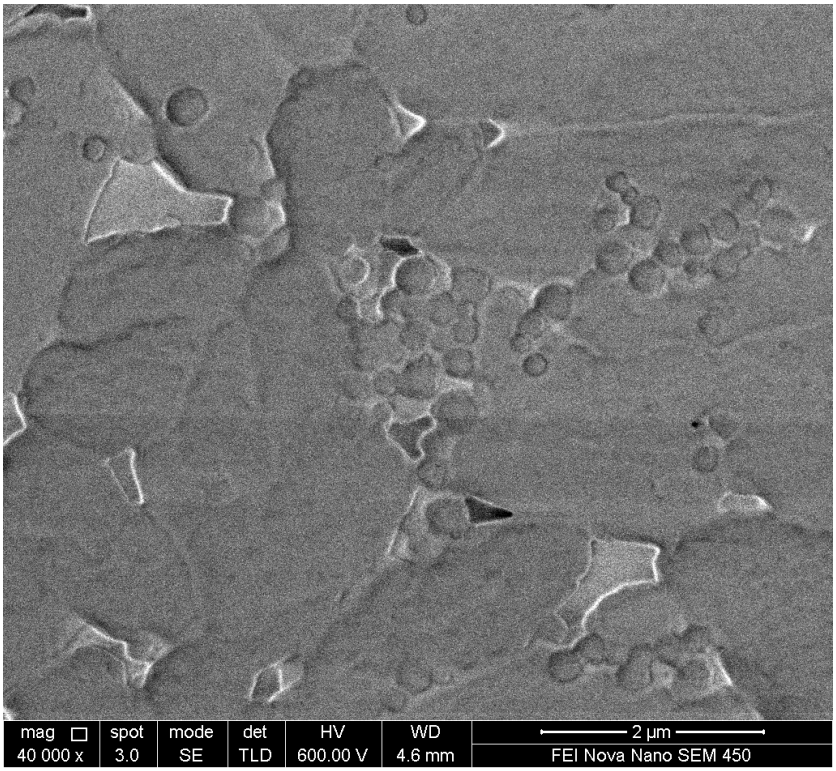

(b)

Figure 7.17: SEM images of BPHA nanoparticles. a) at 80 000x magnification b) at 40 000x magnification.

7.4.3 TRPS of BPHA Particles

BPHA particles were suspended in SEB, as described in Chapter 4, and were analysed using TRPS. 4 datasets were collected sequentially at both $P_{applied}$ = 20 Pa and $P_{applied}$ = -20 Pa using A09174 (NP400). Figure 7.18 compares the results of a single dataset comprising >500 collected pulses for 0.4 and 0.78 μm calibration particles (a and b) and BPHA particles (c). The 0.4 μm particles are monodisperse, with a median magnitude of 0.208 nA and a dimensionless range of 5.6% (0.012 nA). The 0.78 μm calibration particles data has a monodisperse peak between 1.5 and 2 nA and a consistent FWHM of $\sim$0.2 ms. The population of pulses with magnitudes less <0.2 nA is likely either contamination of the sample or particle degradation. Consistency with earlier data from RBCs suggest these pulses are not due to electrical noise.

In contrast, the BPHA particles (Figure 7.18 c)) show a range of pulse magnitudes down to <0.1 nA, approaching the detection limit of the pore. The BPHA data are summarised in Table 7.8, with the 'BPHA1' data presented in Figure 7.18.

The median BPHA pulse corresponds to a median particle diameter of 421 nm, using the 0.4 μm particles for calibration. Of specific note is the difference in the dimensionless range between the calibration particles and the BPHA particles, with the BPHA IQR almost double (1.9) times the median pulse magnitude. Spherical particles showed dimensionless IQRs of 20-30% only, clearly distinguishing the high degree of dispersity present in

the particles. The median magnitude for BPHA particles is slightly larger than that exhibited by the 400 nm calibration particles. This is in contrast with the mean diameter obtained from the SEM images which suggest that the median pulse should be approximately half the observed magnitude. Figure 7.19 a) shows the relationship between particle volume calculated using SEM images and median pulse magnitude. The median observed for BPHA particles is higher than expected. This is likely partly due to aggregation of the particles, as observed in SEM images. Also, BPHA data shows an asymmetric distribution of pulse magnitudes with the mode occurring adjacent to the lower limit of pulse detection for the NP400 pore used at this stretch. Typically this pulse mode location indicates that the pore used for analysis is too large for the particles being sampled, with a more ideal histogram as shown for the 0.78 μm spherical calibration particles.

Pulse FWHM and FWQM durations for the BPHA particles are closer to the 0.4 μm particles than the 0.78 μm particles. The ranges of FWHM and FWQMs are similar to the 0.78 μm particles. The larger FWHM ranges may simply be due to their larger distribution of pulse magnitudes than the 0.4 μm particles, or due to their dispersity.

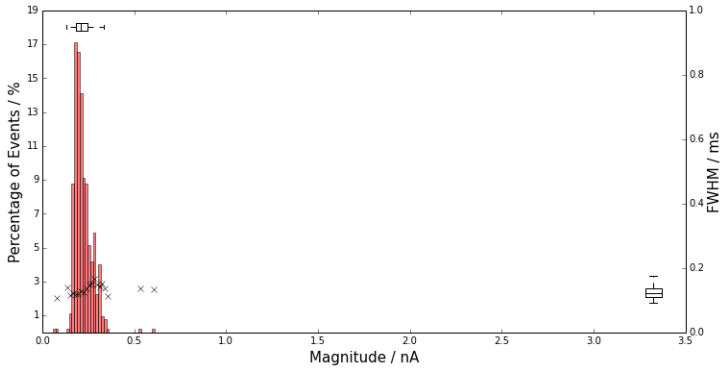

(a)

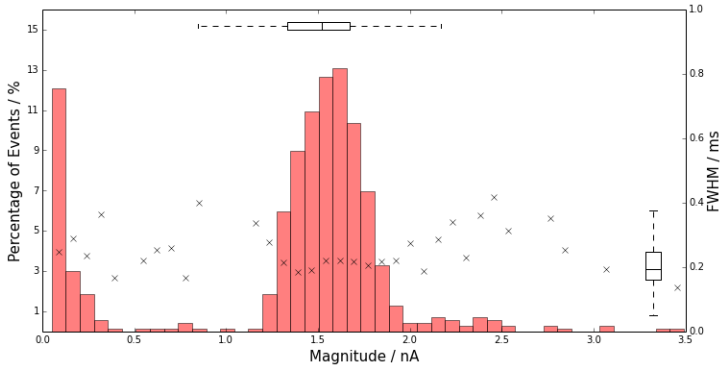

(b)

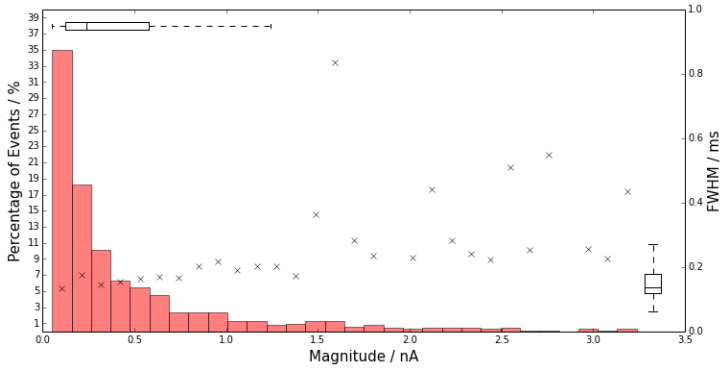

(c)

Figure 7.18: a) Summary data for 0.4 μm carboxylate polystyrene sphere calibration particles from a single measurement. b) indicates the same data for calibration 0.78 μm spheres. c) Summary TRPS data from a positive applied pressure run using the BPHA particles. Data were collected using A09174 (NP400) at 46mm stretch at 0.2V.

Table 7.8: Table summarising repeat BPHA particle measurements. BPHA 'IP' measurements use an inverted pore configuration and their data are omitted from average rows. 0.4 and 0.78 μm particle data are included for comparison with monodisperse calibration particles.

Sample	Pressure	Orientation	Magnitude (nA)			FWHM (ms)			FWQM (ms)		
			Median	IQR	Range	Median	IQR	Range	Median	IQR	Range
0.78 μm spheres	+20 Pa	Normal	1.519	0.339	22%	0.194	0.087	45%	0.407	0.187	46%
0.4 μm spheres	+20 Pa	Normal	0.208	0.059	28%	0.121	0.026	22%	0.267	0.074	28%
BPHA 1	+20 Pa	Normal	0.240	0.457	190%	0.138	0.063	46%	0.294	0.113	38%
BPHA 2	+20 Pa	Normal	0.232	0.368	159%	0.150	0.061	41%	0.323	0.125	39%
BPHA 3	+20 Pa	Normal	0.248	0.480	194%	0.205	0.118	58%	0.429	0.235	55%
BPHA 4	+20 Pa	Normal	0.250	0.400	160%	0.168	0.076	45%	0.353	0.170	48%
BPHA Average	+20 Pa	Normal	0.242	0.422	174%	0.163	0.084	52%	0.340	0.171	50%
BPHA IP	+20 Pa	Inverted	0.238	0.496	208%	0.157	0.073	46%	0.327	0.145	44%
BPHA 1	-20 Pa	Normal	0.240	0.381	159%	0.315	0.152	48%	0.649	0.335	52%
BPHA 2	-20 Pa	Normal	0.245	0.357	146%	0.261	0.112	43%	0.562	0.261	46%
BPHA 3	-20 Pa	Normal	0.204	0.313	153%	0.310	0.163	53%	0.652	0.346	53%
BPHA 4	-20 Pa	Normal	0.256	0.458	179%	0.276	0.140	51%	0.567	0.305	54%
BPHA Average	-20 Pa	Normal	0.234	0.374	160%	0.291	0.153	53%	0.605	0.316	52%
BPHA IP	-20 Pa	Inverted	0.207	0.376	182%	0.260	0.116	45%	0.564	0.278	49%

Sample	Pressure	Orientation	Asymmetry			Post-peak Gradient (s^{-1})			Pre-peak Gradient (s^{-1})		
			Median	IQR	Range	Median	IQR	Range	Median	IQR	Range
0.78 μm spheres	+20 Pa	Normal	0.480	0.083	17%	4.450	2.820	63%	-2.990	0.990	-33%
0.4 μm spheres	+20 Pa	Normal	0.459	0.102	22%	7.566	3.068	41%	-4.331	1.576	-36%
BPHA 1	+20 Pa	Normal	0.477	0.145	30%	6.870	4.310	63%	-3.870	1.750	-45%
BPHA 2	+20 Pa	Normal	0.460	0.125	27%	6.700	3.600	54%	-3.440	1.630	-47%
BPHA 3	+20 Pa	Normal	0.456	0.149	33%	4.690	2.660	57%	-2.630	1.540	-59%
BPHA 4	+20 Pa	Normal	0.468	0.124	26%	5.730	3.270	57%	-3.250	1.730	-53%
BPHA Average	+20 Pa	Normal	0.466	0.135	29%	5.810	3.400	59%	-3.410	1.870	-55%
BPHA IP	+20 Pa	Inverted	0.580	0.119	21%	3.300	1.780	54%	-7.010	2.530	-36%
BPHA 1	-20 Pa	Normal	0.573	0.126	22%	1.750	1.030	59%	-3.060	1.370	-45%
BPHA 2	-20 Pa	Normal	0.583	0.114	20%	1.900	1.070	56%	-3.840	1.420	-37%
BPHA 3	-20 Pa	Normal	0.578	0.126	22%	1.710	1.000	58%	-3.230	1.490	-46%
BPHA 4	-20 Pa	Normal	0.582	0.135	23%	1.960	1.140	58%	-3.920	1.770	-45%
BPHA Average	-20 Pa	Normal	0.579	0.125	22%	1.830	1.070	58%	-3.540	1.670	-47%
BPHA IP	-20 Pa	Inverted	0.466	0.139	30%	3.750	1.750	47%	-2.000	1.300	-65%

Figures 7.19 b), c) and d) show pulse asymmetry and gradient data. All particles show only low levels of asymmetry, with median asymmetries over 0.45. For all gradient and asymmetry measurements BPHA particles are indistinguishable from 0.4 μm particles. Figure 7.19 d) shows that BPHA and 0.4 μm spheres are further from the symmetry line than 0.78 μm particles. In earlier experiments, spherical particles produced data further from the symmetry line. Again the ratio between gradients appears linked to blockade magnitude, with smaller particles showing the highest gradient ratio. However this may be an effect of the sampling rate for small particles, investigated in more detail in Section 7.4.4. Other than pulse magnitudes, pulse FWHM, FWQM, asymmetry and gradient data are almost exactly as expected for spherical particles of the size distribution described in Figure 7.18 c).

Reproducibility

With monodisperse particle sets such as the calibration particles used in many TRPS experiments, it is expected that collecting 500 pulses over $>$30s provides a sufficient amount of data to characterise the particle population. Implicit within this is the assumption that, if a suitable pore size, stretch and voltage are used, a tightly clustered histogram such as in Figure 7.18 a) can be reproduced. It is not clear that this reproducibility extends to highly disperse particle sets such as the BPHA particles. Measurements of the BPHA particles were repeated 4 times at two different

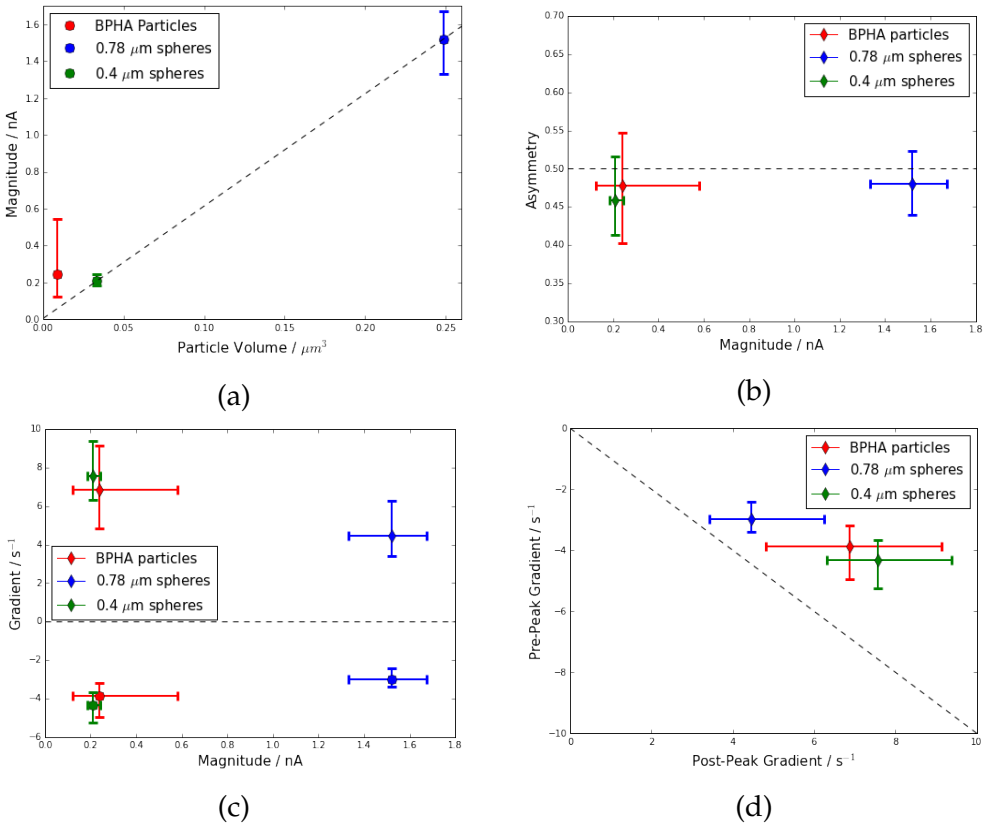

Figure 7.19: Pulse magnitude, asymmetry and gradient data for BPHA particles (single measurement indicated as BPHA 1 in Table 7.8) and 0.4 and 0.78 μm calibration spheres. Data were collected using A09174 (NP400) at 46mm stretch at 0.2V. Error bars indicate the IQR for each measurement. a) Pulse magnitude (with the BPHA particle volume equivalent to the mean value determined from SEM images), b) asymmetry, c) gradients, d) gradient ratios.

applied pressures to establish the inter-measurement variability in each metric, with results summarised in Table 7.8. The data presented in the previous section (NP400, X = 46mm, V_0 = 0.2 V) are taken from the first of these repeats, referred to as 'BPHA 1' in Table 7.8. As with all measurements, the fluid cell was removed and cleaned between measurements, and a new aliquot of BPHA SEB solution was placed in it for each repeat.

All of the repeated BPHA measurements indicate similar median pulse magnitudes and display a skewed distribution of pulse magnitudes with the mode occurring at the lower limit of pulse detection of the NP400 pore used, similar to what is shown in Figure 7.18 c). The standard error in the mean of the median magnitude is 0.004 nA (1.7% of median magnitude), despite the IQRs ranging from 0.36-0.48 nA. The standard error in the mean of the median FWHM and FWQM were 0.015 ms (9.0% of median FWHM) and 0.029 nA (8.6% of median FWQM) respectively. Standard errors in asymmetry, post-peak and pre-peak gradients were 0.005 (1.0% of median asymmetry), 0.503 (8.7% of median) and 0.258 (7.6% of median) respectively. As such, a single run can be expected to yield metric values within $\sim$10% of the mean over repeated measurements, as shown in Table 7.8.

Pressure and Pore Orientation Effects

Pressure driven flow is expected to dominate transport in most pores larger than NP200, except at high voltages or for highly charged particles. Also,

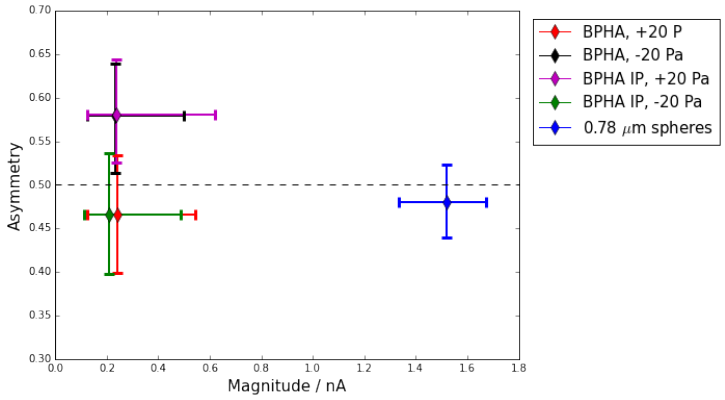

(a)

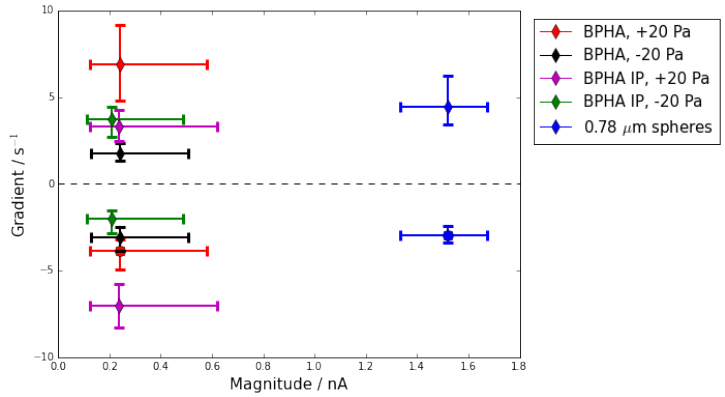

(b)

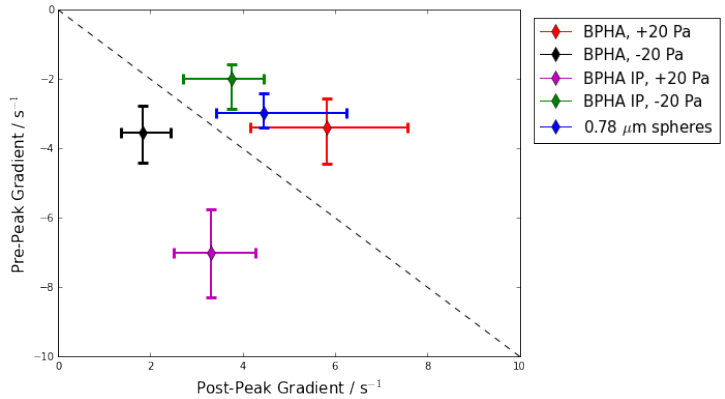

(c)

Figure 7.20: Data from 4 repeat measurements of BPHA particles compared to 0.78 μm calibration particles. Repeated measurements were performed at 46mm stretch at 0.2V. a) asymmetry, b) gradients, c) gradient ratios. IP indicates the inverted pore configuration. Error bars indicate IQRs.

the pore geometry has a large effect on the range and absolute value of many metrics measured. Table 7.8 includes single measurements made at $P_{applied}$=-20 Pa (i.e. with reversed fluid flow through the pore), at $P_{applied}$=+20 Pa, and at both pressures with the pore in an inverted orientation. Data collected from pulses under negative pressure conditions show on average a 75% larger FWHM and a 78% larger FWQM. The increase in pulse duration is to be expected because of the inherent pressure head in the fluid cell.

Asymmetry measurements presented in Table 7.8 and 7.20 a) show that pulse asymmetry is strongly linked to the applied pressure, because of the direction of particle flow through the asymmetric nanopore (see also Section 7.4.4). Inverting the pore produces a similar effect to reversing the pressure, with the median asymmetry changing from 0.45-0.48 under normal operating conditions to 0.57-0.59 in either the inverted pore or reversed pressure state. Asymmetry ranges seem invariant under these same changes and return to $\sim$0.45 when both the pore is inverted and the pressure is reversed. This suggests that the distribution of asymmetry measurements about 0.5 for different pressures is due to pore geometry rather than the pressure across the membrane. Ensemble averages are sufficiently distinct to enable identification of the direction of particle transport. However because the IQRs of both positive and negative pressure pulses (shown as error bars in Figure 7.20 a) overlap a value of 0.5, asymmetry cannot be used to accurately report the direction of particle flow

through the pore for individual pulses.

The gradient measurements presented in Figure 7.20 b) and c) provide clearer differentiation between individual pulse shapes than the aforementioned asymmetry measurements. Plot c) most clearly displays the overarching trend associated with particle direction relative to pore orientation. Particles that approach the pore from the small opening side have greater pre-minimum gradient than post-minimum gradient and also exhibit more variation in that gradient. Conversely, particles that approach the pore from the large opening have a smaller pre-minimum gradient than post-minimum and show similar levels of variation in both. When particles travel from the bottom to the top of the pore (i.e. $P_{applied}$ = -20 Pa) the gradients are expected to have smaller absolute values than for particle travelling in the other direction because of the inherent pressure head. However, comparison of pulse gradient ratio is still able to differentiate the direction of travel for individual particles.

Further information would likely be obtainable through the use of an NP200 pore. When this was attempted however, the presence of a significant proportion of large particles generated pore blockage events that did not allow collection of a sufficient amount of data to quantify the particles under these conditions. Prior filtration of the sample may allow measurement but would also significantly reduce the detected distribution of particles, which is the target of analysis for this particle set. BPHA and calibration particles were therefore re-examined with the same NP400 pore at

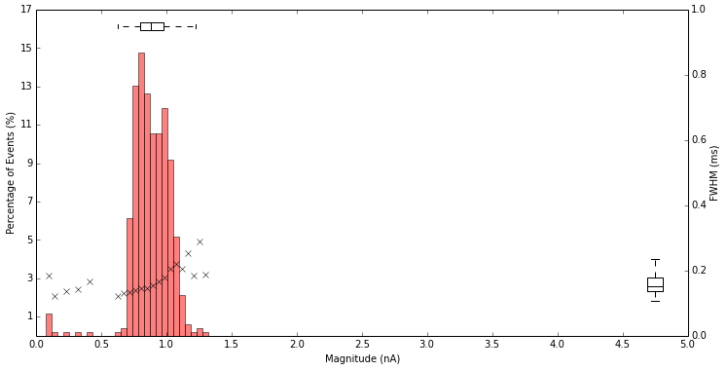

(a)

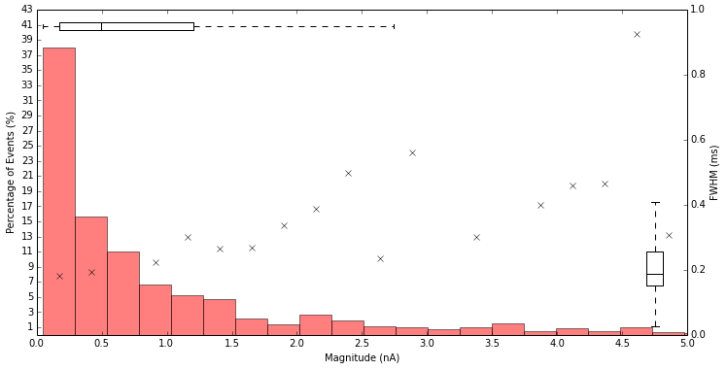

(b)

Figure 7.21: NP400 data (A09174) at 0.5V and 44mm stretch. a) shows data from NIST400 calibration particles and b) shows measurements made on BPHA particles.

a lower stretch (44 mm rather than 46 mm) and higher voltage with results shown in Table 7.9, Figure 7.21 and Figure 7.22. Results for 0.78 μm calibration particles were unable to be collected at this reduced stretch as they were too large for the pore. Data for the 0.4 μm calibration particles are shown in Figure 7.21 a), and exhibit an increased magnitude (>4 times larger) than for measurements made previously at a larger stretch. Calibration particles show a correlation gradient between pulse magnitude and FWHM of 0.38 ms/nA over a 0.4 nA region, similar to what was observed previously.

Table 7.9: Table summarising repeat BPHA particle measurements in A09174 at 0.5V and 44mm stretch.

	n	Magnitude (nA)			FWHM (ms)			FWQM (ms)		
		Median	IQR	Range	Median	IQR	Range	Median	IQR	Range
BPHA	586	0.485	1.031	212.73%	0.189	0.102	54.02%	0.401	0.187	46.63%
0.4 μm spheres	522	0.880	0.178	20.24%	0.152	0.042	27.48%	0.315	0.097	30.73%
		Asymmetry			Post-peak Gradient (s^{-1})			Pre-Peak Gradient (s^{-1})		
		Median	IQR	Range	Median	IQR	Range	Median	IQR	Range
BPHA	586	0.481	0.131	27.32%	5.000	3.002	60.04%	-3.087	1.326	-42.95%
0.4 μm spheres	522	0.474	0.086	18.08%	5.814	2.433	41.84%	-3.931	0.846	-21.52%

Again, BPHA particles show a skewed distribution and a dimensionless range an order of magnitude larger than for the calibration particle sets used. Figure 7.21 b) shows that a modal peak for the BPHA particles occurs at pulse magnitudes below 0.25 nA. Using 0.4 μm for calibration, 0.25 nA is equivalent to 0.26 μm diameter spherical particles.

BPHA particles exhibit FWHM and FWQM pulses 24% and 27% longer than calibration particles respectively. Median asymmetry measurements for both BPHA and 0.4 μm particles are 3.2% larger than the values from

the experiments at larger stretch, whilst the IQRs have grown slightly smaller (Figure 7.22 a)). Gradients for both particle sets have reduced by 10-30%, however the gradient ratios have increased for both particle sets. Altering the stretch of the pore does not change prior result of gradient ratios indication the direction of particle travel through the pore. At 44 mm stretch the -20 Pa BPHA data from Figure 7.22 still show an opposite gradient ratio to that of the +20 Pa sample. The most important result from the gradient and asymmetry data presented in Table 7.9 is that, as with previous results in Table 7.8, gradient ratio is best for determining the direction of travel of individual particles.

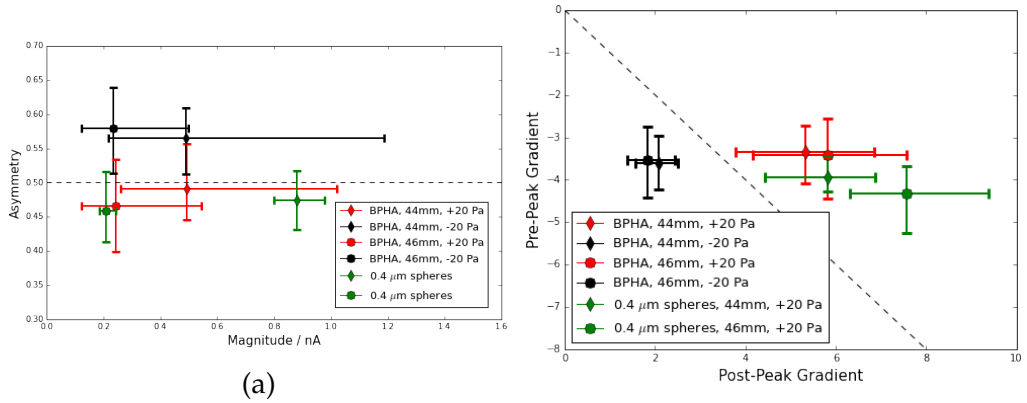

(a) (b)

Figure 7.22: a) Asymmetry and b) gradient data for BPHA and calibration data collected at 44mm stretch at 0.5V.

7.4.4 Characteristic Pulse Comparison

A comparison of the median individual pulses between the BPHA particles, from 'BPHA 1' in Table 7.8, and the 0.78 μm calibration particles at

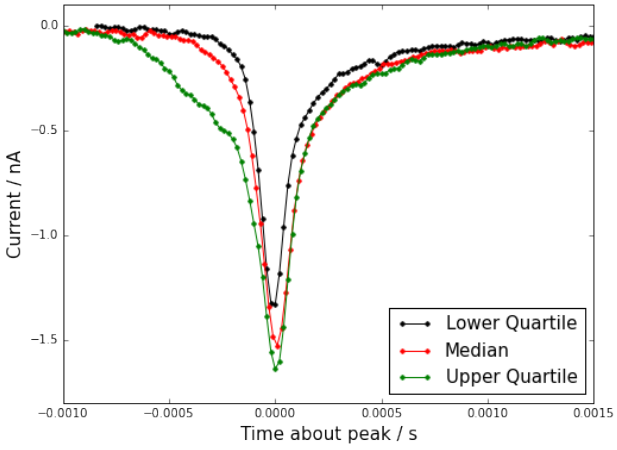

(a)

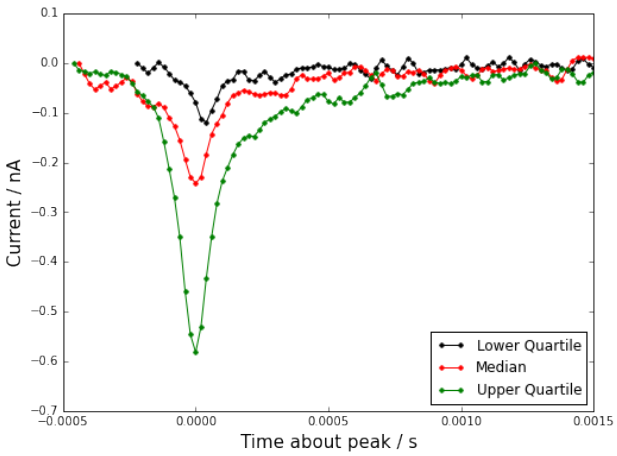

(b)

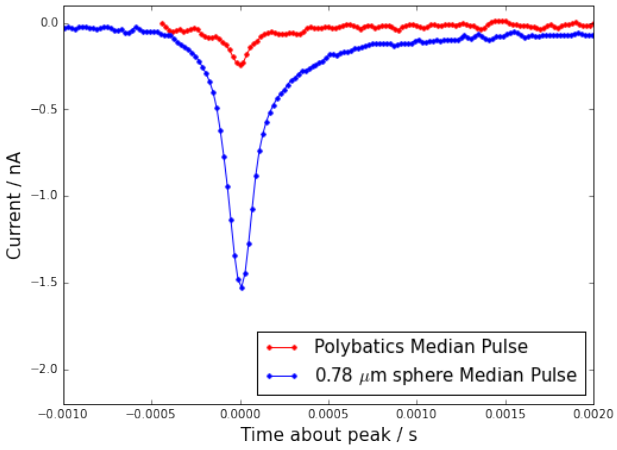

(c)

Figure 7.23: Individual trace events for BPHA and 0.78 μm calibration particles. a) calibration quartile events, b) BPHA quartile events c) BPHA and calibration median events

the same pressure at is shown in Figure 7.23. Whilst previous individual event comparisons in Chapter 7 have shown highly similar events even at the upper and lower quartiles, the BPHA particles exhibit far larger differences in pulse shape. This is another signature of a highly disperse particle population. Data from individual pulses is entirely consistent with previously presented ensemble data trends for BPHA particles. As such, individual pulses are not studied in further detail as pulse shape specifics (e.g. asymmetry, gradients) are of less interest here.

7.4.5 BPHA Summary

Bacterially produced BPHA particles present a complex particle system to analyse, not due to complexities of particle shape or of the particle suspension (as was the case for *Rattus* blood and *Shewanella* samples) but with the high degree of dispersity of the particles themselves. BPHA particles are reported by the manufacturer to have a mean diameter of 100-500 nm [127] yet the size distribution of the particles that gives rise to this number is not well-known. Prior to our work, repeated TEM measurements of BPHA particles provided the only available size distribution data for this particle set.

Our SEM images of 141 particles suggest a mean diameter of 260 nm with a symmetric IQR (from SEM data) of over 100 nm about the median. These data may be influenced by SEM imaging conditions and selection effects. TRPS investigations of the BPHA particles using an NP400 pore

show a skewed distribution of spherical particle diameters from 1000 nm to 350 nm (approximately the lower detection limit of the pore), with a median pulse magnitude from repeated measurements equivalent to a sphere with diameter between 416 and 421 nm. The asymmetry and gradient characteristics of these particles are consistent with spherical particles (Figure 7.19). High-quality data could not be obtained using an NP200 pore without further filtration of the sample, so an NP400 pore was used with a lower stretch setting. At the lower stretch setting a similar skewed particle distribution was produced, with a median pulse magnitude equivalent to a 328 nm diameter sphere and an IQR extending from 260 to 450 nm. The high relative population of smaller particles in these distributions contrasts with results from both the manufacturer and SEM data. Although all samples were sonicated immediately prior to TRPS, this measurement inconsistency may be due to the presence of aggregates (also observed during SEM), or directly due to a high dispersity sample. High dispersity likely affects all BPHA measurements and precludes obtaining quality data using an NP200 pore.

The dimensionless range of each measurement provides further information about the measured particle system, with calibration particles exhibiting a typical dimensionless magnitude range of 15-30%, and any measurement beyond this indicating variation in either particle dispersity or particle geometry. BPHA particles show a magnitude dimensionless range of 150-200% by comparison. BPHA particle gradient ratios are consistent

with those from a spherical particle.

Metric medians varied by less than 10% between subsequent measurements, even for a high dispersity sample. This reproducibility allows detection of changes in the TRPS system to be observed from the collected data. Examples of such changes include an inversion of the pore (indicated only by pulse asymmetry and gradient measurements) or a change in the direction of the particles through the pore caused by a reversal of the pressure applied to the system (detectable only by gradient measurements).

Comparisons of individual particle pulses from population quartiles provide further evidence for high dispersity. Monodisperse particle sets demonstrate little magnitude variation between upper quartile and lower quartile pulses, whereas highly disperse particle sets exhibit large differences in both pulse shape and magnitude when comparing similar pulses.

7.5 Conclusion

In summary we have used TRPS to obtain perform size distribution measurements of three unique particle sets: *Rattus rattus* RBCs, *Shewanella marintestina* bacteria and BPHA particles. Each of these samples presents a complex measurement, given the nature of the dispersity and shape of the particles involved or the additional constituents of the particles, when compared to the measurements performed in Chapters 5 and 6.

TRPS measurements of RBCs return a volume consistent with that ex-

pected from literature values, and may provide more accurate cell volume measurements than literature values calculated from optical microscopy measurements. Additionally, the average pulse magnitudes, the shallower relationship between RBC pulse magnitudes and ensemble FWHM data are consistent with measurements of a population of oblate spheroids or a highly disperse range of particles. Ensemble gradient and asymmetry data however show that RBC pulses are more symmetric than would be expected for spherical particles and suggest that particle dispersity alone is insufficient to explain these observations. TRPS measurements in a smaller pore also indicate a population of particles smaller than RBCs with effective diameters 150-200 nm that are consistent with that expected for exosomes and similar sized blood constituents.

TRPS measurements of rod-shaped *Shewanella marintestina* yielded a reproducible size measurement of a disperse population of *Shewanella* particles consistent with their expected size from literature values and optical microscopy. As with RBCs however, pulse magnitude and FWHM measurements are consistent with both measurements of a highly disperse population of particles or rod-shaped particles traversing the pore with different orientations (or a combination). However, *Shewanella* gradient data indicate that pulses are more symmetric than could be expected for pulses produced by spherical particles.

TRPS investigations of BPHA particles showed a skewed distribution of spherical particle diameters from 1000 nm to 350 nm, with a median

pulse magnitude from repeated measurements equivalent to a sphere with diameter between 416 and 421 nm. Additional measurement at a different pore stretch produced a median pulse magnitude equivalent to a 328 nm diameter sphere and an IQR extending from 260 to 450 nm. Whilst ensemble pulse magnitude data are broadly consistent with size measurements of the particle from SEM images, the high relative population of smaller particles in the size distributions contrasts with results from both the manufacturer and SEM data. The asymmetry and gradient characteristics of TRPS measurement of BPHA particles are consistent with spherical particles. Repeated TRPS measurements showed metric medians varying by less than 10% between subsequent measurements, even for a high dispersity sample.

For all samples measured, the semi-analytic model produced reasonable agreement with the observed pulse magnitudes. This model underestimates the FWHM and over-estimates pulse asymmetry and gradients, despite using pore geometry data from SEM calibrated pores. The semi-analytic model provides reasonable accuracy for known volume calibration particles. These results suggest that a component of particle transport is currently being overestimated or neglected.

Chapter 8

Conclusions and Future Work

This thesis has investigated the use of TRPS in the quantitative measurement of both the charge and shape of nanopartices in both simple and complex solutions. This work adds to the existing knowledge of the physical phenomena present in TRPS nanopores. TRPS is not strongly affected by the presence of a low number of large particles in solution, which is a major experimental issue with the most common comparable technique for high-throughput particle size and charge measurement, DLS. Therefore TRPS is a measurement technique with wide ranging potential applications from biological sensing to emulsion measurements. In this Chapter key results and advances are recounted and possible future work is discussed.

8.1 Development and Modelling of TRPS

Prior experiments and theory have suggested that the dominant phenomena governing the transport of fluid and particles through a tuneable nanopore are pressure driven flow, electro-osmosis, and electrophoresis. Other transport phenomena, such as diffusion, dielectrophoresis and magnetic transport certainly can be important, however Fisk *et al.* [56] showed they were comparatively negligible in the particles and TRPS system under study in this thesis. Therefore, in order to simulate and understand the transport of nano- and microparticles through a TRPS nanopore, the nanopore must first be well characterised in terms of both charge and geometry. As such, we have measured the large and small openings of a range of conical pores in TPU with small pore opening diameters between $\sim$500 nm and several microns (rated NP200, NP400 or NP1000) using both optical and SEM methods. SEM provides the optimal present technique for such measurements, due to the diffraction limit of optical techniques. Furthermore, we have measured the width of the elastomeric membrane (and thus the length of the pore) as a function of strain applied to the membrane across the common range of use.

Due to the inherent pressure head in the fluid cell, the dominant flow phenomenon for many TRPS measurements is the applied pressure which produces flow of the electrolyte through the pore. The precise velocity of this flow is also highly dependant on the geometry of the pore; in particular the diameter of the small pore opening. We have developed and ap-

plied a variable pressure manometer, with resolution higher than that of the version commercially available, which affords user control over the net pressure applied across the pore to a precision of 0.5 mm H_2O. The ability of this manometer to both continuously and discretely change the pressure applied across the pore allows the relative strengths of both pressure and electrokinetic flow phenomena to be tuned, enabling nanoparticle charge measurements.

Measurements of electrophoretic mobility are used to determine the ζ-potential of particles moving through a tuneable pore. The net electrokinetic motion of a particle also depends on the surface charge and thus the ζ-potential of the pore itself, as electro-osmotic flow opposes the electrophoretic motion of particles within the pore. We have measured the ζ-potential of TPU in KCl by fabricating microchannels from the material, determining a ζ-potential of -12 $\pm$ 2.5 mV at 0.1 M concentration. Additionally, we have measured the conductivity of SEB across a range of KCl concentrations and conclude that the conductivity of SEB is within 1 mS/cm of the KCl conductivity at the same concentration.

We have additionally implemented a semi-analytic model of the resistive pulses produced by TRPS in conical tuneable nanopores. This semi-analytic model requires the inputs of experimental parameters such as applied voltage, applied pressure, ζ_{pore}, large and small pore opening diameters, $\zeta_{particle}$, particle size, electrolyte viscosity and conductivity. Assuming an internal pore geometry, the model is able to calculate not only the ex-

pected background current through the pore, but also the pulse height and shape of resistive pulses produced by spherical particles. We extended this model to simulate the passage of non-spherical particles that are able to adopt specific orientations as they traverse the pore. The semi-analytic model predicts characteristic changes in pulses depending on the geometry of the particle generating the pulse. Despite SEM measurements of the small pore opening across a variety of pores at various strains, uncertainty in pore geometry remains the largest source of uncertainty in the semi-analytic model.

A clear direction for future work is refinement of the semi-analytic model along two distinct directions: reducing the uncertainty in the inputs, and expanding the scope of the model to include the complexities of realistic particle motion through an enclosed aperture. Of the former of these, the most pressing is the need for better information about the internal geometry of the pore and the precise diameter of the small pore opening of a specific pore at a specific stretch. Despite pores being 'rated' by the manufacturer, the diameter of the small pore opening can vary, even in pores with the same rating. Furthermore, despite the precision of SEM measurements, the difficulties associated with locating the pores and accurate pore measurements suggest that additional measurement methods could be investigated. Further information about the hygroscopic characteristics of the pore at the nanoscale, and their effect on fluid flow adjacent to the pore surface is also another important area for future investigation.

Finally, there is mounting evidence (including in Chapters 6 and 7) that whilst the approximate truncated cone geometry used in the model is sufficient to generate TRPS pulse magnitudes with reasonable accuracy, it is insufficiently accurate when predicting the details of pulse shape. Willmott *et al.* [17] have previously shown that the internal geometry of the pore is more akin to a cubic than a cone. Potentially, comparison between the pore geometry and that of the needles used to create them may provide a more robust assumption of the internal pore geometry.

The current semi-analytic model is also limited by the assumptions concerned with the passage of both spherical and non-spherical particles. For both classes of particles, the model assumes a centrally-located trajectory of the particle through the pore. Given the additional assumption of the homogenous resistivity of the electrolyte across the pore (at least for the length scale of the particle), the trajectory of the particles would not be expected to markedly alter the pulse magnitude. However, steric or electrostatic interactions between the particle and pore walls (or their respective double layers), the competing parabolic and plug flow profile of pressure driven flow and electro-osmotic flow respectively through the pore, and the constriction of electric field lines near the pore mouth, all suggest that small changes in the entry position of the particle into the pore may alter the characteristics of a resistive pulse produced. Expanding the semi-analytic model to include off-axis effects would, at a minimum, suggest a range of pulse magnitudes for spherical particles traversing off-axis

trajectories. Such work would have an impact on the precision of TRPS size measurements of nanoparticles.

When measuring the shape of non-spherical nanoparticles, a model should incorporate the rotation of particles as they traverse the pore. The current model utilises the assumption that once particles enter the pore with a certain orientation, that orientation is maintained relative to the pore for the entirety of the translocation. In reality, particles will rotate both axially and radially and may tumble, based on the flow characteristic of the fluid field around them. Work on larger particles has suggested that rod-shaped particles with large aspect ratios align with the direction of Hagen-Poiseuille flow in converging flows and rotate perpendicularly to it in divergent flow [128]. The asymmetry of the convergence and divergence of the fluid flow about the small pore opening will no doubt make this analysis complex, but may allow the fabrication of pores with geometry that is optimal for shape measurements.

8.2 Charge Measurement

Chapter 5 discussed the development and comparison of a number of methods for measuring nanoparticle charge based on the 'balance point' between pressure driven flow and electrokinetic motion of particles. Five sets of polystyrene nanoparticles with different surface chemistry were measured, each approximately 200 nm in diameter. Previous work by Vogel *et al.* [52] had shown that continuous variation of the pressure applied

across the pore produced a 'S'-bend shape in a plot of cumulative pulses over applied pressure. The stationary point of this curve was then a measurement of the 'balance point' of the specific particle set being measured, with the pressure at this point directly related to the ζ-potential of the particle using Equation 5.2. This method is referred to as the continuous rate method. However, as particle rate and particle FWHM data are also collected during TRPS, Chapter 5 also examined 3 other novel methods of determining P_0; namely the discrete rate method, the continuous duration method and the discrete duration method.

The conclusion was that all TRPS ζ-potential measurements yield results comparable to those obtained from DLS, yet those produced from FWHM duration data are more reproducible than those from rate measurement methods. Additionally, this work established the environment (low conductivity electrolytes and higher voltages) required for higher precision TRPS ζ-potential measurements, and found an upper limit (-0.4 C m^{-2}) for the surface charge on particles measured using this technique. Simulation of competing transport mechanisms around the pore opening suggested that a discontinuity in the net flow of particles adjacent to the pore mouth is the likely cause of this limitation.

8.3 Shape Characterisation

Investigation of dominant flow characteristics for pores of varying sizes [56] and previous attempts to characterise TRPS pulses in detail [18] lead

to an investigation of the relationship between particle geometry and pulse shape in NP400 and NP1000 pores. Chapter 6 showed that the traditional TRPS metrics of pulse magnitude and FWHM would likely be insufficient to differentiate between spherical and non-spherical particles of similar volume. Hence, the TRPS measurement repertoire was expanded to include a previously-used measurement of pulse asymmetry [18] and a novel measurement of pulse asymmetry: the pre- and post-peak pulse gradients.

After first testing these metrics using the same particles as in Chapter 5 to establish expected levels of variation for spherical particles, measurements were made on both spherical and rod-shaped, gold particles in an NP400 pore. Results showed that rod-shaped particles had longer FWHM (on average) and larger variation in pulse magnitudes than spherical particles across a range of pressures. Additionally, spherical particles generated more asymmetric pulses than rods, with the asymmetry from spherical particles being sufficient to determine the direction of travel through the pore. However absolute pulse asymmetry measurements were observed to depend more strongly on the specific pore used than other parameters and hence asymmetry measurements are only informative when particles have been studied using the same pore.

Pulse gradient measurements showed a relationship with both particle surface charge and with the net pressure applied to the pore. This suggests that gradient characteristics could be used as an additional method

for determining P_0, or possibly even individual particle ζ-potential measurements, in future work. Whilst, as with asymmetry measurements, absolute gradient values depended on the specific pore used, the gradient ratio was consistently lower for rod-shaped particles than for non-spherical particles. These characteristics were consistent with the detection of non-spherical particles, but it was not clear that these characteristics could not also be produced by a highly disperse particle set, and the rods used for measurements had markedly higher dispersity than the spherical calibration particles. These measurements could be further refined by their application to a monodisperse set of non-spherical particles of known geometry. As noted previously, more accurate knowledge of pore geometry would also likely increase the quality of data obtained using these methods. Finally, the complexity associated with particle orientations could also be addressed in future work either through the use of large aspect ratio particles, or through the use of magnetic alignment [56] to constrain the orientation of particles during translocation.

8.4 TRPS of Complex Systems

In Chapter 7, we presented the result of TRPS measurements on complex particle sets, in contrast to the monodisperse, carboxylate polystyrene calibration particles that comprised the majority of data presented in Chapters 5 and 6. TRPS measurements on the first of these sets, whole *Rattus rattus* blood, showed conclusively that TRPS was able to provide high preci-

sion size measurements of the red blood cell component of blood. Sample preparation required only dilution and the addition of an anticoagulant. As with non-spherical rod particles observed in Chapter 6, disc-shaped red blood cells exhibited a lower gradient ratio than comparable spherical particles. This ratio was larger than that observed for the rod-shaped particles, as was expected from their low aspect ratio. Further measurements following centrifugation to isolate blood particulates smaller than red blood cells showed a highly disperse population of particles between 150 and 400 nm in diameter, sizes consistent with exosomes. Given the recent interest in exosomes, microvesicles and other blood constituents, refinement of TRPS measurement of this small sub-population of blood particles is a clear direction for future work, following either more stringent filtration protocols to establish which exact blood particulates are being detected, or measurements in an NP100 pore. Indeed, the most recent TRPS research elsewhere is focussed on this application area [64].

The marine bacteria *Shewanella marintestina* was also measured using TRPS after dilution in PBS, directly after removal from their growth matrix. TRPS measurements were reproduced using two NP1000 pores with results indicating a distribution of particle sizes from less than 0.25 μm^3 to 1.25 μm^3. The smaller pore showed an approximately uniform distribution of particles over this range, whereas the larger pore indicated a distribution skewed towards lower particle sizes. FWHM and FWQM data for *Shewanella* particles were almost double those observed for either

of the calibration particles used. These data are consistent with a highly disperse mixture of particles, the passage of rod-shaped particles at various orientations as they traverse the pore, or some combination of the two. Asymmetry data from both pores were unable to distinguish between *Shewanella* particles and spherical calibration particles, but the gradients and gradient ratios of pulses could do so.

For this study, examination of individual pulses in comparison to pulses produced using the semi-analytic model are in reasonable agreement for spherical particles. Model pulses for *Shewanella* particles systematically underestimate pulse FWHM and over-estimate pulse asymmetry. This disparity, whilst being linked to the small pore opening size and pore geometry, is a clear direction for future refinement of the semi-analytic model. In particular, measurements of particle velocity would provide greater insight into the causes of these disparities. Overall, results suggest that TRPS may be able to be used to monitor the growth rates, lysis or aggregation behaviour of bacteria and this application warrants further investigation.

Bacterially produced BPHA particles, reported by the manufacturer to have a mean diameter of 100-500 nm [127] with a poorly-known size distribution, were measured using both SEM and TRPS. SEM images suggest a mean particle of diameter of 260 ± 50 nm with a symmetric distribution and the presence of some aggregates. TRPS measurements show a reproducible, skewed distribution of spherical particle diameters from 1000 nm

to 350 nm with a median particle size between 416 and 421 nm. Repeated measurements at a lower pore stretch reproduce this skewed distribution with a median particle diameter of 328 nm. The high relative population of smaller particles in these distributions contrasts with results from both the manufacturer and SEM data. This degree of precision in the relative populations of particle sizes has not been possible for this particle set prior to the application of TRPS. Further filtration of the particles could enable further measurements of the particles using an NP200 pore which would improve the lower limit of detection to ∼100 nm diameter particles. Additional functionalisation of the BPHA particles, or the addition of the antigen to which they are sensitive, may allow TRPS to be used in an aggregation assay or to study BPHA particle surface charge.

8.5 Summary

TRPS has been shown as a viable, reproducible method for measuring the size, concentration and charge of nanoparticles in liquid samples, at least to levels of similar precision to other comparable modern methods. TRPS has now been applied to measuring the shape of nanoparticles and complex mixtures of nanoparticles, and it also shows promise in these areas. Whilst the tuneable pores studied in this thesis are too large for sequencing applications, the RPS field will likely continue progression towards this commercial application in the near future. However the ease of production and tuning capabilities of TRPS pores also suggest that they may find

additional applications involving particles 100 nm in size or larger, including some viruses, bacteria, environmental pollutants, synthetic nanoparticle characterisation and more. Despite the lack of analyte specificity compared to antibody-binding detection methods, the ease of use and lack of reagents required for TRPS also hint at potential applications in drug delivery, viral analysis and exosome studies. The results presented in this thesis however indicate that ζ-potential and shape measurements may ultimately be incorporated into a TRPS benchtop apparatus, alongside size and concentration measurements, for a price comparable to or cheaper than existing technologies.

Bibliography

[1] R.P. Feynman. There's plenty of room at the bottom. *Engineering and Science*, 23(5):22–36, 1960.

[2] W H Coulter. Means for counting particles suspended in a fluid. United States Patent US 2,656,508, October 1953.

[3] Stephen J. Sowerby, Murray F. Broom, and George B. Petersen. Dynamically resizable nanometre-scale apertures for molecular sensing. *Sensors and Actuators B*, 123(1):325–330, April 2007.

[4] E Regis. *Nano: The Emerging Science of Nanotechnology: Remaking the World-Molecule by Molecule*. Little Brown and Company, Boston, 1995.

[5] Andrew R Parker and Helen E Townley. Biomimetics of photonic nanostructures. *Nature nanotechnology*, 2:347–353, 2007.

[6] MTANZ Ltd. MEDICAL TECHNOLOGY INDUSTRY SECTOR BLUEPRINT 2011 A global ambition A thriving medtech econ-

omy. Technical report, The Medical Technology Association of New Zealand, Greenlane Central, Auckland, Auckland, 2011.

[7] New Zealand Izon Science Limited, Christchurch. About us. Retrieved from http://www.izon.com/about-us/, April 2012.

[8] G R Willmott and P W Moore. Reversible mechanical actuation of elastomeric nanopores. *Nanotechnology*, 19(47):475504, November 2008.

[9] H Bayley and C R Martin. Resistive-Pulse sensing - from microbes to molecules. *Chem. Rev.*, 100:2575–2594, 2000.

[10] R W DeBlois and C P Bean. Counting and Sizing of Submicron Particles by the Resistive Pulse Sensing Technique. *The Review of Scientific Instruments*, 41(7):909–916, July 1970.

[11] R W DeBlois and C P Bean. Electrokinetic Measurements with Submicron Particles and Pores by the Resistive Pulse Technique. *Journal of Colloid and Interface Science*, 61(2):323–335, September 1977.

[12] R DeBlois, E E Uzgiris, D H Cluxton, and H M Mazzone. Comparative measurements of size and polydispersity of several insect viruses. *Anal. Biochem.*, 90:273–288, 1978.

[13] R R Henriquez, T Ito, L Sun, and R M Crooks. The resurgence of Coulter counting for analyzing nanoscale objects. *The Analyst*, 129:478–482, 2004.

[14] J Kasianowicz, E Brandin, D Branton, and D Deamer. Characterization of individual polynucleotide molecules using a membrane channel. *Proceedings of the National Academy of Sciences USA*, 93:13770–13773, 1996.

[15] K Healy, B Schiedt, and A P Morrison. Solid-state nanopore technologies for nanopore-based DNA analysis. *Nanomedicine*, 2(6):875–897, 2007.

[16] C Dekker. Solid-state nanopores. *Nature Nanotechnology*, 2:209–215, April 2007.

[17] G Roberts, D Kozak, W Anderson, M F Broom, R Vogel, and M Trau. Tunable Nano/Micropores for Particle Detection and Discrimination: Scanning Ion Occlusion Spectroscopy. *Small*, 6:2653–2658, 2010.

[18] Geoff R. Willmott and Beth E. T. Parry. Resistive pulse asymmetry for nanospheres passing through tunable submicron pores. *Journal of Applied Physics*, 109(9):094307, 2011.

[19] W H Coulter. High speed automatic blood cell counter and cell size analyzer. In *Proceedings of the National Electronics Conference*, volume 12, pages 1034–1042, 1956.

[20] E Gregg and K D Steidley. Electrical counting and sizing of mammalian cells in suspension. *Biophysical Journal*, 5:393–405, 1965.

[21] P B Price and R L Fleischer. High-resolution study of low-eergy heavy cosmic rays with lexan track detectors. *Physical Review Letters*, 21(9):630–633, August 1968.

[22] L Song, M R Hobaugh, C Shustak, S Cheley, H Bayley, and J E Gouaux. Structure of staphylococcal alpha-hemolysin, a heptameric transmembrane pore. *Science (New York, N.Y.)*, 274(5294):1859–66, December 1996.

[23] S Majd, E C Yusko, Y N Billeh, M X Macrae, J Yang, and M Mayer. Applications of biological pores in nanomedicine, sensing, and nanoelectronics. *Current Opinion in Biotechnology*, 21:439–476, 2010.

[24] S Howorka and Z Siwy. Nanopore Analytics: sensing of single molecules. *Chemical Society Reviews*, 38:2360–2384, 2009.

[25] Zuzanna S Siwy and Matthew Davenport. Nanopores: Graphene opens up to DNA. *Nature nanotechnology*, 5(10):697–8, October 2010.

[26] Amit Meller, Lucas Nivon, and Daniel Branton. Voltage-Driven DNA Translocations through a Nanopore. *Physical Review Letters*, 86(15):3435–3438, April 2001.

[27] J Clarke, H Wu, L Jayasinghe, A Patel, S Reid, and H Bayley. Continuous base identification for single-molecule nanopore DNA sequencing. *Nature Nanotechnology*, 4, April 2009.

[28] D Branton, D W Deamer, A Marziali, H Bayley, S A Benner, T Butler, M Di Ventra, S Garaj, A Hibbs, X Huang, S B Jovanovich, P S Krstic, S Lindsay, X S Ling, C H Mastrangelo, A Meller, J S Oliver, Y V Pershin, J M Ramsey, R Riehn, G V Soni, V Tabard-Cossa, M Wanunu, M Wiggin, and J A Schloss. The potential and challenges of nanopore sequencing. *Nature Biotechnology*, 26:1146–1153, 2008.

[29] M Rincon-Restrepo, E Mikhailova, H Bayley, and G Maglia. Controlled Translocation of Individual DNA Molecules through Protein Nanopres with Engineered Molecular Brakes. *Nano Letters*, 11(2):746–750, January 2011.

[30] J E Hall. Access resistance of a small circular pore. *The Journal of general physiology*, 66(4):531–2, October 1975.

[31] Philip M Ashton, Satheesh Nair, Tim Dallman, Salvatore Rubino, Wolfgang Rabsch, Solomon Mwaigwisya, John Wain, and Justin O'Grady. MinION nanopore sequencing identifies the position and structure of a bacterial antibiotic resistance island. *Nature Biotechnology*, 33(3), December 2014.

[32] J Li, D Stein, C McMullan, D Branton, M J Aziz, and J a Golovchenko. Ion-beam sculpting at nanometre length scales. *Nature*, 412(6843):166–169, July 2001.

[33] A J Storm, J H Chen, X S Ling, H W Zandbergen, and C Dekker. Fab-

rication of solid-state nanopores with single-nanometre precision. *Nature*, 2:537–540, August 2003.

[34] Miloslav Karhanek, Jennifer T Kemp, Nader Pourmand, Ronald W Davis, and Chris D Webb. Single DNA molecule detection using nanopipettes and nanoparticles. *Nano letters*, 5(2):403–7, February 2005.

[35] B Zhang, J Galusha, P G Shiozawa, G Wang, A J Bergren, R M Jones, R J White, E N Ervin, C C Cauley, and H S White. Bench-top method for fabricating glass-sealed nanodisk electrodes, glass nanopore electrodes, and glass nanopore membranes of controlled size. *Analytical Chemistry*, 79(13):4778–4787, July 2007.

[36] T Ito and R M Crooks. Simultaneous determination of the size and surface charge of individual nanoparticles using a carbon nanotube-based coulter counter. *Analytical Chemistry*, 75(10):2399–2406, May 2003.

[37] L T Sexton, L P Horne, and C R Martin. Developing synthetic conical nanopores for biosensing applications. *Mol. BioSyst.*, 3:667–685, 2007.

[38] Omar a. Saleh and Lydia L. Sohn. An artificial nanopore for molecular sensing. *Nano Letters*, 3(1):37–38, January 2003.

[39] S Wu, S R Park, and X S Ling. Lithography-free formation of

nanopores in plastic membranes using laser heating. *Nano Letters*, 6:2571–2576, 2006.

[40] R An, J D Uram, E C Yusko, K Ke, M Mayer, and A J Hunt. Ultrafast laser fabrication of submicrometer pores in borosilicate glass. *Optics Letters*, 33:1153–1155, 2008.

[41] Dario Anselmetti. Nanopores: Tiny holes with great promise. *Nature nanotechnology*, 7(2):81–2, January 2012.

[42] G R Willmott, R Vogel, S Yu, L G Groenewegen, G Roberts, D Kozak, W Anderson, and M Trau. Use of tunable nanopore blockade rated to investigate colloidal dispersions. *Journal of Physics: Condensed Matter*, 22:454116, 2010.

[43] Geoff R. Willmott, Murray F. Broom, Murray L. Jansen, R M Young, and W. Mike Arnold. Tunable Elastometic Nanopores. In *Molecular- and Nano-Tubes:*, chapter 7, pages 209–261. Springer, 2013.

[44] Murray L. Jansen, Geoff R. Willmott, Ingrid Hoek, and W. Mike Arnold. Fast piezoelectric actuation of an elastomeric micropore. *Measurement*, 46(9):3560–3567, November 2013.

[45] D Kozak, W Anderson, R Vogel, and M Trau. Advances in resistive pulse sensors: Devices bridging the void between molecular and microscopic detection. *Nano Today*, 6:531–545, 2011.

[46] Robert Vogel, Geoff Willmott, Darby Kozak, G Seth Roberts, Will Anderson, Linda Groenewegen, Ben Glossop, Anne Barnett, Ali Turner, Matt Trau, and L Groenewgen. Quantitative Sizing of Nano-Microparticle with a Tunable Elastomeric Pore Sensor. *Analytical Chemistry*, 83(9):3499–3506, May 2011.

[47] Darby Kozak, Will Anderson, Robert Vogel, Shaun Chen, Fiach Antaw, and Matt Trau. Simultaneous Size and ζ-Potential Measurements of Individual Nanoparticles in Dispersion Using Size-Tunable Pore Sensors. *ACS nano*, 6(8):6990–6997, July 2012.

[48] Geoff R Willmott, Mark Platt, and Gil U Lee. Resistive pulse sensing of magnetic beads and supraparticle structures using tunable nanopores. *Biomicrofluidics*, 6(1):14103, March 2012.

[49] Basf Polyurethanes Gmbh. General product information Elastollan ® 1160 D. Technical report, BASF, Boston, Mass., September 2010.

[50] Eva Weatherall and Geoff R Willmott. Conductive and biphasic pulses in tunable resistive pulse sensing. *The journal of physical chemistry. B*, 119(16):5328–35, April 2015.

[51] G S Roberts, S Yu, Q Zeng, L C L Chan, W Anderson, A H Colby, M W Grinstaff, S Reid, and R Vogel. Tunable pores for measuring concentrtions of synthetic and biological nanoparticle dispersions. *Biosenors and Bioelectronics*, 2011.

[52] Robert Vogel, Will Anderson, James Eldridge, Ben Glossop, and Geoff Willmott. A variable pressure method for characterizing nanoparticle surface charge using pore sensors. *Analytical chemistry*, 84(7):3125–31, April 2012.

[53] J Maxwell. *A Treatise on Electricity and Magnetism*, volume 1. Clarendon Press, Oxford, 3rd edition, 1904.

[54] Lord Rayleigh. LVI. On the influence of obstacles arranged in rectangular order upon the properties of a medium. *Philosophical Magazine Series 5*, 34(211):481–502, 1892.

[55] Geoff R. Willmott, Samuel S. C. Yu, and Robert Vogel. Pressure dependence of particle transport through resizable nanopores. In *ICONN conference proceedings*, pages 128–131. Ieee, February 2010.

[56] Geoff R Willmott, Matthew G Fisk, and James Eldridge. Magnetic microbead transport during resistive pulse sensing. *Biomicrofluidics*, 7(6):64106, January 2013.

[57] G R Willmott, R Vogel, S S C Yu, L G Groenewegen, G S Roberts, D Kozak, W Anderson, and M Trau. Use of tunable nanopore blockade rates to investigate colloidal dispersions. *Journal of physics. Condensed matter : an Institute of Physics journal*, 22(45):454116, November 2010.

[58] Z.S. Siwy. IonCurrent Rectification in Nanopores and Nanotubes

with Broken Symmetry. *Advanced Functional Materials*, 16(6):735–746, April 2006.

[59] E Garza-Licudine, D Deo, S Yu, A Uz-Zaman, and W B Dunbar. Portable Nanoparticle Quantization using a Resizable Nanopore Instrument - The IZON qNano(tm). In *32nd Annual International Conference of the IEE EMBS*, pages 5736–5739, 2010.

[60] Martin a. M. Gijs. Magnetic bead handling on-chip: new opportunities for analytical applications. *Microfluidics and Nanofluidics*, pages 22–40, October 2004.

[61] M Low, S Yu, M Y Han, and X Su. Investigative Study of Nucleic Acid-Gold Nanoparticle Interactions Using Laser-based Techniques, Electron Microscopy, and Resistive Pulse Sensing with a Nanopore. *Aust. J. Chem.*, 64:1229–1234, 2011.

[62] Geoff R Willmott. Modelling Resistive Pulse Sensing of Antibody-Modified Nanospheres and Dimers using Izon's qNano. Technical Report June, Industrial Research Limited, Wellington, 2011.

[63] Omar a Alsager, Shalen Kumar, Geoff R Willmott, Kenneth P McNatty, and Justin M Hodgkiss. Small molecule detection in solution via the size contraction response of aptamer functionalized nanoparticles. *Biosensors & bioelectronics*, 57:262–8, July 2014.

[64] Eva Weatherall and Geoff R. Willmott. Applications of tunable resistive pulse sensing. *The Analyst*, 140:3318–3334, 2015.

[65] Emma L. C. J. Blundell, Laura J. Mayne, Emily R. Billinge, and Mark Platt. Emergence of tunable resistive pulse sensing as a biosensor. *Anal. Methods*, 00:1–12, 2015.

[66] Satinder K. Brar and M. Verma. Measurement of nanoparticles by light-scattering techniques. *TrAC Trends in Analytical Chemistry*, 30(1):4–17, January 2011.

[67] Malvern Instruments. Zeta Potential Theory. In *Nano Series and HPPS training Manual*, chapter 5, pages 45–65. Malvern Instruments Ltd, Worcestershire, 2010.

[68] Robert D. Boyd, Siva K. Pichaimuthu, and Alexandre Cuenat. New approach to inter-technique comparisons for nanoparticle size measurements; using atomic force microscopy, nanoparticle tracking analysis and dynamic light scattering. *Colloids and Surfaces A: Physicochemical and Engineering Aspects*, 387(1-3):35–42, August 2011.

[69] James B Falabella, Tae Joon Cho, Dean C Ripple, Vincent a Hackley, and Michael J Tarlov. Characterization of gold nanoparticles modified with single-stranded DNA using analytical ultracentrifugation and dynamic light scattering. *Langmuir : the ACS journal of surfaces and colloids*, 26(15):12740–7, August 2010.

[70] Frank Thielbeer, Ken Donaldson, and Mark Bradley. Zeta potential mediated reaction monitoring on nano and microparticles. *Bioconjugate chemistry*, 22(2):144–50, February 2011.

[71] Hiran Vegad. An introduction to particle size characterisation by DCS: Do you know the real size of your nanoparticles? Technical report, Analytik Ltd, Cambridge, 2010.

[72] Tae Joon Cho and Vincent a Hackley. Fractionation and characterization of gold nanoparticles in aqueous solution: asymmetric-flow field flow fractionation with MALS, DLS, and UV-Vis detection. *Analytical and bioanalytical chemistry*, 398(5):2003–18, November 2010.

[73] Rolf Erni, Marta Rossell, Christian Kisielowski, and Ulrich Dahmen. Atomic-Resolution Imaging with a Sub-50-pm Electron Probe. *Physical Review Letters*, 102(9), March 2009.

[74] a Bogner, P-H Jouneau, G Thollet, D Basset, and C Gauthier. A history of scanning electron microscopy developments: towards "wet-STEM" imaging. *Micron (Oxford, England : 1993)*, 38(4):390–401, January 2007.

[75] Thomas P Burg, Michel Godin, Scott M Knudsen, Wenjiang Shen, Greg Carlson, John S Foster, Ken Babcock, and Scott R Manalis. Weighing of biomolecules, single cells and single nanoparticles in fluid. *Nature*, 446(7139):1066–9, April 2007.

[76] Michel Godin, Andrea K. Bryan, Thomas P. Burg, Ken Babcock, and Scott R. Manalis. Measuring the mass, density, and size of particles and cells using a suspended microchannel resonator. *Applied Physics Letters*, 91(12):123121, 2007.

[77] Philip Dextras, T.P. Burg, and S.R. Manalis. Integrated measurement of the mass and surface charge of discrete microparticles using a suspended microchannel resonator. *Analytical chemistry*, 81(11):4517–4523, 2009.

[78] P Walstra. Approximation formulae for the light scattering coefficient of dielectric spheres. *British Journal of Applied Physics*, 15:1545–1552, 1964.

[79] Bob Carr. Real-time nanoparticle detection and analysis on a particle-by-particle basis. *SPIE Newsroom*, 2(c):2–3, 2009.

[80] Vasco Filipe, Andrea Hawe, and Wim Jiskoot. Critical evaluation of Nanoparticle Tracking Analysis (NTA) by NanoSight for the measurement of nanoparticles and protein aggregates. *Pharmaceutical research*, 27(5):796–810, May 2010.

[81] S.T. Fitzpatrick. Structure and method for centrifugal sedimentation particle size analysis of particles of lower density than their suspension medium. United States Patent US 5,786,898, July 1998.

[82] George Gabriel Stokes, Joseph Larmor, and John William Strutt

Rayleigh. *Mathematical and physical papers (1880)*. Cambridge : University Press, volume3 edition, 1880.

[83] Elizabeth a Heins, Zuzanna S Siwy, L A Barker, Charles R Martin, and Lane a Baker. Detecting single porphyrin molecules in a conically shaped synthetic nanopore. *Nano Letters*, 5(9):1824–1829, September 2005.

[84] G. R. Willmott, R. Chaturvedi, S. J. W. Cummins, and L. G. Groenewegen. Actuation of Tunable Elastomeric Pores: Resistance Measurements and Finite Element Modelling. *Experimental Mechanics*, September 2013.

[85] G R Willmott and B G Smith. Modelling of resistive pulse sensing : flexible methods for submicron particles. *Bull. Austal. Math. Soc.*, 0:1–6, 2012.

[86] H.E. Kubitschek. Electronic Measurement of particle size. *Research*, 13:128–35, 1960.

[87] W Smythe. Flow Around a Spheroid in a Circular Tube. *Phys. Fluids*, 7:633–638, 1964.

[88] J. C. Cooke. On Potential Problems Involving Spheroids inside a Cylinder. *ZAMM - Zeitschrift für Angewandte Mathematik und Mechanik*, 42(7-8):305–316, 1962.

[89] R Schoch, J Han, and P Renaud. Transport phenomena in nanofluidics. *Reviews of Modern Physics*, 80:839–883, July 2008.

[90] Todd M Squires. Microfluidics : Fluid physics at the nanoliter scale. *Reviews of Modern Physics*, 77(July), 2005.

[91] S Devasenathipathy and J Santiago. *Micro- and Nano-Scale Diagnostic Techniques*. Springer Verlag, 2003.

[92] R.J. Hunter. *Foundations of Colloid Science*. Clarendon Press, 1989, volume 2 edition, 1989.

[93] CL Rice. Electrokinetic flow in a narrow cylindrical capillary. *The Journal of Physical Chemistry*, 69(11):4017–4024, 1965.

[94] M. von Smoluchowski. No Title. *Bull. Int. Acad. Sci. Cracovie*, 184, 1903.

[95] A Delgado, F Gonzalez-Caballero, R Hunter, L Koopal, and J Lyklema. Measurement and interpretation of electrokinetic phenomena. *Journal of Colloid and Interface Science*, 309:194–224, 2007.

[96] P Attard, D Antelmi, and I Larson. Comparison of the Zeta Poptential with Diffuse Layer Potential from Charge Titration. *Langmuir*, 16:1542–1552, 2000.

[97] K Ohsawa, M Murata, and H Ohshima. Zeta potential and surface charge density of polystyrene-latex; comparison with synaptic vesi-

cle and brush border membrane vesicle. *Colloid and Polymer Science*, 264:1005–1009, 1986.

[98] B Kirby and E Hasselbrink. Zeta potential of microfluidic substrates: 1. Theory, experimental techniques, and effects on separation. *Electrophoresis*, 25:187–202, 2004.

[99] Yuejun Kang, Dongqing Li, Spyros a Kalams, and Josiane E Eid. DC-Dielectrophoretic separation of biological cells by size. *Biomedical microdevices*, 10(2):243–9, April 2008.

[100] Mohammad a. Charsooghi, Ehsan a. Akhlaghi, Sharareh Tavaddod, and H.R. Khalesifard. A MATLAB program to calculate translational and rotational diffusion coefficients of a single particle. *Computer Physics Communications*, 182(2):400–408, February 2011.

[101] D.C. Golibersuch. Observation of aspherical particle rotation in Poiseuille flow via the resistance pulse technique. II. Application to fused sphere"dumbbells". *Journal of Applied Physics*, 44(6):2580–2584, 1973.

[102] Robert C. Weast. *CRC Handbook of Chemistry and Physics*. The Chemical Rubber Co, Boca Raton, Fl, 52nd edition, 1971.

[103] Basf Polyurethanes Gmbh. General product information Elastollan ® 1160 D. Technical Report September, BASF, 2010.

[104] John H L Beal, Andrea Bubendorfer, Tim Kemmitt, Ingrid Hoek, and W Mike Arnold. A rapid, inexpensive surface treatment for enhanced functionality of polydimethylsiloxane microfluidic channels. *Biomicrofluidics*, 6(3):36503, September 2012.

[105] John R. Martin and Robert J. Gardner. Effect of long term humid aging on plastics. *Polymer Engineering and Science*, 21(9):557–565, June 1981.

[106] Mark Platt, Geoff R Willmott, and Gil U Lee. Resistive pulse sensing of analyte-induced multicomponent rod aggregation using tunable pores. *Small (Weinheim an der Bergstrasse, Germany)*, 8(15):2436–44, August 2012.

[107] Robert J. Hunter. *Zeta potential in colloid science: Principles and Applications*. Academic Press, London, 1981.

[108] Andrei S. Dukhin and Philip J. Goetz. *Ultrasound for Characterizing Colloids Particle Sizing, Zeta Potential Rheology*. Elsevier, 2002.

[109] T Ito, L Sun, M A Bevan, and R M Crooks. Comparison of Nanoparticle size and electrophoretic mobility measurements using a carbon-nanotube-based coulter counter, dynamic light scattering, transmission electron microscopy, and phase analysis light scattering. *Langmuir*, 20:6940–6945, 2004.

[110] James a Somerville, Geoff R Willmott, James Eldridge, Marjorie Grif-

fiths, and Kathryn M Mcgrath. Size and charge characterisation of a submicrometre oil-in-water emulsion using resistive pulse sensing with tunable pores. *Journal of colloid and interface science*, 394:1–26, March 2013.

[111] Nima Arjmandi, Willem Van Roy, Liesbet Lagae, and Gustaaf Borghs. Measuring the electric charge and zeta potential of nanometer-sized objects using pyramidal-shaped nanopores. *Analytical chemistry*, 84(20):8490–6, October 2012.

[112] James a. Eldridge, Geoff R. Willmott, Will Anderson, and Robert Vogel. Nanoparticle ζ-potential measurements using tunable resistive pulse sensing with variable pressure. *Journal of Colloid and Interface Science*, 429:45–52, September 2014.

[113] TechNote 206 9025: Equations. Retrieved from www.bangslabs.com /sites/default/files/bangs/docs/pdf/206.pdf, March 2001.

[114] JA Osborn. Demagnetizing factors of the general ellipsoid. *Phys. Rev.*, 67(11-12):351–357, 1945.

[115] Matthew Pevarnik, Ken Healy, and ME Toimil-Molares. Polystyrene particles reveal pore substructure as they translocate. *ACS nano*, 6(8):7295–7302, 2012.

[116] Justin Menestrina, Crystal Yang, Matthew Schiel, Ivan Vlassiouk, and Zuzanna S. Siwy. Charged Particles Modulate Local

Ionic Concentrations and Cause Formation of Positive Peaks in Resistive-Pulse-Based Detection. *The Journal of Physical Chemistry C*, 118(5):2391–2398, February 2014.

[117] WJ Lan, Clemens Kubeil, and JW Xiong. Effect of surface charge on the resistive pulse waveshape during particle translocation through glass nanopores. *The Journal of Physical Chemistry C*, 118:2726–2734, 2014.

[118] David Freedman and Persi Diaconis. On the histogram as a density estimator:L 2 theory. *Zeitschrift fr Wahrscheinlichkeitstheorie und Verwandte Gebiete*, 57(4):453–476, December 1981.

[119] M Platt. Personal Communciation, 2013.

[120] C W Jackson, N K Hutson, S A Steward, R A Ashmun, D S Davis, H H Edwards, J E Rehg, and M E Dockter. The Wistar Furth Rat: An Animal Model of Heredity Macrothrombocytopenia. *Blood*, 71(6):1676–1686, 1988.

[121] C. Johnson-Delaney. *Exotic Animal Companion Medicine Handbook for Veterinarians*. Zoological Education Network, Lake Worth, FL, 1996.

[122] P Mangin, P Ohlmann, A Eckly, J Cazenave, F Lanza, and C Gachet. The P2Y1 receptor plays an essential role in the platelet shape change induced by collagen when TxA2 formation is prevented. *Journal of Thrombosis and Haemostasis*, 2:969–977, 2004.

[123] T R Gregory. Nucleotypic effects without nuclei: genome size and erythrocyte size in mammals. *Genome / National Research Council Canada = Génome / Conseil national de recherches Canada*, 43(5):895–901, October 2000.

[124] M. Arnold and J. Ryan. Personal Communication, 2013.

[125] M. Satomi. Shewanella marinintestina sp. nov., Shewanella schlegeliana sp. nov. and Shewanella sairae sp. nov., novel eicosapentaenoic-acid-producing marine bacteria isolated from sea-animal intestines. *International Journal of Systematic and Evolutionary Microbiology*, 53(2):491–499, March 2003.

[126] Will Anderson, Darby Kozak, Victoria a Coleman, Sa K Jämting, and Matt Trau. A comparative study of submicron particle sizing platforms: Accuracy, precision and resolution analysis of polydisperse particle size distributions. *Journal of colloid and interface science*, March 2013.

[127] K Grage and A Jahns. Bacterial Polyhydroxyalkanoate Granules: Biogenesis, Structure, and Potential Use as Nano-/Micro-Beads in Biotechnological and Biomedical Applications. *Biomacromolecules*, 10:660–669, 2009.

[128] Martin Trebbin, Dagmar Steinhauser, Jan Perlich, Adeline Buffet, Stephan V Roth, Walter Zimmermann, Julian Thiele, and Stephan

Förster. Anisotropic particles align perpendicular to the flow direction in narrow microchannels. *Proceedings of the National Academy of Sciences of the United States of America*, 110(17):6706–11, April 2013.